CARDIFF
UNIVERSITY
PRIFYSGOL
CAERDYDD

BINDING SERVICES
Tel +44 (0)29 2087 4949
Fax +44 (0)29 20371921
e-mail bindery@cardiff.ac.uk

CARDIFF
UNIVERSITY
PRIFYSGOL
CAERDYDD

Heterogeneous Catalytic Oxidation, a Theoretical Study.

Rudy Coquet

PhD thesis, September 2005

UMI Number: U584749

All rights reserved

INFORMATION TO ALL USERS
The quality of this reproduction is dependent upon the quality of the copy submitted.

In the unlikely event that the author did not send a complete manuscript
and there are missing pages, these will be noted. Also, if material had to be removed,
a note will indicate the deletion.

UMI U584749
Published by ProQuest LLC 2013. Copyright in the Dissertation held by the Author.
Microform Edition © ProQuest LLC.
All rights reserved. This work is protected against
unauthorized copying under Title 17, United States Code.

ProQuest LLC
789 East Eisenhower Parkway
P.O. Box 1346
Ann Arbor, MI 48106-1346

« L'avenir n'est jamais que du présent à mettre en ordre.
Tu n'as pas à le prévoir, mais à le permettre. »

Antoine de Saint-Exupéry

Acknowledgements

First of all, I would like to express my gratitude to my supervisor, Dr David J. Willock. We had many work related discussions (and not only), which had an important role in my research and in my scientific development. I would also like to thank my two other academic supervisors, Prof. Graham J. Hutchings and Dr Stuart H. Taylor for their useful remarks on my work. I should also mention my co-worker Javier Franqueira-Valo, who started his PhD with me and was involved with the experimental side of the methane activation project.

I want to thank all the members, present and past, of the Theoretical Chemistry group at Cardiff University. Prof. Peter J. Knowles, Dr Jamie A. Platts, Dr Massimo Mella, Dr Nicholas T. Wilson and all my co-workers and friends from the office 1.95. This includes the past PhD students (Bob, Chris, Farah, John, Olivier and Rajinder) and the present ones (Arturo, Ed, Gareth, James, Mike and Steve). Without them, my PhD would have been much more difficult.

Thank you Benoit, Camille, Caroline, Gaspard, Ousseynou, Manue and Thierry for the good time we all had in Cardiff. Thank you to all my friends in France and Japan for the great moments we had together. I hope the life I have chosen will allow us to meet up again soon.

For the patience, comprehension, love and support I would like to thank my beloved Kaoru who managed to open my eyes and to show me the important things in life. Those three years far from each other have only managed to strengthen the links that exist between us.

Here is the place to express my profound gratitude to my parents. I could never have become who I am now without their love, support and trust. Thank you also to my sister Caroline, who proved to me that courage and willpower are a real treasure in this complicated society. I am thankful to all my family and wish to dedicate this thesis to my grandparents, who I know, would have been so proud of me.

Finally, I would like to thank SASOL Ltd for funding my PhD and providing me with enough freedom to follow my own ideas. Thanks also to the Materials Chemistry Consortium for the time on the supercomputer HPCx and to the Helix cluster committee of Cardiff University. I am grateful to Dr Ian Thomas for his help with compilers and libraries on Helix.

Contents

Acknowledgements IV

Declaration and statements V

Contents VI

List of papers VIII

Summary IX

1. General introduction 1

2. Literature review 8

2.1 Methane activation 8

2.2 Supported gold catalysts 29

References 46

3. Theory 50

3.1 Density functional theory 50

3.2 Geometry optimisers 56

3.3 Vibrational frequency calculations 58

3.4 Bader charge analysis 60

3.5 Density of states 62

3.6 Implementation of DFT 63

References 68

4. Methodology **69**
4.1 Pseudopotential generation 69
4.2 Converging the calculation parameters 79
4.3 Lattice parameters optimisation 82
4.4 Basis set superposition error and adsorption energy 84
4.5 Bader charge calculations 86
4.6 Transition states search 88
References 92

5. Methane activation over molybdena **93**
5.1 Introduction 93
5.2 Computational details 96
5.3 Bulk and perfect (010) surface 99
5.4 Defective (010) surface and O_2 adsorption 105
5.5 H and CH_3 adsorption 120
5.6 C–H bond activation 133
5.7 Conclusions 148
References 151

6. Gold adsorption and catalysis over magnesia **154**
6.1 Introduction 154
6.2 Computational details 157
6.3 Au on the perfect MgO(001) surface 160
6.4 Au on the defective MgO(001) surface (F centre) 171
6.5 Au on the kinked surfaces MgO(1 3 10) and MgO(1 3 12) 183
6.6 Au oxidation state: effects on CO adsorption 193
6.7 Conclusions 210
References 213

7. General conclusions **215**

Appendix

List of papers

Chapter 5: **Methane activation on molybdena**

- Methane activation on $MoO_3(010)$, a DFT+U study. *J. Phys. Chem. B*, in preparation.

- The (010) surface of α-$MoO_3(010)$, a DFT+U study. *Phys. Chem. Chem. Phys.*, 2005, DOI: 10.1039/b511044k.

Chapter 6: **Gold adsorption and catalysis on magnesia**

- Gold nanoclusters supported on MgO, a DFT study. *J. Mat. Chem.*, in preparation.

- CO adsorption on supported Au particles and the influence of Au oxidation state, a DFT perspective. *Chem. Comm.*, in preparation.

Summary

Methane activation over molybdenum trioxide and gold catalysts supported on magnesium oxide were studied employing state of the art computational modelling.

The localisation of electrons at a terminal oxygen point defect on $MoO_3(010)$ was well represented by DFT+U whereas conventional DFT failed to localise the two unpaired electrons on Mo. The hybrid DFT functional PBE0 was employed within a cluster model and a spin population of 1.96 was calculated for Mo and used to fit the Dudarev's parameter U–J at a value of 6.3 eV.

The asymmetric oxygen centre was found to be the preferred adsorption site for both hydrogen and methyl radical adsorption, losing its asymmetric character. Mo exhibited the weakest interaction with the adsorbates and methyl was found to be weakly adsorbed between Mo and its closest asymmetric oxygen, suggesting mobility on the surface.

A transition state for methane activation was located with hydrogen and carbon respectively interacting with terminal oxygen and Mo. A Bader charge analysis of this transition state coupled with a spin population analysis indicated a heterolytic cleavage. An activation energy of 129.7 kJ mol^{-1} was calculated using the NEB method.

On MgO(001), atomic gold was found to preferentially adsorb at five-coordinated oxygen sites and the Au–O bond was partially covalent in nature. F centres represented anchoring points with increased adsorption energy and charge transfer to Au. A three-dimensional growth was favoured over two-dimensional growth and the adsorbed Au_{10} clusters were negatively charged at the interface.

Atomic gold on the oxygen kink site of MgO(1 3 10) presented an adsorption energy 0.30 eV higher than that on a five-coordinated oxygen centre of MgO(001). Au_{10} was also found to strongly interact with the oxygen kink site of MgO(1 3 12).

Hydroxyl groups were employed to tailor the gold oxidation state and CO was used as a probe molecule. For both atomic gold and Au_{10}, the CO stretching vibrational frequency increased with the oxidation state. CO had an unfavourable binding energy on Au(III) but was strongly adsorbed on Au(I). An increase in the number of adsorbates reduced the negative charge of Au_{10}, also increasing the CO stretching vibrational frequency and bringing it closer to the experiment. It is thus expected that CO will bind to $Au^{\delta+}$ particles in the working catalyst.

Chapter 1

General introduction

The work described in this thesis focuses on methane activation over molybdenum trioxide and gold catalysts supported on magnesium oxide. In sections 1.1 and 1.2, we will provide some background in these two fields. Then we will discuss the scope of the thesis and the questions it addresses.

1.1 Methane activation

The world economy depends on petroleum; not just gasoline and heating oil, but the majority of our industrial chemicals, the raw materials for everything from paint to plastic to fertiliser. While oil is a raw material which has allowed these fields to develop, it is a finite resource whose life time is often quoted in decades rather than hundreds of years. Natural gas, many chemists believe, could take up some of the burden since the world reserves of natural gas are in excess of those of petroleum. The problem is figuring out how to make efficient use of the available gas reserves since whenever petroleum is pumped out of the ground, there is some methane too. While the first can easily be loaded onto ships and moved to where it is needed, the low boiling point and flammability of methane make transportation too dangerous. What is required is a conversion process for converting methane to a form which is liquid at source.

The idea of making liquid synthetic fuels is not new. In 1923, two German coal researchers, Franz Fischer and Hans Tropsch, discovered a way to turn the copious coal reserves of the Ruhr Valley into synthetic oil. The scientists found that by passing methane over metal catalysts they could make synthetic fuel. During World War II, the German government used the Fischer-Tropsch process to produce around 600,000 barrels per year of military fuel from the plentiful coal deposits of the country.

In the 1950s, the South African government found itself with little or no access to petroleum and turned to the Fischer-Tropsch process, building several plants to convert coal from the extensive deposits of the country into synthetic fuels.

Nowadays, Exxon Mobil, Shell and South Africa's SASOL are all involved in projects to convert natural gas into liquid and the major oil companies plan to spend nearly £6 billion on gas-to-liquid capacity in future plants.

However, the Fischer-Tropsch process is inherently inefficient and expensive. It requires temperatures of around 800 to 900 °C, and those are achieved by burning part of the gas being converted. The technology is also relatively non-selective, producing a large range of hydrocarbon molecules, some of which are useless. The fundamental problem is that it is technology from 1940s and uses brute force and high temperature to achieve the conversions.

Natural gas is mainly methane and transforming it into methanol, an easily transportable liquid, is "simply" a matter of adding an oxygen atom to the methane molecule. There are, however, some dramatic problems in turning this direct-synthesis theory into chemical reality. The catalyst needs to break the strong carbon–hydrogen bond in methane to allow the oxygen to react and the reaction needs to add a single oxygen atom to each methane molecule; if more oxygen atoms are added, useless products are created, ultimately CO_2 and H_2O.

Catalysts developed in laboratories for the direct conversion of methane to methanol under milder conditions than Fischer-Tropsch are currently not efficient enough to produce the yields required to compete with oil. An economic process is needed but it also needs to be understood and that is why even major oil companies like SASOL, investing in converting methane into liquid fuels through indirect approaches, are funding research on direct conversion.

1.2 Supported gold catalysts

Gold has always been believed to be among the most stable, incorruptible, substances known to humankind and, although it has been known and used in jewellery since ancient Egyptian times, it has to date found fewer practical applications than other precious metals. The annual usage of gold is more than 20 times that of platinum, which partly reflects the fact that there is considerably more gold than platinum group metals in the world. However, jewellery accounts for almost 80 per cent of this usage, compared with 50 per cent for platinum.

Other uses for gold and its derivatives have been developed much more recently. Gold and its alloys have significant applications in dentistry, while gold drugs are used for treating arthritis and have potential for chemotherapy. Gold is also used for infrared reflective coatings on glass for aircraft cockpit, space shuttle windows and architectural glass in office buildings. Brazing alloys – useful for joining together two metals – containing gold are used in the aerospace industry and have general engineering applications. Gold foil is used for decorative gilding coatings in, for example, books, church furniture, steeples and statues. The element is also familiar on ceramic tableware and glassware. However, the chemical community had to wait until the 1980s before work in two laboratories demonstrated spectacular examples of the chemical reactivity of gold.

First, Graham Hutchings, then working at AECI in South Africa, used gold on carbon catalysts for vapour phase hydrochlorination of acetylene. Subsequent research confirmed the prediction that gold cations should be the most active catalysts for this reaction and it was found to be about three times more active than the commercial mercuric chloride catalysts. However, one ton of gold would have been necessary for each plant and in the 1980s the price of gold was about three times its present value.

The other demonstration of gold activity at about the same time was made by Masatake Haruta, then at the Osaka National Research Institute in Japan. Haruta was the first to show that gold catalysts could be effective at ambient temperature. When gold is coprecipitated with certain metal oxide supports, Haruta found that the resulting catalysts are very active for carbon monoxide oxidation; this was a major breakthrough.

Many chemical reactions are now known to be catalysed by supported gold systems. Gold catalysts are already used in Japan for odour removal from toilets, the gold on iron oxide catalyst being used to oxidise nitrogen containing odour compounds.

One of the key behaviours of gold catalysts is their ability to operate in the temperature range 200–350 K, while platinum catalysts show an optimum performance in the range 400–800 K. Unlike many platinum group metal catalysts, the presence of humidity is actually beneficial to the activity.

It is unlikely that gold will largely replace platinum group metals from their dominant position in precious metal catalysis. More likely is the potential to catalyse new reactions and in some cases offer alternative cost-effective solutions. The reduction of nitrogen oxides from diesel exhausts and oxidative decomposition of harmful dioxins are among possible future applications.

1.3 Aim and scope of the thesis

Catalysis is a discipline at the border of many other disciplines: chemical engineering, physical chemistry, solid-state physics, organic and inorganic chemistry. Therefore, an understanding of catalytic processes requires knowledge from a broad area of sciences.

Theoretical chemistry, particularly quantum chemistry, is of increasing use for a better understanding of chemical processes at the molecular level. It will not replace experiments; it is a tool, which can be used as a complementary technique. Computational modelling is the theory of the experiment and the experiment of the theory.

The aim of this thesis is to develop, to explain and to understand the mechanisms of methane activation on molybdena and gold adsorption and catalysis on magnesia. These systems are both examples of oxidation catalysis. Molybdena is well known for its ability to partially oxidise methane and a plethora of experimental results are available in the literature. However, the exact mechanism for the C–H bond breaking remains a matter of debate. Active sites and transition states have been proposed but clear evidence still needs to be presented. During the course of this work, we were able to prove that DFT is unable to correctly describe defects on $MoO_3(010)$ and we proposed a mechanism for methane activation based on DFT+U which is in good agreement with recent experimental work.

Gold supported on metal oxide catalysts are becoming increasingly popular in the research community and this is clearly reflected by the extensive literature available. Nevertheless, while these catalysts are well known to be very active for several reactions, there is an ongoing debate on the reasons why. We will discuss the importance of charge transfer to gold clusters supported on magnesia and we will use CO adsorption to explain why gold oxidation state in these catalysts is a crucial parameter.

1.4 Outline of this thesis

This short chapter summaries the aim and implications of this study.

In the next chapter, we will discuss the literature available on methane activation and gold catalysts. The methane activation section will consist of details on the direct conversion of methane to oxygenates in both homogeneous and heterogeneous catalysts, the structure and properties of the $MoO_3(010)$ surface and finally the methane activation by molybdenum trioxide. The gold catalysis section will deal with the unusual chemical activity of supported gold nanoclusters, followed by a presentation of previous work on gold supported on magnesium; finally, carbon monoxide adsorption on gold will be reviewed.

In chapter 3, the necessary theoretical background will be introduced. A few aspects of density functional theory (DFT) and its implementation in two codes, VASP and SIESTA, will be discussed. The theory behind these codes, applied to geometry optimisation, vibrational frequencies, atomic charges and density of states calculations, will be discussed.

In chapter 4, details of the methodology used in this work will be presented. A substantial part of it will deal with pseudopotential generation. We will then explain how the calculation parameters were converged and the lattice parameters optimised. Finally, three important concepts for this study will be detailed; adsorption energies, atomic charge calculations and transition state searching.

After these introductory chapters, the results of this study will be presented. In chapter 5, we discuss methane activation on the $MoO_3(010)$ surface. After a brief introduction, the computational details for VASP are given. The third section of this chapter presents the study of bulk MoO_3 and the perfect $MoO_3(010)$ surface with DFT and is followed by a fourth section dealing with the terminal oxygen defective $MoO_3(010)$ surface. The ability of DFT to treat this kind of defect is discussed and results employing DFT+U are presented. Re-oxidation of the surface by molecular oxygen is also studied and discussed in terms of O_2 activation on a catalyst. After these two sections on “pure” molybdena, sections 5 and 6 deal with methane activation on $MoO_3(010)$. First in section 5, we discuss hydrogen and methyl adsorption at different sites of this surface in order to obtain the end states for C–H bond breaking in methane. In section 6, the Nudged Elastic Band method is employed to locate a transition state and an energy profile for the activation of methane on defective $MoO_3(010)$ is given. The spin localisation, its influence on the reaction and the C–H bond cleavage are further discussed. Finally, the last section presents the conclusions drawn from the results presented in this chapter.

Chapter 6 deals with gold supported on MgO used as a catalyst. A brief introduction is given and computational details for SIESTA are then presented. In the third section of this chapter, we present results for atomic gold, gold dimer and ten atom gold cluster adsorption on the flat MgO(001) surface. The bonding mechanism is compared to the literature. The fourth section is similar to the third one, but an oxygen vacancy is introduced on the MgO(001) surface. Results are discussed in terms of geometry, adsorption energies and charge transfer. In the next section we make use of a kinked surface, namely the MgO(1 3 12) surface. Atomic gold and the ten atom gold cluster are studied on this surface and results are compared to those obtained with flat MgO(001). Finally, section 6 deals with carbon monoxide adsorption on gold supported on MgO. Several oxidation states of gold are used and the charges on the gold species are calculated. The effects on CO adsorption are discussed in terms of charge transfer, and vibrational frequencies for CO are calculated. The last section of this chapter presents the conclusions on gold supported on MgO.

Finally, some interconnections between chapters are discussed in the general conclusions, chapter 7.

The thesis is preceded with a short summary as well as a list of papers published and in preparation. At the end, an appendix introducing the Metal–CO bonding model is given.

Chapter 2

Literature review

The theme of this thesis is oxidation catalysis and the mechanisms by which this can be achieved using heterogeneous catalysts. The two examples to be studied in depth are methane activation and partial oxidation over MoO_3 and CO oxidation by supported Au catalysts. There is a vast literature on these and related catalysts and in this chapter we will draw together work on catalyst characterisation and reaction mechanisms suggested by experimental results. In addition the current state of simulation of these systems will be reviewed.

2.1 Methane activation

2.1.1 The direct conversion of methane

Much attention has been paid to the conversion of methane into useful chemicals and easily transportable liquid fuels from the point of view that the abundant methane resources will play a significant role in the production of energy and chemicals in the new century. It has been recognized for a long time that a direct conversion process for methane to useful chemicals such as methanol would have many advantages over the indirect technology via synthesis gas. However, the current state-of-the-art technology for the direct conversion process is not competitive with the indirect one via synthesis gas. Among the direct conversion processes, the partial oxidation of methane to useful oxygenates, particularly methanol, possesses a great potential and is seen as one of the biggest challenges in catalysis.[1] In past decades, several reviews were published on this topic.[2-8] We will attempt here to provide highlights for the novel methods and catalysts developed for the partial oxidation of methane into oxygenates.

A - Catalytic oxidation of methane to oxygenates in liquid homogeneous systems

Methane can be activated by electrophiles such as Pt^{II} and Pd^{II}. In early studies, metal cations with high valence state such as Pt^{IV} were generally used as oxidants, *e.g.* using a Pt^{II}/Pt^{IV} system, both CH_3OH and CH_3Cl can be formed from CH_4 and Cl^--containing aqueous solution at 393 K.[9] Kao *et al.*[10] using H_2O_2 as an oxidant, succeeded in converting CH_4 to CF_3COOCH_3 in CF_3COOH medium with a Pd^{II} catalyst. The best yield for the ester, CF_3COOCH_3, approached 1% based on CH_4 at 453 K.

Periana *et al.*[11] found that CH_4 could be converted to methyl bisulfate (CH_3OSO_3H) by Hg^{II} in concentrated sulphuric acid. The selectivity to CH_3OSO_3H reached 85 % at a CH_4 conversion of 50 % with a 0.1 M solution of $Hg(OSO_3H)_2$ in concentrated sulphuric acid at 453 K and CH_4 pressure of 34.5 bar. The reactor design and the details about the reaction kinetics for the oxidation of CH_4 to CH_3OH in oleum (H_2SO_4–SO_3) catalysed by $HgSO_4$ have been reported recently.[12] Based on the pressure–time relationship, a first-order reaction was found, where the rate constant is proportional to the $HgSO_4$ concentration. Higher reaction temperatures and pressures lead to higher reaction rates.

A bipyrimidyl Pt^{II} complex (figure 2.1) has also been used as catalyst instead of $HgSO_4$ for the conversion of CH_4 in oleum.[13] CH_4 was converted into methyl bisulfate with a conversion of ca. 90 % and a selectivity of 81 % at 493K at 35 bar of CH_4 pressure. The reaction has been proposed to proceed by the mechanism shown in figure 2.1.

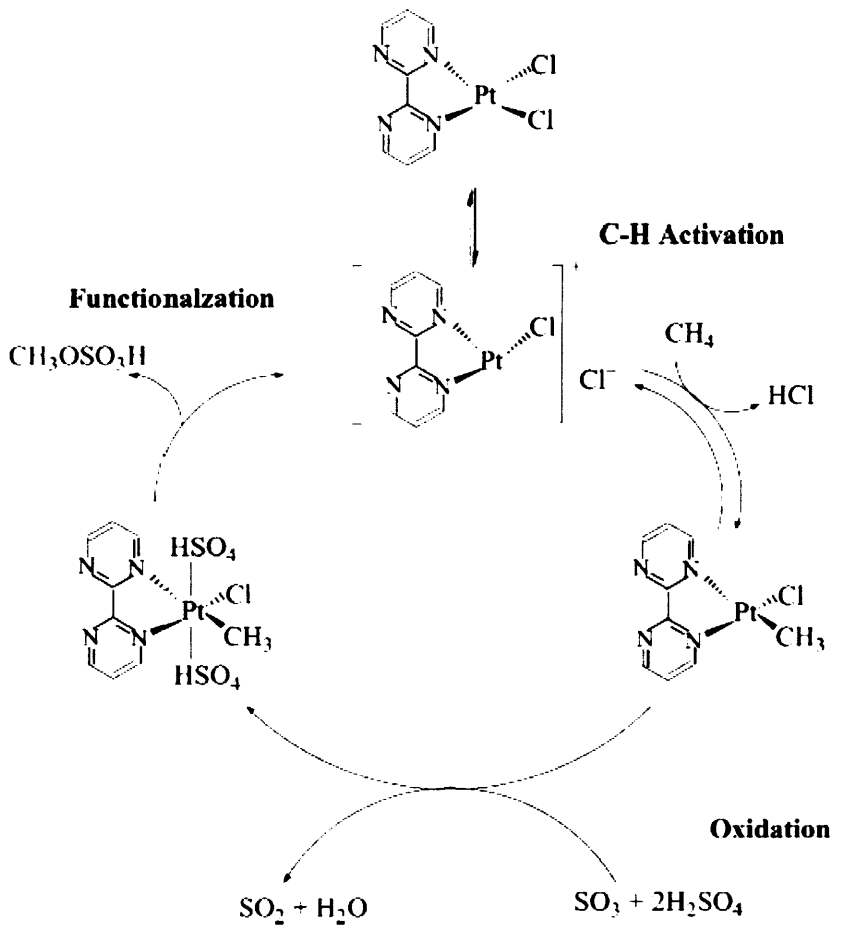

Figure 2.1 Reaction mechanism for the oxidation of methane to methyl bisulfate with a Pt-complex catalyst in oleum.[13]

Methane monooxygenase (MMO) in methanotropic bacteria catalyses the selective oxidation of CH_4 to CH_3OH by oxygen under ambient conditions.[14] Cytochrome P-450 monooxygenase catalyses the partial oxidation of many kinds of alkanes to oxygenates.[15] A number of metal complexes have been proposed to mimic the chemistry of these enzymes[16-18], but the systems which generate potent active oxygen species capable of converting CH_4 to CH_3OH are not so numerous. MMO is a very strong oxidiser and is known to degrade more than 250 compounds. It consists of three proteins; a hydroxylase, a reductase, and the Component B. The largest is the hydroxylase, comprised of three polypeptides and it contains the active site shown in figure 2.2.

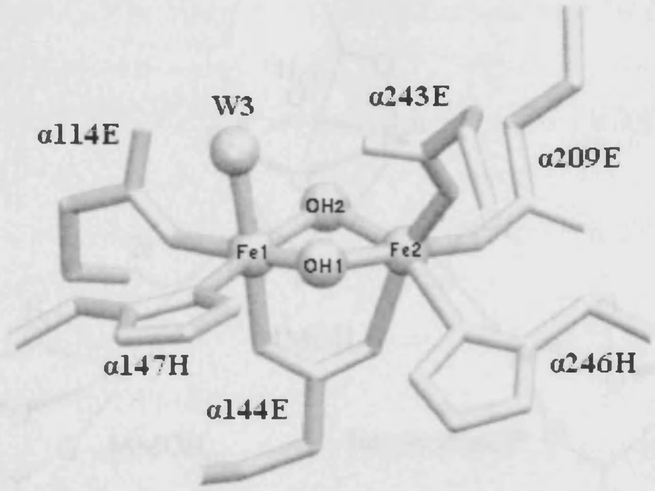

Figure 2.2 Hydroxylase protein of MMO with its dinuclear iron active site.[19]

This active site is a dinuclear iron centre responsible for methane hydroxylation. In a study of methane hydroxylation on the diiron active site of soluble MMO, Yoshizawa proposed a reaction pathway identical to that for the gas-phase reaction by the bare FeO^+ complex.[20] A H atom abstraction via a four-centred transition state and a recombination of the OH and CH_3 groups via a three-centred transition state successively occur on the dinuclear iron–oxo species, leading to the formation of a methanol complex corresponding to intermediate **T**. This mechanism for methane hydroxylation by MMO is different from the radical mechanism usually reported for the conversion of methane to methanol catalysed by MMO (figure 2.3). It was established that $MMOH_{red}$, "red" meaning reduced, reacts very fast with O_2 and forms a metastable compound, which spontaneously converts to another compound called **P**. The latter spontaneously converts to compound **Q**, proposed to be the key oxidising species for MMO. Basch *et al.*[21] using DFT/B3LYP found the overall CH_4 oxidation reaction to be exothermic by 163 kJ mol^{-1}. Knops-Gerrits and Goddard III,[22] using unrestricted HF, reported on the structure–activity relationships of MMO mimics in alkane activation, with a reaction with methane exothermic by 211 kJ mol^{-1}.

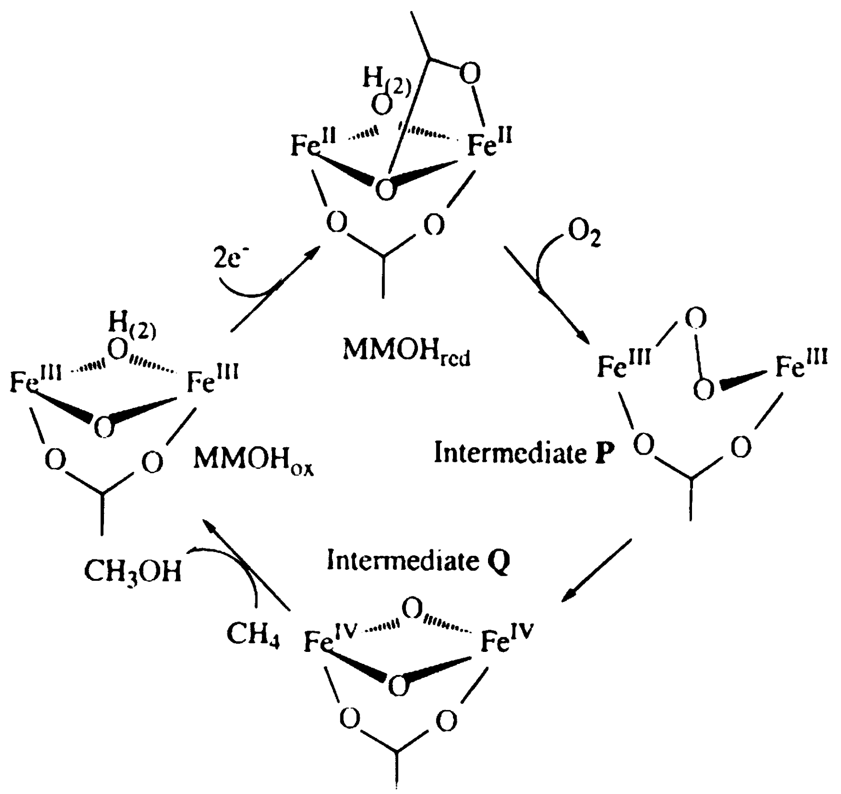

Figure 2.3 Experimentally proposed catalytic cycle of MMO.[21]

B – Catalytic oxidation of methane to oxygenates in solid heterogeneous systems

Homogeneous catalysts still require very forcing conditions and expensive organometallic catalysts. MMO is very selective but the turnover frequency is too low for use as a commercial catalyst for the processing of a raw material like methane. Many publications have contributed to the partial oxidation of methane at high pressure (10 bar and above) in the heterogeneous field. The gas phase radical reaction is dominant under high pressure, and it seems there is no positive role of the presence of solid catalyst in this case.[23, 24] Methanol could be obtained with moderate selectivity by controlling the factors influencing the gas phase radical reactions such as reactor type and geometry, gas-residence time and quenching of unstable products (CH_3OH, HCHO) at the exit of the reactor.

Although a few reports suggest useful yields to methanol and formaldehyde (7–10%)[25, 26], a large number of studies agree on a level of CH_3OH selectivity of 30–40 % with CH_4 conversion of 5–10 % under the best reaction conditions, *i.e.* temperatures of 723–773 K and pressures of 30–60 bar.[23, 24, 27] A 7–10% yield for methane to methanol can be thought of as good since it is possible to easily extract liquid methanol during conversion.

At lower pressure (1 atm), the catalyst plays a crucial role in the partial oxidation of methane. Sugino *et al.*[28] reported a high selectivity (90 %) to oxygenates (CH_3OH + HCHO) at CH_4 conversions of 20–25 % at 873 K in an excess amount of water vapour over a MoO_3 supported on SiO_2 (MoO_3/SiO_2) catalyst prepared by a sol–gel method. It is also reported that although HCHO can usually be obtained with a few percent yield, the synthesis of CH_3OH seems to be unsuccessful by the oxidation of CH_4 with O_2 over solid catalysts. High pressure is beneficial to produce CH_3OH [29, 30] but the oxidation under such conditions is mainly controlled by gas phase radical reactions.

The elucidation of reaction mechanism is helpful for explaining the reason why CH_3OH cannot be produced in the partial oxidation of CH_4 with O_2 on most solid catalysts. Otsuka *et al.*[31] investigated the reaction mechanism for the activation of CH_4 and the formation of HCHO using $Fe_2(MoO_4)_3$ as an example catalyst and proposed a reaction scheme over this catalyst based on detailed kinetic measurements and isotopic studies.

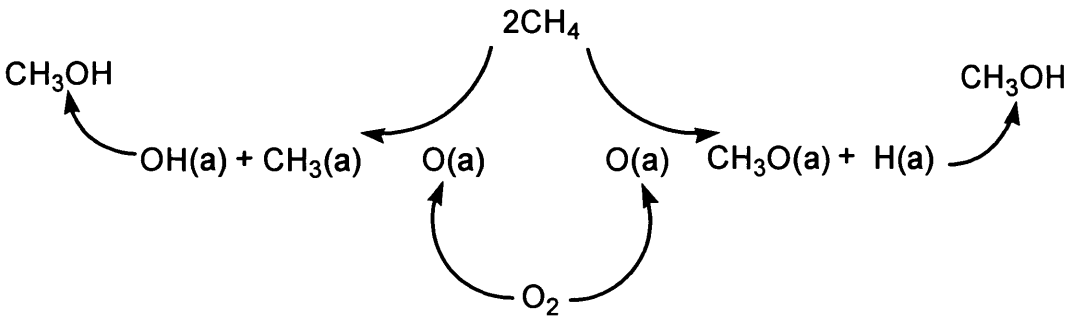

Figure 2.4 Schematic reaction model for the partial oxidation of methane on the surface of iron molybdate catalyst.[31] The suffix "(a)" refers to adsorbed species on the catalyst surface.

This scheme, shown in figure 2.4, is in essence similar to that reported for silica-supported MoO_3 and V_2O_5.[32] CH_4 is activated by surface oxygen species derived from the dissociative adsorption of gaseous oxygen (or from the bulk lattice through diffusion to the surface). The possible intermediates, *i.e.* adsorbed methyl species CH_3 or methoxide species CH_3O, would be attacked by the activated surface oxygen and quickly oxidized into HCHO or CO_x. Otsuka *et al.*[31] speculate that this is one of the reasons why the formation of CH_3OH, which is caused by the protonation of CH_3O, has been so difficult. For selective synthesis of CH_3OH, a special structure of active site that can provide a Brönsted acid site for the protonation of CH_3O^- and protect the intermediate from further oxidation by the surface oxygen atoms on neighbouring sites should be required. Furthermore, a high temperature, generally >773 K, is required for the activation of CH_4. At such high temperature, the produced CH_3OH would be quickly decomposed or oxidised into HCHO and CO_X. CH_3OH conversion was always 100 % over the $Fe_2(MoO_4)_3$ catalyst under the conditions used for the partial oxidation of CH_4.[31] Silica supported MoO_3 and V_2O_5 were also good catalysts for the oxidation of CH_3OH.[32] Thus, the development of novel catalysts or catalytic systems capable of activating CH_4 at lower temperature is vital for the direct synthesis of CH_3OH from CH_4.

The C–H bond scission of alkanes in their oxidation over metal compounds such as oxides, phosphates, silicates or aluminates is believed to be initiated by active oxygen species on the catalyst. Active oxygen species are thus considered to be very important in heterogeneous oxidation of CH_4 or other low alkanes. Adsorbed oxygen species such as O_2^-, O^- and O_2^{2-} have been well characterized on many oxide surfaces[33-37], but the identification of the nature of active oxygen species for selective oxidation of alkanes, particularly under reaction conditions, still remains an open question.

Some researches have contributed to the elucidation of the active oxygen species for selective oxidation of CH_4. Li/MgO is probably the most thoroughly investigated catalyst for oxidative coupling of CH_4.[38, 39] The formation of O^- (known as the $[Li^+O^-]$ centre) has been detected by Electron Spin Resonance (ESR) and its possible role in oxidative coupling of CH_4 has been discussed. Substitutional Li^+ ions reacted with molecular oxygen to form a $[Li^+O^-]$ centre which was also capable of abstracting a hydrogen atom from methane. Other ESR studies[40] suggested the involvement of O_2^- in the oxidative coupling of CH_4 over La_2O_3-based catalysts. La_2O_3 was found to be effective in the activation of CH_4 to form $CH_3\bullet$ radicals which then combine in the gas phase to produce C_2H_6. Surface lattice oxygen species M=O coordinated with a double bond to molybdenum or vanadium have been suggested to be responsible for the partial oxidation of CH_4 to HCHO over silica supported MoO_3 or V_2O_5, while bridging oxygen sites Mo–O–M lead to complete oxidation.[41-43]

2.1.2 The $MoO_3(010)$ surface

Elemental molybdenum and molybdenum oxides are involved in many processes, for example, as catalysts as we have discussed earlier as well as several other applications like anodes for X-ray tubes or as nanometre layers for optical devices in extreme ultra violet (EUV) lithography[44]. A large number of molybdenum oxides with different chemical compositions and crystallographic structures are known. Molybdenum trioxide is formed by layers which are weakly bonded via van der Waals interactions. The crystal system is orthorhombic with parameters *a*= 3.9628, *b*= 13.855 and *c*= 3.6964 Å.[45] The unit cell contains four MoO_3 units. The atomistic structure consists of bilayers parallel to the (010) plane and bonded via van der Waals interactions; the (010) surface being the easiest to cleave. The bilayers consist of two sublayers of distorted MoO_6 octahedra (figure 2.5). There are three structurally distinct oxygen atoms: asymmetric, symmetric and terminal. The asymmetric bridging oxygen atoms are 2-fold co-ordinated forming one long (2.25 Å) and one short (1.73 Å) bond with two Mo atoms in the same layer. The symmetric bridging oxygen atoms are 3-fold co-ordinate with two equal bonds (1.95 Å) to Mo atoms in the same layer and one much longer interaction (2.33 Å) with a Mo atom of the other sublayer. Finally, the terminal oxygen is bonded to only one Mo atom forming the shortest Mo–O bond in the system (1.67 Å).[45]

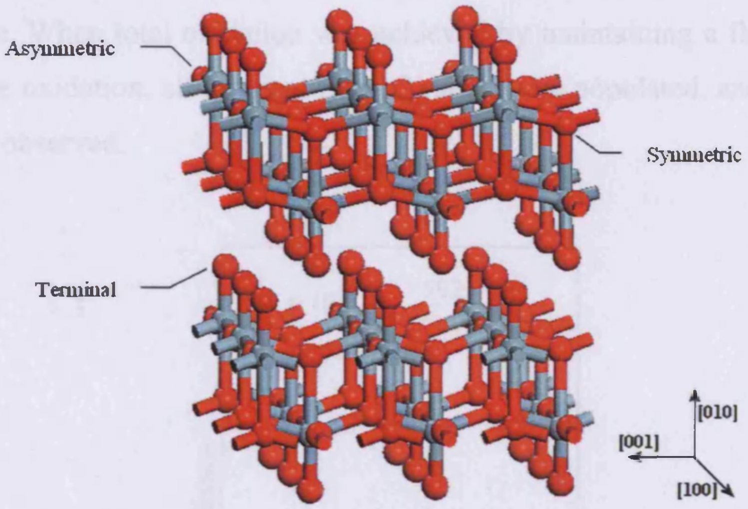

Figure 2.5 Two bilayers of bulk α-MoO_3. The three different types of O atoms are indicated (terminal, symmetric and asymmetric). Oxygen atoms in red, molybdenum in blue.

It has been reported that not only the surface, but also the bulk structure of the molybdenum oxide catalysts is involved in the oxygen insertion process via the exchange of surface and lattice oxygen as indicated in figure 2.4.[46, 47] The reduction of 50 % MoO_3/50 % MoO_2 mechanical mixture generates new interfaces within the grains of MoO_3 and hence increases the total number of transient oxygen species, active in total oxidation. For the MoO_6 octahedral basic structural unit, the removal of oxygen species introduces considerable rearrangement. The crystallographic shear defect is a way for the oxide to accommodate such changes. Crystallographic shearing eliminates planes of anion vacancies by shear from corner to edge sharing of octahedra and therefore generates extended crystallographic shear plane defects.

Wang *et al.*[48] presented the identification of the two common molybdenum sub-oxides $Mo_{18}O_{52}$ and Mo_8O_{23}, derived from MoO_3 by crystallographic shearing, by means of electron diffraction and High-resolution Transmission Electron Microscopy (HRTEM) in combination with image simulation. The $Mo_{18}O_{52}(100)$ surface with steps in the $Mo_{18}O_{52}[010]$ direction is built up of $MoO_3(010)$ terraces with $MoO_3(100)$ edges and $MoO_3(001)$ kinks.[49]

Queeney and Friend managed to synthesise oxidised Mo(110) surfaces with specific types of oxygen coordination and characterise them using infrared and electron energy loss techniques.[50, 51] During the oxidising process, two distinct vibrational frequencies υ(Mo=O) peaks were resolved at 992 and 1016 cm^{-1} using infrared spectroscopy (figure 2.6).[51] This evidence points to the existence of two structurally distinct Mo=O sites on this oxidised Mo(110) surface. When total oxidation was achieved by maintaining a flow of O_2 following high-temperature oxidation, all terminal (Mo=O) sites were populated, and a single υ(Mo=O) at 996 cm^{-1} was observed.

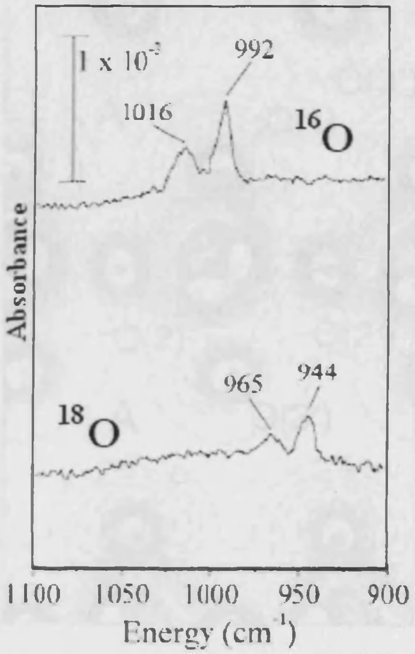

Figure 2.6 Infrared spectra with the υ(Mo=^{18}O) peaks from the isotopically labelled overlayer and the signature υ(Mo=^{16}O) peaks, created by preparation of the same overlayer with ^{16}O and shown for reference.[51]

Different theoretical approaches have been used to study α-MoO_3. Two major *ab initio* periodic Hartree–Fock (HF) studies were published almost at the same time: Papakondylis and Sautet[52] in 1996 and Corà *et al.*[53] in 1997. Papakondylis and Sautet reported that the (100) surface of α-MoO_3 contains pentacoordinated Mo atoms possessing a Lewis acid character. They also studied the adsorption of H_2O and CO molecules on these sites and found that the interaction is essentially of electrostatic nature, restoring a bulk-like environment around Mo atoms. Corà *et al.* investigated the structural and ground-state electronic properties of α-MoO_3 and reported that the nature of the Mo–O interaction changes considerably with the equilibrium bond distance, and varies from strongly covalent for the shortest bond to a predominantly ionic interaction for the longest bonds in the MoO_6 octahedron. They analysed the degree of covalence in the bonding by using electron density maps (figure 2.7) and Mulliken population analysis. The oxygen atoms denoted O(2) and O(2') are asymmetric and this is clearly reflected in the asymmetry of the accumulation of charge density between the central Mo and O(2) or O(2'). Terminal oxygen O(1) presents a Mo=O bond and as such, exhibits a significant build up of charge density with Mo.

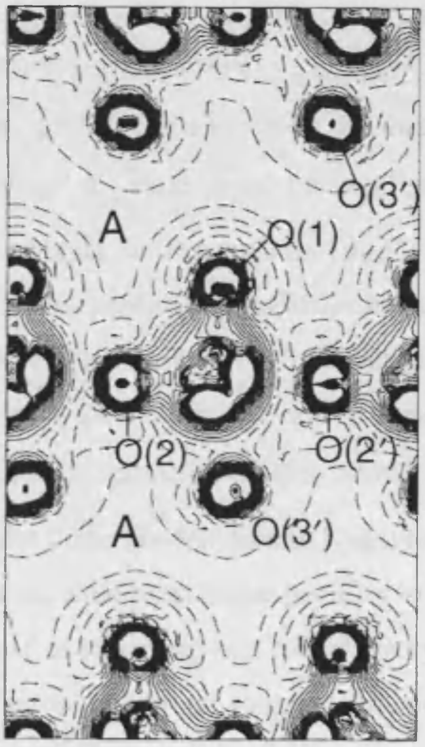

Figure 2.7 Difference electronic charge density map (solid minus isolated Mo^{6+} O^{2-}), displayed in the crystallographic plane containing the central Mo and the vertices O(1)O(2')O(3')O(2) of one isolated MoO_6 octahedron. Continuous, dashed and dot-dashed lines correspond to positive, negative and zero difference respectively. The interval between the isodensity lines is 0.005 a.u. (electrons a_0^{-3}). The map extends beyond the central octahedron and includes part of the interlayer space, denoted by A.[53]

They also found that the energy as a function of the interlayer spacing has a minimum, both at the correlated and the HF level, indicating the presence of a weak attractive Coulombic force. This is shown by the lack of charge density accumulation in the interlayer space A in figure 2.7. We know however that the Density Functional Theory (DFT) is not able to locate this minimum as it fails to treat the weak interaction between layers (see section 5.3).

An approach also based on periodic calculations has been employed by Friend and co-workers, using LDA DFT. Their work on MoO_3 consists of three publications. The first was a DFT study of clean and hydrogen-covered α-MoO_3(010) in which the surface is modelled by a one-layer slab.[54] In their last publication, they modelled the intermediate stages of the reduction of NO in the presence of MoO_3(010).[55] It was found that the replacement of an oxygen of MoO_3 by NO is energetically favourable, and that the system lowers its energy further by the formation of $(NO)_2$. However, the most interesting study from our point of view, is their work on the chemical nature of surface point defects on MoO_3(010).[56] Again using DFT, they modelled the terminal oxygen (O_{term}) vacancy and claimed that removal of O_{term} does not significantly alter the surface structure. However, they found a new state in the energy spectrum of the MoO_3(010) surface with O_{term} vacancy. This state is a d_{xz} nonbonding state of Mo that is localized on the Mo atom to which the missing O_{term} was bonded (figure 2.8). They also found a "dangling" d_{z^2} state in the conduction band that is localised on the Mo atom and directed perpendicular to the surface (figure 2.8). Figure 2.8a shows the calculated density of states for the perfect MoO_3(010) surface. On creation of a terminal oxygen vacancy, additional features are observed as indicated in figure 2.8b. These states are plotted in figure 2.8d and e and show that the crystal orbitals concerned have a large contribution from d_{xz} and d_{z^2} orbitals respectively. This allows the assignment of the states in the DOS diagram shown in figure 2.8b. The addition of hydrogen to the terminal oxygen atom also causes the appearance of a d_{xz} state in a similar position to that seen for defect formation (figure 2.8c). The energetic cost of removing one out of every four terminal oxygen atoms was 10.1 eV, calculated by subtracting the total energy of the perfect surface from the sum of energies of the vacancy surface and a free oxygen atom.

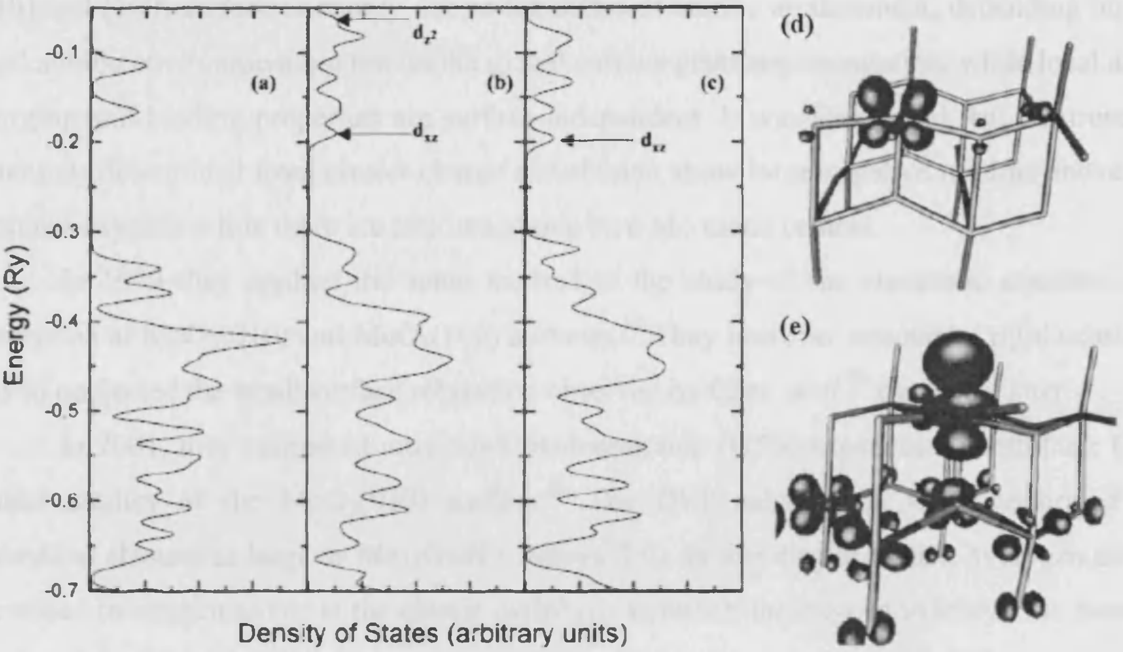

Figure 2.8 Density of states plots (only the states near the band gap are shown): (a) "Perfect" $MoO_3(010)$ surface; (b) $MoO_3(010)$ surface with a (2x2) array of O_{term} vacancies. The symbols d_{xz} and d_{z^2} indicate the energy of individual orbitals related to the creation of the vacancy and (c) hydrogen adsorbed over the O_{term} vacancy. Isoelectronic plots of vacancy-localised states: (d) d_{xz} orbital and (e) d_{z^2} orbital.[56]

Wang *et al.*[57] studied the transformation of MoO_3 induced by electron beam irradiation with electron energy-loss spectroscopy (EELS) in combination with electron diffraction and high-resolution transmission electron microscopy (HRTEM) techniques. They reported that the oxygen vacancies exist in the early stage of the irradiation as point defects. With the increasing concentration of these vacancies, aggregation occurs into planar defects and they are accommodated by forming crystallographic shear planes. Wang *et al.* also pointed out that in MoO_2, the t_{2g} orbitals have two electrons. This was observed in the electron energy loss near edge structure (ELNES) spectra of the O *K*-edge of Mo oxide subjected to prolonged irradiation by electron beam of high current density (about 57.6 A cm^{-2}).[57] This supports the hypothesis of electron localisation on molybdenum after reduction.

Unlike Kaxiras and co-workers, Witko and co-workers applied DFT not to periodic models but to cluster models. The first paper mentioning their method for MoO_3 surfaces was published in 1996.[58] They chose clusters as finite sections of the ideal MoO_3 surface for which cluster embedding is achieved by bond saturation with hydrogens, yielding cluster sizes of up to $Mo_7O_{30}H_{18}$. They reported the difference in electronic structure between the (010) and (100) surface is mainly due to the different atomic arrangement, depending on the local atomic environment but not on the global surface geometry/orientation, while local atom charging and binding properties are surface-independent. It was also found that electrostatic potentials determined from cluster charge distribution show large negative minima above the terminal oxygens while there are maxima above bare Mo metal centres.

In 1999 they applied the same method to the study of the electronic structure and adsorption at $MoO_3(010)$ and $MoO_3(100)$ surfaces.[59] They however assumed a rigid substrate and so neglected the small surface relaxation observed by Chen *et al.*[56] two years later.

In 2001, they compared ultraviolet photoemission (UPS) experiments with their DFT cluster studies of the $MoO_3(010)$ surface.[60] The DFT calculations were performed on embedded clusters as large as $Mo_{15}O_{56}H_{22}$ (figure 2.9). In this cluster model, hydrogen atoms are added to oxygen atoms at the cluster periphery to satisfy the oxygen valency. The latter is implied from its type and distance from Mo atoms in the cluster (see section 5.4).

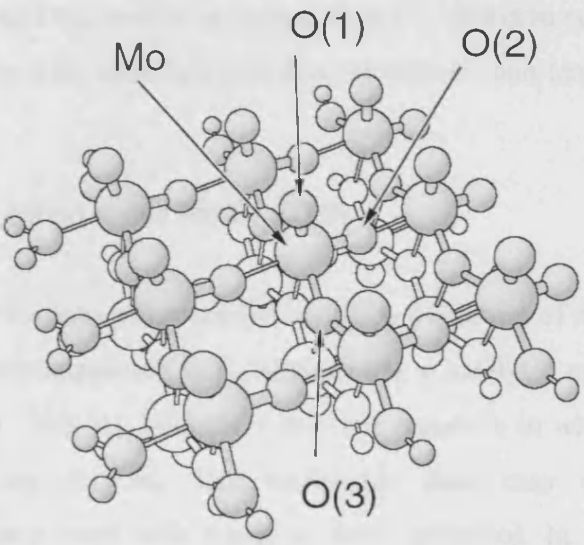

Figure 2.9 Geometric structure of the $Mo_{15}O_{56}H_{22}$ cluster modelling a bi-layer section at the $MoO_3(010)$ surface. Cluster atoms of the top (bottom) part are shown as shaded (white) balls where the ball size decreases from Mo to O to H. The central molybdenum atom and its three neighbouring non-equivalent surface oxygen centres, O(1–3), are labelled accordingly. O(1) is a terminal oxygen, O(2) is an asymmetric oxygen and O(3) is a symmetric oxygen.[60]

Witko and co-workers then reported rather large (6.8–7.6 eV) vacancy energies for the different surface oxygen sites at $MoO_3(010)$, but again, they did not allow the surface to relax after vacancy creation, which could lower the vacancy energies by as much as 3.3 eV[56]. A very relevant point to our work was also made: in terms of Mo–O binding the asymmetric bridging oxygen O(2) takes the place of the original terminal O(1) atom which has been removed in the vacancy creation process. This finding becomes important for the vacancy properties when surface relaxation is included in the vacancy calculation.

In 2004, Witko and co-workers published two papers on transition metal oxides MoO_3 and V_2O_5.[61, 62] These studies concentrated on the re-oxidation of $MoO_3(010)$ and $V_2O_5(010)$ surfaces. It was found that re-oxidation proceeding *via* molecular oxygen is a localised process and that all created surface oxygen vacancies may become re-oxidised either through exchange with gaseous oxygen or via diffusion of bulk oxygen atoms. The process of oxygen vacancy formation could be facilitated by adsorption of hydrogen resulting in surface hydroxyl and water species, which might easily be desorbed. For all vacancy sites, parallel O_2 adsorption was preferred over perpendicular and the oxygen molecule became activated with an O–O bond elongated with respect to the gas phase and the corresponding bond order decreased. It was also noticed that, generally, the rearrangement at the $V_2O_5(010)$ surface is negligible, whereas at the $MoO_3(010)$ surface changes are larger (especially connected with the removal of terminal and symmetric oxygen centres).[61] This is in contrast with the assertion by Chen *et al.*[56] that there is no significant surface relaxation upon terminal oxygen removal.

2.1.3 Methane activation over $MoO_3(010)$

Lunsford and co-workers proposed the selective oxidation of methane to methanol and formaldehyde occurs over supported molybdenum via a catalytic cycle in which O^- is the reactive form of oxygen. This ion initiates a reaction sequence in which methyl radicals and then methoxide ions are formed. The methoxide ions may decompose directly to formaldehyde or they may react with water to form methanol. In this cycle molybdenum begins and ends as Mo(V), an oxidation state evidenced by EPR spectroscopy.[63]

Using electron diffraction and scanning electron microscopy, Volta and Tatibouet have shown that the acidic Lewis centres of $MoO_3(100)$ correspond to uncoordinated Mo cations associated with the breaking of the long Mo–O bonds and that dehydrogenating centres are associated with the short Mo–O bond with a double-bond character equivalent to that observed on the (010) face.[64]

The MoO_3/SiO_2 catalyst has been used for the partial oxidation of CH_4 to HCHO and CH_3OH.[63, 65] As showed by the number of publications, the catalytic oxidation of methane to produce valuable hydrocarbons has been extensively studied. However, a lot of controversial results have been reported about the active species and reaction intermediates which are responsible for the partial oxidation of methane on the catalyst surface. One of the questions regarding catalytic oxidation of methane over MoO_3 is the role of lattice oxygen during the oxidation process. It has not been clearly determined whether lattice oxygen is directly related to the oxidation process. Isotopic labelling techniques have been employed to probe the origin of the oxygen species incorporated into reaction products.[66] However, a definitive proof could not be obtained because of the isotopic exchange between the reaction products and labelled oxygen.

Parmaliana and co-workers studied the working mechanism of oxide catalysts, including MoO_3/SiO_2, in the partial oxidation of methane to formaldehyde.[67, 68] It was found that a sequential reaction path ($CH_4 \rightarrow HCHO \rightarrow CO \rightarrow CO_2$) accounts for the formation of oxygenated products on all SiO_2 based oxide catalysts at $T < 650$ °C, while a surface assisted gas-phase reaction pathway leads to the formation of minor amounts of C_2 products both on SiO_2 and MoO_3/SiO_2 catalysts at $T \geq 700$ °C.[67] Employing H_2 and CH_4 temperature programmed reduction (TPR) and high temperature oxygen chemisorption measurements, Parmaliana and co-workers also investigated the redox and surface properties of MoO_3/SiO_2. They reported that the most effective reaction path of methane partial oxidation on silica based oxide catalysts involves the direct participation of gas-phase oxygen activated on the surface reduced sites.[68]

Takemoto *et al.*[69] examined the selective oxidation of methane in CH_4–O_2–NO_2 using MoO_3 catalyst at atmospheric pressure. The presence of MoO_3 catalyst increased CH_2O selectivity and decreased CH_3OH selectivity, compared with those for the gas-phase reaction in CH_4–O_2–NO_2. Based on variations of selectivity under different reaction conditions, their conclusion was that formaldehyde is a main product on the MoO_3 catalyst and methanol is formed through gas-phase reactions.

Yamada *et al.*[70] measured methane oxidation catalysis for each of 43 elements doped on silica prepared by an impregnation method. Overall, they found that the elements suitable for partial methane oxidation are V, Fe, Sc, W, Mo and Os. They however only screened catalyst composition and not reaction conditions. Regarding the second row transition metals, no remarkable selective oxidation catalysis was found, except for Mo/SiO_2 (figure 2.10). The optimal concentration of these elements was 1% (except for Ag). This indicates that the metal oxide partially covering the silica is required for the reaction. It was also found that 0.1% Mo/SiO_2 is highly selective, although conversion is low using this composition.

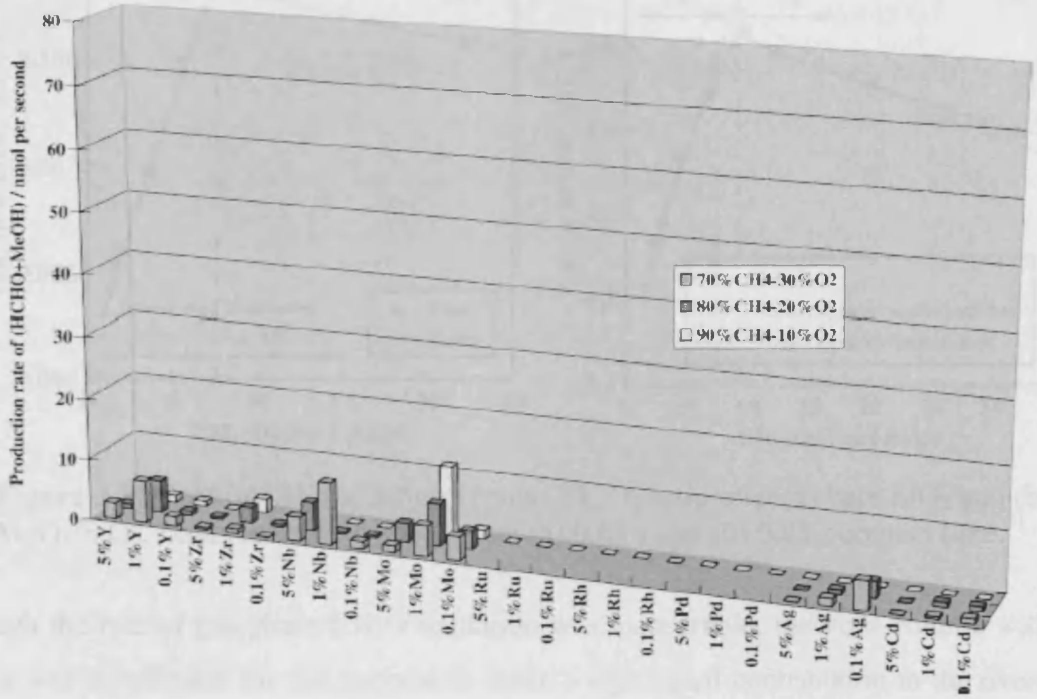

Figure 2.10 Production rate of formaldehyde and methanol over second row transition-metal-doped silica. Metal/silicon = 0.1/100, 1/100, 5/100; feed gas composition: CH_4/O_2 = 70/30, 80/20, 90/10.[70]

Ohler and Bell investigated the selective oxidation of methane to formaldehyde over MoO_x/SiO_2 in order to identify the contributions of methane and formaldehyde reactions occurring in the gas phase and on the surface of SiO_2 and dispersed MoO_x to the overall reaction rate.[71] Experiments were conducted with 4.5 wt% MoO_3/SiO_2 at a nominal surface concentration of 0.44 Mo nm^{-2}. Data were acquired for CH_4/O_2 ratios from 2 to 34 and temperature from 848 to 923 K. The oxidation of CH_4 was found to proceed almost exclusively over the supported molybdena. The rate of homogeneous oxidation was negligible at the pressure used and the rate of CH_4 oxidation over bare SiO_2 was about an order of magnitude less than that over the supported MoO_x (figure 2.11).

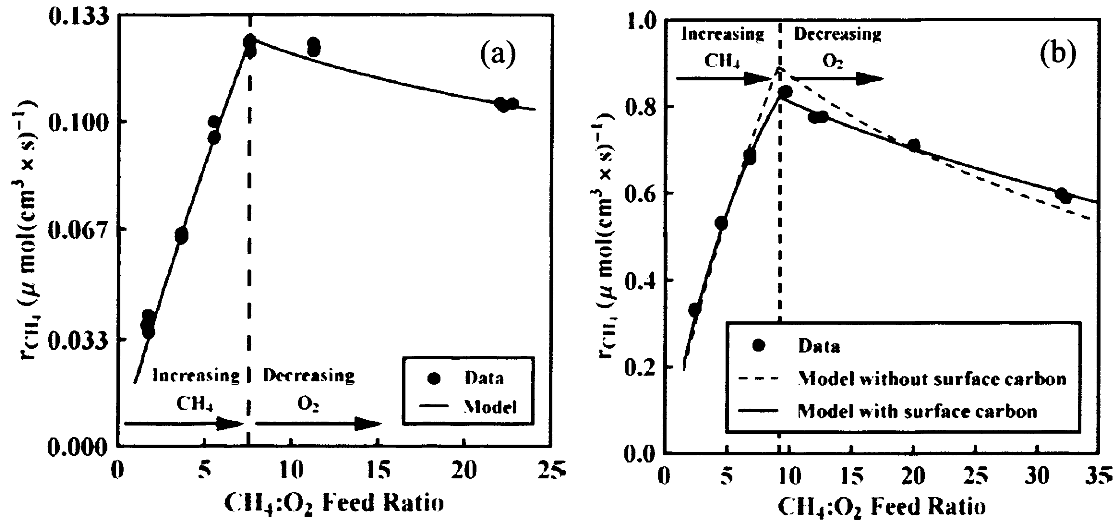

Figure 2.11 Rate of CH_4 oxidation versus CH_4:O_2 ratio over (a) bare SiO_2 and (b) MoO_x/SiO_2. Data recorded at 873 K with (a) 0.65 s and (b) 0.85 s contact time.[71]

Although the rate of gas-phase CH_2O oxidation was measurable, the void volume within the catalyst was insufficient for this process to make a significant contribution to the overall rate of CH_2O decomposition to form CO and H_2. CH_2O decomposition also occurred on the supported MoO_x and when O_2 was present in the feed, all of the H_2 formed from CH_2O decomposition was combusted on the supported MoO_x. A maximum CH_2O yield of 7.0 % could be achieved at a temperature of 973 K with a feed composed of 5% CH_4 and 10% O_2 in He. Making the surface of SiO_2 completely inactive further increased the yield by 2.5%.

Ozkan and Watson recently published an extensive review of their work on the structure-function relationships in selective oxidation reactions over metal oxides, including methane partial oxidation (MPO) and molybdenum oxide.[72] The synergy effects and oxygen spillover phenomenon existing in the mixed phase catalyst $MnMoO_4/MoO_3$ is reported and it is suggested that there may be a competition between oxygen and the hydrocarbon for the same catalytic site over MoO_3 surface; the oxygen "acceptor" sites on the (010) face of MoO_3 being likely reduced sites created by reaction with hydrocarbons. The importance of Mo(V) is also discussed and it is suggested that while Mo(V) is, in all probability, related to the active site of MoO_x catalysts, it seems more likely that the electronic structure of MoO_x domains (explicitly the nature of the oxygen atoms) is the underlying factor in determining "activity" over the supported Mo catalysts. Molybdenum oxide based catalysts are indeed believed to operate effectively as oxidation catalysts under slightly reduced conditions where the presence of Mo(V) is essential and it has been cited that Mo(V) is the active site in propane oxidative dehydrogenation and other oxidation reactions over MoO_x based catalysts.[73-75] After reduction with propane, the intensity of the Mo=O Raman band relative to the Mo–O–Mo bands decreases indicating a preferential interaction of the hydrocarbon with this bond.

One approach to studying elementary steps important in processes on metal oxide surfaces is to synthesise model systems using controlled oxidation of a metal surface. Queeney and Friend have made use of the fact that different types of oxygen coordination sites are populated via controlled oxidation of Mo(110) in order to investigate how the nature of the oxygen coordination site affects reactivity.[51] By varying the degree of oxidation of the surface by controlling the oxidation conditions thin-film oxides were formed, with differing populations of terminal oxygen atoms (Mo=O). By doing this, they could limit the types of oxygen species available for reaction and evaluate the role of oxygen coordination in $\bullet CH_3$ oxidation on a molybdenum oxide surface. Using high resolution infrared spectroscopy, Queeney and Friend showed that Mo=O species are not necessary for $\bullet CH_3$ addition to oxygen and, furthermore, that addition to oxygen in high coordination sites is preferred. They suggested that the presence of Mo–O π bonding at the terminal site leads to constraints on the transition state for methyl addition.

It is widely accepted that the activation of methane involves a cleavage of the C–H bond; however, it is not clear whether that cleavage is heterolytic, resulting in the formation of methyl ions [76] CH_3^+ or [77-79] CH_3^-, or homolytic, leading to the direct formation of a methyl radical released into the gas phase[38, 80]. In similar work to earlier studies of methane exchange on solid bases by Tanabe *et al.*[81], Martin and Mirodatos[82] provided strong evidence that the reversible activation of methane on oxidative coupling of methane (OCM) catalysts is initiated by the heterolytic abstraction of an H^+ on the basic sites O^{2-} of the surface, the remaining methyl anion CH_3^- being linked to the surface cations M^{n+} according to

$$CH_4 + M^{n+} + O^{2-} \leftrightarrow CH_3^- M^{n+} + OH^- . \tag{2.1}$$

The thesis of the heterolytic splitting of the methane C–H bond in the OCM process was also recently supported by Maitra[79], on the basis of a critical evaluation of the performance of a wide range of OCM catalysts, where only basic oxides constituted good catalysts. Moro-oka[83], however, concluded that no such strong basic sites exist on most metal oxide surfaces, but did not rule out the possibility of some homolytic character in the C–H bond dissociation. The homolytic process is mainly supported by EPR studies. Kuba *et al.*[84] in a study of redox properties of tungstated zirconia catalysts, reported that when *n*-pentane flowed through the catalyst, W^{5+} centres and organic radicals formed as shown by EPR. This experiment has been thought of as lending a direct support to the radical mechanism[85] but as already stated by

Martin and Mirodatos[82], the relative importance of "reversible" *vs.* "irreversible" activation of methane tends to be highly sensitive to the nature of the catalyst.

From a computational point of view, studies on CH_4 partial oxidation with MoO_3 are relatively few in number. Using single metal centre cluster models and DFT, Xu *et al.*[86] reported methane activation by transition metal oxides, MO_x (M = Cr, Mo, W; x=1, 2, 3). It was found that MO_2 (M = W, Mo) is the best oxidation state (+4) for this class of metal oxides toward methane activation. σ-Bond metathesis to produce the hydride product (H–MoO_{x-1}–OCH_3) was the most favourable reaction for the high oxidation state of MoO_3. Oxidative addition of MoO_3, leading to methyl metal hydride (H–Mo(Ox)–CH_3), was the most favourable reaction for the low oxidation states of MoO_x (x = 1, 2). The proposed reaction scheme is shown in figure 2.12. **M1** and **M2** indicate molecular complexes with methane in pseudo-C_{2v} and -C_{3v} coordinating positions, respectively. **T1** and **T2** are the TS for two possible σ bond metathesis reactions. **T3** indicates the TS for the oxidative addition pathway. **D** refers to a dissociative product and **R** to a radical product with the M–CH_3 or O–CH_3 bonds homolytically cleaved. The electrostatic interactions in **T1** are not as favourable as those in **T2**. Both **T1** and **T2** involve breaking of the M–O π bond making **T3** lower in energy.

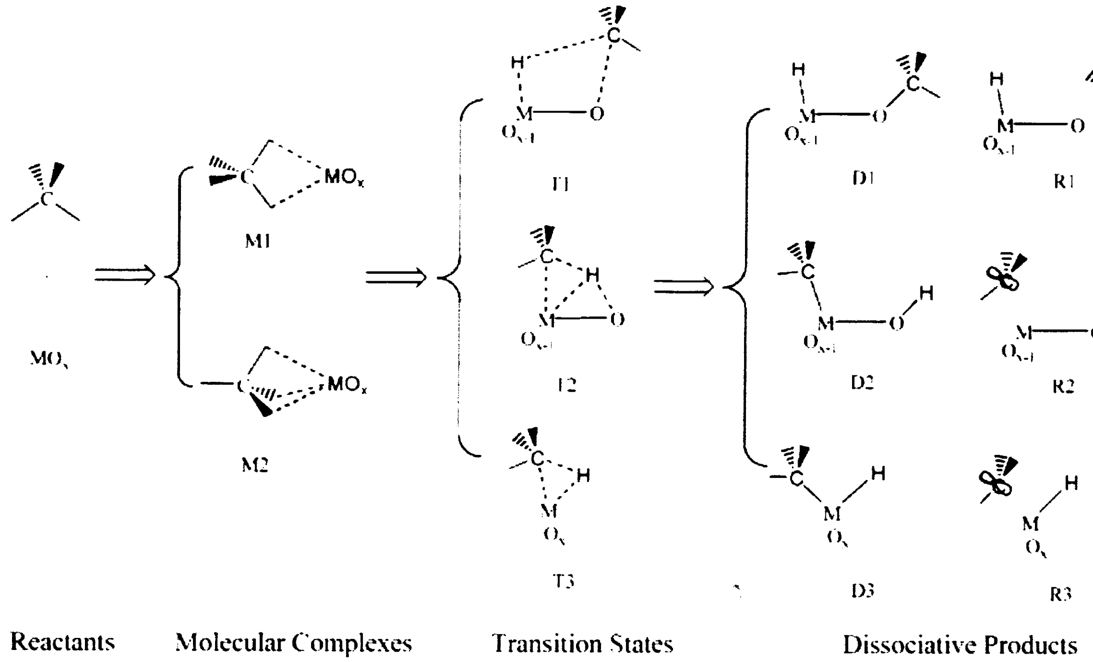

Figure 2.12 Activation of the methane C–H bond by metal oxide molecules.[86]

Fu *et al.*[85] also used DFT and cluster models, but with a slightly bigger system (Mo_3O_9). They proposed several mechanisms for the activation of C–H bond in alkanes (figure 2.13) and they also calculated the energetics for CH_4 activation by Mo_3O_9 at 873 K.

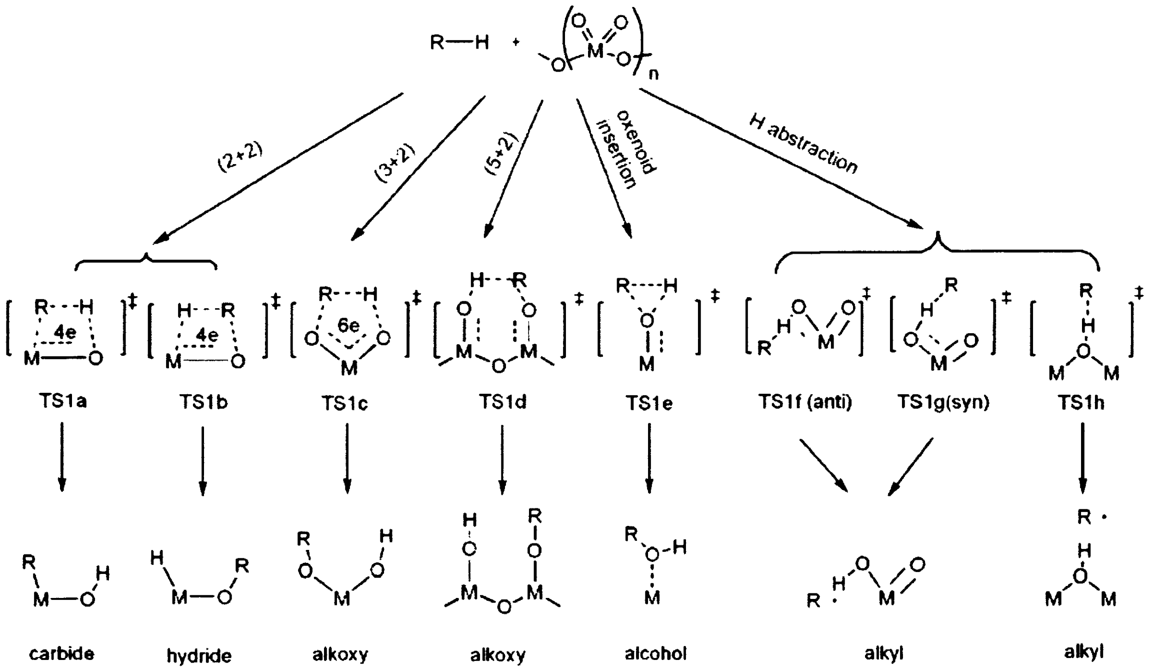

Figure 2.13 Possible mechanisms for the activation of C–H bond in alkanes[85]

The calculated activation barriers for TS1a and TS1b are 209 and 363 kJ mol^{-1} respectively. As already mentioned by Xu *et al.*[86], electrostatic factors are claimed to be the main reason for this 156 kJ mol^{-1} difference between TS1a and TS1b. In TS1b the interaction between the dipoles associated with the C–H and M–O bonds tends to raise the energy. TS1c and TS1d correspond to (3+2) and (5+2) additions. The former involves two terminal oxygen atoms connected to the same metal centre, using the (O=Mo=O) unit as the active site, while the latter involves two Mo=O connected by a bridge O, using the (O=Mo–O–Mo=O) as the active site. The calculated barriers are 287 kJ mol^{-1} for (3+2) and 264 kJ mol^{-1} for (5+2). The two oxygen atoms interacting with C and H in (5+2) could be compared to two terminal oxygens in α-MoO_3. However, the d(O–O) distance in Mo_3O_9 (5.37 Å) is different from the d(O_{term}–O_{term}) distance in α-MoO_3 (3.70 Å) and this could change the activation energy. The high barrier (290 kJ mol^{-1}) calculated for TS1e suggests that the electrophilicity of the terminal oxo in Mo_3O_9 is relatively weak. TS1f, TS1g and TS1h are for H abstraction, which leads to the formation of radicals. The H abstraction by terminal oxygens (barriers of 188 and 208 kJ mol^{-1} for TS1f and TS1g) is favoured over that by bridging oxygen (barrier 266 kJ mol^{-1}). The radical pair formed in this H abstraction process can decompose to free methyl radicals in the gas phase or rebound with the surface oxygen to give methoxy species. It is found that the distribution of the final products for methane oxidation depends critically on the rebound pathway. If the methyl radical could rebound quickly with the surface oxygen atoms, the main primary products would be methanol and formaldehyde.

Zhang and Hu have reported on the possibility of single C–H bond activation in CH_4 on a MoO_3-supported catalyst, using periodic DFT.[87] Their system consisted of isolated Pt atoms on a $MoO_3(010)$ surface and it was found that the first C–H bond in methane can readily be activated with a very low reaction barrier of 29 kJ mol^{-1}. The further dehydrogenation of methyl was very energetically unfavourable.

Finally, Chen *et al.*[56] used hydrogen and methyl as probes to model the interactions at the $MoO_3(010)$ surface with a terminal oxygen defect, after initial C–H bond breaking of methane. They employed periodic DFT with (2×2) ordered arrays of terminal oxygen vacancies on the $MoO_3(010)$ surface and found that hydrogen is most strongly adsorbed over the terminal oxygen, while methyl is most strongly adsorbed over the Mo atom exposed by removal of a terminal oxygen. Analysis of the bonding showed that methyl is bound more strongly than hydrogen over the Mo atom because the C $2p$ orbital has better overlap with the Mo d_{z^2} orbital than the hydrogen $1s$. Chen *et al.* pointed out that while the terminal oxygen vacancy is necessary energetically for methane dissociation, a methyl created as a result of methane activation could end up bound to the Mo atom and this would represent a "dead end" in an oxidation reaction. They also used the binding energies of H and CH_3 to the vacancy surface to compare the energetics for methane dissociation to the "perfect" surface. The vacancy surface was found to be energetically more favourable with a reaction exothermic by 172 kJ mol^{-1}, while the same reaction on the perfect surface was endothermic by 59 kJ mol^{-1}. However, they did not address the role that the terminal oxygen vacancy could play in breaking the first C–H bond of methane.

2.2 Supported gold catalysts

2.2.1 Gold, an unexpected catalyst

In its bulk form, gold is regarded as chemically inert towards chemisorption of reactive molecules such as oxygen and hydrogen. Consequently, pure gold was considered to be an uninteresting metal from the point of view of catalysis. However, recently, gold catalysts have attracted a dramatic growth of interest, since Haruta found that once Au is deposited as nanoparticles on selected metal oxides, it exhibits surprisingly high catalytic activity for CO oxidation, even at 200 K.[88, 89] Hutchings also predicted that Au would be the best catalyst for ethyne hydrochlorination.[90] There has been an explosion of interest in the study of catalysis by gold as shown by the data on publications and patents in figure 2.14. The rate of academic publications, shown in red, is climbing almost exponentially and patent activity, shown in blue, has climbed since 1990 and is fairly steady at 20-25 new patents per annum.[91]

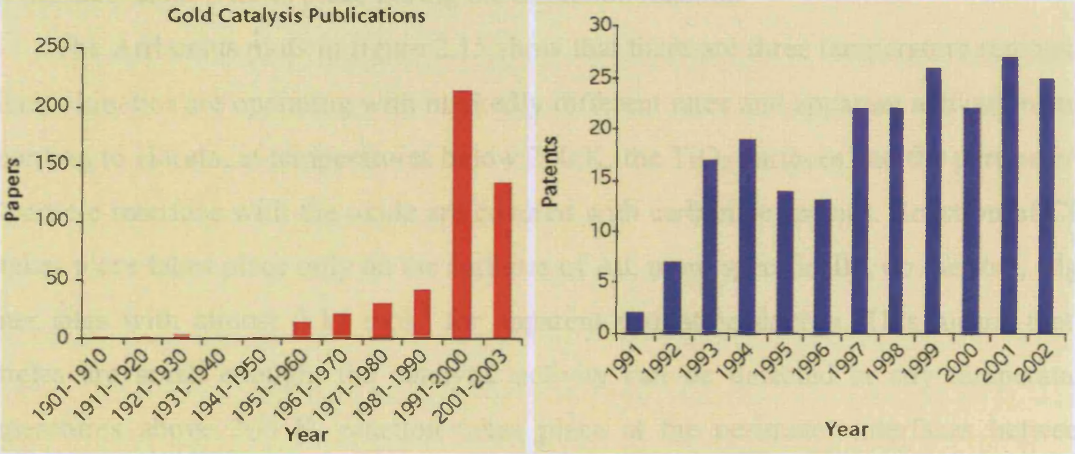

Figure 2.14 Publications on gold catalysis, red academic publications, blue patents.[91]

Substantial reviews on gold catalysis have recently been published by Haruta[92-94], Hutchings[91] and Freund[95] to cite only a few and a large range of chemical reactions are now known to be catalysed by gold catalysts including total and selective oxidation.

A – Chemical reactions catalysed by supported gold nanoclusters

i) CO oxidation

The oxidation of CO (equation 2.2) is probably the most widely studied reaction for which gold is an excellent catalyst at room temperature.

$$CO + O_2 + H_2 \rightarrow CO_2 + H_2O \qquad (2.2)$$

Other noble metals catalysts do not perform as well below 400 K. The Au/TiO_2 system has been extensively studied to date as neither Au nor TiO_2 alone is active for CO oxidation but a combination of them leads to surprisingly high catalytic activity.[92]

There is no direct experimental evidence yet whether the oxygen molecule is dissociatively or non-dissociatively adsorbed and on which site of the supported catalysts it is adsorbed. So far, the most convincing evidence for molecularly adsorbed oxygen has been obtained by a temporal analysis of products (TAP) study of O_2 adsorption[96] and by $^{18}O_2$ isotope experiments[97]. However, there is still a debate as to whether the dissociation of molecularly adsorbed oxygen takes place before reacting with CO adsorbed on the Au surface or if the dissociation takes place during the oxidation reaction.

The Arrhenius plots in figure 2.15 show that there are three temperature regions where different kinetics are operating with markedly different rates and apparent activation energies. According to Haruta, at temperatures below 200 K, the TiO_2 surfaces and the perimeter of the Au particle interface with the oxide are covered with carbonate species. Reaction of CO with O_2 takes place takes place only on the surfaces of Au, more specifically, on the step, edge, and corner sites with almost 0 kJ mol^{-1} for apparent activation energy. This means that when particles are small enough, the catalytic activity can be detected at any temperature. At temperatures above 300 K, reaction takes place at the perimeter interfaces between CO adsorbed on the surface of Au particles and molecular oxygen adsorbed on the support surface. This reaction also gives nearly zero apparent activation energy but proceeds much faster by more than one order of magnitude than the reaction over the Au surfaces. At intermediate temperatures from 200 K to 300 K, the reaction proceeds at the perimeter interface which is partly covered with carbonate species. The coverage of the species may change depending on temperature, thus giving rise to apparent activation energy around 30 kJ mol^{-1}.

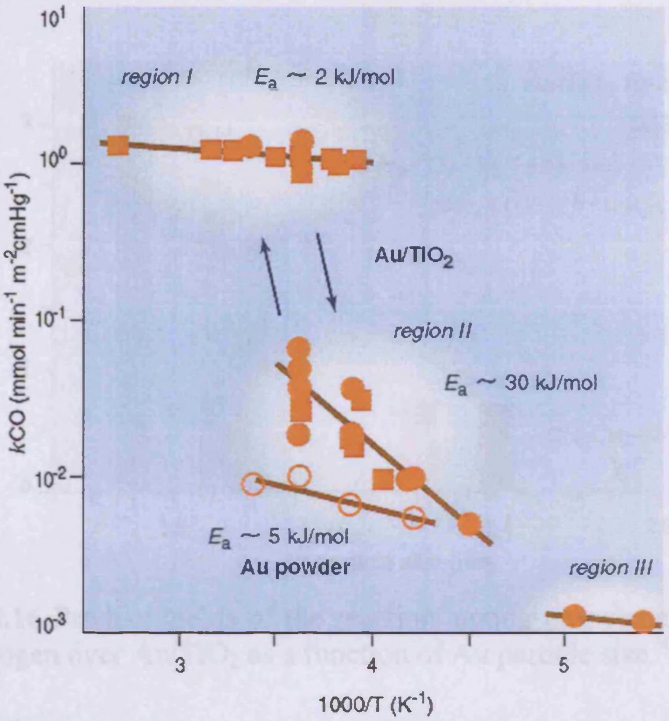

Figure 2.15 Dependence of the reaction rates for CO oxidation over Au/TiO_2 as well as unsupported Au powder on the reaction temperature.[93]

ii) Epoxidation of propylene

Propylene oxide is an important chemical, used for the production of polyurethane and polyols. It is produced world wide at 3.5 million tonnes per year, representing a market of £ 4 billion and this is one where Au could provide a new catalyst. There are four important factors for Au catalysts in the direct epoxidation of propylene:

$$C_3H_6 + O_2 + H_2 \rightarrow C_3H_6O + H_2O \qquad (2.3)$$

1) The catalyst preparation method: impregnation method does not result in effective catalysts for selective oxidation, these materials give complete oxidation to H_2O and CO_2 whereas deposition-precipitation method leads to epoxidation catalysts with selectivity above 90 % [98].

2) Appropriate selection of the support materials: Among single metal oxides, only TiO_2 makes Au selective for the reaction. Moreover, the crystalline structure of TiO_2 should be anatase, not rutile or amorphous[98].

3) The size of Au particles: When the mean diameter of Au particles is smaller than 2nm, propylene is hydrogenated to form propane[99] (figure 2.16).

4) Additives: It has been claimed that many alkali and alkali earth chlorides work as good promoters for epoxidation by Au catalysts[100], however the optimum amount, sites effected and the mechanistic role have not been understood yet.

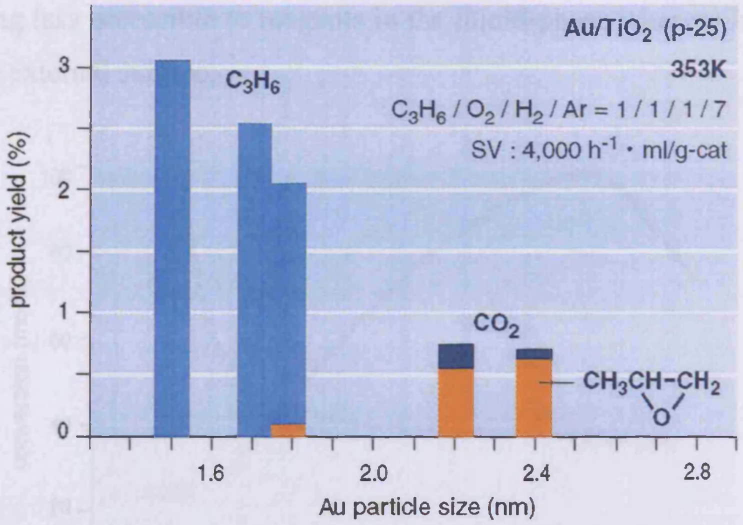

Figure 2.16 Product yields of the reaction among propylene, oxygen and hydrogen over Au/TiO_2 as a function of Au particle size.[93]

iii) Water-gas-shift reaction

Polymer electrolyte fuel cell applications to automobile and residential electricity-heat delivery systems are making the low-temperature water-gas-shift (WGS) reaction

$$CO + H_2O \rightarrow CO_2 + H_2 \tag{2.4}$$

interesting again. Au/TiO_2 has been confirmed to be active for WGS reaction.[101] Andreeva and co-workers were the first to apply Au catalysts to WGS reaction and reported that Au/Fe_2O_3 and Au/ZrO_2 were the most active.[102]

iv) Hydrogenation of unsaturated hydrocarbon

Hydrogenation of hydrocarbons is structure insensitive over supported Au catalysts as well as over most other metal catalysts.[92] However, a characteristic feature of Au catalysts is that partial hydrogenation takes place very selectively. For example: butadiene to butane, acetylene to ethylene.[103]

v) Liquid-phase reactions

Bianchi *et al.* found that Au supported on activated carbon is more active and selective than other noble metal catalysts for oxidation of glycols to α-hydroxy acids in MeOH–H_2O(6:4) solvent.[104] An interesting feature is that with an activated carbon support maximum activity is observed when the mean diameter of Au particles is 7–8 nm, whereas the smaller Au particles give the higher activity on γ-Al_2O_3 and TiO_2 supports[93] (figure 2.17). This is because smaller Au particles can be easily fixed on the internal surfaces of carbon, consequently being less accessible to reagents in the liquid-phase whereas larger Au particles are located on the external surface.

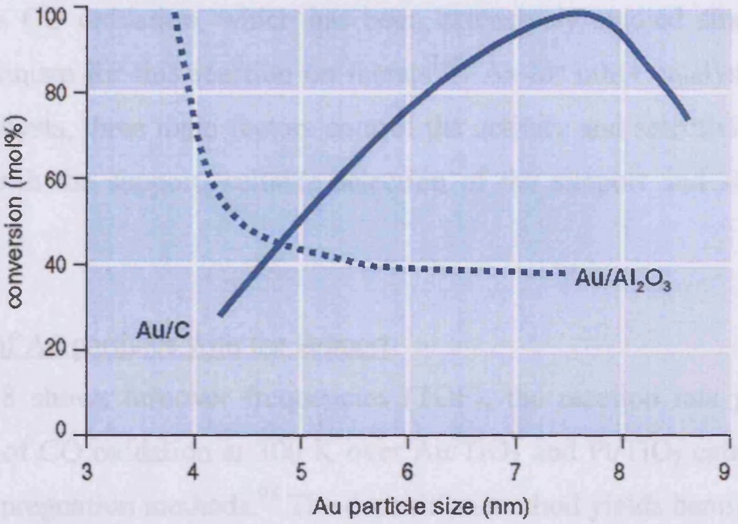

Figure 2.17 Dependence of the conversion for glycol oxidation over Au/Al_2O_3 and Au/C catalysts on the Au particle size.[104]

vi) Other reactions and applications

We have shown that gold catalysts with selected support materials can promote many reactions. Table 2.1 lists such reactions and their applications, which usually take place at much lower temperatures or with much higher degrees of selectivity over Au catalysts than over other metal catalysts.

Fields of applications	**Reactants of reactions**	**Support materials**
Indoor air quality control	Odour (commercialised), CO	Fe_2O_3
	Sick house gases	TiO_2
Pollutant abatement	Dioxin oxidation-decomposition	Fe_2O_3
	NO reduction	Al_2O_3
	N_2O decomposition	Co_3O_4
H_2 energy carrier	Water-gas shift	ZrO_2, CeO_2
	CO removal	Al_2O_3, Mn_2O_3, Fe_2O_3
	Fuel cell anode	Carbon black
Chemical process	Hydrochlorination	$AuCl_3$ / activated carbon
	Hydrogenation	ZnO
	Liquid-phase selective oxidation	Activated carbon
	Propylene epoxidation	TiO_2 (anatase), Ti/SiO_2

Table 2.1 Ongoing and potential applications of Au catalysts.[94]

B – Support and gold cluster size effects

Most reactions are remarkably structure-sensitive over supported Au catalysts. One typical reaction is CO oxidation, which has been extensively studied since Langmuir first presented a mechanism for this reaction on metals[105]. As for other catalysed reactions over supported Au catalysts, three main factors control the activity and selectivity: strong contact of Au particles with the support, suitable selection of the support and size control of Au particles.

i) Strong contact of Au particles with the support

Figure 2.18 shows turnover frequencies (TOF), the reaction rate per surface metal atom per second, of CO oxidation at 300 K over Au/TiO_2 and Pt/TiO_2 catalysts prepared by deposition and impregnation methods.[93] The deposition method yields hemispherical particles while the impregnation method yields spherical particles. The TOF of Au/TiO_2 strongly depends on the shape of the particle with the hemispherical geometry giving much better results and showing that the Au/TiO_2 interface might play a key role in the reaction.

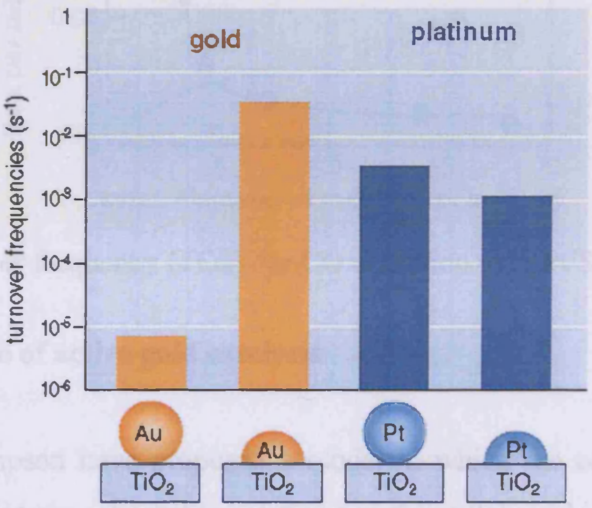

Figure 2.18 Turnover frequencies for CO oxidation over spherical and hemispherical particles of Au and Pt supported on TiO_2.[93]

ii) Selection of the support

For CO oxidation, many oxides other than strongly acidic materials such as Al_2O_3-SiO_2 and activated carbon can be used as a support. Small band gap oxides such as TiO_2 and Fe_2O_3 provide more stable Au catalysts than wide band-gap oxides such as Al_2O_3 and SiO_2

however TOFs at room temperature are almost the same, indicating that contributions of the support are more or less identical.[106] The difference appears in the amount of water required for the CO oxidation to proceed. Al_2O_3 and SiO_2 require a concentration of H_2O of at least 10 ppm higher than TiO_2 does, at room temperature.[107]

iii) Size control of Au particles

Figure 2.19 shows a plot of the TOFs of CO oxidation over Pt/SiO_2 and Au/TiO_2 as a function of the mean diameter of metal particles. While the Pt group of metals shows decreasing or steady TOF, a sharp increase is seen with a decrease in particle diameter for the Au group of metals. The increase in the TOF can be explained if the reaction zone is the periphery of the Au particles, the proportion of which increases in hemispherical Au particles with decreasing size.

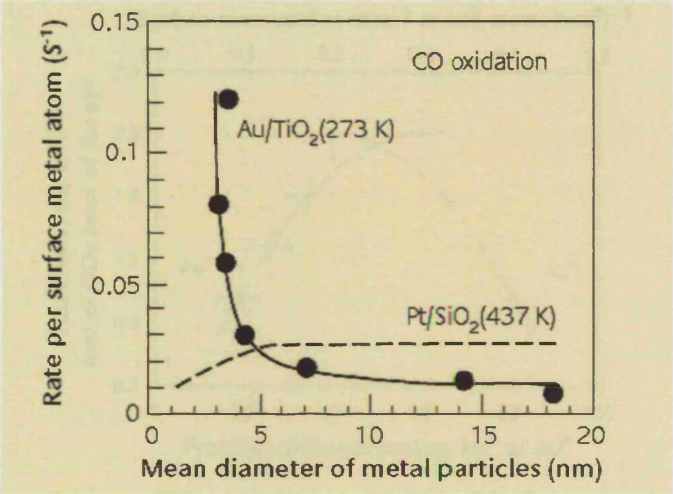

Figure 2.19 Turnover frequency (TOF) for CO oxidation over Pt/SiO_2 and Au/TiO_2 [108]

C – The oxidation state of active gold catalysts

Bond and Thompson have proposed a model in which the active sites are the gold atoms at the interface between the gold particles and the metal oxide surface.[109] However, it remains unclear whether Au^0 or $Au^{\delta+}$ is the active form of gold. This crucial question is at the forefront in the field of gold catalysis and needs to be answered if one wants to understand the fundamental mechanisms of Au catalysed reactions. An increasing number of publications are dealing with this matter, some focusing on metallic gold[110-112] and some focusing on oxidised gold[113-115].

We will give here two opposite examples. Using X-ray absorption near-edge structure (XANES), Guzman and Gates[116] showed that on MgO, both Au(I) and Au(0) are present in the working catalysts for CO oxidation and that the catalytic sites incorporate Au(I) as presented in figure 2.20. This figure shows that the reaction rate is maximised at a surface concentration of 50 % for both Au^+ and Au^0. The rate drops dramatically if only Au^+ or Au^0 is present. They also showed that CO plays a dual role as a reactant and a reducing agent that converts Au(I) into Au(0), diminishing the activity. On the other hand, Schwartz *et al.*[117] studied the influence of oxidation state and particle size on catalytic activity of Au/TiO_2, and concluded that oxidized Au is not necessary for high activity. X-ray absorption spectroscopy (XAS) was used to characterise the catalyst, the oxidation state was determined by XANES, whereas the determination of the neighbouring atoms and their distance were obtained by extended X-ray absorption fine structure (EXAFS).

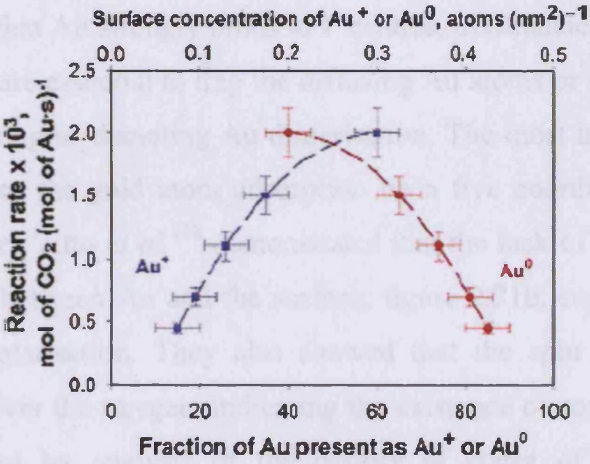

Figure 2.20 Correlation of the catalytic activity with the percentage and surface concentration of cationic and zerovalent gold (the concentrations of gold were calculated on the basis of the approximate surface area of MgO).[116]

Clearly, the support might play an important role and what is true for some metal oxides might not be for others. It is thus important to understand what happens at the atomic level and be able to propose a mechanism based on theoretical work, correlating with the experiment. Au/MgO has already been extensively studied; this is the system we choose as a starting point and it should provide fundamental answers on the oxidation state of active gold catalysts.

2.2.2 Gold supported on MgO

In this section we will present results from previous theoretical studies (mainly DFT) on gold adsorption on magnesium oxide and the mechanism of CO oxidation over this material. Considerable work has been done with single gold atoms, mainly due to the fact that gold clusters require simulation of much larger systems and so more computer resources. Pacchioni has published extensively on Au–support interactions. We will give here some details on the work he has been involved with recently, i.e. Au atoms and dimers on the MgO(100) surface.[118] Magnesium oxide, in particular its (001) surface, is probably to date the most studied oxide both in its stoichiometric form and with the presence of surface oxygen vacancies.

Del Vitto *et al.*[118] adsorbed gold atoms and dimers onto the flat MgO(100) surface and the stepped MgO(310) surface. The flat MgO terrace also contained an oxygen vacancy (F centre). It was found that Au strongly binds to F centres, divacancies and steps and that these defects sites on MgO are essential to trap the diffusing Au atoms or clusters, but do not play a special role in promoting or demoting Au dimerisation. The most interesting result from our point of view concerns the gold atom adsorption on a five coordinated oxygen of the flat MgO(100) surface. Del Vitto *et al.*[118] demonstrated that the lack of accumulation of electron density in the region between Au and the surface, figure 2.21b, suggests important bonding contributions from polarisation. They also showed that the spin density, figure 2.21c, is partially delocalised over the oxygen, indicating the existence of some covalent mixing. This was further confirmed by analysis of the density of states of the MgO(100) and the MgO(100)/Au systems, figure 2.22. The Au 6*s* level is partially mixed with the Au 5*d* state and, to a larger extent, with the 2*p* levels of the oxide anion to which Au is bound, showing that some of the Au–O bond strength comes from a covalent mixing of the Au and O valence levels.

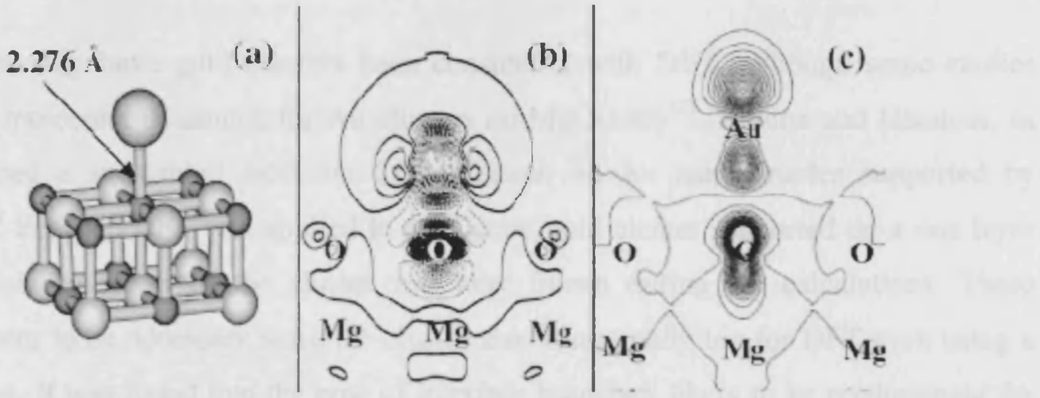

Figure 2.21 (a) Structure of a Au atom adsorbed on a five coordinated oxygen ion on the MgO(100) terrace (white atoms, Mg; black atoms, O; large grey atoms, Au). (b) Charge density difference for Au1/MgO (solid lines, charge accumulation; dotted lines, charge depletion). (c) Spin density for Au$_1$/MgO. Lines are drawn in intervals of 0.01 e Å^{-3}.[118]

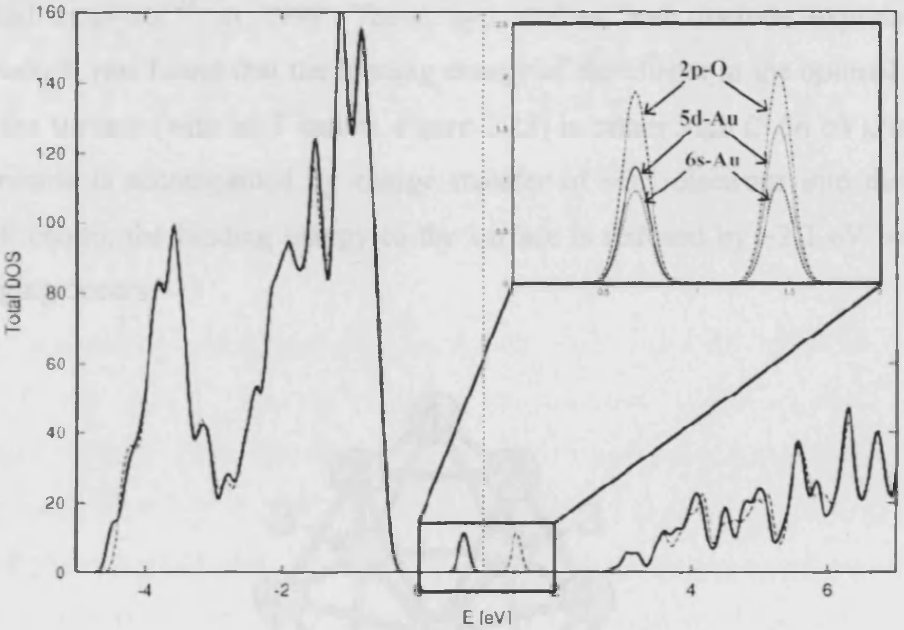

Figure 2.22 Density of states for a Au atom adsorbed on a five-coordinated oxygen ion, on the MgO(100) terrace (solid line, α spin; dotted line, β spin). In the inset are shown the projected DOSs onto the Au 6*s*, 5*d* and O 2*p* states in the energy range 0–2 eV.[118]

In a paper published five years ago, Pacchioni and coworkers[119] wrote that M–O (M= Cu, Ag, Au) bonding is a consequence of the large adatom size (due to singly occupied valence *s* orbital) which determines the long surface–adsorbate distance. They also mentioned that a very small mixing of the metal σ orbitals with the O 2*p* orbital is also found. However, the belief that the nature of this interaction is physisorption only, has been strongly in place until now.[120]

Only recently have gold clusters been considered with DFT, although some studies already used molecular dynamics for Au clusters on MgO(100)[121]. Molina and Hammer, in 2004, published a substantial work on CO oxidation on Au nanoparticles supported by MgO(100).[122] Periodic DFT was applied to a 34 atom gold cluster supported on a one layer MgO(100) slabs and part of the cluster was kept frozen during the calculations. These constraints seem to be necessary since the cluster size is unusually big for DFT even using a supercomputer. It was found that the type of interface boundary likely to be predominant for medium-sized nanoparticles provides the optimal degree of low-coordinated Au atoms in the neighbourhood of the MgO support.

Heiz and co-workers recently published in Science on the charging effects on bonding and catalysed oxidation of CO on Au_8 clusters on MgO[123], after having first published on nanoscale gold catalysts[124] in 1999. These two studies both include experimental and theoretical work. It was found that the binding energy of the cluster in the optimal adsorption geometry to the surface (with an F centre, figure 2.23) is rather high (5.56 eV), and that the adsorption process is accompanied by charge transfer of ~0.5 electrons into the cluster.[124] Without the F centre, the binding energy to the surface is reduced by ~2.2 eV but a similar (partial) charging occurs.

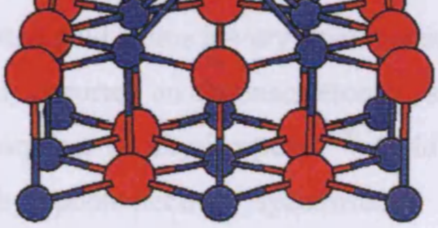

Figure 2.23 View of the energy-optimal structure of Au_8 adsorbed on the MgO(100) surface containing an oxygen-vacancy F-centre. There is a symmetry plane for the Au_8 cluster normal to the page.[124]

More recently, Heiz and co-workers[123] detailed more of the charging effects on bonding of CO on Au_8 clusters on MgO. The charge density difference, $\delta\rho$, is plotted for Au_8 supported on MgO with and without an F centre (figure 2.24). $\delta\rho$ clearly shows that most of the charge transfer occurs at the Au_8/MgO interface and that this does not change whether the gold cluster is on an F centre or not.

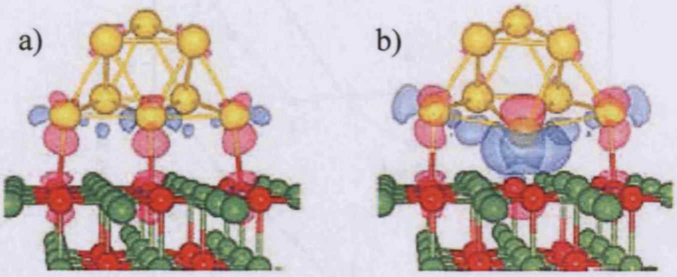

Figure 2.24 (a) Au_8 cluster adsorbed on defect-free MgO, $\delta\rho = \rho_{tot} - (\rho_{Au8} + \rho_{MgO})$, where $\rho_{tot} = \rho[Au_8/MgO]$. (b) Au_8 cluster anchored to a surface F centre of MgO, $\delta\rho = \rho_{tot} - (\rho_{Au8} + \rho_{MgO(FC)})$, where $\rho_{tot} = \rho[Au_8/MgO(FC)]$.[123] Pink isosurfaces represent $\delta\rho < 0$ (depletion) and blue ones correspond to $\delta\rho > 0$ (excess).

2.2.3 CO adsorption on Au_N/MgO

Using temperature programmed desorption and infrared reflection absorption spectroscopy, Lemire *et al.*[125] showed that at low temperatures (T<500 K) small Au deposits adsorb CO more strongly. However, the interaction of CO with Au monolayer islands, formed at a low Au coverage, and relatively large 3D particles, formed at higher coverages, is found to be essentially similar. Hence, Lemire *et al.* proposed that the adsorption of CO only involves low coordinated atoms and is consequently independent of the particles dimensions. The particle size effects are therefore attributed not to quantum size effects but rather to the presence of highly uncoordinated gold atoms in very small particles.[125]

Zhai and Wang recently reported on chemisorption sites of CO on small gold clusters and transitions from chemisorption to physisorption.[126] Gold clusters with adsorbed CO, $Au_m(CO)_n^-$ were studied by photoelectron spectroscopy (PES). Their experimental observation suggests that the first few CO molecules interact more strongly with the Au_m^- clusters than later additions, inducing significant redshift to the electron binding energy and representing chemisorption. Once the available sites on the Au_m^- clusters are used up, further CO adsorption has little effect on the electronic structure of the chemisorbed $Au_m(CO)_n^-$ clusters, indicating the physisorption regime. Figure 2.25 shows the adiabatic detachment energies of the $Au_m(CO)_n^-$ complexes versus the number of CO. The transition from chemisorption to physisorption is clearly seen after a number n = m – 1 of adsorbed CO molecules, for n > 2.

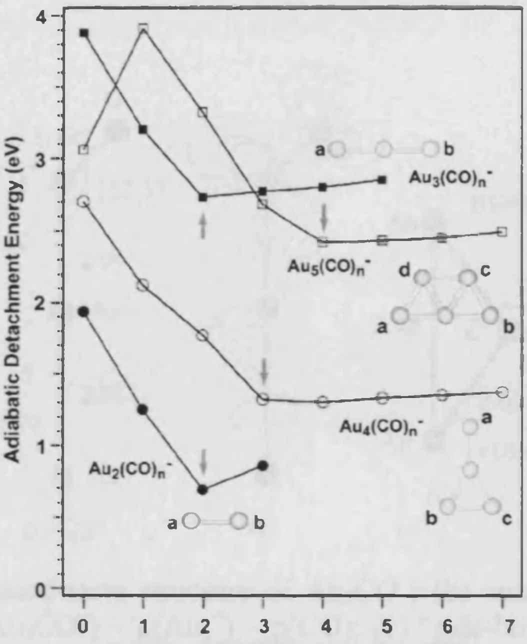

Figure 2.25 Adiabatic electron detachment energies of the $Au_m(CO)_n^-$ complexes versus the number of CO. The arrows indicate the transition from chemisorption to physisorption.[126]

The groups of Landman and Heiz have been very active recently, producing joint papers with both experimental and theoretical results. In a theoretical study of gas-phase catalytic oxidation of CO by Au_2^-, Häkkinen and Landman[127] used Born–Oppenheimer local-spin-density molecular dynamics[128] and found two bonding configurations for Au_2CO^-, shown in figure 2.26. The ground-state “end-bonded” configuration (figure 2.26a) is 0.41 eV more stable than the “side-bonded” (figure 2.26c) configuration. Figure 2.26b presents the charge density difference and one can clearly see the electronic transfer to the π* orbital of CO. It was found that 0.4 |e| is donated to the CO(π*) orbital, accompanied by 0.24 |e| back-donation to gold giving a net transfer of 0.16 |e| to CO, reflected in the calculated vibrational frequency ν(CO)= 1841 cm^{-1}. This has to be compared to the ground-state neutral linear Au_2CO complex, for which the Au–Au, Au–C, and C–O bond lengths are 2.52, 1.93 and 1.149 Å, respectively, the CO adsorption energy is 1.60 eV and the vibrational frequency is ν(CO)= 2147 cm^{-1}. Häkkinen and Landman conclude that the extra electron of the anionic ground-state complex weakens both the Au–CO and C–O bonds, and induces a large red-shift in the CO frequency, causing a change in the structure with the adsorption angle being a possible indicator of the charge state of the gold dimer. The tilted adsorption geometry was believed to be due to symmetry breaking by electron promotion to only one of the initially degenerated CO(π*) orbitals.

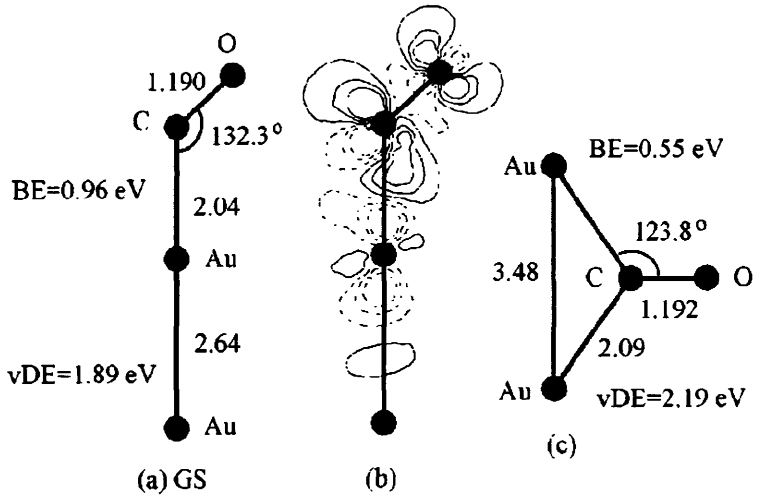

Figure 2.26 (a) Ground-state structure of Au_2CO^-; (b) contour plot of density difference, $\Delta\rho = \rho(Au_2CO^-) - \rho(Au_2^-) - \rho(CO)$; (c) "side-bonded" isomer. BE is the binding (adsorption) energy of CO, vDE is the vertical electron detachment energy. The contours of $\Delta\rho$ are shown in the range of -0.015/0.015 au with 0.006 intervals. Dashed (solid) line denotes depletion (accumulation) of the density. The indicated bond lengths are given in Å.[127]

Lee and Ho[129, 130] also reported tilted adsorption geometries for CO ligands of FeCO and $Fe(CO)_2$ complexes on Ag(110) using Scanning Tunnelling Microscope (STM). This was interpreted to be caused by the local electronic structure of the Fe atom (figure 2.27). Figure 2.27a represents a 25×25 $Å^2$ image of Fe(CO) recorded at 70 mV and 1 nA. Letters *A* through *I* denote the tip position for the corresponding tunnelling current shown in figure 2.27b. The side view (figure 2.27c) and top view (figure 2.27d) of Fe(CO) show the CO to be tilted by an angle τ and bent by an angle β as suggested by the asymmetry in the image (figure 2.27a) and the spatial distribution of the signal (figure 2.27b). Figure 2.27e shows the background subtracted *dI*/*dV* spectra recorded over the positions labelled in figure 2.27a. Later on, Yuan *et al.* performed a DFT cluster model investigation for this system.[131] Employing Frontier Orbital Theory[132] (FOT), Yuan *et al.* found that metal atoms with partially occupied *d* orbitals (Fe, Co and Ni) correspond to the tilted geometry for M(CO) and metal atoms with fully occupied *d* orbitals correspond to the perpendicular geometry for M(CO), *i.e.* perpendicular to the metal surface. The Fe $3d_{xz}$ orbital in Fe(CO) has a weight of 71 % in the HOMO-1 and can distinguish orientations markedly due to its diffuse distribution (figure 2.28a). The Fe 4*s* and $3d_{z^2}$ orbitals were found to be overwhelmed by $3d_{xz}$. On the contrary, for Cu(CO) the 4*s* and $3d_{z^2}$ orbitals occupy 50 % and 80 % in the HOMO and HOMO-1, respectively, and occupations of the other Cu atomic orbitals in the frontier orbitals are small (figure 2.28b). The orientation with CO perpendicular to the surface is slightly favoured.

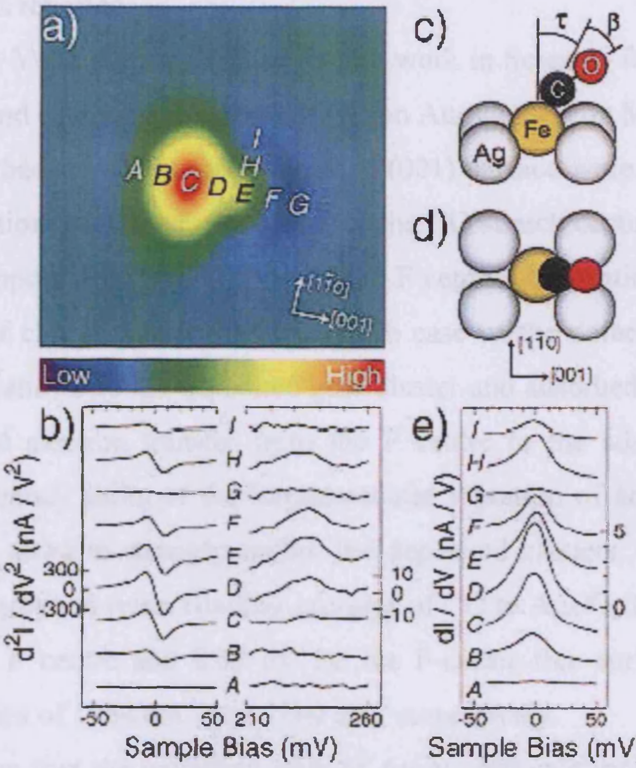

Figure 2.27 Tilted adsorption geometry for CO of the FeCO complex on Ag(110) using STM.[130] Details are given above in the text.

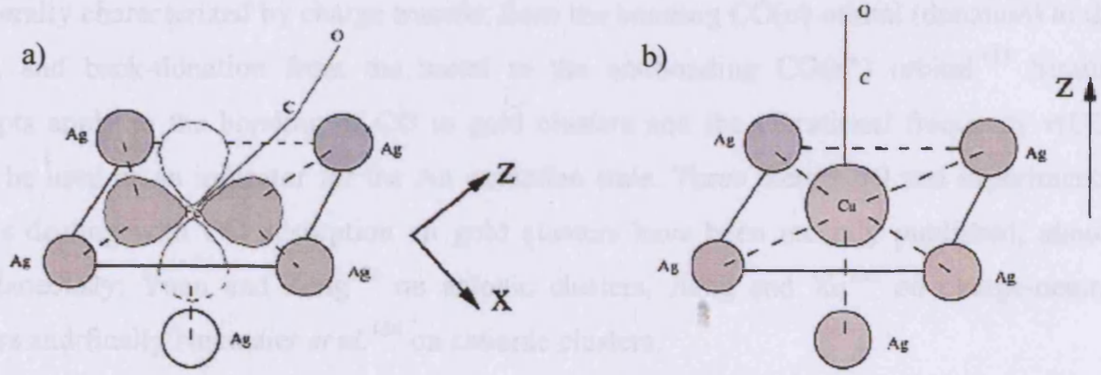

Figure 2.28 Metal atomic orbitals in the frontier orbitals of the metal carbonyls which contribute most to the bonding with Ag(110). a) Fe(CO)Ag (tilted geometry) and b) Cu(CO)Ag (vertical geometry).[131]

The work was then naturally extended to nanoscale gold catalysts by the groups of Landman and Heiz.[123, 124] In a first report, Sanchez *et al.*[124] found that CO binds on top of an Au atom of the upper triangular facet of the adsorbed Au_8 cluster (figure 2.23) with an observed single sharply peaked stretch frequency ν(CO)= 2102 cm^{-1} compared to ν(CO)= 2143 cm^{-1} for the free $^{12}C^{16}O$ molecule. The calculated bond lengths, using the same method as in reference [127], were d(C–O)= 1.14 Å and d(Au–C)= 1.92 Å, but no calculated vibrational frequency ν(CO) was reported.

More recently, Yoon *et al.* published similar work in Science, focusing on the charging effects on bonding and catalysed oxidation of CO on Au_8 clusters on MgO.[123] They found that gold octamers adsorbed on an F-centre-free MgO(001) surface were essentially inactive for the combustion reaction. Moreover, a red shift of the CO stretch occurs when the molecule is adsorbed on Au_8 supported on MgO(001) with an F centre. Adsorption is accompanied by a significant degree of charge transfer, which in the case of the defective surface is directed from the oxygen vacancy into the deposited gold cluster and adsorbed molecules. Yoon *et al.* conclude that partial electron transfer from the F centre to the adsorbed cluster complex correlates with frequency shifts of the intramolecular vibration of adsorbed CO and that in addition, these sites serve to strongly anchor the deposited clusters, thereby inhibiting their coalescence into larger inert ones. Binding energies of CO to $Au_8/O_2/MgO$ were calculated to be 0.72 eV for the F centre and 0.85 eV for the F-centre-free surface, with C–O stretch vibrational frequencies of 1934 cm^{-1} and 1980 cm^{-1} respectively.

We have shown that the oxidation state of Au in gold catalysts is crucial information. The CO molecule is often used as a probe and its intramolecular vibrational frequency calculated in order to assign adsorption sites. The bonding of CO to transition metal surfaces is generally characterized by charge transfer from the bonding CO(σ) orbital (donation) to the metal, and back-donation from the metal to the antibonding CO(π*) orbital.[133] Similar concepts apply to the bonding of CO to gold clusters and the vibrational frequency ν(CO) could be used as an indicator for the Au oxidation state. Three theoretical and experimental studies dealing with CO adsorption on gold clusters have been recently published, almost simultaneously: Yuan and Zeng[134] on anionic clusters, Jiang and Xu[135] on charge-neutral clusters and finally Neumaier *et al.*[136] on cationic clusters.

As already observed experimentally by Zhai and Wang[126], Yuan and Zeng[134] calculated using relativistic DFT, that the adsorption ability of CO reduces with the increase of the number of CO molecules bound to gold cluster anions, resulting in saturated adsorption at a certain amount of absorbed CO molecules.

Jiang and Xu used matrix-isolation infrared spectroscopy to study reactions of laser-ablated Au atoms with CO molecules in solid argon. They also performed DFT calculations and obtained good agreement between the experimental and calculated vibrational frequencies, relative absorption intensities, and isotopic shifts. On the basis of the isotopic substitution, change of CO concentration, and comparison with DFT calculations, the absorptions at 2131.9, 2075.4, 2115.9 and 1852.9 cm^{-1} are assigned to Au_2CO, Au_3CO, Au_4CO and Au_5CO.

Finally, Neumaier *et al.*[136] performed a detailed kinetic study of low-pressure CO adsorption on gold cluster cations Au_n^+ over a large size range in a FT-ICR mass spectrometer. DFT calculations were performed in order to predict ground state structures of gold cluster carbonyls. The bond energy between CO and gold cluster cations was observed to fall off rapidly with cluster size and was attributed to the increasingly "diluted" charge in the metal particle. The most stable isomers were characterized by CO binding to Au atoms having low coordination numbers of two or three.

References

1. J.F. Roth, *Appl. Catal. A.: Gen.*, 1994, **113**, 131.
2. M.J. Brown and N.D. Parkyns, *Catal. Today*, 1991, **8**, 305.
3. R.H. Crabtree, *Chem. Rev.*, 1995, **95**, 987.
4. H.D. Gesser, N.R. Hunter, and C.B. Prakash, *Chem. Rev.*, 1985, **85**, 235.
5. T.J. Hall, J.S.J. Hargreaves, G.J. Hutchings, R.W. Joyner, and S.H. Taylor, *Fuel Proc. Technol.*, 1995, **42**, 151.
6. O.V. Krylov, *Catal. Today*, 1993, **18**, 209.
7. N.D. Parkyns, C.I. Warburton, and J.D. Wilson, *Catal. Today*, 1993, **18**, 385.
8. R. Pitchai and K. Klier, *Catal. Rev. Sci. Eng.*, 1986, **28**, 13.
9. A.E. Shilov and G.B. Shul'pin, *Russ. Chem. Rev.*, 1987, **56**, 442.
10. L.C. Kao, A.C. Huston, and A. Sen, *J. Am. Chem. Soc.*, 1991, **113**, 700.
11. R.A. Periana, D.J. Taube, E.R. Evitt, G. Loffler, P.R. Wentrcek, G. Voss, and T. Masuda, *Science*, 1993, **259**, 340.
12. X. Gang, H. Birch, Y. Zhu, H.A. Hjuler, and N.J. Bjerrum, *J. Catal.*, 2000, **196**, 287.
13. R.A. Periana, D.J. Taube, S. Gamble, H. Taube, T. Satoh, and H. Fujii, *Science*, 1998, **280**, 560.
14. J. Colby, S.I. Stirling, and H. Dalton, *Biochem. J.*, 1977, **165**, 395.
15. *Cytochrome P-450, Structure, Mechanism and Biochemistry*, ed. O. de Montellano. 1986, New York: Plenum Press.
16. *Metalloporphyrins Catalyzed Oxidations*, ed. F. Montanari and L. Casella. 1994, Dordrecht: Kluwer Academic.
17. D.H.R. Barton and D. Doller, *Acc. Chem. Res.*, 1992, **25**, 504.
18. A.M. Khenkin and A.E. Shilov, *New J. Chem.*, 1989, **13**, 659.
19. N. Elango, R. Radhakrishnan, W.A. Froland, B.J. Wallar, C.A. Earhart, J.D. Lipscomb, and D.H. Ohlendorf, *Prot. Science*, 1997, **6**, 556-568.
20. K. Yoshizawa, *J. Inorg. Biochem.*, 2000, **78**, 23-34.
21. H. Basch, K. Mogi, D.G. Musaev, and K. Morokuma, *J. Am. Chem. Soc.*, 1999, **121**, 7249-7256.
22. P.-P.H.J.M. Knops-Gerrits and W.A. Goddard III, *Catal. Today*, 2003, **81**, 263-286.
23. R. Burch, G.D. Squire, and S.C. Tsang, *J. Chem. Soc., Faraday Trans. I*, 1989, **85**, 3561-3568.
24. G.S. Walker, J.A. Lapszewicz, and G.A. Foulds, *Catal. Today*, 1994, **21**, 519.
25. N.R. Hunter, H.D. Gesser, L.A. Morton, and P.S. Yarlagada, *Appl. Catal.*, 1990, **57**, 45.
26. W.Y. Feng, F.C. Knopf, and K.M. Dooley, *Energy Fuels*, 1994, **8**, 815.
27. D.W. Rytz and A. Baiker, *Ind. Eng. Chem. Res.*, 1991, **30**, 2287.
28. T. Sugino, A. Kido, N. Azuma, A. Ueno, and J. Udagawa, *J. Catal.*, 2000, **190**, 118.
29. J.E. Lyons, P.E. Ellis Jr., and V.A. Dutante, *Stud. Surf. Sci. Catal.*, 1991, **67**, 99.
30. J.S.J. Hargreaves, G.J. Hutchings, R.W. Joyner, and S.H. Taylor, *Chem. Commun.*, 1996, 523.
31. K. Otsuka, Y. Wang, I. Yamanaka, and A. Morikawa, *J. Chem. Soc., Faraday Trans.*, 1993, **89**, 4225.
32. M.D. Amiridis, J.E. Rekoske, J.A. Dumesic, D.F. Rudd, N.D. Spencer, and C.J. Pereira, *AIChe J.*, 1991, **37**, 87.
33. J.H. Lunsford, *Catal. Rev. Sci. Eng.*, 1973, **8**, 135.
34. M. Che and A.J. Tench, *Adv. Catal.*, 1982, **31**, 78.
35. M. Che and A.J. Tench, *Adv. Catal.*, 1983, **32**, 1.

36. K. Aika and J.H. Lunsford, *J. Phys. Chem.*, 1977, **81**, 1393.
37. K. Aika and J.H. Lunsford, *J. Phys. Chem.*, 1978, **82**, 1794.
38. D.J. Driscoll, W. Martir, J.-X. Wang, and J.H. Lunsford, *J. Am. Chem. Soc.*, 1985, **107**, 58-63.
39. J.-X. Wang and J.H. Lunsford, *J. Phys. Chem.*, 1986, **90**, 5883.
40. C.-H. Lin, K.D. Campbell, J.-X. Wang, and J.H. Lunsford, *J. Phys. Chem.*, 1986, **90**, 534.
41. M.A. Banares, I. Rodriguez-Ramos, A. Guerrero-Ruiz, and J.L.G. Fierro, *Stud. Surf. Sci. Catal.*, 1993, **75**, 1131.
42. M.R. Smith and U.S. Ozkan, *J. Catal.*, 1993, **141**, 124.
43. B. Kartheuser and B.K. Hodnett, *J. Chem. Soc., Chem. Commun.*, 1993, 1093.
44. T. Leisegang, D.C. Meyer, A.A. Levin, S. Braun, and P. Paufler, *Appl. Phys. A*, 2003, **77**, 965.
45. L. Kihlborg, *Ark. Kemi*, 1963, **21**, 357-364.
46. J. Haber and E. Lalik, *Catal. Today*, 1997, **33**, 119.
47. B. Grzybowska-Swierkosz, *Top. Catal.*, 2000, **11/12**, 23.
48. D. Wang, S. Dangsheng, and R. Schlögl, *Cryst. Res. Technol.*, 2003, **38**, 153-159.
49. N. Floquet and O. Bertrand, *Surf. Sci.*, 1988, **198**, 449-460.
50. K.T. Queeney and C.M. Friend, *J. Phys. Chem. B*, 1998, **102**, 5178-5181.
51. K.T. Queeney and C.M. Friend, *J. Phys. Chem. B*, 2000, **104**, 409-415.
52. A. Papakondylis and P. Sautet, *J. Phys. Chem.*, 1996, **100**, 10681-10688.
53. F. Corà, A. Patel, N.M. Harrison, R. Dovesi, and C.R.A. Catlow, *J. Mater. Chem.*, 1997, **7**, 959.
54. M. Chen, U.V. Waghmare, C.M. Friend, and E. Kaxiras, *J. Chem. Phys.*, 1998, **109**, 6854-6860.
55. I.N. Remediakis, E. Kaxiras, M. Chen, and C.M. Friend, *J. Chem. Phys.*, 2003, **118**, 6046-6051.
56. M. Chen, C.M. Friend, and E. Kaxiras, *J. Am. Chem. Soc.*, 2001, **123**, 2224-2230.
57. D. Wang, D.S. Su, and R. Schlögl, *Z. Anorg. Allg. Chem.*, 2004, **630**, 1007-1014.
58. A. Michalak, K. Hermann, and M. Witko, *Surf. Sci.*, 1996, **366**, 323-336.
59. K. Hermann, M. Witko, and A. Michalak, *Catal. Today*, 1999, **50**, 567-577.
60. R. Tokarz-Sobieraj, K. Hermann, M. Witko, A. Blume, G. Mestle, and R. Schlögl, *Surf. Sci.*, 2001, **489**, 107-125.
61. M. Witko and R. Tokarz-Sobieraj, *Catal. Today*, 2004, **91-92**, 171-176.
62. R. Tokarz-Sobieraj, R. Grybos, M. Witko, and K. Hermann, *Collect. Czech. Chem. Commun.*, 2004, **69**, 121-139.
63. H.-F. Liu, R.-S. Liu, K.Y. Liew, R.E. Johnson, and J.H. Lunsford, *J. Am. Chem. Soc.*, 1984, **106**, 4117.
64. J.C. Volta and J.M. Tatibouet, *J. Catal.*, 1985, **93**, 467-470.
65. K. Suzuki, T. Hayakawa, M. Shimizu, and K. Takehira, *Catal. Lett.*, 1995, **30**, 159.
66. R. Mauti and C. Mims, *Catal. Lett.*, 1993, **21**, 201.
67. A. Parmaliana and F. Arena, *J. Catal.*, 1997, **167**, 57-65.
68. F. Arena, N. Giordano, and A. Parmaliana, *J. Catal.*, 1997, **167**, 66-76.
69. T. Takemoto, K. Tabata, Y. Teng, L.-X. Dai, and E. Suzuki, *Catal. Today*, 2001, **71**, 47-53.
70. Y. Yamada, A. Ueda, H. Shioyama, and T. Kobayashi, *Appl. Catal. A: Gen.*, 2003, **254**, 45-58.
71. N. Ohler and A.T. Bell, *J. Catal.*, 2005, **231**, 115-130.
72. U.S. Ozkan and R.B. Watson, *Catal. Today*, 2005, **100**, 101-114.
73. M.A. Banares, *Catal. Today*, 1999, **51**, 319.

74. L.E. Cadus, M.C. Abello, M.F. Gomez, and J.B. Rivarola, *Ind. Eng. Chem. Res.*, 1996, **35**, 14-18.
75. B. Zhang, N. Liu, Q. Lin, and D. Lin, *J. Mol. Catal. A: Chem.*, 1991, **62**, 15.
76. W. Bytyn and M. Baerns, *Appl. Catal.*, 1986, **28**, 199-207.
77. V.D. Sokolovskii and E.A. Mamedov, *Catal. Today*, 1992, **14**, 331-486.
78. M. Hatano and K. Otsuka, *J. Chem. Soc., Faraday Trans. I*, 1989, **85**, 199-206.
79. A.M. Maitra, *Appl. Catal.*, 1993, **104**, 11-59.
80. Y. Feng, J. Niiranen, and D. Gutman, *J. Phys. Chem.*, 1991, **95**, 6558-6563.
81. M. Utiyama, H. Hattori, and K. Tanabe, *J. Catal.*, 1978, **53**, 237-242.
82. G.A. Martin and C. Mirodatos, *Fuel Proc. Technol.*, 1995, **42**, 179-215.
83. Y. Moro-oka, *Appl. Catal. A.: Gen.*, 1999, **181**, 323-329.
84. S. Kuba, P.C. Heydorn, R.K. Grasselli, B.C. Gates, M. Che, and H. Knözinger, *Phys. Chem. Chem. Phys.*, 2001, **3**, 146-154.
85. G. Fu, X. Xu, X. Lu, and H. Wan, *J. Am. Chem. Soc.*, 2005, **127**, 3989-3996.
86. X. Xu, F. Faglioni, and W.A. Goddard III, *J. Phys. Chem. A*, 2002, **106**, 7171-7176.
87. C.J. Zhang and P. Hu, *J. Chem. Phys.*, 2002, **116**, 4281.
88. M. Haruta, N. Yamada, T. Kobayashi, and S. Iijima, *J. Catal.*, 1989, **115**, 301.
89. M. Haruta, S. Tsubota, T. Kobayashi, H. Kageyama, M.J. Genet, and B. Delmon, *J. Catal.*, 1993, **144**, 175.
90. G.J. Hutchings, *J. Catal.*, 1985, **96**, 292.
91. G.J. Hutchings, *Gold Bull.*, 2004, **37**, 3-11.
92. M. Haruta and M. Daté, *Appl. Catal. A.: Gen.*, 2001, **222**, 427-437.
93. M. Haruta, *CATTECH*, 2002, **6**, 102-115.
94. M. Haruta, *Gold Bull.*, 2004, **37**, 27-36.
95. R. Meyer, C. Lemire, S.K. Shaikhutdinov, and H.-J. Freund, *Gold Bull.*, 2004, **37**, 72-124.
96. M. Olea, M. Kunitake, T. Shido, and Y. Iwasawa, *Phys. Chem. Chem. Phys.*, 2001, **3**, 627.
97. H. Liu, A.I. Kozlov, A.P. Kozlova, T. Shido, K. Asakura, and Y. Iwasawa, *J. Catal.*, 1999, **185**, 252.
98. M. Haruta, B.S. Uphade, S. Tsubota, and A. Miyamoto, *Res. Chem. Intermed.*, 1998, **24**, 329.
99. G. Mul, A. Zwijnenburg, B. Linden, M. Makkee, and J.A. Moulijn, *J. Catal.*, 2001, **201**, 128-137.
100. B.S. Uphade, N. Yamada, T. Nakamura, and M. Haruta, *Appl. Catal. A.: Gen.*, 2001, **215**, 137.
101. H. Sakurai, A. Ueda, T. Kobayashi, and M. Haruta, *J. Chem. Soc., Chem. Commun.*, 1997, 271.
102. D. Andreeva, V. Idakiev, T. Tabakova, and A. Andreev, *J. Catal.*, 1996, **158**, 354.
103. J. Jia, K. Haraki, J.N. Kondo, K. Domen, and K. Tamaru, *J. Phys. Chem. B*, 2000, **104**, 11153.
104. C. Bianchi, F. Porta, L. Prati, and M. Rossi, *Top. Catal.*, 2000, **13**, 231.
105. I. Langmuir, *J. Am. Chem. Soc.*, 1918, **40**, 1361.
106. M. Okumura, S. Nakamura, S. Tsubota, T. Nakamura, N. Azuma, and M. Haruta, *Catal. Lett.*, 1998, **51**, 53.
107. M. Daté and M. Haruta, *J. Catal.*, 2001, **201**, 221.
108. M. Haruta, *Catalysis and Electrocatalysis on Nanopaticles*, A. Wieckowski, E.R. Savinova, and C.G. Vayenas, Editors. 2003, Marcel Dekker: New York. p. 645.
109. G.C. Bond and D.T. Thompson, *Gold Bull.*, 2000, **33**, 41.
110. M. Valden, X. Lai, and D.W. Goodman, *Science*, 1998, **281**, 1647.

111. H.-G. Boyen, G. Kästle, F. Weigl, B. Koslowski, G. Dietrich, P. Ziemann, J.P. Spatz, S. Rietmüller, T. Hartmann, M. Nöller, G. Smid, M. Garnier, and P. Oelhafen, *Science*, 2002, **297**, 1533.
112. N. Lopez and J.K. Nørskov, *J. Am. Chem. Soc.*, 2002, **124**, 11262.
113. N.A. Hodge, C.J. Kiely, R. Whyman, M.R.H. Siddiqui, G.J. Hutchings, Q.A. Pankhurst, F.E. Wagner, R.R. Rajaram, and S.E. Golunski, *Catal. Today*, 2002, **72**, 133.
114. Q. Fu, H. Saltsburg, and M. Flytzani-Stephanopoulos, *Science*, 2003, **301**, 935.
115. B.C. Gates and J. Guzmann, *J. Phys. Chem. B*, 2002, **106**, 7659.
116. J. Guzmann and B.C. Gates, *J. Am. Chem. Soc.*, 2004, **126**, 2672-2673.
117. V. Schwartz, D.R. Mullins, W. Yan, B. Chen, S. Dai, and S.H. Overbury, *J. Phys. Chem. B*, 2004, **108**, 15782-15790.
118. A. Del Vitto, G. Pacchioni, F. Delbecq, and P. Sautet, *J. Phys. Chem. B*, 2005, **190**, 8040-8048.
119. I. Yudanov, G. Pacchioni, K. Neyman, and N. Rösch, *J. Phys. Chem. B*, 1997, **101**, 2786-2792.
120. Y.F. Zhukovskii and E.A. Kotomin, *Phys. Stat. Sol. (c)*, 2005, **2**, 347-350.
121. M. Kubo, R. Miura, R. Yamauchi, R. Vetrivel, and A. Miyamoto, *Appl. Surf. Sci.*, 1995, **89**, 131-139.
122. L.M. Molina and B. Hammer, *Phys. Rev. B*, 2004, **69**, 155424.
123. B. Yoon, H. Häkkinen, U. Landman, A.S. Wörz, J.-M. Antonietti, S. Abbet, K. Judai, and U. Heiz, *Science*, 2005, **307**, 403-407.
124. A. Sanchez, S. Abbet, U. Heiz, W.-D. Schneider, H. Hakkinen, R.N. Barnett, and U. Landman, *J. Phys. Chem. A*, 1999, **103**, 9573-9578.
125. C. Lemire, D.C. Meyer, S.K. Shaikhutdinov, and H.-J. Freund, *Surf. Sci.*, 2004, **552**, 27-34.
126. H.-J. Zhai and L.-S. Wang, *J. Chem. Phys.*, 2005, **122**, 051101.
127. H. Häkkinen and U. Landman, *J. Am. Chem. Soc.*, 2001, **123**, 9704-9705.
128. R.N. Barnett and U. Landman, *Phys. Rev. B*, 1993, **48**, 2081-2097.
129. H.J. Lee and W. Ho, *Science*, 1999, **286**, 1719.
130. H.J. Lee and W. Ho, *Phys. Rev. B*, 2000, **61**, R16347-RR16350.
131. L.-F. Yuan, J. Yang, Q. Li, and Q.-S. Zhu, *Phys. Rev. B*, 2001, **65**, 035415.
132. R. Hoffmann, *Solids and Surfaces: A Chemist's View of Bonding in Extended Structures*. 1988: VCH, Verlag GmbH.
133. G.A. Somorjai, *Introduction to Surface Chemistry and Catalysis*. 1994, New York: Wiley-VCH.
134. D.W. Yuan and Z. Zeng, *J. Chem. Phys.*, 2004, **120**, 6574-6584.
135. L. Jiang and Q. Xu, *J. Phys. Chem. A*, 2005, **109**, 1026-1032.
136. M. Neumaier, F. Weigend, O. Hampe, and M.M. Kappes, *J. Chem. Phys.*, 2005, **122**, 104702.

Chapter 3

Theoretical background

This chapter will present the theory that underpins our work: Density Functional Theory (DFT), geometry optimisers, vibrational frequencies, Bader charges, density of states and implementation of DFT in the codes used for this study.

3.1 Density Functional Theory and beyond

The aim of an *ab initio* method is to find the solution of the many-body Schrödinger equation for the system being studied. The first simplification to this goal is the Born-Oppenheimer approximation[1], where the electronic and nuclear degrees of freedom are separated. The justification for this is that the electrons are much less massive than the nuclei but experience similar forces and therefore the electrons will respond almost instantaneously to the movement of the nuclei. Thus, the energy for a given nuclear configuration will be that of the ground state of the electrons in that configuration. The equation to solve is therefore,

$$\hat{H}\Psi = E\Psi \qquad (3.1)$$

where Ψ is the many body wavefunction for the N electronic eigenstates, an anti-symmetric function of the electronic coordinates $\{r_i : i = 1...N\}$, and E is the is the total energy. The Hamiltonian $\hat{H}$ is given by

$$\hat{H} = -\frac{\hbar^2}{2m_e}\sum_i \nabla^2 r_i + V_{ext}(\{R_I\}) + V_{e-e}(\{r_i\}) \qquad (3.2)$$

where V_{ext} is the external potential imposed by the nuclear configuration $\{R_I\}$ and V_{e-e} is the electron – electron interaction given by the Hartree term $\sum_{j>i} \frac{e^2}{|r_i - r_j|}$.

In principle, this equation may be solved to arbitrary accuracy by representing Ψ as a direct product wavefunction and diagonalising the Hamiltonian. However, the cost of this calculation scales exponentially with the number of electrons in the system and is intractable for all but the smallest systems. Another approach is clearly needed for this problem.

3.1.1 DFT

DFT is based on the notion of the single particle electron density as a fundamental variable. This is a consequence of the Honenberg-Kohn theorem[2] which states that the ground state electron density $n_0(r)$ minimises the energy functional

$$E[n(r)] = F[n(r)] + \int n(r)V_{ext}(r)d^3r \tag{3.3}$$

where F[n(r)] is a universal functional. Furthermore, the minimum value of E is E_0, the ground state electronic energy. This is an exact result and in principle, means that the ground state energy and electron density may be found using a variational minimisation over the electrons density n(r), a process which scales linearly with the system.

Unfortunately, the proof of the Honenberg-Kohn theorem is not constructive, hence the form of the functional F[n(r)] in Equation 3.3 is not known. Kohn and Sham postulated[3] that this functional could be written

$$F[n(r)] = T_S[n(r)] + \frac{e^2}{2}\iint \frac{n(r)n(r')}{|r-r'|}d^3rd^3r' + E_{XC}[n(r)]\,. \tag{3.4}$$

Here the first term $T_S[n(r)]$ is the kinetic energy of a system of non-interacting electrons with density n(r) and the second is the electron – electron Hartree interaction. The final term, $E_{XC}[n(r)]$, is the exchange-correlation energy. By writing the electron density in terms of a set of single particle wavefunctions $\{\psi_i\}$ such that

$$n(r) = \sum_i |\psi_i(r)|^2 \tag{3.5}$$

the kinetic energy term may be written

$$T_S[n(r)] = -\frac{\hbar^2}{2m_e}\sum_i \int \psi_i(r)\nabla^2\psi_i(r)d^3r\,. \tag{3.6}$$

Minimising E[n(r)] with respect to n(r), subject to the constraint that the number of electrons must be constant, leads to a set of equations

$$\left(-\frac{\hbar^2}{2m_e}\nabla^2 + V_{eff}(r)\right)\psi_i(r) = \varepsilon_i\psi_i(r) \tag{3.7}$$

for each *i*, where V_{eff} is an "effective potential",

$$V_{eff} = V_{ext}(r) + e^2\int \frac{n(r')}{|r-r'|}d^3r' + V_{XC}(r) \tag{3.8}$$

and $V_{XC}(r)$ is the exchange-correlation potential $\frac{\delta E_{XC}}{\delta n(r)}$. Equation 3.6 can be seen as a set of Schrödinger-like equations for the single particle Kohn-Sham orbitals

$$\hat{H}_{KS}\left|\psi_i\right\rangle = \varepsilon_i\left|\psi_i\right\rangle. \tag{3.9}$$

Thus, the problem of a system of interacting electrons has been mapped onto a system of non-interacting electrons moving in an effective potential given by Equation 3.8. However, the expression of the density in terms of a set of single particle orbitals has increased the complexity of the problem. The minimisation must now be performed over *NM* degrees of freedom where *M* is the number of basis functions used to represent the $\{\psi_i\}$.

The Kohn-Sham DFT approach to the solution of the many-body Schrödinger equation has not required any approximation so far. However, the exchange-correlation energy, $E_{XC}[n(r)]$ in Equation 3.4, is defined as the difference between the true functional $F[n(r)]$ and the remaining terms. As the true form of F is unknown, we must use an approximation for E_{XC}.

A number of possible approximations may be made. The simplest, known as the Local Density Approximation (LDA), defines E_{XC} as

$$E_{XC} = \int \varepsilon_{XC}(n(r))n(r)d^3r, \tag{3.10}$$

where $\varepsilon_{XC}(n(r))$ is the exchange-correlation energy per unit volume of a homogeneous electron gas of density n(r). The values of $\varepsilon_{XC}(n(r))$ were calculated by Ceperley and Alder using quantum Monte Carlo techniques[4] and parameterised by Perdew and Zunger[5]. Although a gross approximation, LDA has been found to give good results in a wide range of solid state systems. Generalised Gradient Approximation (GGAs) adds a term in the gradient of the electron density to the parameterisation of E_{XC}. Although GGAs do not offer a consistent improvement over LDA in all types of system, they have been shown to improve on the LDA for calculations of molecular structures and in representing weak inter-molecular bonds.[6] Meta-GGA functionals using the Laplacian of the density or the kinetic energy density in addition to the density and the magnitude of the gradient of the density, have much less difficulties in describing systems with long range interactions such as van der Waals forces between molecular fragments and surfaces.[7]

The reasons for the success of these approximations are not well understood, although this may be partially attributed to the fact that both obey the sum rule for the exchange-correlation hole in the electron density.[8] Certainly, LDA and GGAs give rise to a systematic overestimation of the electronic binding energy. However, differences in energies may be accurately computed and it is these which are important for the estimation of physical and chemical properties.

An interesting class of functionals are hybrids[9], which combine exact (Hartree-Fock) exchange with conventional GGAs, the general form is,

$$E_{xc}^{hybrid} = \alpha(E_x^{HF} - E_x^{GGA}) + E_{xc}^{GGA} \tag{3.11}$$

where E_x^{HF} is the Hartree-Fock exchange expression[10, 11], except Kohn-Sham rather than Hartree-Fock orbitals are used, hence the wording "exact-exchange". The coefficient α that determines the amount of exact-exchange mixing cannot be assigned from first-principles and so is fitted semi-empirically.

The logic behind this prescription was put forward by Becke[9] who noted that the limits of the adiabatic connection integral for the exact exchange-correlation energy[12] could be approximated as:

$$E_{xc} = \int_0^1 U^\lambda d\lambda = \frac{1}{2}U^0 + \frac{1}{2}U^1 . \tag{3.12}$$

Since λ = 0 corresponds to the exchange only limit, this could well be described using Hartee-Fock theory, while λ = 1 represents the most local part of the electron interactions, as a result of correlation, and so could be amenable to a local-type density functional treatment. As result, Becke proposed the so-called half-and-half functional,

$$E_{xc} = \frac{1}{2}E_x^{HF} + \frac{1}{2}E_{xc,\lambda=1}^{DF} \tag{3.13}$$

where $E_{xc,\lambda=1}^{DF}$ is obtained from a density functional approximation such as LDA. It later emerged from semi-empirical fits to atomic and molecular data that the optimum amount of exchange mixing should be reduced to ~ 0.25, although the precise value to employ depends upon the fitting data.[13]

Hybrids give significant improvement over GGAs for many molecular properties, consequently they are a very popular choice in quantum chemistry. They are not generally used in solid state physics because of the difficulty of computing the exact-exchange part within a plane-wave basis set.

3.1.2 Pseudopotentials

If all of the electrons in a system were explicitly included when performing a calculation, the computational cost would still be prohibitive for atoms as heavy as selenium. Fortunately, many chemical and physical processes are governed by the valence states but only indirectly involve the core states. Thus, the core electron states may be assumed to be fixed and a "pseudopotential" may be constructed for each atomic species which takes into account the effects of the nucleus and core electrons in an effective manner.

In the norm-conserving pseudopotential approach, only the chemically active valence electrons are dealt with explicitly. The chemically inert core electrons are eliminated within a frozen-core approximation. All electrostatic and quantum-mechanical interactions of the valence electrons with the ion cores (the nuclear Coulomb attraction screened by the core electrons, Pauli repulsion and exchange correlation between core and electrons) are accounted for by angular momentum dependent pseudopotentials. The pseudopotential is expressed as:

$$\hat{V}^{ps} = \hat{V} + (\varepsilon - \hat{T} - \hat{V})\hat{P} \tag{3.14}$$

where $\hat{P}$ is the projection operator which projects any state onto the core states.

The pseudo-Schrödinger equation provides the same eigenvalues as the original Schrödinger equation for the valence electrons but it also considers the effects the core has onto atoms without explicitly calculating the core wave functions. This is a big advantage for the bulk material (or even molecular system) calculation since we can construct the pseudo potential from the exact all-electron calculation of the single atom system, and use the constructed pseudopotential to calculate the bulk properties without considering the core electrons for all the atoms in the bulk system. More details on pseudopotential generation are given in section 4.1.

3.1.3 DFT+U

DFT often fails to describe strongly correlated systems with localized *d* and *f* electrons. This error can be corrected with the DFT+U method, which is a combination of DFT and a Hubbard Hamiltonian for the Coulomb repulsion and exchange interaction. The simplest DFT+U version has been proposed by Dudarev *et al.*[14] and yields the rotational invariant energy functional:

$$E_{DFT+U} = E_{DFT} + \frac{U-J}{2}\sum_{\sigma} T_r\left[\rho^{\sigma} - \rho^{\sigma}\rho^{\sigma}\right] \tag{3.15}$$

where U is a spherically averaged Hubbard parameter[15] describing the energy increase for placing an extra electron on a particular site, J is a parameter representing the screened exchange and ρ^{σ} is the on-site density matrix of the *d* electrons.

This can be understood as adding a penalty functional to the DFT total energy expression that forces the on site occupancy matrix in the direction of idempotency. While U depends on the spatial extension of the wave functions and on screening, J is an approximation to the Stoner exchange parameter and is an almost constant ~ 1 eV. When $U = J$, the DFT+U functional yields exactly the same energy as the DFT functional. If $U > J$, the second term in Equation (3.15) is positive, since the eigenvalues υ_i of the on-site occupancy matrix can vary only between 0 and 1:

$$\rho^{\sigma} - \rho^{\sigma}\rho^{\sigma} = \sum_i (\upsilon_i^{\sigma} - \upsilon_i^{\sigma 2}) > 0 \tag{3.16}$$

where the sum on the right-hand side of Equation (3.16) is over all eigenvalues υ_i of the on-site occupancy matrix ρ^{σ}. Thus the second term in Equation (3.15) can be interpreted as a positive-definite penalty function. The DFT+U energy obtained in this manner is always less negative than the DFT energy.

It must be noticed that in Dudarev's approach the parameters U and J do not enter separately, only the difference $(U - J)$ is meaningful. A larger $(U - J)$ implies a stronger observance of the on-site idempotency and this is achieved by lowering the one-electron potential locally for a particular metal *d* orbital and in turn modifying the hybridisation with the ligand atoms.

3.2 Geometry optimisers

Two algorithms for geometry optimisation are used in this work: the conjugate gradient scheme[16, 17] and the Residual Minimization Scheme-Direct Inversion in the Iterative Subspace[18] (RMM-DIIS). Starting with the electronic ground state (calculated separately by an iterative matrix-diagonalisation scheme) for a given geometry, those algorithms calculate the forces and then, based on the forces, a new geometry is predicted and those steps are repeated until a criterion is reached (usually when the differences in energies are less than 10^{-4} eV). A "special" algorithm is the RMM-DIIS, where the energy criterion is ignored and only the forces are minimized. Within the finite temperature approach, forces are defined as the derivative of the generalized free energy.

The **conjugate gradient** is recommended for difficult relaxation problems as it presents the most reliable backup routines at the moment. In the first step, the ions (and cell shape) are changed along the direction of the steepest descent (*i.e.* the direction of the calculated forces and stress tensor). The second step is a trial step; the third step is a corrector step and so on until the minimum energy position along the chosen displacement direction is found. In all the steps following the first one, the preconditioned gradient is conjugated to the previous search direction. The relative efficiency of this method has been compared to other methods and increases in rates of convergence greater than an order of magnitude have been observed in large problems.

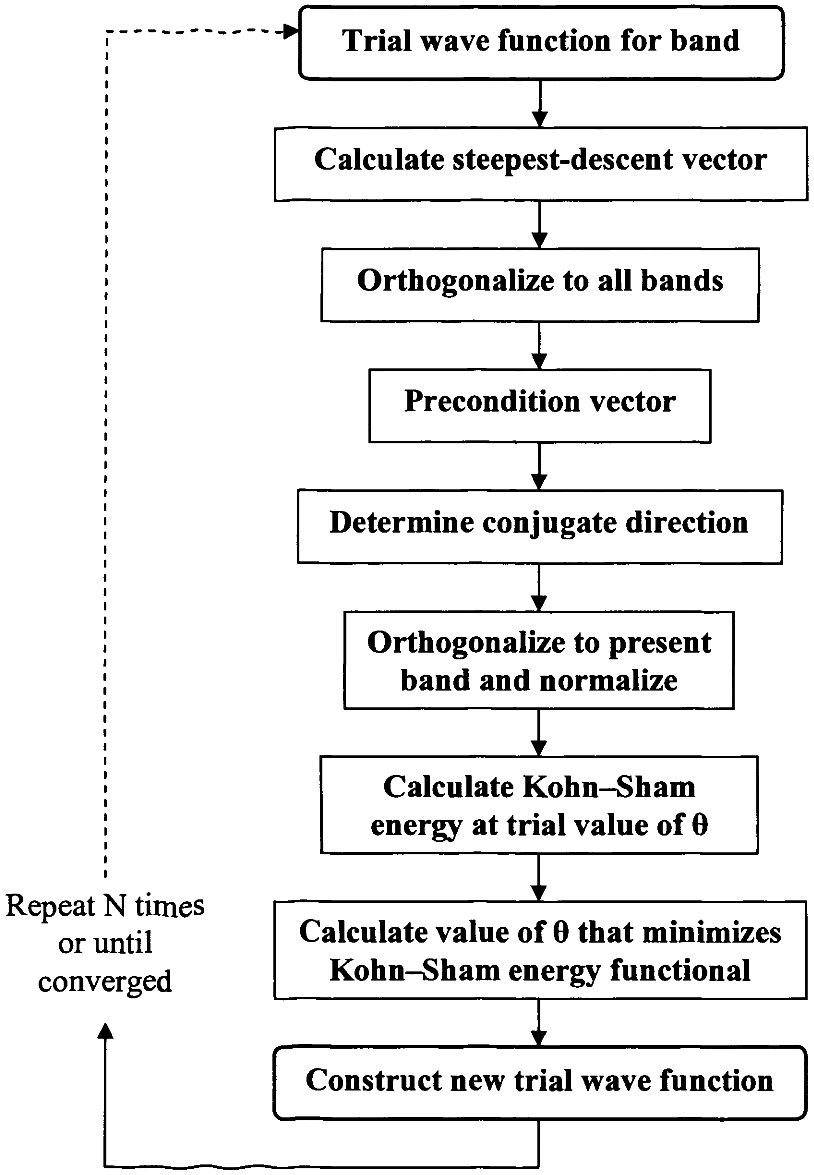
Trial wave function for band
Calculate steepest-descent vector
Orthogonalize to all bands
Precondition vector
Determine conjugate direction
Orthogonalize to present band and normalize
Calculate Kohn–Sham energy at trial value of θ
Calculate value of θ that minimizes Kohn–Sham energy functional
Construct new trial wave function
Repeat N times or until converged

Figure 3.1 Flow diagram for the update of a single band in the (direct-minimization) conjugate-gradient method.[19]

The **RMM-DIIS** (quasi-Newton) is recommended when the system finds itself close to a stationary point on the potential energy surface (a transition state for example). However, this algorithm fails if the initial positions are a bad guess. The forces and the stress tensor are used to determine the search directions for finding the equilibrium positions, the total energy not being taken into account. As the algorithm builds up an approximation of the Hessian matrix it requires very accurate forces or it fails to converge. RMM-DIIS implicitly calculates an approximation of the inverse Hessian matrix by taking into account information from previous iterations.

3.3 Vibrational frequency calculations

For a simple harmonic oscillator the period T is given by:

$$T = 2\pi\sqrt{\frac{\mu}{k}} \tag{3.17}$$

where *k* is the force constant. A molecule can absorb a photon that vibrates at the same frequency as one of its normal vibrational modes. If a molecule, initially in its ground vibrational state, could be excited so that it vibrates at a given frequency, then that molecule could absorb a photon that vibrates at the same frequency.

Although vibrational frequencies are usually expressed as kilohertz or megahertz, in chemistry vibrational frequencies are normally expressed in terms of the number of vibrations that would occur in the time that light travels one centimetre, i.e., $\bar{\upsilon} = \frac{1}{cT}$. Using this equation for simple harmonic motion, the vibrational frequency can be written as:

$$\bar{\upsilon} = \frac{1}{2\pi c}\sqrt{\frac{k}{\mu}} \tag{3.18}$$

In order for $\bar{\upsilon}$ to be in cm^{-1}, *c*, the speed of light must be in $cm.s^{-1}$, *k*, the force constant in $erg.cm^2$ and μ the reduced mass, in grams.

For a molecule, the force constants are obtained by diagonalisation of the mass-weighted Hessian matrix. Most of the work in calculating vibrational frequencies is spent in constructing the Hessian. The elements of the Hessian are defined as:

$$H_{i,j} = \frac{\delta^2 E}{\delta x_i \delta x_j} \tag{3.19}$$

and are generated by use of finite displacements; for each atomic coordinate x_i, the coordinate is first incremented by a small amount, the gradients calculated, then the coordinate is decremented and the gradients re-calculated. The second derivative is then obtained from the difference of the two derivatives and step size:

$$H_{i,j} = \frac{\left(\frac{\delta E}{\delta x_i}\right)_{+0.5\Delta x_j} - \left(\frac{\delta E}{\delta x_i}\right)_{-0.5\Delta x_j}}{\Delta x_j} \tag{3.20}$$

This is done for all 3*N* Cartesian coordinates. Because the Hessian is symmetric, that is $H_{i,j}=H_{j,i}$, the random errors that occur in the gradient calculation can be reduced (by a factor of $\sqrt{2}$) by re-defining the Hessian as:

$$H_{i,j}=\frac{1}{2}\left(\frac{\left(\frac{\delta E}{\delta x_i}\right)_{+0.5\Delta x_j}-\left(\frac{\delta E}{\delta x_i}\right)_{-0.5\Delta x_j}}{\Delta x_j}+\frac{\left(\frac{\delta E}{\delta x_j}\right)_{+0.5\Delta x_i}-\left(\frac{\delta E}{\delta x_j}\right)_{-0.5\Delta x_i}}{\Delta x_i}\right) \tag{3.21}$$

and diagonalisation of this matrix yields the force constants of the system.

In order to calculate the vibrational frequencies, the Hessian matrix is first mass-weighted:

$$H^m_{i,j}=\frac{H_{i,j}}{\sqrt{M_i\cdot M_j}} \tag{3.22}$$

Diagonalisation of this matrix yields eigenvalues, ε, which represent the quantities $\sqrt{\frac{k}{\mu}}$, from which the vibrational frequencies can be calculated:

$$\bar{\upsilon}_i=\frac{1}{2\pi c}\sqrt{\varepsilon_i} \tag{3.23}$$

VASP 4.6 can determine the Hessian matrix and the vibrational frequencies of a system (option IBRION=5) and selective dynamics are supported (only those components of the Hessian matrix are calculated for which the selective dynamics tags are set to .TRUE).

3.4 Bader charge analysis

This section is largely based on the work by Henkelman and co-workers[20].

Atomic charges in molecules or solids are not observables and therefore not defined by quantum mechanical theory. The output of the calculations is a continuous electronic charge density and it is not clear how one should partition it amongst fragments of the system such as atoms or molecules. The most popular orbital based method is the so-called Mulliken analysis. It can be a fast and useful way of determining partial charges on atoms but it has the major drawback that the analysis is sensitive to the choice of the basis set. Furthermore, in the limit of an infinite basis, the assignment becomes arbitrary. Many calculations are carried out with plane wave basis functions which are not associated with any particular atom in the system. Mulliken analysis is not applicable in such cases.

A very different approach is to focus entirely on the charge density as has been proposed by Bader.[21] The space is divided into regions by surfaces that run through minima in the charge density. More precisely, at a point in a dividing surface the gradient of the electron density has no component normal to the surface. Since this analysis is based solely on the charge density, it is rather insensitive to the basis set used in the electron wavefunction calculation and can be used to analyse planewave based calculations such as VASP as well as calculations using atomic basis functions such as SIESTA.

By integrating the electronic charge in the Bader region where the nucleus of an atom is located, and adding the electronic charge in nearby regions that do not include a nucleus, the total electronic charge of an atom can be determined. Henkelman *et al.*[20] have developed a fast method for carrying out Bader decomposition of charge density. Their method is similar to other grid based Bader analysis methods, but is different in that steepest ascent trajectories constrained to the grid points are used to define the Bader regions.

From a grid point (*i,j,k*), a steepest ascent move is made along the direction which maximizes the charge density gradient. The derivative of the charge density, $\nabla\rho$, is calculated along the directions, $\hat{r}$, towards adjacent grid points, using

$$\nabla\rho(i,j,k)\cdot\hat{r}(di,dj,dk)=\frac{\Delta\rho}{|\Delta\vec{r}|} \tag{3.24}$$

where *di*, *dj*, *dk* are each assigned the values [-1,0,1] but excluding *di* = *dj* = *dk* = 0. The change in density

$$\Delta\rho = \rho(i+di, j+dj, k+dk) - \rho(i,j,k) \tag{3.25}$$

and the distance

$$|\Delta\vec{r}| = |\vec{r}(i+di, j+dj, k+dk) - \vec{r}(i,j,k)| \tag{3.26}$$

are evaluated between neighbours, where $\vec{r}(i,j,k)$ is the Cartesian vector to the grid point (*i,j,k*). The steepest ascent step selected, $\vec{r}(di,dj,dk)$, is the one that maximizes the positive values of $\nabla\rho(i,j,k)$. If there are no positive values, the point (*i,j,k*) is considered to be a charge density maximum

When a steepest ascent trajectory has been initiated from all grid points, the partitioning analysis is complete, and all grid points have then been assigned to a Bader region. This assignment of the grid points to Bader regions is all that is needed for further analysis such as calculations of partial charges.

3.5 Density of states

The density of states D is defined as

$$D = \frac{1}{V} \cdot \frac{N(E, E + \Delta E) - N(E)}{\Delta E} = \frac{1}{V} \cdot \frac{dN}{dE} \tag{3.27}$$

with N(E) the number of states per volume unit, and V the reciprocal space volume of the crystal. Taking into account that every state (characterized by its set of quantum numbers) can accommodate two electrons (one with spin up; one with spin down), the final formula for the uniform electron gas is

$$D = \frac{1}{V} \cdot \frac{dN_s}{dE} = \frac{1}{2\pi^2} \left(\frac{2me}{\hbar^2} \right)^{3/2} \cdot E^{1/2} \tag{3.28}$$

with N_s the total number states. It is important to notice a few points. First, D(E) is proportional to $E^{1/2}$. Second, for different (but physically meaningful) boundary conditions the same D is obtained. Then, D is a kind of twofold density: it is first the density of energy states in an energy interval and second, the (trivial) density of that number in space. Finally, D is independent of the system dimension and can be applied to the bulk material. At a temperature of 0 K, the Fermi energy is the energy of the highest occupied state.

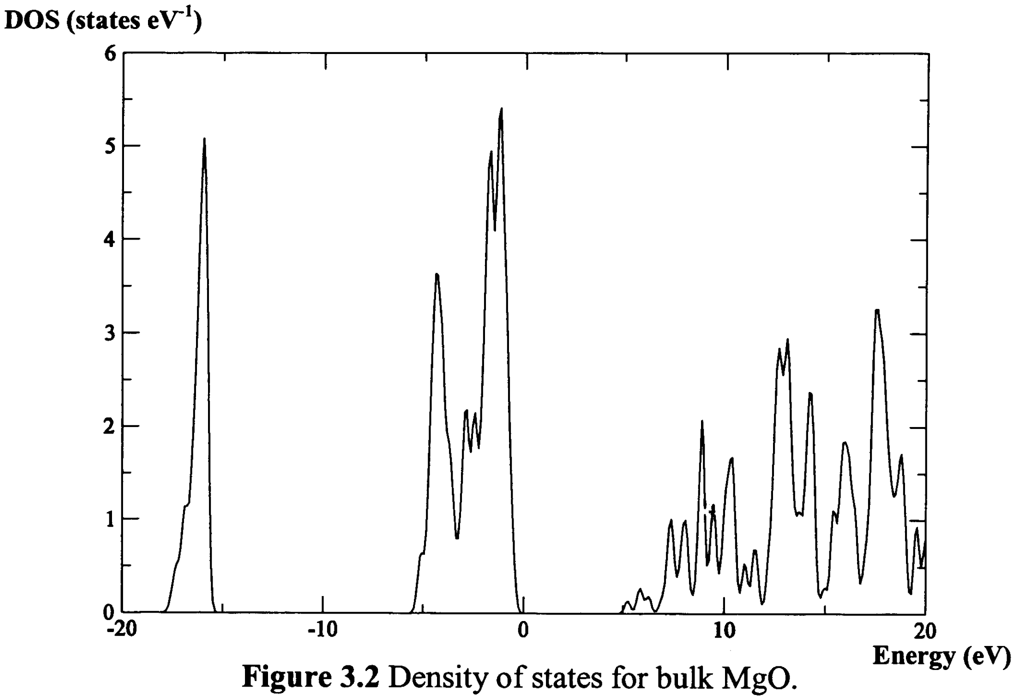

Figure 3.2 Density of states for bulk MgO.

3.6 Implementation of DFT

3.6.1 VASP

The code VASP[22, 23] (Vienna *ab initio* Simulation Package), developed by the group of Professor J. Hafner, has been extensively used to obtain a fundamental understanding of reactions on metal oxides surfaces.

VASP applies DFT to periodic systems, using plane waves and ultrasoft (US-PP)[24, 25] or projector augmented wave (PAW-PP)[26, 27] pseudopotentials. PAW-PP are generally more accurate than the US-PP. There are two reasons for this: first, the radial cut-offs (core radii) are smaller than the radii used for the US pseudopotentials, and secondly, the PAW pseudopotentials reconstruct the exact valence wave function with all nodes in the core region. It is strongly recommended to use the PAW-PP dataset supplied in the VASP-PAW package and this is the method we choose. As the number of plane waves would exceed any practical limits, the core electrons are pre-calculated in an atomic environment and kept frozen in the course of the remaining calculations.

The Kohn-Sham equations are solved self-consistently with an iterative matrix diagonalisation combined with a Broyden mixing method[28] for the charge density. The combination of these two techniques makes the code very efficient, especially for transition metal systems that present a complex band structure around the Fermi level. The forces acting on the atoms are calculated and can be used to relax the geometry of the system.

The PBE functional (Generalized Gradient Approximation) from Perdew, Burke and Ernzerhof[29] has been chosen as it features an accurate description of the linear response of the uniform electron gas, a correct behaviour under uniform scaling, and a smooth potential.

Most of the algorithms implemented in VASP use an iterative matrix diagonalisation scheme (section 3.2) and it is possible to directly calculate vibrational frequencies (section 3.3).

Plane waves are used as the basis set and PAW pseudopotentials replace the core part of atoms. The Hamiltonian is easy to determine in direct and reciprocal space. Fast Fourier Transformations (FFT) are used to switch from direct to reciprocal space and *vice versa*. This allows a decrease of the number of planewaves and allows a partial diagonalisation.

For the mixing of the charge density, an efficient Broyden-Pulay mixing is used for convergence in a self-consistent density functional calculation (figure 3.3).

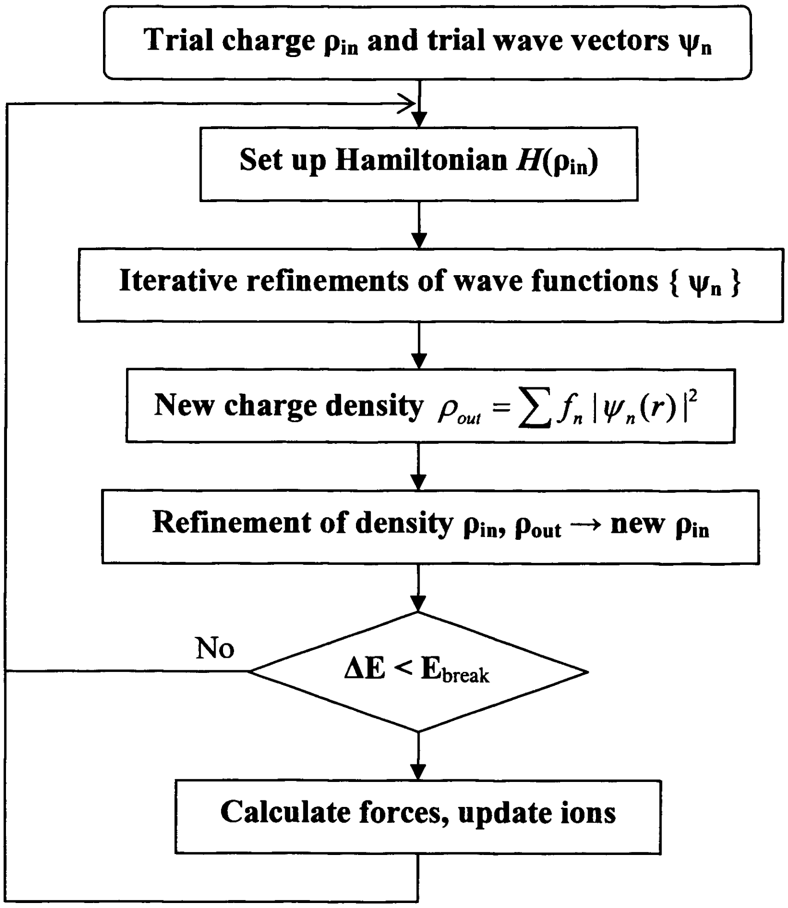
Trial charge ρin and trial wave vectors ψn
Set up Hamiltonian H(ρin)
Iterative refinements of wave functions { ψn }
New charge density $\rho_{out} = \sum f_n \,|\psi_n(r)|^2$
Refinement of density ρin, ρout → new ρin
No
ΔE < Ebreak
Calculate forces, update ions

Figure 3.3 Self-consistency scheme

The linear mix of the two (or more) previous charge densities can be made and this can give significant benefits.[18, 22] It is often important to mix in a small amount of the input charge densities while performing the mixing.

For partial occupancies, different methods are used to improve the convergences with respect to *k*-points sampling: linear tetrahedron method (good for bulk calculations), smearing methods like finite temperature approaches (good for convergence of metallic surfaces), or improved functional form: Methfessel and Paxton method, finite methods like Gaussian or Fermi smearing which are good for accurate calculation (required for DOS diagrams).

The number of *k*-points in the irreducible part of the Brillouin zone is important for the accurate integration of the properties computed in reciprocal space. The *k*-point sampling grid is often calculated by VASP using the Monkhorst-Pack[30] method with a given mesh.

Within the finite temperature approach, forces are defined as the derivative of the total energy and the ion positions are eventually updated if the force in the system has not converged to the required accuracy criterion.

The most time consuming task during a VASP process is the FFT procedure, followed by the calculation of the non-local pseudopotentials and the BLAS subroutines (Basic Linear Algebra Subprograms).

3.6.2 SIESTA

SIESTA[31] (Spanish Initiative for Electronic Simulations with Thousands of Atoms) is both a method and its computer implementation. It belongs to the family of first-principles methods employing DFT and is based on strictly localized numerical atomic orbitals (NAOs).

It uses the standard Kohn-Sham self-consistent density functional method in the local density (LDA) or generalized gradient (GGA) approximations, with norm-conserving pseudopotentials in the fully non-local (Kleyman-Bylander) form.

The building of the Hamiltonian and overlap matrices is performed using a combination of two techniques[32, 33]. The overlap matrix and some terms of the Hamiltonian, including the kinetic energy (the so-called two-centre integrals), allow a very efficient numerical integration in one single variable as a function of only the distance between every two atoms. The remaining terms are calculated by replacing the three-dimensional integrals by summations over a finite grid, a discretization of 3-D space. One parameter controls the precision of these integrations, namely the fineness of the grid, usually expressed as an energy cutoff, an index borrowed from plane waves, the square root of which gives the inverse of that fineness.

The linear-scaling solution of the eigenvalues problem posed by the Kohn-Sham Hamiltonian requires abandoning the standard diagonalisation procedure. In fact, for the ground-state properties sought in the calculations, there is no need to know all the eigenvalues separately; it is just the sum of the occupied ones that is of relevance to the total energy, i.e. the trace of the Hamiltonian in occupied space, $Tr_{occ}\{H\}$. Since this trace is invariant under any change of basis of occupied space, a localized basis along the lines of Wannier functions can be sought instead. They are obtained by minimizing $Tr_{occ}\{H\}$ under the constraint that the wavefunctions vary within localised regions of space.

Finally, it is necessary to avoid the localized-wave-function orthogonalisation (quadratic scaling), and this is accomplished by minimizing a slightly modified functional instead of $Tr_{occ}\{H\}$, which shares the same minimum with it[34].

The linear-scaling solution just described is obviously more efficient than the cube-scaling diagonalisation for large systems. For small systems, however, the diagonalisation is competitive and more convenient. The critical size separating these two regimes depends on the kind of system. Large-gap insulators present highly localized electrons and allow efficient linear scaling, thereby reducing the critical size. As a general rule of thumb for the SIESTA method for non-metallic systems, the critical sizes are to be found around 100 atoms. It is important to stress, however, that within SIESTA, the building of the Kohn–Sham Hamiltonian is always done in a linear-scaling fashion.

For given atomic positions, the self-consistent solution of the electronic problem gives the electronic total energy. Using the Hellmann–Feynman theorem, derivatives of the energy are also obtained, most importantly the forces on the atoms and the stress tensor. This allows the relaxation of the system including atomic positions and/or lattice parameters, with the possible additional constraints of externally applied pressure (*e.g.* hydrostatic, uniaxial).

In order to have a finite range for the matrix elements, one can either neglect them beyond a given distance or use confined basis orbitals, i.e., orbitals that are strictly zero beyond a certain radius[35]. SIESTA adopts this last approach as it keeps the energy strictly variational, thus facilitating the test of the convergence with respect to the radius confinement. There are three main aspects that determine the NAO basis sets: (1) the number of orbitals, (2) their extent (cutoff radii) and (3) their shape.

The number of orbitals per atom in a basis set is defined by the number of angular-momentum channels and the number of different orbitals in a channel. Starting with the simplest, the minimal basis incorporates only those atomic-orbital shells needed for the free atom, with one single orbital per shell (also called single-zeta or SZ). For example, one *s* orbital and one *p* shell for C, O or Si, one *s* orbital and a *d* shell for Fe. The basis can then be doubled (DZ), introducing two different orbitals for an *s* channel, or tripled (TZ), using three different orbitals.

A reasonably balanced definition of all cutoff radii for different orbitals and different atomic species is obtained by defining one single parameter, the energy shift ΔE. This is the raise in energy that the orbital suffers when confined[36].

The shape is defined by solving the isolated atomic problem within DFT and for the same pseudopotential as used in the calculations. This procedure gives reasonable shapes well adapted to the pseudopotentials. Finally, to add angular flexibility to the basis, it is customary to include polarization orbitals, additional basis functions of higher angular momentum. In general, it is found that double-zeta plus single-z-polarization bases reproduce the molecular geometries obtained with a plane-wave basis set to within 1%.

Since the orbitals are associated with the atoms, the adsorption energies obtained have an undesired term due to this; the so-called basis set superposition error (BSSE). It can be corrected by introducing the basis set of both substrate and adsorbate atoms simultaneously, so that both have the same orbitals independent of which atom sits on them (cf. 4.1). In addition to correcting the energy, the change in energy obtained by introducing BSSE will gauge the quality of the basis.

References

1. M. Born and R. Oppenheimer, *Ann. Physik*, 1927, **84**, 457.
2. P. Hohenberg and W. Kohn, *Phys. Rev.*, 1964, **136**, B864-B871.
3. W. Kohn and L.J. Sham, *Phys. Rev.*, 1965, **140**, A1133-A1138.
4. D.M. Ceperley and B.J. Alder, *Phys. Rev. Lett.*, 1980, **45**, 566.
5. J.P. Perdew and A. Zunger, *Phys. Rev. B*, 1981, **23**, 5048.
6. Y.-M. Juan and E. Kaxiras, *Phys. Rev. B*, 1993, **48**, 14944.
7. J. Tao, J.P. Perdew, V.N. Staroverov, and G.E. Scuseria, *Phys. Rev. Lett.*, 2003, **91**, 146401.
8. O. Gunnarson and B.I. Lundqvist, *Phys. Rev. B*, 1976, **13**, 4274.
9. A.D. Becke, *J. Chem. Phys.*, 1992, **98**, 1372.
10. V. Fock, *Z. Phys.*, 1930, **61**, 126.
11. J.C. Slater, *Phys. Rev.*, 1951, **81**, 385.
12. J. Harris, *Phys. Rev. A*, 1984, **29**, 1648.
13. A.D. Becke, *J. Chem. Phys.*, 1997, **107**, 8554.
14. S.L. Dudarev, G.A. Botton, S.Y. Savrasov, C.J. Humphreys, and A.P. Sutton, *Phys. Rev. B*, 1998, **57**, 1505.
15. H. Tasaki, *J. Phys.: Condens. Matter*, 1998, **10**, 4353-4378.
16. M.P. Peter, M.C. Payne, and D.C. Allan, *Phys. Rev. B*, 1989, **40**, 12255.
17. D.M. Bylander, L. Kleinman, and S. Lee, *Phys. Rev. B*, 1990, **42**, 1394.
18. P. Pulay, *Chem. Phys. Lett.*, 1980, **73**, 393.
19. M.C. Payne, M.P. Teter, D.C. Allan, T.A. Arias, and J.D. Joannopoulos, *Rev. Mod. Phys.*, 1992, **64**, 1045-1097.
20. G. Henkelman, A. Arnaldsson, and H. Jónsson, *Comput. Mat. Sci.*, 2005, (in press).
21. R. Bader, *Atoms in Molecules: A Quantum Theory*. 1990, New York: Oxford University Press.
22. G. Kresse and J. Furthmüller, *J. Comp. Mat. Sci.*, 1996, **6**, 15.
23. G. Kresse and J. Furthmüller, *J. Phys. Rev. B*, 1996, **54**, 169.
24. D. Vanderbilt, *Phys. Rev. B*, 1990, **41**, 7892.
25. G. Kresse and J. Hafner, *J. Phys.: Condens. Matter*, 1994, **6**, 8245.
26. P.E. Blöchl, *Phys. Rev. B*, 1994, **50**, 17953.
27. G. Kresse and J. Joubert, *Phys. Rev. B*, 1999, **59**, 1758.
28. D.D. Johnson, *Phys. Rev. B*, 1988, **38**, 12807.
29. J.P. Perdew, K. Burke, and M. Ernzerhof, *Phys. Rev. Lett.*, 1996, **77**, 3865-3868.
30. H.J. Monkhorst and J.D. Pack, *Phys. Rev. B*, 1976, **13**, 5188.
31. J.M. Soler, E. Artacho, J.D. Gale, A. García, J. Junquera, P. Ordejón, and D. Sánchez-Portal, *J. Phys.: Condens. Matter*, 2002, **14**, 2745-2779.
32. P. Ordejón, E. Artacho, and J.M. Soler, *Phys. Rev. B*, 1996, **53**, 10441.
33. D. Sánchez-Portal, P. Ordejón, E. Artacho, and J.M. Soler, *Int. J. Quantum Chem.*, 1997, **65**, 453.
34. P. Ordejón, D.A. Drabold, M.P. Grumbach, and R.M. Martin, *Phys. Rev. B*, 1993, **48**, 14646.
35. O.F. Sankey and D.J. Niklewski, *Phys. Rev. B*, 1989, **40**, 3979.
36. D. Sánchez-Portal, P. Ordejón, A. García, and J.M. Soler, *Phys. Stat. Sol. (b)*, 1999, **215**, 809.

Chapter 4

Methodology

We will present in this section the methodology used for this work. Practical examples will be given and can be considered as applications of the theory chapter. We will first discuss pseudopotential generation, giving extensive details applied to gold and magnesium. Then, we will present the method used to check the convergence of the calculation parameters, and the next two sections will deal with adsorption energy and Bader charge calculations. Finally, we will introduce our method to locate transition states.

4.1 Pseudopotential generation

The techniques used to derive pseudopotentials for this work were largely based on the approach of P. Giannozzi.[1]

The SIESTA pseudo-potentials (PP) are generated using the program ATOM originally written by Sverre Froyen at the University of California at Berkeley. It was modified starting in 1990 by Norman Troullier and Jose Luis Martins at the University of Minnesota and is currently maintained by Alberto García from the Universidad del País Vasco, Bilbao.

PP generation is a step-by-step process and we will go through each step in the following sections, with magnesium and gold employed as practical examples. First, a density functional that will be used to generate the PP must be chosen. The second step consists in choosing the PP generation parameters and that includes choosing valence and core states, choosing a reference configuration, generating all-electrons results, choosing the matching radii and finally deciding to include core correction or not. Then the PP has to be generated with the previously chosen parameters. Last, but not least, transferability and required cutoff must be checked, which includes testing the PP in solid-state or molecular calculations.

4.1.1 Choosing a suitable density functional

PP's must be generated with the same functional that will be later used in calculations. The use of, for instance, gradient-corrected functionals with LDA PP's is inconsistent.

The PBE functional[2] is chosen as it is a well-behaved gradient correction: other gradient corrections may diverge around the core region, as $r \rightarrow 0$, because the pseudocharge in that region is very small or sometimes vanishing (if there are no filled *s* states).

4.1.2 Choosing the pseudopotential generation parameters

A – Valence and core states

This is usually a trivial step; the valence states are those that contribute to bonding, core states are those that do not contribute. However, promoting the highest core states *ns* and *np*, or *nd* (the so-called "semicore" states) into valence may be computationally expensive but will be a good way to improve transferability.

For example, the outer electronic configuration of Mg is $3s^2$: including only these valence states means that two electrons will be treated explicitly and the 10 core electrons $1s^2$ $2s^2$ $2p^6$ will be approximated by the PP. In magnesium oxide, Mg is in a +2 oxidation state and using the previous PP will result in Mg having no electrons left to be treated explicitly. This is a major problem, for example to perform Bader charge analysis[3] (section 3.4), as there is no charge density maxima around the Mg atom, so all charge is associated with the O atoms. It is then necessary to include the semi-core states $2p$ as well as the valence states $3s$ in the explicit part of the calculation. As a result, magnesium in MgO will always have enough electrons left to be treated properly by a Bader charge analysis code[4]. However for optimisations, it is possible to employ the core correction scheme and thus avoid the extra cost of explicitly considering semi-core states (see 4.1.2-E).

B – Choosing a reference configuration

To fit the PP we require some reference data from all electron calculations. This may be any reasonable configuration not too far away from the expected configuration in solids or molecules. The ground state should be used but it is sometimes necessary to do otherwise. For example, when using a single configuration for all angular momenta, PP for different angular momentum valence states can be used. Also, if results are very sensitive to the chosen configuration (for example, III-V zinc blende semiconductors due to the presence of p–d coupling between anion *p* and cation *d* states[5]) or when the atom will be in a given configuration in a particular system and it is desired to stay close to it.

It should be noticed that a completely empty configuration ($s^0p^0d^0$) or configurations with fractional occupation numbers are both acceptable as reference configurations as they correspond to perfectly defined mathematical objects.

In the Troullier-Martins approach[6], the PP is generated for every angular quantum number l on the valence state of lowest main quantum number n. If there are states with the same l and higher n, they must be empty.

C – Generating all-electrons results

It is possible to generate all-electron (AE) wave-functions and one-electron levels for the reference configuration. This can be useful if orbital eigenvalues, total energy and/or charge density of an element in its ground state have to be found.

D – Choosing the matching radii

At the matching radius r_c the AE and PP wave-function of each angular momentum l match, with at least a continuous first derivative. The choice of the r_c is very important and must follow some rules. The r_c must be larger than the outermost node (if any) of the wave-function for any given l and a typical r_c is the outermost peak, beyond if needed (figure 4.1).

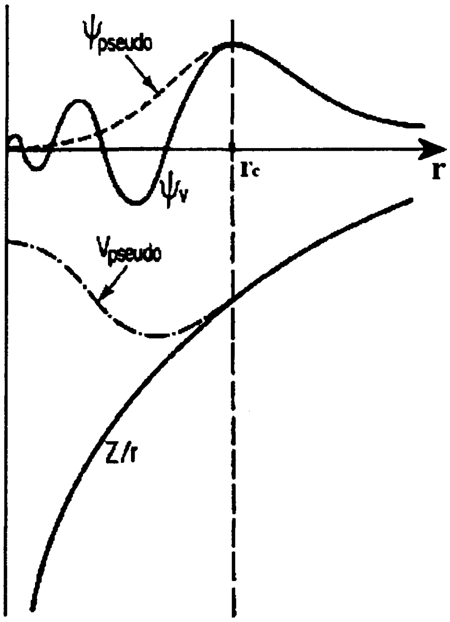

Figure 4.1 A schematic illustration of all-electron (solid lines) and pseudo- (dashed lines) potentials and their corresponding wave functions. The radius at which all-electron and pseudopotential values match is r_c.[7]

The larger the r_c, the softer the potential (less plane-waves needed), but also the less transferable it becomes. Usually there is one *l* that is harder (small radius) than the others (for example in transition metals, the *d* state, in second-row elements and in N, O, F, the *p* state). It is recommended to concentrate on this one and push outwards its r_c as much as possible. Finally, although it is not very important, and usually impossible to achieve, not too different r_c's for different angular momentum should be employed.

In the Troullier-Martins approach[6] the wave-function matching beyond r_c is exact. Also, it is the hardest atom that determines the plane-wave cutoff in a solid or molecule: it is pointless to optimise a soft PP if there are harder atoms around.

E – Choosing the core correction or not

The core correction accounts, at least partially, for the nonlinearity in the exchange-correlation potential. In the generation of a PP, a potential with the desired pseudo wave-functions and pseudo energies is first produced. In order to separate a "bare" PP from the screening part, the screening potential generated by the valence charge only is removed. This introduces an error as the exchange-correlation potential is not linear in the charge density.

With the core correction, a smoothed core charge is added to the valence charge both at the un-screening step and when using the PP.

The core correction is a must for alkali halides and for PP's to be used in LDA calculations. It is recommended whenever there is a large overlap between valence and core charge: for instance, in transition metals if the semi-core states are kept in the core.

The smoothing works by replacing the true core charge with a fake, smoother, core charge for $r<r_{pc}$. At r_{pc}, the core charge density equals the valence charge density multiplied by this number. The ATOM program can generate PP with the non-linear exchange-correlation correction proposed by Louie *et al.*[8] In the traditional approach, the pseudocore charge density equals the charge density outside a given radius r_{pc}, and has the smooth form $\rho_{pc}(r) = A\cdot r\cdot \sin(b\cdot r)$ inside that radius. A smooth matching is provided with suitable A and b parameters calculated by the program. A new scheme has been implemented to fix some problems in the generation of GGA PP. The smooth function is now $\rho_{pc}(r) = r^2\cdot \exp(a + b\cdot r^2 + c\cdot r^4)$ and derivatives up to the second are continuous at r_{pc}. A smaller r_{pc} gives more accurate core correction, but also a harder core charge, and *vice versa*.

4.1.3 Generating the pseudopotential

We will focus on gold and generate its PP using the Troullier-Martins scheme[6]. The input file for the ATOM program is in a fixed column format and a typical input file is shown in figure 4.2.

```
pe       Gold
     tm2        2.00
Au   pbr
      0
12    4
 6    0     1.000     0.000
 6    1     0.000     0.000
 5    2    10.000     0.000
 5    3     0.000     0.000
  2.400     2.700     1.900     2.000     0.000     1.200
```

Figure 4.2 Gold pseudopotential input file

The first line specifies:

- The calculation code: `ae` for "all-electron", `pg` for "pseudo-potential generation", `pe` for core correction included in the PP[8] and `pt` for PP test.
- A title for the job (here `Gold`).

Second line:

- PP fitting approach to use and radius at which to compute logarithmic derivatives for test purposes. Here `tm2` stands for the improved Troullier-Martins method[6].

Third line:

- Chemical symbol of the nucleus (here `Au`)
- Exchange correlation type. We choose a gradient-corrected functional: `pb` indicates the use of the GGA scheme by Perdew, Burke and Ernzerhof[2].
- The character `r` next to `pb` is a flag to perform the calculation relativistically (obviously spin-polarized), solving the Dirac equation instead of the Schrödinger equation.

Fourth line:

- It is used in a somewhat esoteric way and for most calculations it should contain just a `0` in the position shown.

The rest of the file defines the electronic configuration:

Fifth line:

- The number of core and valence orbitals. Here for Au, we have a total of `12` atomic function types in the core ([Xe] $4f^{14}$) and 2 in the valence ($5d^{10}$ $6s^{1}$). However, we define later the four channels (*s*, *p*, *d*, *f*) and input them in the order of increasing angular momentum, so that there is no possible confusion when we define r_c (`2.400, 2.700, 1.900` and `2.000` a.u.). Thus, the number of valence orbital types is `4`, even though we are only interested in the *s* and *d* channels.

Sixth to ninth line (one line for each valence orbital):

- The first value is *n*, the principal quantum number of the orbital.
- The second value is *l*, the angular momentum quantum number of the orbital.
- The final two values on each line are the occupation of the orbital in electrons (there are two descriptors to allow the input of "up" and "down" occupations in spin-polarized calculations).

The last line specifies:

- The values of the r_c's in atomic units (bohrs) for the *s*, *p*, *d* and *f* orbitals. Here the r_c's are `2.400`, `2.700`, `1.900` and `2.000` for *s*, *p*, *d* and *f* orbitals respectively.
- Two extra fields which are relevant only if non-local core corrections are used (jobcode `pe`). The radius r_{pc} (see 4.1.6) should be given in the sixth slot of this last input line (here `1.200`). If it is negative or zero (or blank), the radius is then computed using the fifth number in that line and the following criterion: at r_{pc} the core charge density equals the valence charge density multiplied by this number. It is highly recommended to set an explicit value for the pseudocore radius r_{pc}.

4.1.4 Checking for transferability and required cutoff

A - Transferability

Here we carry on with the gold example. The Au PP has been generated using the input file detailed previously.

There is no well-established criterion for checking PP transferability. An obvious way to check the correctness and get a feeling for transferability is to test the results of PP and AE atomic calculations on atomic configurations differing from the starting one. The differences between the total energy from PP and AE results gives a feeling for how good the PP is. To give an idea: an error of about 1 mRy is very good, 10 mRy may still be acceptable (1 mRy ≈ 1.31 kJ mol^{-1}).

We choose three different atomic configurations: [$5d^{10}$ $6s^{1}$], [$5d^{9}$ $6s^{2}$] and [$5d^{10}$ $6s^{0}$ $6p^{1}$] corresponding respectively to the ground state, an excited state with promotion of a 5*d* electron to the 6*s* orbital and an excited state with promotion of a 6*s* electron to the 6*p* orbital. The following cross-excitations among all the configurations are obtained (in Ry):

```
AE        1          2          3
 1   0.0000
 2   0.1315     0.0000
 3   0.3786     0.2472     0.0000

PP        1          2          3
 1   0.0000
 2   0.1352     0.0000
 3   0.3789     0.2438     0.0000
```

Figure 4.3 Cross-excitation in Ry for Au among the configurations 1) [$5d^{10}$ $6s^{1}$], 2) [$5d^{9}$ $6s^{2}$] and 3) [$5d^{10}$ $6s^{0}$ $6p^{1}$].

The AE-PP differences range between 0.3 mRy (0.3789 - 0.3786) for configuration 3 and 3.7 mRy (0.1352 - 0.1315) for configuration 2. This shows that the transferability will probably be good; even though it is tested for one isolated ion.

It is also important to check that the pseudo-wave functions match the atomic wave functions as accurately as possible beyond r_c (verified in figure 4.4). The AE core charge should match the PP core charge beyond r_c and the AE valence charge should always match the PP valence charge (verified in figure 4.5).

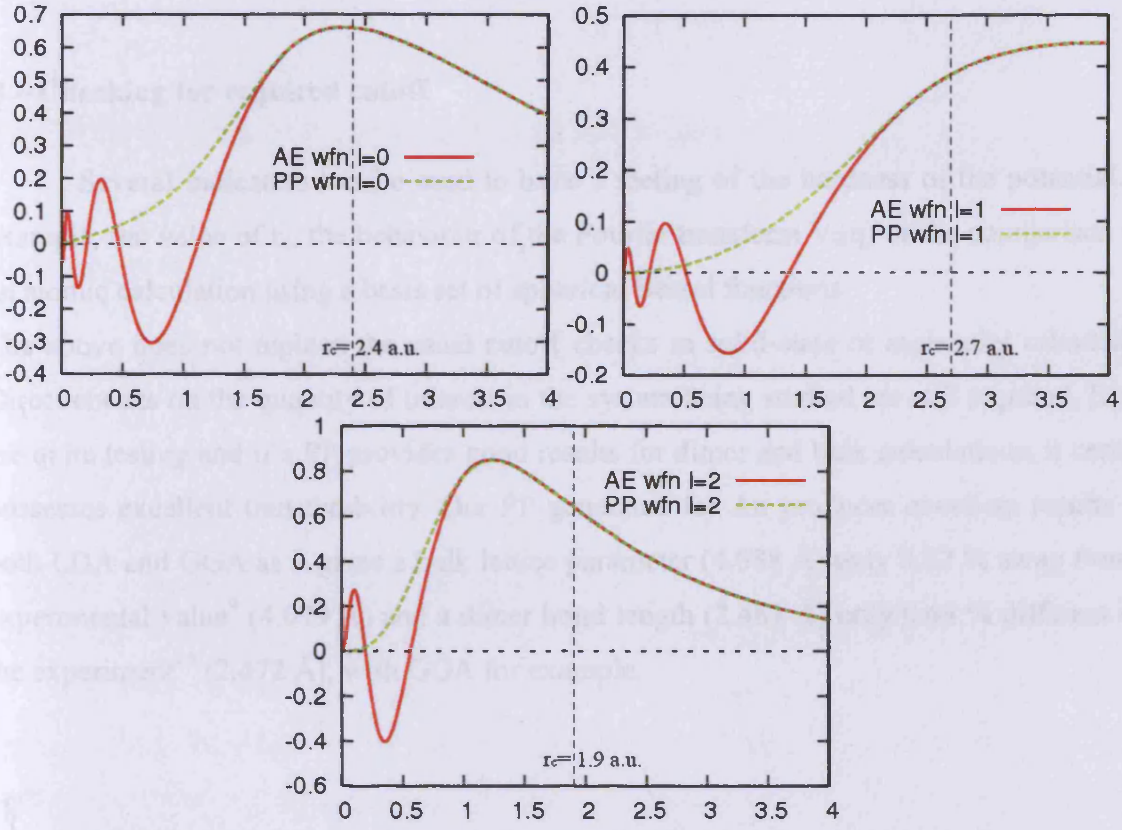

Figure 4.4 All-electrons (AE) and pseudopotential (PP) wave functions for different angular quantum numbers of gold, *l*= {1, 2, 3}. r$_c$ is the radius cutoff in a.u.

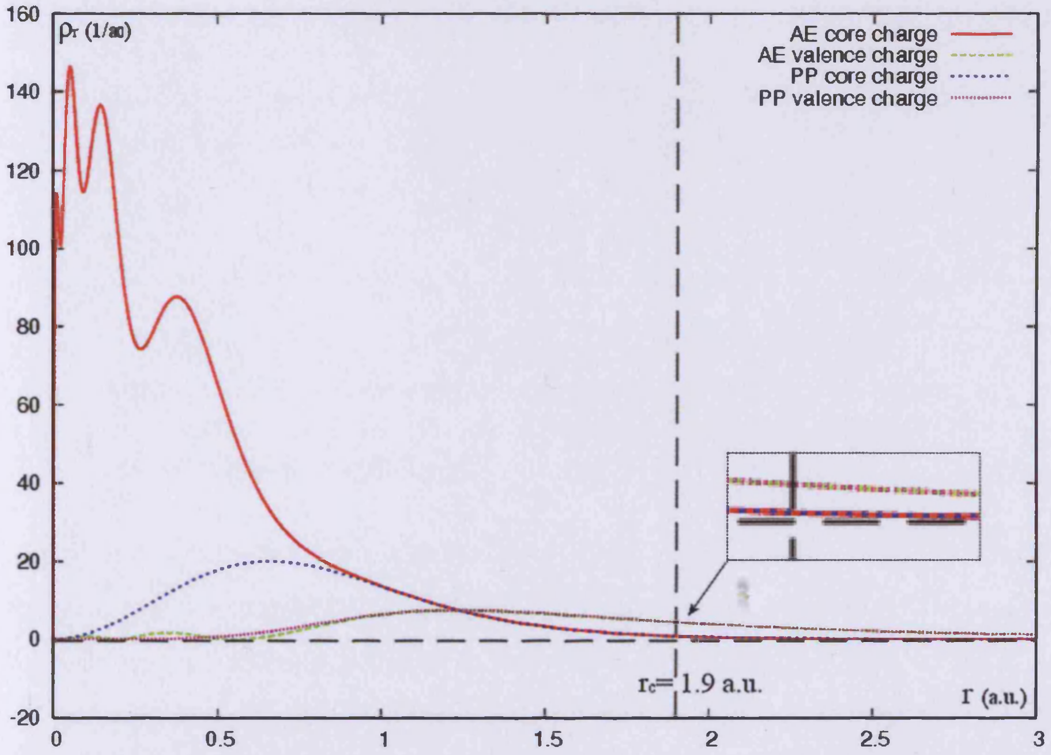

Figure 4.5 All-electrons (AE) and pseudopotential (PP) core and valence charge for gold. r$_c$ represents the smallest radius cutoff used for this PP (1.9 a.u. here).

B – Checking for required cutoff

Several indicators can be used to have a feeling of the hardness of the potential. For example, the value of r_c, the behaviour of the Fourier transform $V_l(q)$ or the comparison with an atomic calculation using a basis set of spherical Bessel functions.

The above does not replace the usual cutoff checks in solid-state or molecular calculations. Direct checks on the quantity of interest in the system being studied are still required. Dimers are quite testing and if a PP provides good results for dimer and bulk calculations, it certainly possesses excellent transferability. Our PP generated for Au produces excellent results with both LDA and GGA as it gives a bulk lattice parameter (4.088 Å) only 0.22 % away from the experimental value[9] (4.079 Å) and a dimer bond length (2.483 Å) only 0.44 % different from the experiment[10] (2.472 Å), with GGA for example.

4.2 Converging the calculation parameters

4.2.1 *k*-points

The number of *k*-points necessary for a calculation depends critically on the required precision and on whether or not the system is metallic. Metallic systems require an order of magnitude more *k*-points than semi-conducting and insulating systems. The k-point mesh is optimized for the bulk and used for the surface model. For a surface calculation there is one long lattice vector and two short lattice vectors. For the long direction one division for the *k*-point mesh is sufficient, as the band dispersion is zero due to the vacuum in this direction. For the short directions the convergence speed with respect to the number of divisions will be approximately the same as for the bulk. It is thus necessary to check the bulk energy convergence with respect to fineness of the *k*-point grid. We choose MoO_3 as an example and we can see that the energy of the bulk is converged to a precision of 10^{-3} eV for a *k*-point grid of 5×3×5 (Table. 4.1).

***k*-points grid**	**MoO_3 bulk energy** (eV)	**ΔE** (eV)
3×1×3	-130.168980	-
3×3×3	-130.171210	-0.002230
5×3×5	-130.271510	-0.100300
7×3×7	-130.272620	-0.001110
9×3×9	-130.272710	-0.000090
11×3×11	-130.272680	0.000030
15×5×15	-130.272680	0.000000

Table 4.1 Convergence of the bulk energy for MoO_3, with respect to the *k*-point grid. ΔE is the difference in energy between two consecutive *k*-points grids.

The bulk MoO_3 lattice parameters are a= 3.963 Å, b= 13.855 Å and c= 3.696 Å.[11] The number of *k*-points along the [010] direction is the smallest (b is the longest among the lattice the parameters) and is converged for a number of *k*-points equal to three. Clearly, a *k*-point grid of 3×3×3 is not sufficient as increasing to 5×3×5 lowers the energy by 0.1 eV. However, 5×3×5 is enough as increasing to 7×3×7 only produces a change of 10^{-3} eV in the MoO_3 bulk energy. As a result, we choose 5×3×5 for the *k*-point grid applied to the bulk material, keeping in mind that a compromise between the required precision and the computational cost has to be made.

4.2.2 Mesh cut-off

We take the example of bulk MoO_3 with VASP but the same method is applied to other systems and DFT codes. With VASP, the use of PREC=High will set the energy cut-off to the maximal ENMAX value found in the PP file plus 30%.

For MoO_3, ENMAX= 400 eV (corresponding to the oxygen) and the energy cut-off chosen by VASP using PREC=High is thus 520 eV. ENMAX is a default energy cut-off and we want to check the convergence of the energy with respect to this cut-off by setting it by hand and computing the resulting energies (figure 4.6).

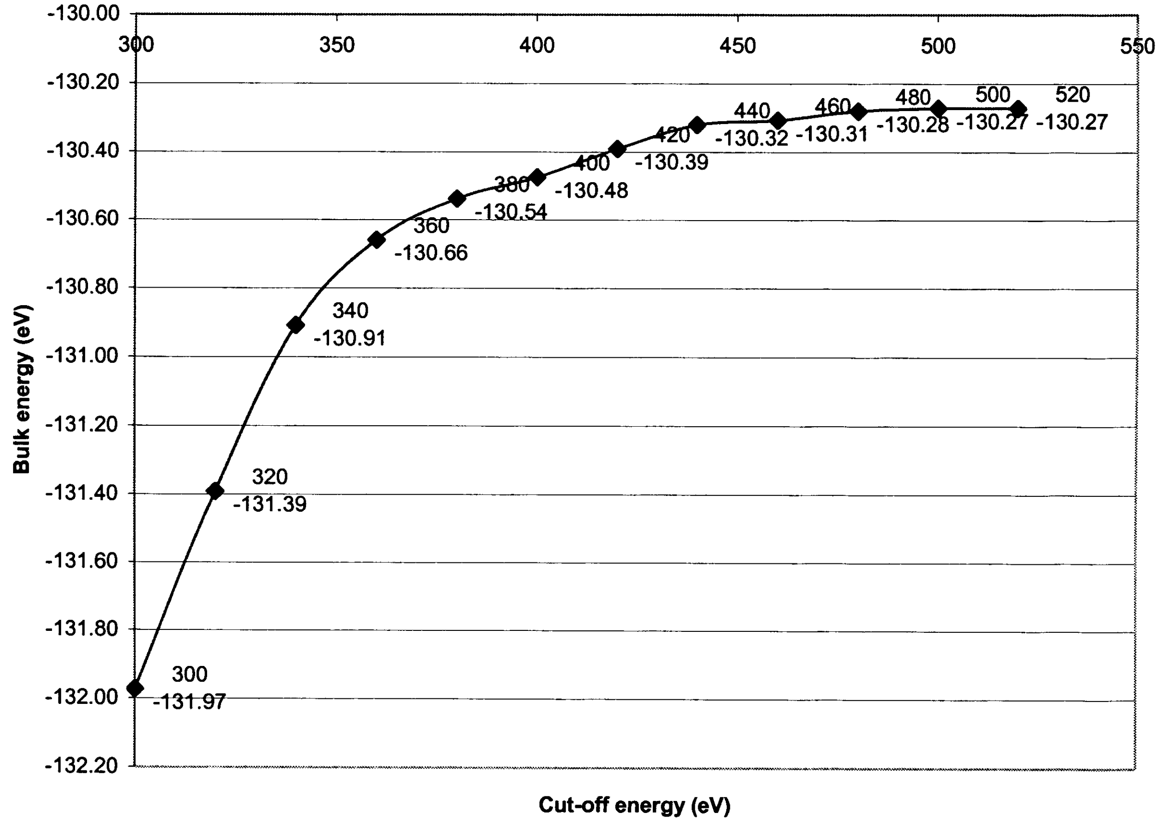

Figure 4.6 Convergence of the bulk energy for MoO_3, with respect to the cut-off energy.

Figure 4.6 shows that the bulk energy is fully converged (within 0.008 eV) for a cut-off energy of 500 eV. A cut-off of 400 eV (which is the default for PREC=Normal or

PREC=Accurate) gives an energy difference of 0.08 eV and is probably enough for "every-day calculations". In general, an increased energy cut-off is only required for accurate evaluations of quantities related to the stress tensor (*e.g.* elastic properties).

4.3 Lattice parameters optimisation

Hellmann-Feynman forces are the derivative of the total energy with respect to atomic positions R$_i$. For many-body Hamiltonians and wave-functions, only terms containing explicit derivatives in the Hamiltonian contribute (Hellmann-Feynman theorem). The terms containing implicit derivatives ($\tilde{F}_i$) through the wave-functions vanish.

$$F_i = -\frac{d}{dR_i} < \Psi | H | \Psi > = - < \Psi | \frac{\partial H}{\partial R_i} | \psi > - \tilde{F}_i \tag{4.1}$$

with $\tilde{F}_i = E \frac{d}{dR_i} < \Psi | \Psi >$ vanishing as it is a derivative of a constant quantity. Partial derivatives are used to indicate explicit derivation; otherwise the total derivative is used.

In DFT the same applies, thanks to the variational character of the energy: one finds that, in perfect analogy to the many-body case, the forces acting on atoms are the matrix elements of the gradient of the external potential plus an ion-ion term.

Unfortunately the terms containing implicit derivatives through the wave-functions vanish only if we have ground state charge density and wave-functions at perfect convergence. In the real world, this is never the case. In particular, the wave-functions are expanded on a finite basis set that is never complete. This may produce a non-zero value of $\tilde{F}_i$, called the Pulay force. This force does not arise because the basis set is incomplete, but because it is "incomplete in a different way" when atoms are moved. This is true with VASP as plane wave basis set is not complete with respect to changes of the volume and it is even worse with localized basis set codes such as SIESTA where the basis set depends on the atomic positions.

In plane wave basis set calculations, Pulay stress can often be neglected if only volume conserving relaxations are performed. This is because the Pulay stress is usually almost uniform and changes the diagonal elements of the stress tensor only by a certain constant amount. In addition, many calculations have shown that Pulay stress related problems can also be reduced by performing calculations at different volumes using the same energy cut-off for each calculation and fitting the final energies to an equation of state. This of course implies that the number of basis vectors is different at each volume. However calculations with many plane wave codes have shown that such calculations give very reliable results for the lattice constant and the bulk modulus and this is the method we choose. For MgO and using SIESTA, the lattice parameter minimising the bulk energy is found to be 99.5

% of the experimental result[9] (figure 4.7). In the stepwise lattice parameter optimization, the lattice parameters are varied in steps of 1% of the initial value.

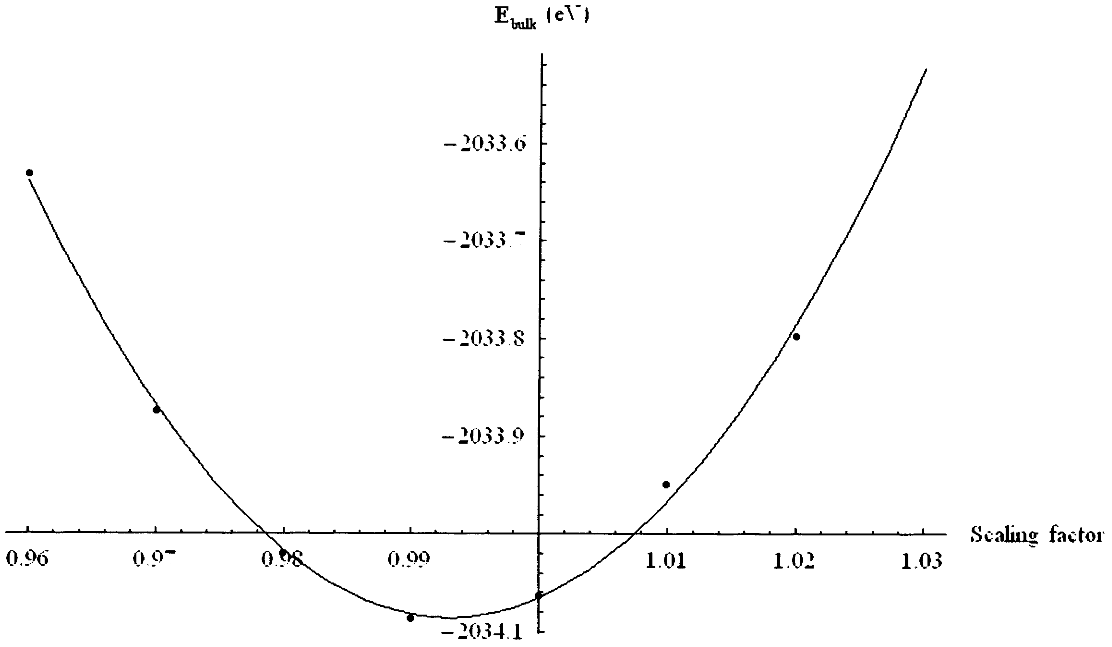

Figure 4.7 Energy of bulk MgO (E_{bulk}) against the scaling factor applied to the experimental lattice parameter[9] of bulk MgO (4.21 Å). Computational details as in chapter 6. $R^2 = 0.991$.

4.4 Basis Set Superposition Error and adsorption energy

As a practical example we will evaluate the adsorption energy E_{ads} of a gold atom on an F centre on the MgO(001) surface, the difference between the energy of AuMgO and the sum of the energy of Au and clean MgO(001) surface in their respective geometries, computed with the basis set of the atoms of the two separate systems only, gives an incorrectly high value E_{ads}:

$$E_{ads} = E(AuMgO)_{AuMgO} - [E(Au)_{Au} + E(MgO)_{MgO}] \tag{4.2}$$

When comparing energies at different geometries, however, the nuclear fixed basis set introduces an error. The quality of the basis set is not the same at all geometries, owing to the fact that the electron density around one nucleus may be described by functions centred at another nucleus. As the basis set used in the calculation are generally far from complete, both the adsorbate Au and the substrate MgO may use additional variational freedom offered by each others basis functions to lower the energy of the whole system. This effect is known as *Basis Set Superposition Error* (BSSE). In the limit of a complete basis set, the BSSE will be zero. However, with localized basis sets (like the ones used within SIESTA), the conceptually simplest approach for eliminating BSSE is to add more and more basis functions, until the interaction energy no longer changes. Unfortunately, this requires very large basis sets and is not feasible. An approximate way of assessing BSSE is the *counterpoise* correction.[12] In this method the BSSE is estimated as the difference between substrate and adsorbate energies with the regular basis and the energies calculated with the full set of basis functions for the whole system. To estimate how much of the adsorption energy is due to BSSE, four additional energy calculations are needed: using the basis set for Au, and the basis for MgO, the energies of each of the "fragments" are calculated with the geometry they have in the optimised whole system (denoted by a superscript *). Two additional energy calculations of Au and MgO at the same geometry are then carried out with the full basis set. In our example, the two contributions of Au and clean MgO(001) surface are computed starting from the geometry of the AuMgO system, and transforming into ghosts the atoms of the adsorbate Au and the substrate MgO, respectively. Ghost atoms are points in space with an associated basis set, but lacking a nuclear charge. They can also be very useful when treating defects like vacancies in a material (*e.g.* F centres in MgO, carbon vacancy in diamond), because they allow a build up of charge density in the defective region.

The counterpoise correction[12] is defined as

$$\Delta E_{CP} = E(Au)^{*}_{AuMgO} + E(MgO)^{*}_{AuMgO} - E(Au)^{*}_{Au} - E(MgO)^{*}_{MgO} \tag{4.3}$$

where the subscript indicates the basis set used in each case.

The counterpoise corrected adsorption energy is then given as $E_{ads}^{CP} = E_{ads} - \Delta E_{CP}$. ΔE_{CP} is an approximate correction, it gives an estimate of the BSSE effect, but it does not provide either an upper or lower limit.

It is usually observed that the CP correction for methods including electron correlation is larger and more sensitive to the size of the basis set, than that at the HF level. This is in line with the fact that the HF wave function converges much faster with respect to the size of the basis set than correlated wave functions.

Using SIESTA and DZP basis sets for the gold atom at the F centre on MgO(001), the energies (in eV) are given in Table 4.2.

$\mathrm{E(AuMgO)_{AuMgO}}$	**$\mathrm{E(MgO)_{Mgo}}$**	**$\mathrm{E(Au)_{Au}}$**	**$\mathrm{E(MgO)^{*}_{AuMgO}}$**	**$\mathrm{E(MgO)^{*}_{Mgo}}$**
-34360.08	-32918.57	-1438.26	-32918.62	-32918.54
$\mathrm{E(Au)^{*}_{AuMgO}}$	**$\mathrm{E(Au)^{*}_{Au}}$**	**$\mathrm{E_{ads}}$**	**$\Delta\mathrm{E_{CP}}$**	E_{ads}^{CP}
-1438.60	-1438.26	**-3.25**	***-0.42***	**-2.83**

Table 4.2 Details for the calculation of the adsorption energy of a gold atom at the F centre on the MgO(001) surface (all energies in eV).

The counterpoise corrected adsorption energy is E_{ads}^{CP} = -2.83 eV, with a counterpoise correction ΔE_{CP} of -0.42 eV representing 13% of the uncorrected adsorption energy E_{ads}.

4.5 Bader charges calculation

The fast algorithm developed by Henkelman *et al.*[4] for doing Bader's analysis (section 3.4) on a charge grid can read charge density output files from VASP (CHGCAR files) or Gaussian03 (*.cube files). The program outputs the total charge associated with each atom and the zero flux surfaces defining the Bader volumes.

However, there are limitations due to the use of pseudo-potentials in *ab initio* codes which actually remove charge from atomic centres in the calculated density. If a charge density is generated without adding the missing charge due to the PP, the Bader volumes around an atom will typically fragment into many separate volumes. If the charge in the bonding regions is still correct, the analysis will get the right total charge for an atom, but the Bader surfaces can look bizarre. To add partial core charges in the VASP code, the 'main.F' file has to be slightly modified.[4] The partial charge is added to the SCF density but not used in the calculation of the density. However doing this, one no longer knows how many electrons should be associated with each atom type. It is then necessary to run a calculation with a single atom of each type in a box by itself (including the partial core charge). Then, running the Bader analysis on the isolated atom will give the total charge associated with that atom.

As discussed above (section 4.1), it is also possible for some elements to include a significant portion of the core in the PP. For example, studying MoO_3, the PP we choose explicitly treats $4p^6$, $4d^5$ and $5s^1$ electrons, which means that six semi-core electrons have been added.

The same kind of problem arises when studying MgO with SIESTA for example. If the Mg PP only treats explicitly the $3s^2$ electrons, then there is no charge density maximum around the Mg atoms in the oxide so that all charge is associated only with the O atoms. Using a PP for Mg explicitly treating the semi-core electrons $2p^6$ fixes the problem, as enough electrons are present for the Bader analysis algorithm to capture the charge density maximum around the core nucleus.

From a practical point of view, Henkelman's algorithm is available as a binary file[4] that can run under the Linux environment. As previously stated, it can read directly CHGCAR files produced by VASP but cannot read *.RHO charge density files produced by SIESTA. However, the utility program 'grid2cube' provided with SIESTA can convert *.RHO files to formatted *.cube files which can then be processed by the Bader's analysis code. It is also possible to perform simple operations like addition and subtraction of *.cube files using the utility ‘cubman’ provided with Gaussian03. This proves very useful if one wants to create a charge density difference file for example.

4.6 Transition states search

Finding a transition state (TS) is one of the most important applications of computational chemistry, but it is also one of the most difficult and daunting to achieve. Having the start and end points of a chemical reaction is usually not enough to guess accurately what the TS will look like. In order to improve the results, several methods have been developed, including the Nudged Elastic Band (NEB)[13-15] and the Eigenvector Following (EF) methods[16]. These two methods are used together in the transition states searches presented in this thesis. Indeed, the EF method is very sensitive to the approximate TS structure and in many cases the latter cannot be generated using the scanning strategies. This may be either too costly or due to the fact that the reaction path is described by more than one structural variable. In this situation, the NEB proves very powerful to locate a good approximation of the TS which can then be used as a starting point for the EF.

A – The Nudged Elastic Band method

The NEB is a method for finding saddle points and minimum energy paths between known reactants and products. In the "normal" elastic band method, the reaction path is described by a discrete representation consisting of the two fixed end points $\vec{P}_0$ and $\vec{P}_M$, and *M–1* intermediate images $\vec{P}_1, \cdots, \vec{P}_{M-1}$.[13-15] $\vec{P}$ is a point in the phase space of the system, *i.e.* a $3 \times N$ list of co-ordinates for a system containing N atoms.

The various images are connected by harmonic "springs" or "elastic bands", added to prevent collapse of the intermediate images to the end points. With this method, optimisation of the system of images and springs suffers from the problems of image sliding towards the minima and corner cutting in the vicinity of the transition state.

The NEB procedure solves these problems by projecting out the perpendicular component of the spring force and the parallel component of the true force from the total force acting on each image.[13-15] Thus, the force on image *i* is given by $F_i = \vec{F}^s_{i\|} + \vec{F}^l_{i\perp}$ where the parallel component of the spring force is $F^s{}_{i\|} = (k_{i+1} | \vec{P}_{i+1} - \vec{P}_i | - k_i | \vec{P}_i - \vec{P}_{i-1} |)\hat{\eta}_i$. Here, k_i is the spring constant between image *i* and *i-1*, and $\hat{\eta}_i$ is the normalized local tangent at image *i*. $\vec{F}^l_{i\perp}$ is the component of the force perpendicular to the tangent $\hat{\eta}_i$ at image *i* as calculated from the DFT equations. If the spring constants between the images are set to the same value, the images are distributed evenly along the pathway; this is the method we apply for saddle point searches in this thesis. It is possible to improve the estimates of $\hat{\eta}_i$ near the saddle point by employing a higher density of images in this region.

VASP 4.6 supports the elastic band method to calculate energy barriers. The usual input files must be located in the directory in which VASP is started. In addition, a set of subdirectories (numbered 00, 01, 02...) must be created, and each subdirectory must contain one POSCAR geometry file. A spring constant can be specified with the SPRING tag. We keep the default value (-5) which applies the NEB as SPRING is set to a negative value.

Often an initial linearly interpolated starting guess is appropriate; however for complex reaction pathways where the reactant geometry is strongly affected, more clever ways of generating the intermediates are required. As part of our utility program Intervasp (http://www.cf.ac.uk/chemy/staff/willock/inter_vasp.htm), we have developed a new interpolation scheme that we call the GRUP method. The system is split into two sections according to the group labels defined for the start file. A central atom is defined for the group of atoms and is interpolated linearly between its position in the start and end file. All other atoms in the group are interpolated by first working out the start and end distances to the central atom. Then the positions of the atoms are moved as if it were to be interpolated linearly but then its position is adjusted so that its distance to the central atom varies smoothly from the starting to the final distance. This approach is particularly important when one has to ensure that bond lengths in the molecule, here CH_4, are not foreshortened as a result of the interpolation process. Intervasp also features a "late centre" option which proves very useful for transfer reactions where the molecule first has to reach a certain point before undergoing any interpolation. Once a good TS approximation has been found using the NEB method, the resulting geometry is used as an input for the EF method.

B – The Eigenvector following method

In the region of correct negative curvature, that is, in the vicinity of the actual TS, one can use a local searching method to optimize the TS structure. In order to work at all it is therefore mandatory to provide a reasonable starting structure, which might either be obtained by guessing well or by series of constrained optimisations (relaxed potential energy scans using NEB).

Taking the example of methane activation on defective $MoO_3(010)$, the TS guess obtained by NEB presents two negative eigenvalues: one assigned to the twist of the methyl protons and one assigned to the C–H bond breaking. These are identified by inspection of the motion in the corresponding eigenvectors.

TS searches will usually only work if there is at least one negative eigenvalue. Multiple negative eigenvalues will not be a problem as long as one of these is significantly larger than the others, which is the case here. The EF optimisation algorithm[16] follows the most negative (largest) eigenvalue in the optimization process.

In our case, the reaction path can be described by one structure variable, namely the C–H bond length, as it is the reaction coordinate. As a result, we stretch only this bond by small steps (0.012 Å) and we then compute the respective energies (no geometry optimisation). The resulting curve giving the energy as a function of d(C–H) is then interpolated to find the C–H bond length maximising the energy (figure 4.8).

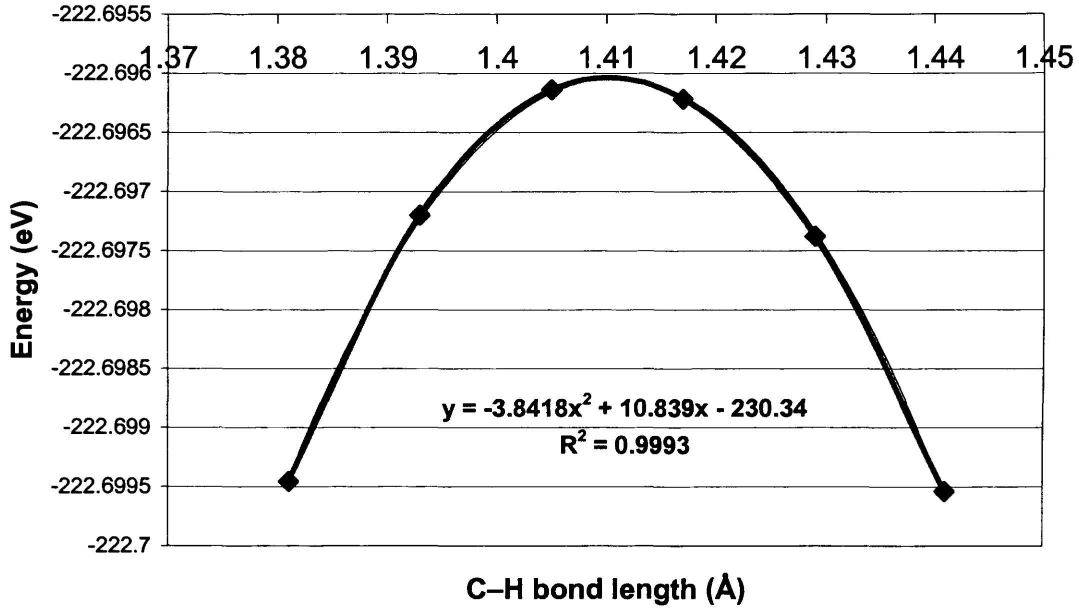

Figure 4.8 Energy of the $CH_4/MoO_3(010)$ system, in eV, plotted against the C–H bond length, in Å, for geometries close to the transition state.

The geometry obtained from the NEB calculations, already close to the true TS with d(C–H)= 1.44 Å, is then adapted to the new C–H bond (1.41 Å) and the resulting geometry is optimised using a Quasi-Newton algorithm: the forces and the second derivatives matrix are used to determine the search directions for finding the equilibrium positions, the total energy not being taken into account.

Quasi-Newton algorithms are very sensitive to the starting geometry but are reliable to locate transition states. Once the TS geometry has been optimised at d(C–H)= 1.42 Å, a vibration frequencies analysis is performed in order to check that there is one and only one negative eigenvalue (1095*i* cm^{-1} in this example). We also need to check that the forces in the system are almost converged to zero (0.01 eV Å^{-1} here). These two conditions are necessary in order to assign the obtained geometry to a transition state since the TS should be a stationary point with zero first derivatives and a single imaginary frequency.

References

1. S. Scandolo, P. Giannozzi, C. Cavazzoni, S. de Gironcoli, A. Pasquarello, and S. Baroni, *Z. Kristallogr.*, 2005, **220**, 574-579.
2. J.P. Perdew, K. Burke, and M. Ernzerhof, *Phys. Rev. Lett.*, 1996, **77**, 3865-3868.
3. R. Bader, *Atoms in Molecules: A quantum Theory*. 1990, New York: Oxford University Press.
4. G. Henkelman, A. Arnaldsson, and H. Jónsson, *Comput. Mat. Sci.*, 2005, (in press).
5. S.H. Wei and A. Zunger, *Phys. Rev. B*, 1987, **37**, 8958.
6. N. Troullier and J.L. Martins, *Phys. Rev. B*, 1991, **43**, 1993.
7. M.C. Payne, M.P. Teter, D.C. Allan, T.A. Arias, and J.D. Joannopoulos, *Rev. Mod. Phys.*, 1992, **64**, 1045-1097.
8. S.G. Louie, S. Froyen, and M.L. Cohen, *Phys. Rev. B*, 1982, **26**, 1738.
9. M.E. Straumanis, *J. Mater. Sci.*, 1988, **23**, 757-760.
10. K.P. Huber and G. Herzberg, *Molecular Spectra and Molecular Structure Constants of Diatomic Molecules*. 1979, New York: Van Nostrand.
11. L. Kihlborg, *Ark. Kemi*, 1963, **21**, 357-364.
12. S.F. Boys and F. Bernardi, *Mol. Phys.*, 1970, **19**, 553.
13. H. Jönsson, G. Mills, and K.W. Jacobsen, *Classical and Quantum Dynamics in Condensed Phase Simulations*, ed. B.J. Berne, G. Ciccotti, and D.F. Coker. 1995, Singapore: World Scientific.
14. G. Mills and H. Jönsson, *Phys. Rev. Lett.*, 1995, **72**, 1124.
15. G. Mills, H. Jönsson, and G.K. Schenter, *Surf. Sci.*, 1995, **324**, 305.
16. J. Simons, A. Banerjee, N. Adams, and R. Shepard, *J. Phys. Chem.*, 1985, **89**, 52.

Chapter 5

Methane activation on molybdena

This chapter concerns methane activation on molybdena, particularly the $MoO_3(010)$ surface. After an introduction to the subject and a presentation of the computational details, the results will be given in four sections: bulk and perfect surface, defective surface and O_2 adsorption, H and CH_3 adsorption and finally C–H bond breaking of CH_4.

5.1 Introduction

Transition metal oxides have an important role in chemistry and in catalysis in particular by virtue of the metal centres' ability to be involved in redox processes. This allows the metal oxide surface to be reduced as an adsorbed species is oxidised and for the surface reaction sites to be replenished by oxidising species, ideally O_2. This Mars-van Krevelen mechanism for oxidation by these catalysts identifies lattice oxygen species as a source of oxygen atoms in the product of a reaction.[1, 2]

Molybdenum oxide is an important example of a redox active solid catalyst as discussed in chapter 2; it is known to activate C–H bonds in alkanes including methane and, under the correct conditions, methane is selectively converted to partial oxidation products, methanol and formaldehyde. In mixed oxides molybdenum also takes part in partial oxidation reactions such as the dehydrogenation of propane to propene.[3]

On an atomic scale redox processes are usually considered to occur as local events, one or two metal centres are reduced as lattice oxygen is consumed and then re-oxidised through surface adsorption. The theoretical treatment of such effects using a periodic density functional theory (pDFT) representation of the surface is hampered by the self interaction problem. This is inherent in density functional theory since the density used to generate the potential for the one electron Kohn-Sham states includes the electron for which the wave function is sought, *i.e.* the electron will play a part in its own repulsion. In general this leads to a tendency for pDFT to produce de-localised solutions which contradict experimental electron spin resonance measurements[3] and calculations employing post-Hatree-Fock schemes[4].

More accurate treatment of spin localisation in DFT is possible using hybrid functional approaches[5] or by introducing additional on site potential terms to compensate for the self interaction effects[6]. The latter approach sits more easily with plane wave basis sets in periodic calculations but requires the introduction of parameters to control the additional potential. In the fourth section of this chapter we examine the effect of such a potential on the structure of defective MoO_3 surfaces and show how the parameter required can be obtained by reference calculations employing the hybrid functional approach.

The orthorhombic MoO_3 layered structure (α-MoO_3) can be described with distorted edge- and corner-sharing MoO_6-octahedra (figure 5.1), as already presented in section 2.1.

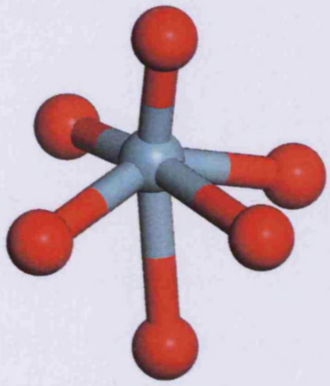

Figure 5.1 MoO_6-octahedra building unit of α-MoO_3. Oxygen atoms in red, molybdenum in blue.

Molybdenum oxide based catalysts are believed to operate effectively as oxidation catalysts under slightly reduced conditions where the presence of Mo^V is essential.[7, 8] Oxygen vacancies exposed at the surfaces may undergo re-oxidation by gaseous oxygen or may give rise to extended defects.[9] The latter process, known as crystallographic shear, changes the metal-to-oxygen stoichiometry and is accompanied by rearrangements of the metal-oxygen units. The existence of point defects at MoO_3 surfaces is also expected.[10, 11]

It has been proposed that the terminal oxygen is the active species in partial oxidations.[12] The standard partial oxidation of methane to formaldehyde was studied and the terminal oxygen was found to be the most likely for partial oxidation, while bridging oxygen is involved in complete oxidation. Therefore, the (010) surface which has the terminal oxygen atoms exposed, should be the most reactive face for partial oxidation. More details on methane activation in general and with MoO_3 are given in the section 2.1 of this thesis.

The work presented in this chapter consists of results obtained from the codes VASP and Gaussian03[13]. We will first study bulk MoO_3 and its (010) surface. Then, we will model the oxygen defective $MoO_3(010)$ surface, emphasizing the ability of the Density Functional Theory coupled with a simple Hubbard model to correctly treat unpaired electrons in that system and molecular oxygen will be adsorbed at the defect site in an attempt to study O_2 activation. Finally, methane activation will be considered on the defective surface, employing VASP and the Nudged Elastic Band (NEB) method[14-16] to locate transition states.

5.2 Computational details

All periodic calculations were carried out using the Vienna *ab initio* Simulation Program (VASP)[17, 18]. Convergence of the bulk lattice energy was found for a value of E_{cut} of 400 eV for the molybdenum oxide system and this was used throughout the work presented here. The calculations are performed within the generalized-gradient approximation (GGA), using the exchange-correlation potential developed by Perdew, Burke and Ernzerhof (PBE).[19] The improvements of this functional over PW91[20] include an accurate description of the linear response of the uniform electron gas, correct behaviour under uniform scaling, and a smoother potential. It is important to note that when doing spin-polarized PW91 calculations with VASP, the interpolation for the correlation part of the exchange correlation functional should be done according to Vosko, Wilk and Nusair.[21] For consistency with studies using the PW91 functional, we also choose the Vosko, Wilk and Nusair method. We also employ the tetrahedron method with Blöchl corrections[22] to determine how partial occupancies are set for each wave-function.

For pseudopotentials we choose the Projector Augmented Wave method (PAW)[23, 24] since it requires less parameters in the construction of the potentials than the ultra-soft potentials method[25] and gives good agreement with all electron results. In our calculations, the core states represented in this way consist of orbitals up to and including the 4*s* orbital for molybdenum, leaving the 4*p*, 4*d* and 5*s* electrons to be treated explicitly; so the semi-core 4*p* states are treated as valence. For carbon and oxygen, only the 1*s* orbital is included in the core and for hydrogen, the 1s orbital is explicitly treated. The VASP pseudopotentials database was used in which the pseudopotential radii are: Mo, 2.6 a.u. for the *s* states and 2.5 a.u. for the *p* and *d* states; for O, 1.2 a.u. for the *s* states and 1.52 a.u. for the *p* states, for C, 1.2 a.u for the *s* states and 1.5 a.u. for the *p* states and finally for H, 1.1 a.u. for the *s* states.

Several Monkhorst-Pack[26] *k*-point grid densities were tested for calculations on the bulk structure and a mesh of (5×3×5) was selected based on convergence of the bulk energy to within 0.01 kJ mol^{-1}. Finer *k*-point grids are used for calculations of the density of states as discussed later.

For surface calculations on the (010) face, we use a slab consisting of one bilayer separated from its periodic image perpendicular to the surface by a vacuum gap of 14 Å. The bilayers interact only weakly in the *b*-direction, as evidenced by the difficulty found using

DFT to converge the bulk geometry discussed in section 5.3. Accordingly the (010) surface can be modelled using a single bilayer slab with little loss of accuracy. For calculations on the bare oxygen vacancies we use a p(3×3) surface unit cell so that 18 molybdenum atoms are included. The larger real space unit cell compared to the bulk calculations reduces the number of *k*-points required and for this surface cell a mesh of (3×3×1) was found to give convergence of the total energy to a similar accuracy as that found for the bulk. To study the adsorption of molecular oxygen and methane activation at the defect site a p(2×2) surface unit cell is used together with a (5×5×1) *k*-point mesh.

For models involving the oxygen defect surface, the calculations are performed within the DFT+U methodology (section 3.1) using the simplified approach due to Dudarev *et al.*[27] and applied to the molybdenum centres only. A value of 6.3 eV is chosen for the U-J parameter (U and J being specified in terms of the effective on site Coulomb and exchange parameters). A justification of this choice and more details on the DFT+U approach are given in section 5.3.

The optimization of the atomic coordinates (and unit cell size/shape for the bulk material) is performed via a conjugate gradients technique which utilizes the total energy and the Hellman-Feynman forces on the atoms (and stress on the unit cell).

A high quality charge density is first generated, using the *k*-point grid we defined earlier. Then, a calculation using the charge density file from this self-consistent run is obtained with denser grids. This is the only way to calculate the band structure as for band structure calculations the supplied *k*-points usually form no regular three-dimensional grid. Furthermore, high quality densities of states often require very fine *k*-meshes.

To obtain the atomic charges[28], we use a fast algorithm for carrying out Bader analysis on the charge density grid provided from VASP. The analysis program required was developed recently by Henkelman *et al.*[29] (section 3.4). To identify the atom centres Bader analysis assumes that they are located at charge density maxima. However, the pseudopotentials used in VASP calculations remove charge from atomic centres and so to obtain correct Bader charges we re-introduce this core charge into the calculated density prior to Bader analysis. The spin populations are directly calculated by VASP when the keyword LORBIT is set to 10.

VASP can determine the matrix of the second derivatives of the energy with respect to the atomic positions, called the Hessian matrix. From this and the atomic masses the vibrational frequencies of the system are also calculated (section 3.3). To build the Hessian we use a central difference, by specifying two displacements, *i.e.* each ion is moved in each direction by a small positive and negative displacement, set to 0.04 Å. Frequencies in cm^{-1} are given directly at the end of the VASP output file and can be compared to experimental results in the instance of MoO_3 there is Raman spectroscopy data available.[30]

In order to assess the effect of Hartree-Fock exchange on the electron localization, a cluster model of the defective $MoO_3(010)$ surface is studied with Gaussian03[13] using the Density Functional Theory and the PBE0 hybrid functional[31] for consistency with the PBE functional used in VASP. The molybdenum centres are treated with the LANL2DZ[32, 33] basis set (Los Alamos effective core potential plus double-ζ). The oxygen and hydrogen centres are treated with the 6-31G(d)[34-43] basis set which is a split valence basis with polarization added on oxygen. Details of the methodology for the cluster study are given in the relevant section.

Finally, the NEB method is used with VASP to locate transition states for the C–H bond activation, as explained in details in section 4.6.

5.3 Bulk and perfect (010) surface

The layered structure shown in figure 5.2 suggests that the lattice constant in the *b*-direction is determined by non-covalent interlayer forces. Indeed, Corà *et al.* who have also studied MoO_3 using an *ab initio* Hartree-Fock method[44] found that changing the interlayer spacing does not involve changing any of the nearest-neighbour Mo–O distances, consistent with the interlayer interactions involving only a weak Coulombic and van der Waals interaction. Van der Waals forces are difficult to reproduce correctly with DFT methods since the dispersion force is poorly represented. In this case a minimum for the *b*-parameter was not found and so we choose to keep this lattice parameter at the experimental value of 13.855 Å in all bulk calculations.

The remaining lattice parameters were optimised by relaxing the atomic co-ordinates at a series of fixed volumes around the experimentally reported lattice parameters. The final equilibrium lattice vectors were then obtained by a fit to an equation of state in order to reduce the effect of the Pulay stress. The values obtained are compared with literature values in Table 5.1.

Lattice parameter	**Lattice constant (Å)**			
	GGA	LDA[45]	HF[44]	Expt[46]
a	4.022	3.729	3.910	3.963
b	*13.855*	13.036	14.271	13.855
c	3.752	3.478	3.680	3.696

Table 5.1 Lattice parameters (Å) for bulk MoO_3

Bond	**Bond length (Å)**			
	Bulk	Bulk Expt[46]	(010)	(010) LDA[45]
Mo–O$_t$	1.70	1.67	1.70	1.67
Mo–O$_s$[a]	1.97	1.95	1.97	1.92
	2.34	2.33	2.41	2.30
Mo–O$_a$	1.75	1.73	1.76	1.76
	2.29	2.25	2.28	2.19

Table 5.2 Mo–O bond lengths for MoO_3 bulk and the (010) surface. Note: a) lower values indicate interaction distance between sub-layers

The gradient corrected DFT approach used here gives a small over estimate of the optimised lattice parameter. However the error is less than the LDA underestimated parameters from Chen *et. al.*[45] The calculated Mo–O bond lengths (Table 5.2) are also in good agreement with the experimental values; in general we find bonds longer than the experimental values by a few hundredths of an Angstrom.

The charge density calculated at the optimised bulk geometry is shown in figure 5.2.

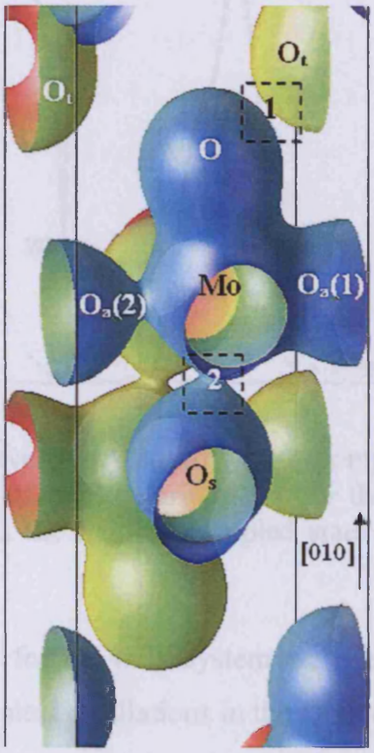

Figure 5.2 0.3 $Å^{-3}$ electron density isosurface for bulk MoO_3. Region 1 and 2 highlight the close contact positions between bilayers and single layers respectively. $O_a(1)$ and $O_a(2)$ are asymmetric bridging oxygen centres.

The closest contact between bi-layers is highlighted by region 1 in the figure. At the electron density contour used there is no sharing of electron density between the bi-layers in this region. The Mo-O_t bond shows a covalent nature and the anisotropy in bonding for Mo-O_a can be seen clearly in the diagram with the bond to the right of the central Mo in the diagram showing a higher bond density than that to the left. The interaction between the Mo centre and the O_s oxygen atom below it within a bilayer (see region 2) does have a small region of shared density confirming that O_s ions can be thought of as 3-fold co-ordinated.

The covalent character of the bonding in this oxide can also be seen in the DOS plot shown in figure 5.3.

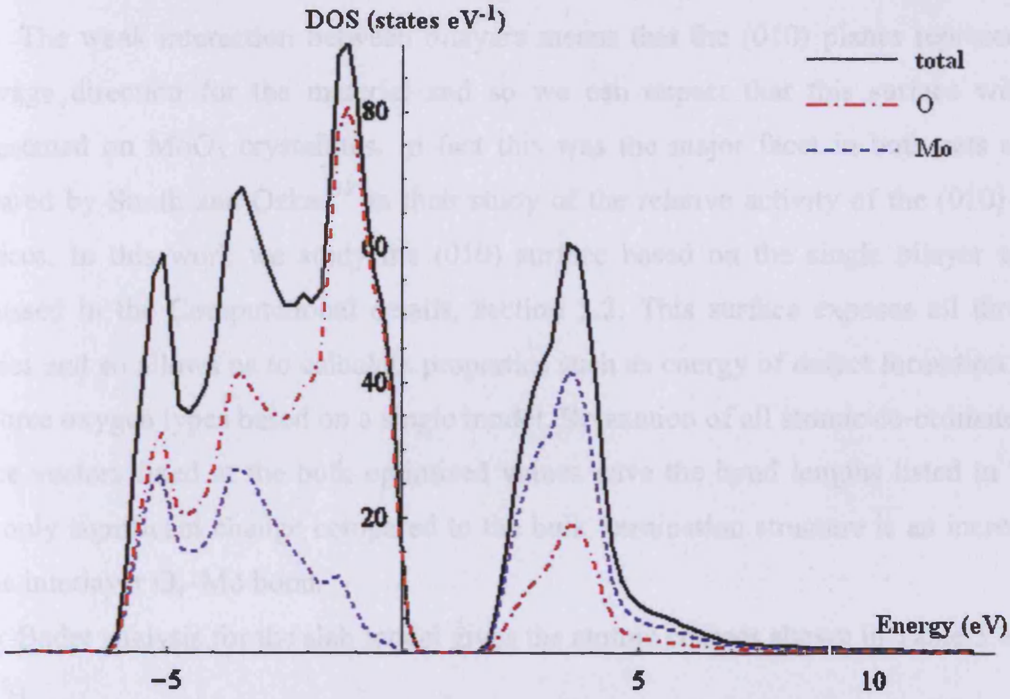

Figure 5.3 Total DOS curve (black solid) with decomposition into molybdenum (dashed) and oxygen (dot-dashed) contributions, for the MoO_3 bulk system. The energy origin is chosen as the highest occupied state and a Gaussian smearing width of 0.2 eV is applied.

To obtain a smooth DOS for the bulk system we use a rather large *k*-points grid of 15×9×15. This eliminates unphysical oscillations in the DOS due to the *k*-space grid, the DOS has been smoothed by centring Gaussian functions with a 0.2 eV width on the calculated points. The highest occupied state is chosen as the reference energy and, for clarity, figure 5.3 shows only the valence and conduction band regions of the total DOS curve. The calculated valence band region has a width of 5.8 eV. The computed band gap is 2.1 eV and is consistent with experimental results; MoO_3 is an n-type semiconductor with an indirect band gap that has been reported to be between 2.9 eV and 3.15 eV.[47, 48] A calculated underestimate of the band gap is a well-known short-coming due to the failure of DFT to describe the relative energies of occupied and unoccupied electron energy levels.[49] Our analysis will concentrate on the properties of the electron density which is more accurately reproduced. Figure 5.3 also includes a decomposition of the DOS into molybdenum and oxygen contributions. This shows clearly that the major contribution to the valence states is from oxygen, while molybdenum contributions are smaller and concentrated in the lower energy region of the valence band. In very ionic systems such as MgO the valence band would be completely oxygen in character. The presence of metal orbitals in the valence states re-enforces the idea that there is a significant covalent character in the bonding of this solid.

The weak interaction between bilayers means that the (010) planes represent an easy cleavage direction for the material and so we can expect that this surface will be well represented on MoO_3 crystallites. In fact this was the major facet in both sets of samples prepared by Smith and Ozkan[12] in their study of the relative activity of the (010) and (100) surfaces. In this work we study the (010) surface based on the single bilayer slab model discussed in the Computational details, section 5.2. This surface exposes all three oxygen species and so allows us to calculate properties such as energy of defect formation for any of the three oxygen types based on a single model. Relaxation of all atomic co-ordinates with the lattice vectors fixed at the bulk optimised values gave the bond lengths listed in Table 5.2. The only significant change compared to the bulk termination structure is an increase (+3%) of the interlayer O_s–Mo bond.

Bader analysis for the slab model gives the atomic charges shown in Table 5.3.

	Atom charge (|e|)		
Species	Bulk	(010) surface	(010) cluster[50]
Mo	2.59	2.56	2.16
O_t	-0.68	-0.65	-0.48
O_s	-1.04	-1.05	-0.97
O_a	-0.86	-0.85	-0.72

Table 5.3 Atomic charges for MoO_3 and its (010) surface

The values obtained are very similar to those from the reference bulk calculation. These charges are higher in magnitude than previously reported by Tokarz-Sobieraj *et al.*[50]. However their paper quotes Mulliken charges for a $Mo_{15}O_{56}H_{22}$ cluster model of the $MoO_3(010)$ surface and so the differences in methodology could explain this observation.

Raman spectra of MoO_3 samples show bands characteristic of the three oxygen species present in the structure[30]. For comparison we have calculated the vibrational modes associated with the oxygen atoms around a single Mo centre in the slab model. The vibrational frequencies of the system are calculated by displacing the atoms in the direction of each Cartesian coordinate and building the Hessian matrix from the forces. The main modes to be considered here are the Mo–O stretching vibrations and so in the interests of computer time we build a reduced Hessian by considering the movement of only a sub-set of atoms around one of the surface terminal oxygen atoms. Figure 5.4 presents the convergence of the terminal oxygen atom stretching frequency with the number of atoms in this sub-set.

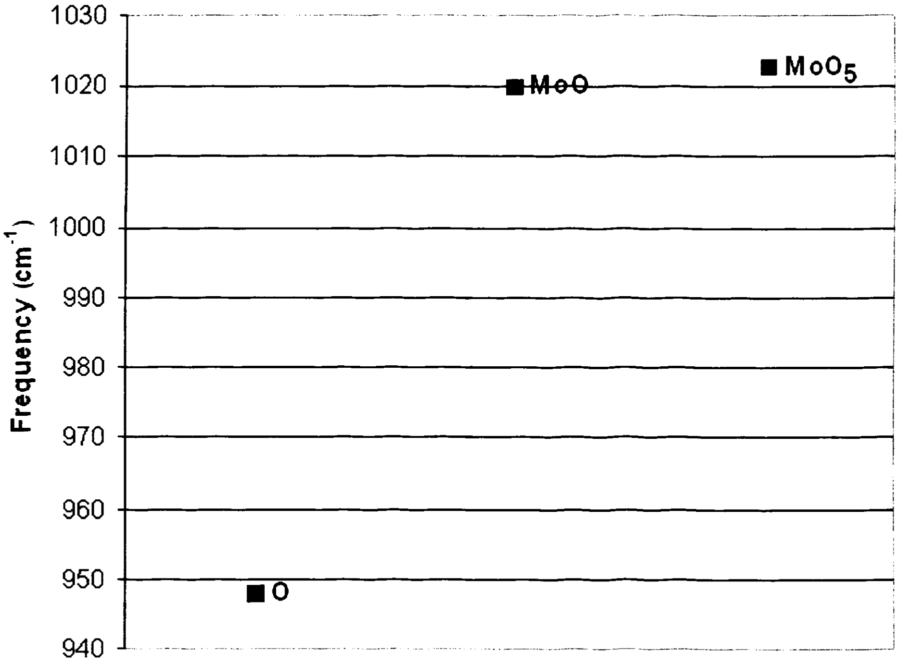

Figure 5.4 Convergence of the terminal oxygen vibration frequency with the number of atoms used in the calculation.

Three ensemble sizes are shown; the single terminal oxygen atom, the terminal oxygen atom and its associated Mo, and the MoO_5 surface layer section from one complete MoO_6 distorted octahedron. The frequency of the terminal oxygen stretching vibration is converged for a region size of MoO_5 since this point and the MoO case differ by only 3 cm^{-1}. This indicates that this mode is not strongly coupled to long range vibrations of the simulation slab. Table 5.4 shows the main vibrational modes calculated for the $MoO_3(010)$ surface using the MoO_5 ensemble of atoms.

Mode	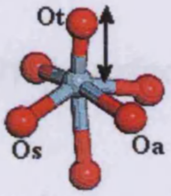	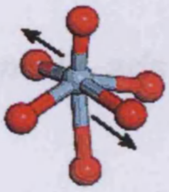	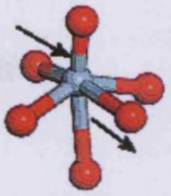
Frequency	**1023**	**898**	**746**
Expt[51]	997	820	-

Mode	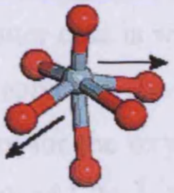	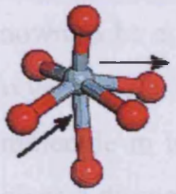	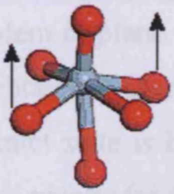	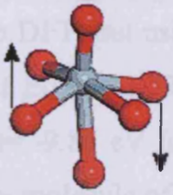
Frequency	**711**	**520**	**420**	**380**
Expt[51]	668	-	-	286

Table 5.4 Vibration modes calculated for the $MoO_3(010)$ surface (cm^{-1}). The positions of the oxygen species are as labelled in the first frame.

Site symmetry arguments have been used by Beattie *et al.* [51] to identify the vibrational modes consistent with Raman selection rules according to the local symmetry of each oxygen species. The calculated vibrations are compared with experiment according to their assignment and we note that only modes that are *gerade* with respect to an idealised O_h symmetry about the Mo centre are found to be active. The stretching modes 1023, 898 and 711 cm^{-1} are in good agreement with the experimental results. The bending mode 380 cm^{-1} is further from the experimental value (286 cm^{-1}), probably due to the size of the group of atoms considered since the other Mo neighbours of the moving oxygen atoms were fixed.

5.4 Defective (010) surface and O_2 adsorption

5.4.1 Defective surface

The formation energy of an oxygen vacancy can be calculated with respect to different gas phase species; either the O_2 molecule or the oxygen atom, both of which have triplet ground states. The latter case is well known to be a problem in plane wave DFT, but using a "broken symmetry" approach for the oxygen atom we obtain an energy of E(O)= -1.52 eV. The computed energy for the oxygen molecule in its triplet state is $E(O_2)$= -9.85 eV for an optimized bond length of 1.24 Å. This gives a dissociation energy for the O_2 molecule of 6.81 eV, somewhat higher than the experimental value of 5.2 eV.

We will use the neutral atom as the reference state so that the values quoted do not depend on the particular reaction used to create the defect but are consistent with earlier calculations. The removal of a surface oxygen leaves two electrons on the surface which on a reducible oxide such as MoO_3 will reside at a metal centre. So the defect creation energy is the difference between the total energy calculated for the perfect surface and the sum of the relaxed defective surface energy and E(O). The defect energies calculated in this way are summarised in Table 5.5.

	Method		
Defect	DFT p(2×2)	DFT+U p(2×2)	DFT+U p(3×3)
O_t	6.29	4.85	4.85
O_s	7.75	6.99	6.86
O_a	6.21	5.47	5.34

Table 5.5 Defect energies (eV) calculated for $MoO_3(010)$ and relative to atomic oxygen

At the DFT level using a p(2×2) simulation cell we find the easiest oxygen species to remove is O_a with O_t having a very similar defect energy. A defect at the O_s site requires an additional 1.5 eV. The calculated defect energies are close in magnitude to the cluster calculations of Witko *et al.*[52], who find energies of 6.80 eV (O_t), 6.50 eV (O_s) and 6.75 eV (O_a), while the terminal and asymmetric oxygen atoms were found to have similar defect energies the symmetric oxygen is actually reported to be the easiest species to remove. We have seen in the analysis of the bulk unit cell that O_s is more ionic in character than the other two oxygen species and so this discrepancy may arise from the poor treatment of the Madelung potential inherent in a cluster model. At the DFT+U level using a p(2×2) cell we find vacancy formation energies of 4.85 eV for the terminal oxygen, 6.99 eV for the symmetric oxygen and 5.47 eV for the asymmetric oxygen. To test the effect of the size of the super-cell we also report results from a p(3×3) cell. The terminal oxygen vacancy energy is identical to the p(2×2) case and the bridging oxygen defect energies are within 0.15 eV of those from the smaller cell. The DFT+U values are significantly less than the corresponding DFT values. In addition the O_t vacancy now has a formation energy 0.62 eV lower than that for O_a. Considerable differences in the electronic and atomic structure are also seen when comparing the DFT and DFT+U models but before considering these we deal with the choice of parameter for the DFT+U case.

To create the O_t defect the central terminal oxygen of the p(3×3) $MoO_3(010)$ super-cell was removed and the system optimized. Upon reduction, the molybdenum atom at the defect site should be reduced to a +4 oxidation state, with a d^2 configuration. Since the metal site has a distorted octahedral environment the ground state is expected to be a triplet. At the DFT level, however, we find no magnetization at all on any centre. DFT is well known to artificially delocalize unpaired electrons to reduce the Coulomb repulsion because of the self-interaction.[4]

To examine the charge localisation in this system we first turn to a hybrid DFT scheme. This is not available in plane wave codes such as VASP and so we employ a cluster model and the Gaussian03 program[13]. A Mo_7O_{32} cluster was cut from the perfect surface which included a central Mo atom, its nearest four Mo neighbours in the surface layer and the two second layer Mo atoms bridged by the O_s atom beneath the central atom. All oxygen neighbours of each Mo centre are also included. To terminate the cluster model we use the same protocol as Witko and co-workers[53, 54], with H placed at the standard O–H distance of 0.97 Å, in the direction of the appropriate Mo–O bonds. The oxygen valency is implied from its type and distance from Mo atoms in the cluster. Terminal oxygen atoms require no termination, asymmetric oxygen atoms have one hydrogen atom added if they are a close neighbour of a cluster Mo atom (*e.g.* $O_a(1)$ in Fig. 5.2) and two otherwise (*e.g.* $O_a(2)$ in Fig. 5.2). O_s atoms have one terminating hydrogen added if they are in the same sub-layer as a cluster Mo atom but two if in the other layer of the cluster. The cluster is also chosen so that each Mo centre retains six oxygen neighbours. This adds twenty-two hydrogen atoms to satisfy the valency of the cluster. The terminal oxygen vacancy was then created and the resulting $Mo_7O_{31}H_{22}$ cluster was geometry optimised with only the surface atoms allowed to relax (13 atoms in total). In this way the relaxed zone of the model is bounded by a region frozen at the optimised surface geometry. For consistency the cluster calculations use the PBE exchange and correlation functional with additional exact exchange following the PBE0[31] hybrid functional scheme.

The spin density derived from the cluster model is shown in figure 5.5a. This shows the spin density to be well localized on the reduced Mo centre in the *d*-orbitals that are perpendicular to the surface. An orbital population analysis performed with Gaussian03 on the cluster model showed that mostly $4d_{xz}$ and $4d_{yz}$ orbitals are involved. The atomic spin density on the molybdenum centre from which the terminal oxygen atom was removed is 1.96, indicating that the model represents a metal atom in the triplet state at the defect.

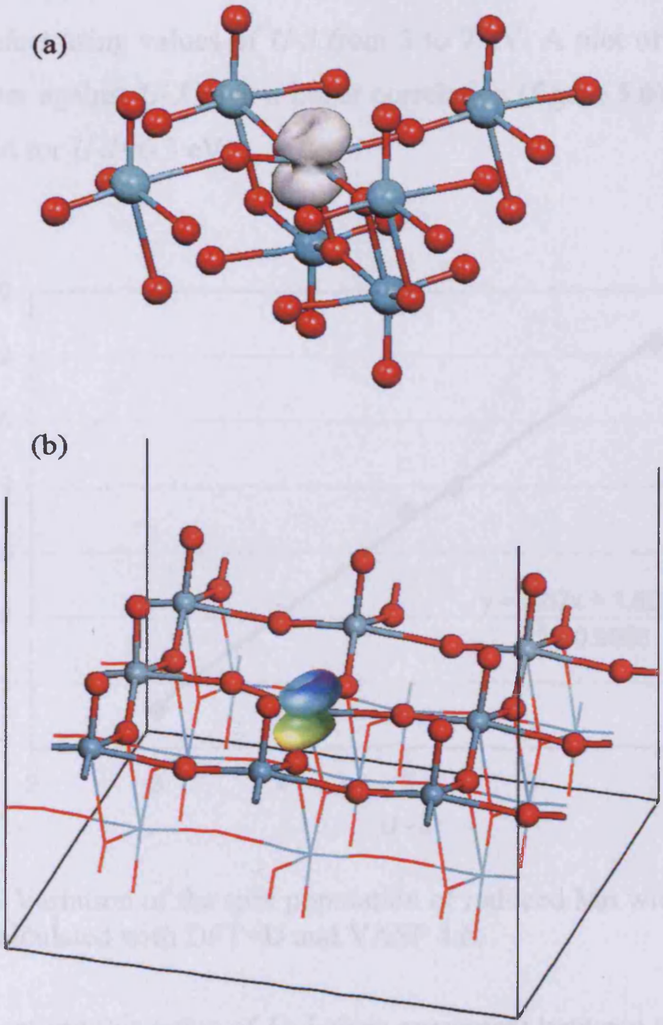

Figure 5.5 Spin density iso-surfaces for the defective $MoO_3(010)$ surface at 0.3 e Å^{-3}. a) $Mo_7O_{31}H_{22}$ cluster (hydrogen atoms omitted for clarity). b) DFT+U periodic calculation.

Although the cluster model does reproduce the expected localised electronic state we have noted earlier that the neglect of the Madelung potential will lead to difficulty in predicting the relative defect energies for the three surface oxygen sites. VASP does not include any hybrid DFT functionals, but it does feature the DFT+U scheme that uses an adaptation of the Hubbard model to provide an on-site representation for electron repulsion for transition metals with partially filled *d*-shells. We employ the approach from Dudarev *et al.*[27] in which the Hubbard *U* parameter is reduced by a factor *J* for interactions between electrons in orbitals with different orbital momenta. The combination of DFT with this on-site repulsion model leads to an energy functional which depends only on *U-J* and so requires only a single parameter to be set. To obtain this parameter we use the atomic spin density from our cluster model as reference data. We have optimized the p(3×3) model with the terminal oxygen defect using values of *U-J* from 3 to 7 eV. A plot of the spin population at the reduced Mo atom against *U-J* gave a linear correlation (figure 5.6) and a spin population of 1.96 was obtained for *U-J*=6.3 eV.

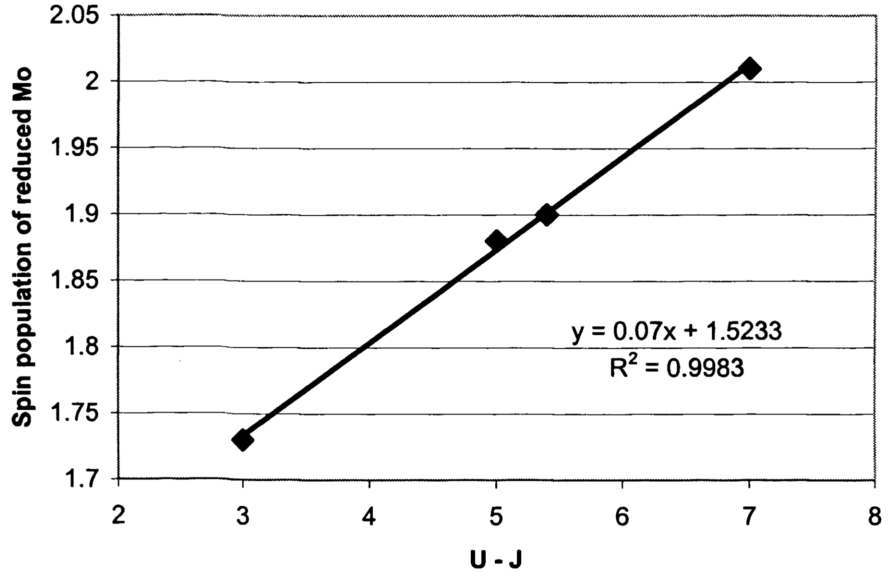

Figure 5.6 Variation of the spin population of reduced Mo with the value of U – J, as calculated with DFT+U and VASP 4.6.

Accordingly, since setting this value of *U-J* gives agreement between the cluster and periodic models, it is used throughout the DFT+U calculations presented here. It is interesting to note that this value is close to that obtained for bulk NiO by fitting to experimental electron energy loss spectra[27] and that used recently for CeO_2[6].

Aside from the charge localisation achieved using the DFT+U method we also find considerable differences in the atomic structure around the defect. A section of the surface structure relaxed at the DFT level is shown in figure 5.7a.

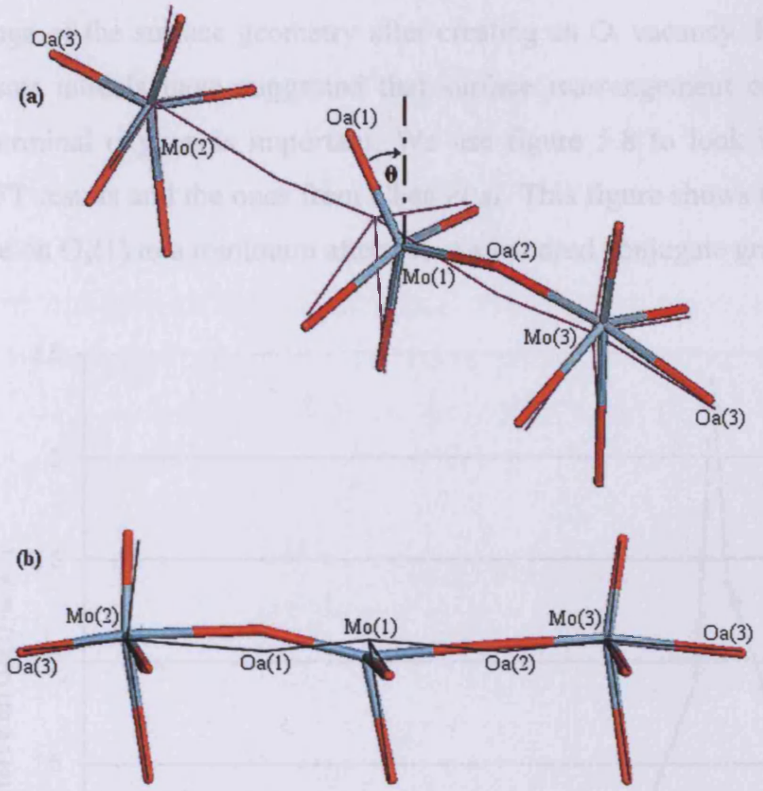

Figure 5.7 Geometry comparison between the perfect (line) and defective (tubes) (010) surfaces for a) DFT and b) DFT+U relaxations. These diagrams are taken from periodic p(3×3) calculations.

A significant relaxation of the surface occurs involving mainly the Mo and O_a atoms. In the perfect surface Mo(1)–O_a(1) is 1.76 Å, *i.e.* O_a(1) is the nearer of the two O_a neighbours to Mo(1). This bond length is found to be shorter (1.70 Å) in the defective surface, taking on the same value as the Mo–O_t bonds in the perfect surface. In addition O_a(1) moves out of the surface so that the angle between Mo(1)–O_a(1) and the surface normal (θ in figure 5.7a) changes from 94.8° in the perfect surface to 37.4° after relaxation of the defective surface. It appears, then, that O_a(1) is moving to acquire a terminal oxygen-like geometry in the DFT calculation. Accompanying this re-structuring the Mo(1)-O_a(2) bond is also found to be shorter in the defective surface than in the stoichiometric slab (1.81 *vs.* 2.28 Å). In fact the Mo(1)–O_a(2) bond is shorter in the defective surface than the Mo(3)-O_a(2) bond (1.95 Å), a reversal of the situation found in the perfect surface, indicating that the alternation of short and long Mo–O_a bonds along the [100] direction is disrupted by the presence of the defect. This structural rearrangement significantly affects the reported defect energy at the DFT level since the energy is reduced during the optimisation by 1.98 eV.

These results are different to earlier work by Chen *et al.*[55] who did not report any significant change of the surface geometry after creating an O_t vacancy. However, Witko *et al.*[52] using cluster models have suggested that surface rearrangement connected with the removal of a terminal oxygen is important. We use figure 5.8 to look into the difference between our DFT results and the ones from Chen *et al.* This figure shows the convergence of the R.M.S. force on $O_a(1)$ to a minimum after about a hundred conjugate gradient cycles.

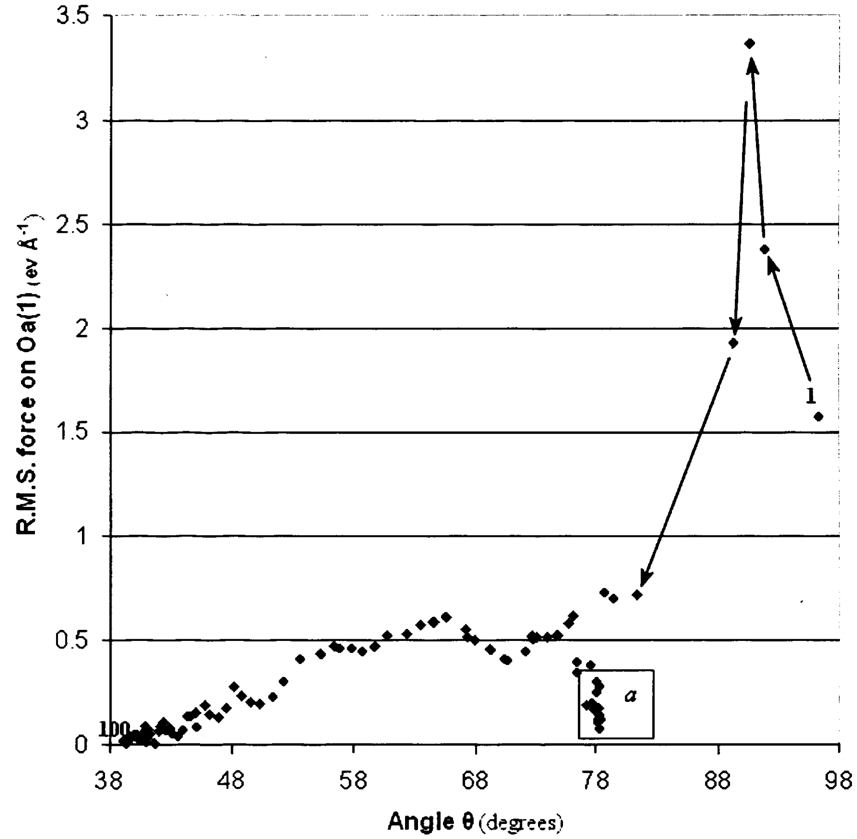

Figure 5.8 R.M.S. force on $O_a(1)$ versus the angle θ defined in figure 5.7 during geometry optimisation.

Region *a* features a point with a small R.M.S. force of 0.084 eV $Å^{-1}$ for an angle θ of 78.2°. If the convergence criterion was higher than this value, the calculation might stop here at an angle θ close to 78°. Chen *et al.*[55] used a convergence criterion of 0.136 eV $Å^{-1}$ and did not find any significant surface rearrangement. However, the VASP results presented here clearly indicate that removing a terminal oxygen from $MoO_3(010)$ leads to a rearrangement of this surface, as far as DFT is concerned at least.

Having produced a model describing the oxygen vacancy, we can calculate the defect energy and analyse the geometry of the defective $MoO_3(010)$ surface. DFT+U gives Mo^{4+}, which has the same charge state as the molybdenyl (Mo=O) in the perfect surface so we expect less re-arrangement of the surface for localised electrons. The rearrangement of the surface treated with DFT+U is indeed minor compared to that found with DFT in VASP as shown in figure 5.7b. The bare molybdenum sinks down towards its bridging oxygen atom, with a new Mo–O_s bond length of 2.12 Å compared to 2.41 Å for the perfect surface. Also, the angle θ is now 75.5° with DFT+U, a value close to the "pseudo minimum" DFT value of 78.2° in figure 5.8. We finally notice that using DFT+U, an unfavoured spin state (0.20 eV less stable) for the defective surface was also found with a spin of one on Mo(1) and a spin of one on a molybdenum centre belonging to the bottom bilayer (see section 5.6).

A Bader charge analysis was performed for both DFT and DFT+U and the results are shown in Table 5.6.

Species	Atom charge (|e|) (010) DFT	(010)+defect DFT	(010)+defect DFT+U
Mo(1)	2.56	2.47	2.27
Mo(2), Mo(3)		2.45	2.70
O_t	-0.65	-0.66	-0.69
O_s	-1.05	-1.06	-1.10
$O_a(1)$	-0.85	-0.75	-0.99
$O_a(2)$, $O_a(3)$		-0.90	-0.93

Table 5.6 Bader charges for the atoms represented in figure 5.7

After creation of the vacancy, the charge on the symmetric oxygen centres is practically unchanged. The charge on the asymmetric oxygen $O_a(1)$ is the same as the other asymmetric oxygen atoms with DFT+U but differs from DFT results. DFT gives a charge of -0.75 |e|, closer to a terminal oxygen charge (-0.66 |e|) than the O_a charge of the perfect surface. The charges on the molybdenum centres with DFT are similar to one another. There is a significant difference with DFT+U, Mo(1) has gained electrons compared to the other molybdenum centres in the system or compared to the perfect $MoO_3(010)$ surface. This can be explained by the localisation of the electrons with DFT+U method at the defect site.

The system is characterized with DFT+U by a well localised spin density (figure 5.5a) presenting a similar shape to the spin density calculated with the cluster model using hybrid DFT (figure 5.5b). Furthermore, the geometry of the hybrid DFT and DFT+U optimised surfaces are very similar. The angle θ is 75.5° with DFT+U, 74.4° with hybrid DFT and Mo(1) sinks down towards its symmetric oxygen at a distance d(Mo–O_{sym})=2.12 Å with DFT+U and 2.10 Å with hybrid DFT. This shows that the DFT+U scheme is appropriate to study this local defect system and that local cluster models and periodic supercell calculations give the same answer.

Defect spin densities have been reported in the literature for more reducible oxides. For example, the model for the $[AlO_4]^0$ defect centre in irradiated quartz, an Al impurity having replaced a four-coordinated Si atom, is that a hole forms in a non-bonding orbital of an oxygen atom, with consequent asymmetric relaxation along that particular Al–O direction.[4] Unlike Pacchioni *et al.*[4] for the hole localization in a quartz Al centre, we do not find that hybrid DFT leads to the incorrect picture of delocalized electrons and notice that Al oxidation state is not likely to vary in same ways as Mo. The two unpaired electrons left after terminal oxygen removal are localized on Mo(1) as the spin population on this atom is 1.96 and the new oxidation state is now indeed +IV.

A representation of the density of states separated in "spin up" and "spin down" shows unambiguously that DFT+U produces a spin-polarized system with a "spin up - spin down" curve different from zero for the valence band in figure 5.9a, while DFT gives symmetric "spin up" and "spin down" in figure 5.9b, typical of a non spin-polarized system.

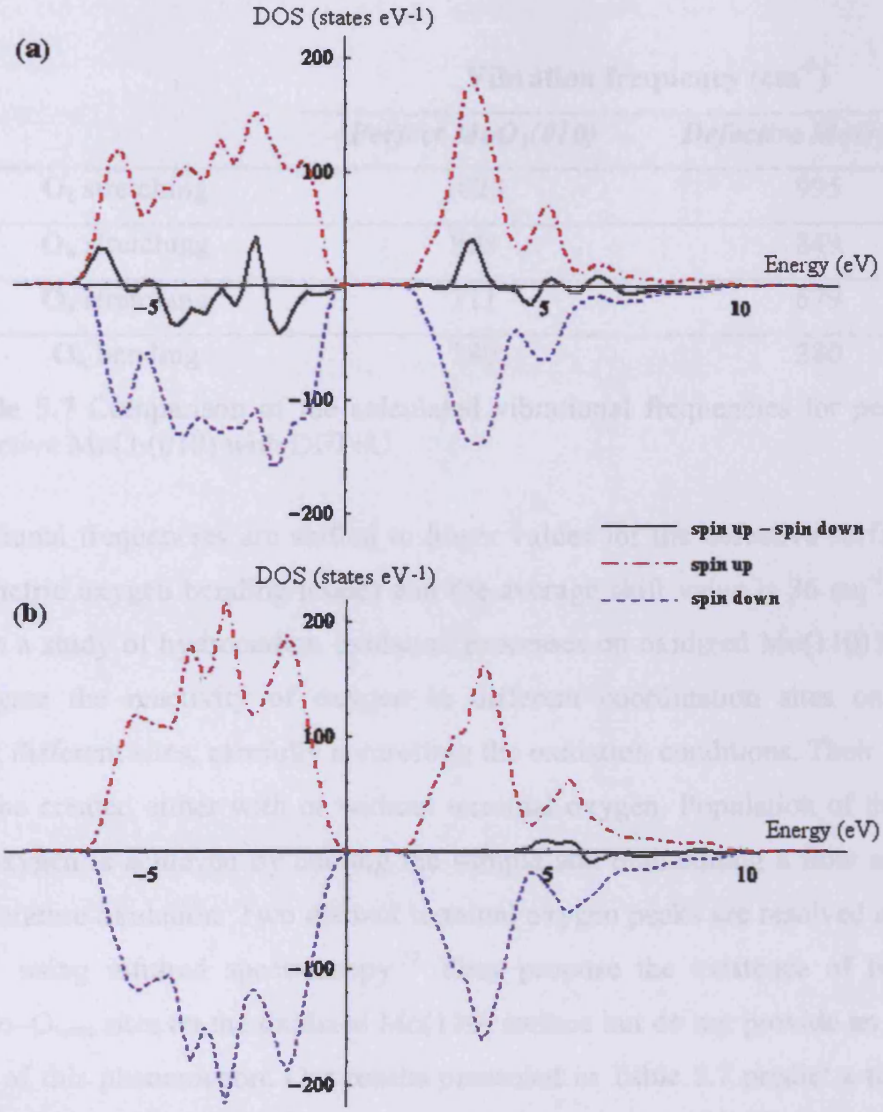

Figure 5.9 Spin up and spin down densities of states for the defective $MoO_3(010)$ surface with a) DFT+U and b) DFT

We also performed a vibrational frequency calculation on the defective $MoO_3(010)$ surface in order to compare with the results obtained for the perfect surface (Table 6). For the defective system we include all of the atoms shown in figure 5.7, as the local defect affects the geometry of these centres.

	Vibration frequency (cm^{-1})	
	Perfect $MoO_3(010)$	***Defective $MoO_3(010)$***
O_t stretching	1023	995
O_a stretching	898	849
O_s stretching	711	679
O_a bending	380	380

Table 5.7 Comparison of the calculated vibrational frequencies for perfect and defective $MoO_3(010)$ with DFT+U

The vibrational frequencies are shifted to lower values for the defective surface (except for the asymmetric oxygen bending mode) and the average shift value is 36 cm^{-1}. Queeney and Friend[56] in a study of hydrocarbon oxidation processes on oxidized Mo(110) have been able to investigate the reactivity of oxygen in different coordination sites on Mo(110), by populating different sites, carefully controlling the oxidation conditions. Their thin film oxide layer can be created either with or without terminal oxygen. Population of the surface with terminal oxygen is achieved by cooling the sample and maintaining a flow of O_2 following high-temperature oxidation. Two distinct terminal oxygen peaks are resolved at 992 cm^{-1} and 1016 cm^{-1} using infrared spectroscopy.[57] They propose the existence of two structurally distinct $Mo–O_{term}$ sites on the oxidized Mo(110) surface but do not provide an explanation on the origin of this phenomenon. Our results presented in Table 5.7 predict a terminal oxygen vibration frequency of 1023 cm^{-1} for perfect $MoO_3(010)$ and 995 cm^{-1} for the reduced surface with a terminal oxygen vacancy concentration of one per p(3×3) $MoO_3(010)$ supercell. These theoretical results are in excellent agreement with the experimental work of Queeney and Friend. We are now able to explain the origin of the two distinct peaks found by infrared spectroscopy; they correspond to the vibration modes of the terminal oxygen atoms in different environments, *i.e.* reduced or oxidized. As Queeney and Friend oxidized their Mo(110) surface in a stepwise manner, they saw both vibration frequencies as they were filling the thin layer with terminal oxygen.

5.4.2 Molecular oxygen adsorption

Local defects may be re-oxidized with molecular oxygen which then replaces the missing terminal oxygen. Three different orientations for O_2 are possible: perpendicular to the surface with only one oxygen in contact with Mo(1), parallel to the surface with the atoms of O_2 above the symmetric oxygen centres (denoted O_s in figure 5.10), and parallel to the surface with the atoms of O_2 above the asymmetric oxygen centres, denoted O_a in figure 5.10. The results are presented in Table 5.8.

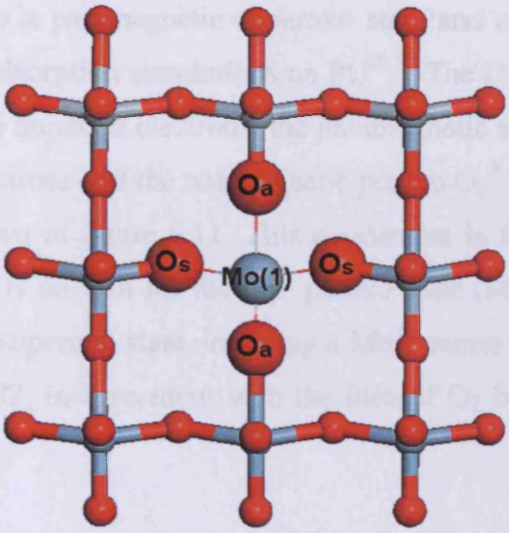

Figure 5.10 Top view of the $MoO_3(010)$ surface with its terminal oxygen vacancy. Mo(1) is represented as a blue sphere, symmetric oxygens are noted "O_s" and asymmetric oxygen are noted "O_a".

	Symmetric	**Asymmetric**	**Vertical**
E_{ads} (eV)	-0.74	-0.35	-0.19
d(O–O)^a (Å)	1.44	1.33	1.25
d(O–Mo)^a (Å)	1.94 / 1.94	2.13 / 2.15	2.02
q(Mo) (|e|)	2.68	2.50	2.41
q(O)^a (|e|)	-0.36	-0.21	+0.2 / -0.4
Spin on Mo	0	1.04	1.60
Spin on O^a	0	0.4 / 0.42	-0.74 / -0.55

Table 5.8 O_2 adsorption on the terminal oxygen vacancy. ^{a} "O" refers to the oxygen atoms of the O_2 molecule.

The adsorption is an exothermic process occurring preferably with the O_2 molecule parallel to the surface, its oxygen atoms above the symmetric oxygen centres since there is less steric hindrance compared to the asymmetric case. The atoms of the O_2 molecule are closer to Mo(1) when adsorbed in this way than for the alternatives with d(O–Mo)= 1.94 Å, while it is 2.14 Å on average for the asymmetric case, decreasing the interaction with Mo(1).

The vertical O_2 configuration has a dimer bond length of 1.25 Å similar to the gas phase molecule (1.24 Å) and the charge on the atom directly bound to Mo(1) is +0.2 |e|. In the symmetric configuration, O_2 is almost four times more strongly adsorbed (-0.74 eV) than the vertical case (-0.19 eV) and two times the asymmetric one (-0.35 eV). The O_2 dimer bond length is 1.44 Å in the symmetric configuration and 1.33 Å for the asymmetric one. This corresponds respectively to a paramagnetic superoxo state and a nonmagnetic peroxo state and is consistent with O_2 adsorption simulations on Pt.[58, 59] The O_2 molecule in the gas phase is in a triplet state with two unpaired electrons, the paramagnetic superoxo O_2^- is in a doublet state with one unpaired electrons and the nonmagnetic peroxo O_2^{2-} is in a singlet state with no unpaired electrons, as shown in figure 5.11. This assessment is further justified by the spin population analysis. There is no spin for the O_2^{2-} peroxo state (Mo^{+6}, singlet) while the spin on Mo(1) is +1 for the O_2^- superoxo state, implying a Mo^{+5} centre in a doublet state. The spin on the O_2 molecule is +0.82, in agreement with the idea of O_2 being a paramagnetic triplet species.

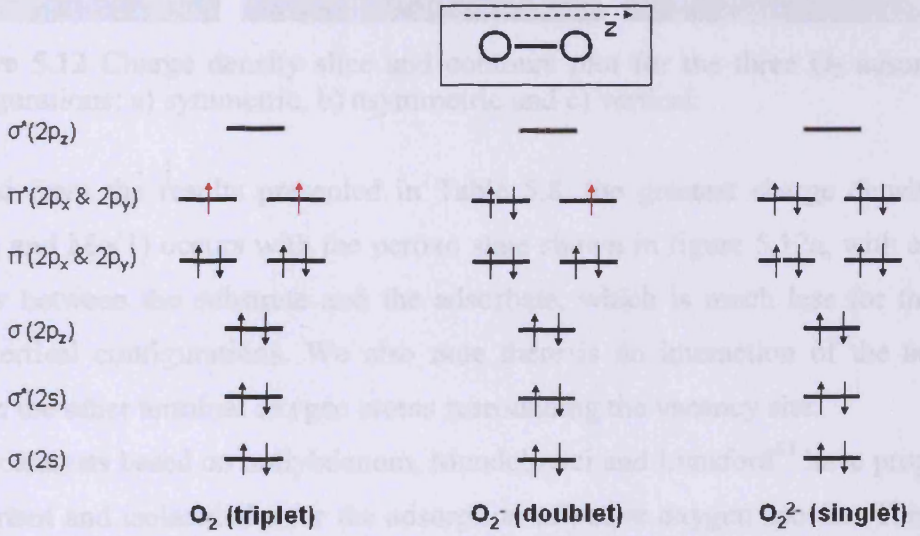

Figure 5.11 Molecular orbital diagrams for molecular oxygen in its triplet O_2, doublet O_2^- and singlet O_2^{2-} states. Only the valence electrons are shown and unpaired electrons are represented in red.

In recent work employing DFT cluster models[52], Witko *et al.* obtained an adsorption energy of -2.98 eV for O_2 on the terminal oxygen vacancy in a parallel orientation to the $MoO_3(010)$ surface. This is four times higher than our present result and may be explained by a possible rearrangement of the surface with DFT contributing to a lowering of the energy of the cluster reference state. Using VASP to study molecular precursors in the dissociative adsorption of O_2 on Pt(111), Eichler and Hafner[58] calculated adsorption energies ranging from -0.58 eV to -0.72 eV, in quantitative agreement with our results. Experimentally on Pt, the adsorption energy for the O_2^{2-} and O_2^- precursors has been estimated as -0.4 eV[60] and -0.5 eV[61] and this difference can be explained by the well known tendency of the LDA theory to overbind, not completely fixed by the GGA.

To better understand the adsorption mechanism, we plot the slice of the charge density for each adsorbate configuration in figure 5.12.

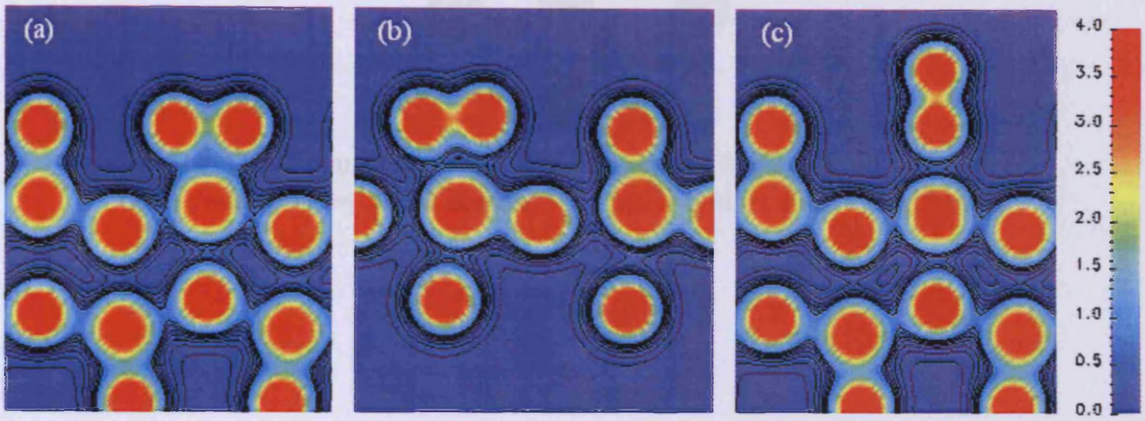

Figure 5.12 Charge density slice and contours plot for the three O_2 adsorption configurations: a) symmetric, b) asymmetric and c) vertical.

As expected from the results presented in Table 5.8, the greatest charge density build up between O_2 and Mo(1) occurs with the peroxo state shown in figure 5.12a, with a significant charge flow between the substrate and the adsorbate, which is much less for the superoxo state and vertical configurations. We also note there is no interaction of the adsorbed O_2 species with the other terminal oxygen atoms surrounding the vacancy site.

For catalysts based on molybdenum, Mendelovici and Lunsford[62] have proposed Mo^{+5} as an important and isolated site for the adsorption of active oxygen species. They proposed this Mo^{+5} centre should be a molybdenum atom missing a terminal oxygen. In a more recent work including EPR studies[3], Cadus *et al.* reported a coordinatively unsaturated form of Mo^{+5} site as the active site in Mg–Mo–O catalysts for oxidative dehydrogenation of propane. EPR is a very powerful technique indeed but can only give information on the spin state of an atom: the observed Mo^{+5} "active site" could actually be a molybdenum with O_2 adsorbed in a superoxo state. The molybdenum centre would then indeed be in a +5 oxidation state with a spin of one. We also notice the spin density obtained here (figure 5.13) is similar to that obtained for the superoxo species on Pt(111).[58] The orbital structure presented in figure 5.13

shows that on Mo, only one of d_{xz} and d_{yz} is now half filled to give the *d*-orbital shape, aligned with O_s. Also, we notice that the spin on O_2 is clearly in a π^* orbital.

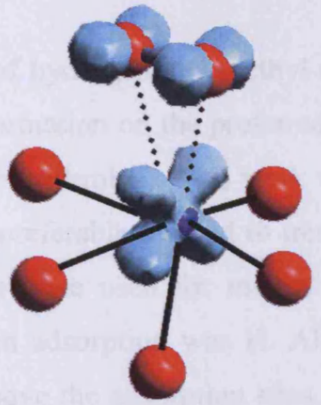

Figure 5.13 Isosurface of the spin density for the superoxo species O_2^-. Only part of the sytem is shown, *i.e.* Mo(1) and its direct neighbours.

5.5 H and CH_3 adsorption

Studying the adsorption of hydrogen and methyl at selected sites on the O_t-defective $MoO_3(010)$ surface provides information on the preferred configuration of products once the first C–H bond of methane has been broken. This work was first started with DFT and then DFT+U was applied as it is the preferable method to treat the terminal oxygen vacancy (see previous section). The reference state used for methyl adsorption was a gas phase CH_3• radical and the one for hydrogen adsorption was H. All calculations were set up with the adsorbates positioned directly above the adsorption sites. We compare our DFT+U and DFT results to Chen and co-workers' DFT results in table 5.9. The adsorption energies presented here using DFT+U are quite different from those reported by Chen *et al.*[55] using LDA DFT. Although different quantitatively, our DFT results are qualitatively similar to Chen and co-workers' DFT results: hydrogen is most strongly bound to the terminal oxygen and methyl is most strongly bound to molybdenum in the vacancy.

	Adsorption energies (eV)		
Adsorbate / site	**DFT+U**	**Theory[55] (DFT)**	**DFT**
H / Mo(1)	*-1.78*	-3.8	-3.32
H / O_t	-3.04	**-4.4**	**-3.84**
H / O_s	-2.73	-2.0	-3.61
H / O_a	**-3.28**	-4.1	-3.37
CH_3 / Mo(1)	*-1.67*	**-4.0**	**-3.21**
CH_3 / O_a	**-2.35**	-3.7	-2.58
CH_3 / O_t	-2.11	-3.9	-3.02

Table 5.9 Comparison of DFT and DFT+U adsorption energies for H and CH_3 adsorbed at different sites of the terminal oxygen defective $MoO_3(010)$ surface. Bold figures highlight the most favourable adsorption site in each case.

Chen *et al.* claim that after terminal oxygen removal, two vacancy-localized states appear: one Mo d_{xz} orbital in the band gap and one Mo d_{z^2} orbital in the conduction band. They explain that for hydrogen and methyl adsorption, the main interaction is through the Mo d_{z^2} orbital and that differences in bonding are expected because of the higher degree of localisation and directionality of the *d* orbitals. The directed orbitals for both Mo and methyl allow for better overlap than the hydrogen 1*s* orbital, the latter more strongly interacting with the terminal oxygen 2*p* orbitals.

However, we have previously demonstrated that after removal of a terminal oxygen, two unpaired electrons are localized on the molybdenum; pure DFT (as used by Chen *et al.*) failing to treat this case and wrongly delocalising the two electrons. By carefully analysing the spin population calculated by Gaussian03 for each orbital of Mo in the cluster model (section 5.4), we were able to assign these electrons to their respective orbitals. The two orbitals profiting from this electron localisation on Mo were found to be $4d_{xz}$ and $4d_{yz}$, with an α-spin population increase of 43 % and 56 % respectively, the increase for the $4d_{z^2}$ orbital being only 19 %. Finally, after terminal oxygen vacancy formation, $4d_{z^2}$ is 36% less populated than $4d_{yz}$ and 30 % less populated than $4d_{xz}$. We notice that these three orbitals were almost equally populated in bulk MoO_3. In Table 5.10 we summarise the results obtained from Gaussian03 using the Natural Atomic Orbital (NAO) scheme[63]. In a polyatomic molecule the NAOs (in contrast to natural orbitals that become delocalised over all nuclear centres) mostly retain once-centre character, and thus are optimal for describing the molecular electron density around each atomic centre.[64] We notice that the population in d_{xz} and d_{yz} is higher than in d_{z^2} as they are in orbitals with lower energy (Table 5.10).

NAO atomic orbital type	**α spin occupancy of the NAO**	**α spin orbital NAO energy** (eV)
d_{xz}	0.73	-0.259
	0.42	*-0.214*
d_{yz}	0.91	-0.291
	0.40	*-0.218*
d_{z^2}	0.47	-0.219
	0.38	*-0.218*

Table 5.10 α spin occupancy and orbital energy of the *d* type NAOs for molybdenum with (numbers in italic) and without O_t, as calculated by Gaussian03 and using the cluster model (figure 5.5a).

The interaction of any adsorbate with the d_{z^2} orbital is much less than quoted by Chen *et al.*, due to the preferential occupation of the $4d_{xz}$ and $4d_{yz}$ orbitals at the defect site. The $MoO_3(010)$ surface lies in the (x, y) plane, so the $4d_{xz}$ and $4d_{yz}$ orbitals cannot be expected to strongly interact with either the 1*s* or 2p_z orbitals of hydrogen and carbon atoms. The adsorption of H and CH_3 on the molybdenum will not be favoured and indeed, the adsorption energies obtained with DFT+U correlate this tendency (Table 5.9).

Finally, DFT+U reflects what was found experimentally by Queeney *et al.*[56, 65, 66], *i.e.* that methyl addition to Mo=O would lead to unstable binding. The calculated adsorption energy of CH_3 onto O_t is indeed 0.24 eV less than that of CH_3 onto O_a. DFT fails to reproduce this trend and actually favours the O_t site (Table 5.9). Methyl bound to open metal centres is also detected at low temperature but unlike CH_3 on oxygen atoms, it decomposes after heating to 500 K, showing that it is probably weakly bound compared to the oxygen sites.[56] Again, only DFT+U can reflect this experimental result, DFT giving the Mo metal centre as the site with the highest CH_3 adsorption energy.

Although there is strong evidence that methoxy binds at a high coordination site on oxygen-modified Mo(110), the exact structure of that site, which may be different from the methoxy adsorption sites on clean Mo(110), is not known.[66] In the rest of this section, we will present in detail the DFT+U results for H and CH_3 adsorption on the O_t defective MoO_3(010) surface.

5.5.1 H adsorption

Site	**E_{ads} (eV)**	**d(H–site) (Å)**	**q(H) (|e|)**	**q(site) (|e|)**	**q(Mo(1)) (|e|)**
Mo(1)	-1.78	1.70	-0.22	2.32	2.32
O_t	-3.04	0.98	-	-1.44	2.26
O_s	-2.73	0.99	-	-1.58	2.24
O_a	-3.28	0.98	-	-1.63	2.03

Table 5.11 Adsorption energy E_{ads}, distance to the adsorption site d(H–site) and Bader charges of the hydrogen atom, adsorption site and Mo(1) atom upon H adsorption. Three-dimensional representations are given in figure 5.14.

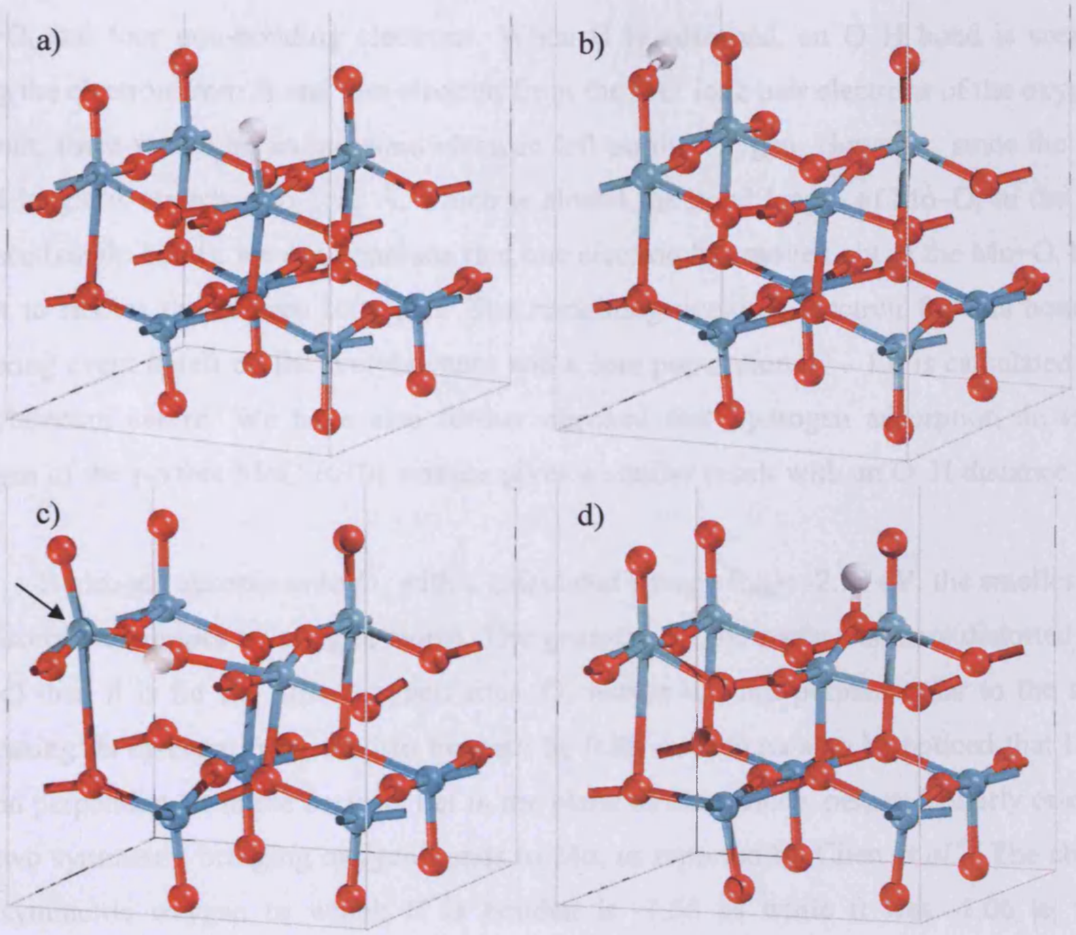

Figure 5.14 Adsorption geometries for a) H on Mo(1), b) H on O_t, c) H on O_s and d) H on O_a. The arrow in c) indicates the molybdenum atom with an extra spin due to H adsorption on O_s.

Hydrogen is least strongly bound over the terminal oxygen vacancy (-1.78 eV) and adopts the position of the previously removed terminal oxygen (figure 5.14a) with exactly the same bond length to the molybdenum (1.70 Å) while using DFT, Chen *et al.* report a shortening of the bond from 1.72 Å to 1.67 Å[55]. The hydrogen becomes negatively charged, -0.22 |e| (Table 5.11), the molybdenum acquires 0.15 electrons and has a spin population of ~ 1.0 compared to ~ 2.0 without H: one of the two electrons left in the vacancy after removal of the terminal oxygen has been used to create the Mo–H bond.

The binding of the H atom over the terminal oxygen is quite strong (E_{ads}= -3.04 eV) with a distance H–O similar to the other oxygen adsorption sites (~1.00 Å). However, the Mo–O_t bond length is increased from 1.70 Å to 1.92 Å upon hydrogen adsorption (figure 5.14b) and the charge on O_t becomes -1.44 |e| compared to -0.66 |e| without any adsorbate, representing a gain of 0.78 electrons. Furthermore, no Bader charge is found on H. Before H adsorption, O_t possesses six valence electrons: two shared with Mo to make the double bond

Mo=O_t and four non-bonding electrons. When H is adsorbed, an O–H bond is created by using the electron from H and one electron from the four lone pair electrons of the oxygen. As a result, there would be an unpaired electron left on the oxygen. However, since the Mo–O_t bond length is stretched to 1.92 Å, which is almost the bond length of Mo–O_s in the perfect surface (single bond), we can conclude that one electron has moved out of the Mo=O_t bond in order to reform the oxygen lone pair. The remaining unpaired electron for this bond order lowering event is left on the molybdenum and a spin population of ~ 1.0 is calculated for the molybdenum centre. We have also further checked that hydrogen adsorption on terminal oxygen of the perfect $MoO_3(010)$ surface gives a similar result with an O–H distance of 0.97 Å.

Hydrogen adsorbs onto O_s with a calculated energy E_{ads}= -2.73 eV, the smallest of the H adsorption energies on oxygen atoms. The geometry of the surface is more distorted (figure 5.14c) than it is for the other oxygen sites. O_s moves upward perpendicular to the surface, increasing its distance from the Mo beneath by 0.85 Å. It must also be noticed that H is not bound perpendicular to the surface, but in the plane of the surface, perpendicularly oriented to the two symmetric bridging oxygen bonds to Mo, as reported by Chen *et al.*[45] The charge of the symmetric oxygen to which H is bonded is -1.58 |e| while it was -1.06 |e| without adsorbate. As in the case of the adsorption on O_t, a spin population of ~ 1.0 is found on the molybdenum atom marked by an arrow in figure 5.14c. The unpaired electron left after the O–H bond formation is localised on this molybdenum and not the one missing a terminal oxygen as the latter is already reduced.

Finally, hydrogen is most strongly bound to the asymmetric oxygen (-3.28 eV) with the Mo–O_a bond length increasing from 1.80 Å for the defective surface to 2.13 Å and O_a to which H is bonded moved upward (figure 5.14d). This O_a atom acquires a charge of -1.63 |e| compared to -0.75 |e| without hydrogen, representing a gain of 0.88 electrons. The molybdenum atom at the vacancy site has also gained electrons (0.44) and now presents a spin population of 2.75, some spin (0.12) being also present on the other molybdenum connected to O_a. A similar effect is seen for CH_3 adsorption on O_a which we discuss in more detail in the next subsection.

5.5.2 CH_3 adsorption

Site	**E_{ads} (eV)**	**d(C–site) (Å)**	**q(C) (|e|)**	**q(site) (|e|)**	**q(Mo(1)) (|e|)**
Mo(1)	-1.67	2.15	-0.27	2.33	2.33
O_a	-2.35	1.43	0.80	-1.37	1.99
O_t	-2.11	1.43	0.60	-1.15	2.54

Table 5.12 Adsorption energy E_{ads}, distance to the adsorption site d(C–site) and Bader charges of the carbon atom, adsorption site and Mo(1) atom upon CH_3 adsorption. Three-dimensional representations are given in figures 5.15a, 5.16a and 5.17.

The methyl radical is less strongly bound to Mo(1) than hydrogen (-1.67 eV *vs.* -1.78 eV). The C–Mo distance is 2.15 Å and the C–H bond lengths are all 1.10 Å. The average Mo–C–H bond angle is 109.02°, which is close to the tetrahedral angle expected for sp^3 carbon. The carbon is negatively charged (-0.27 |e|) and the molybdenum has gained 0.14 electrons. The bonding mechanism is essentially the same as it was for H adsorption, with a spin population of ~ 1.0 on Mo(1). As methyl on Mo(1) will be one of the configurations involved with CH_4 activation (see section 5.6 for details), we plot the iso-surface and a slice of the charge density (figure 5.15) in order to better understand the interaction with the surface. The electron density accumulation between the substrate and the adsorbate is important (figure 5.15b) and is typical of a covalent bond, correlating the adsorption energy and the proposed adsorption mechanism. Compared to the vacancy without any adsorbate, the charge distribution on the molybdenum and oxygen centres (figure 5.15c) is more or less the same and CH_3 behaves like a terminal oxygen substitute. The shortest distance between a bridging oxygen and a methyl hydrogen is 2.49 Å, which cannot let us consider a "substantial" interaction and also suggests only minor steric repulsion between surface and H atoms.

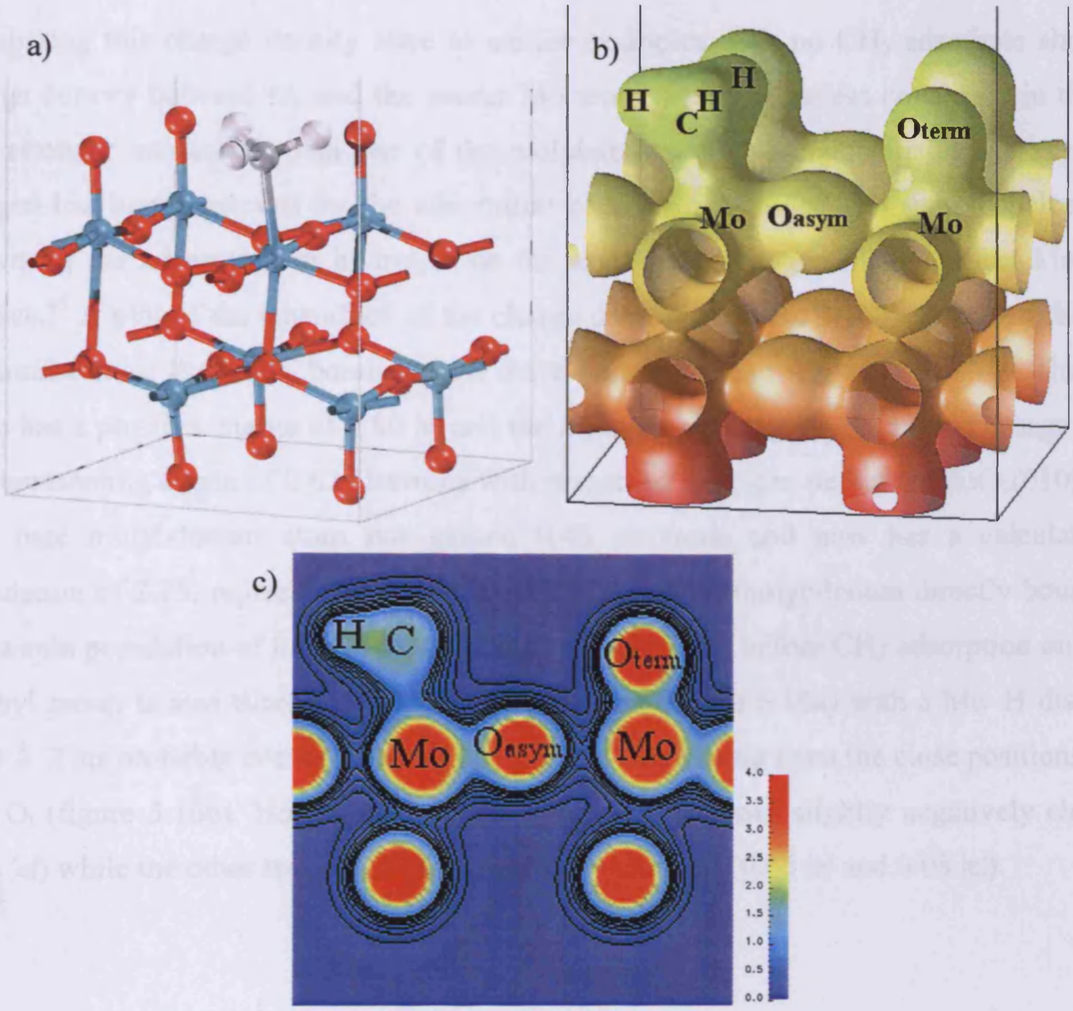

Figure 5.15 CH_3 adsorption on Mo(1) at the vacancy site: a) Geometry, with Mo in blue, O in read, C in grey and H in white, b) 0.3 $Å^{-3}$ electron density iso-surface and c) charge density slice and contours plot (drawn in intervals of 0.1 e $Å^{-3}$) where only one H of CH_3 is in the plane of slice.

In contrast to hydrogen, no energy minimum was found for the symmetric oxygen site and the methyl group moved to the molybdenum atom to become bound directly over Mo in the vacancy site.

Methyl most strongly binds over the asymmetric oxygen (E_{ads}= -2.35 eV) and is 0.68 eV more stable than over the terminal oxygen vacancy and 0.24 eV more stable than over the terminal oxygen. The C–O distance is 1.43 Å and the methyl pulls the asymmetric oxygen out of the surface by 0.25 Å (figure 5.16a), in close agreement with Chen *et al.*[55] who found a shift of 0.24 Å. As a result, O_a becomes more weakly bound to its two neighbouring molybdenum atoms with bond lengths differing by only 3 % (2.14 Å *vs.* 2.21 Å) while there was a difference of ~ 19 % without adsorbate (1.82 Å *vs.* 2.24 Å). The asymmetric character has been lost and a slice of the charge density (figure 5.16c) confirms this assertion.

Comparing this charge density slice to earlier examples with no CH_3 adsorbate shows less charge density between O_a and the nearer Mo atom, *i.e.* there is less covalency in the bond. The stronger interaction with one of the molybdenum atoms characterising the asymmetric oxygen has been removed by the adsorption of a methyl group. The same conclusion was drawn for the adsorption of hydrogen on the asymmetric oxygen of the perfect $MoO_3(010)$ surface.[45] A plot of the isosurface of the charge density in figure 5.16b shows that the charge accumulation at the C–O_a bond is even more important than it was for C–Mo. The carbon atom has a positive charge of 0.80 |e| and the asymmetric oxygen possesses a charge of -1.37 |e|, representing a gain of 0.62 electrons with respect to the clean defective $MoO_3(010)$ surface. The bare molybdenum atom has gained 0.48 electrons and now has a calculated spin population of 2.75, representing a gain of 0.79. The other molybdenum directly bound to O_a has a spin population of 0.11 while there was no spin at all before CH_3 adsorption on O_a. The methyl group is also tilted toward the molybdenum (figure 5.16a) with a Mo–H distance of 2.20 Å. This probably comes from the steric hindrance arising from the close positions of CH_3 and O_t (figure 5.16b). However, the hydrogen atom becomes slightly negatively charged (-0.13 |e|) while the other two are slightly positively charged (0.06 |e| and 0.08 |e|).

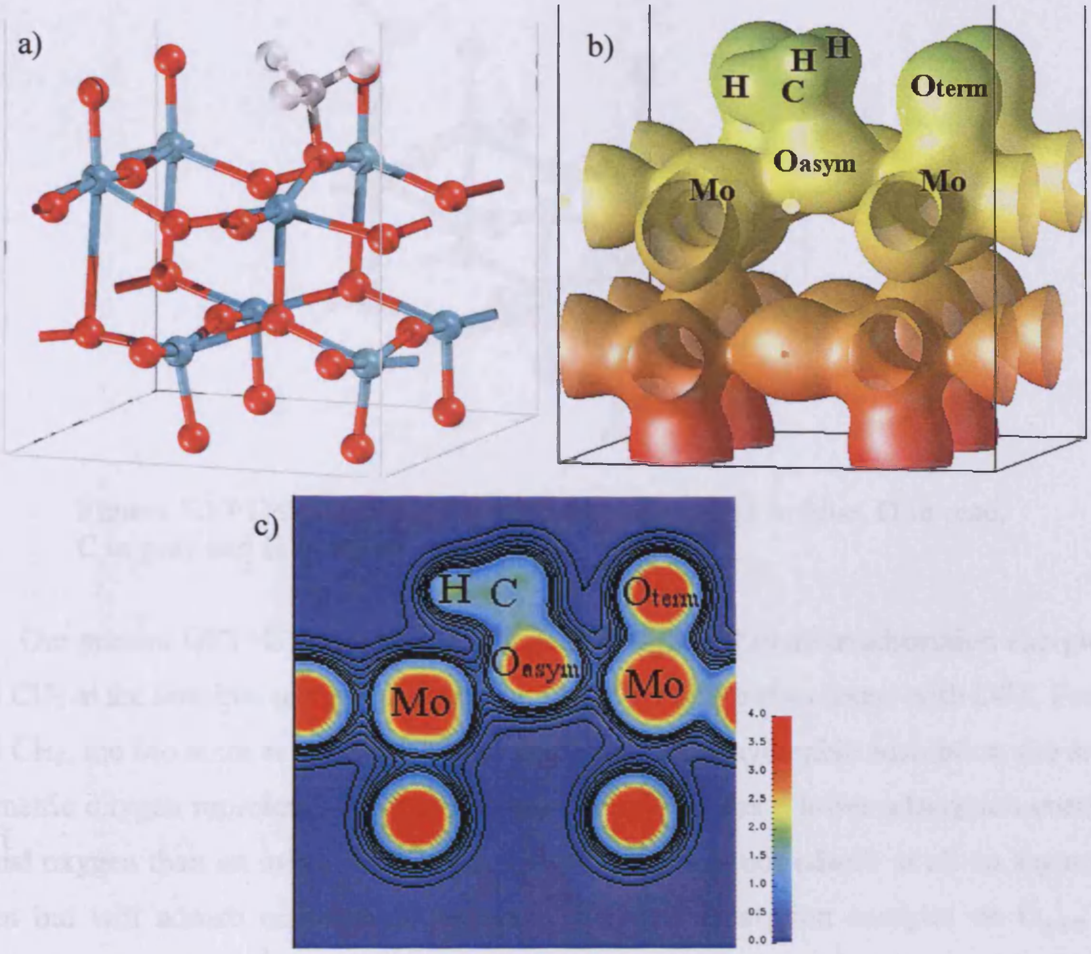
a)
b)
H
H H
C
Oterm
Oasym
Mo
Mo
c)
H C
Oterm
Oasym
Mo
Mo
4.0
3.5
3.0
2.5
2.0
1.5
1.0
0.5
0.0

Figure 5.16 CH_3 adsorption on O_a: a) Geometry, with Mo in blue, O in read, C in grey and H in white, b) 0.3 $Å^{-3}$ electron density iso-surface and c) charge density slice and contours plot (drawn in intervals of 0.1 e $Å^{-3}$) where only one H of CH_3 is in the plane of slice.

Finally, methyl binds to a terminal oxygen atom (figure 5.17) with an adsorption energy E_{ads}= -2.11 eV. The O_t–C distance is 1.43 Å, equal to the C–O_a bond length for the adsorption of CH_3 on O_a. Similar results are obtained for the adsorption of CH_3 on O_t of the perfect $MoO_3(010)$ surface, with an O_t–C distance of 1.45 Å.

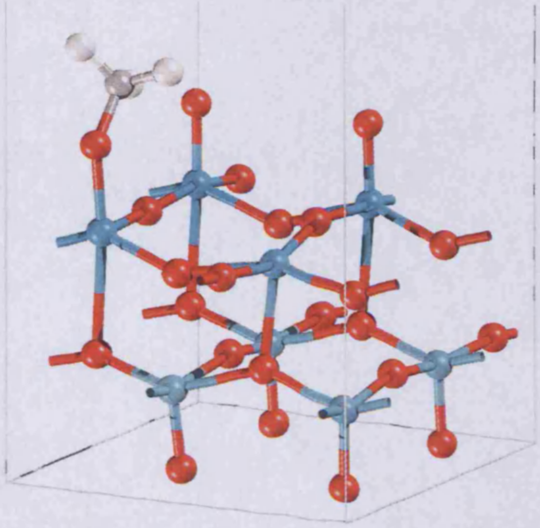

Figure 5.17 Geometry of CH_3 adsorbed on O_t. Mo in blue, O in read, C in grey and H in white

Our present DFT+U results clearly indicate a different trend in adsorption energies for H and CH_3 at the terminal oxygen vacancy $MoO_3(010)$ surface than found with DFT. For both H and CH_3, the Mo atom at the vacancy represents the least favourable adsorption site and the asymmetric oxygen represents the most favourable one. H has a lower adsorption energy on terminal oxygen than on symmetric oxygen, while CH_3 will not adsorb at all on asymmetric oxygen but will adsorb on terminal oxygen. The high adsorption energies on O_{asym} arise directly from the asymmetric character of this species, which is reduced once it adsorbs H or CH_3. Chen *et al.*[55] already mentioned that after adsorption on Mo, methyl could eventually move to another site under experimental conditions. Our DFT+U results show clearly that a high probability exists for this to happen, as the asymmetric oxygen site has higher adsorption energy.

5.5.3 CH_3 jump from Mo to O_a

We will focus here on methyl moving from Mo to O_a, as we will show in the next section that this is a way for the catalyst not to reach a dead end after methane activation. During the course of this study we found an intermediate geometry between CH_3 on Mo and CH_3 on O_a (figure 5.19a), with a relatively weak interaction with the surface (E_{ads}= -0.66 eV). No imaginary frequency characterising a TS was found and the intermediate is quite stable. The carbon is then almost equidistant from Mo (2.46 Å) and O_a (2.67 Å). The methyl has also flattened, but is not planar, and this reflects the weak interaction with the surface. In order to compare with other adsorption sites, we employ the improper angle of CH_3 shown in figure 5.18 and defined as the angle between the (H_1-C) line and the plane (H_2-C-H_3) with H_1 chosen as the nearest H neighbouring Mo(1). The improper dihedral angle is 149° for the intermediate (figure 5.18), 121° for the Mo adsorption site and 112° for the O_a adsorption site.

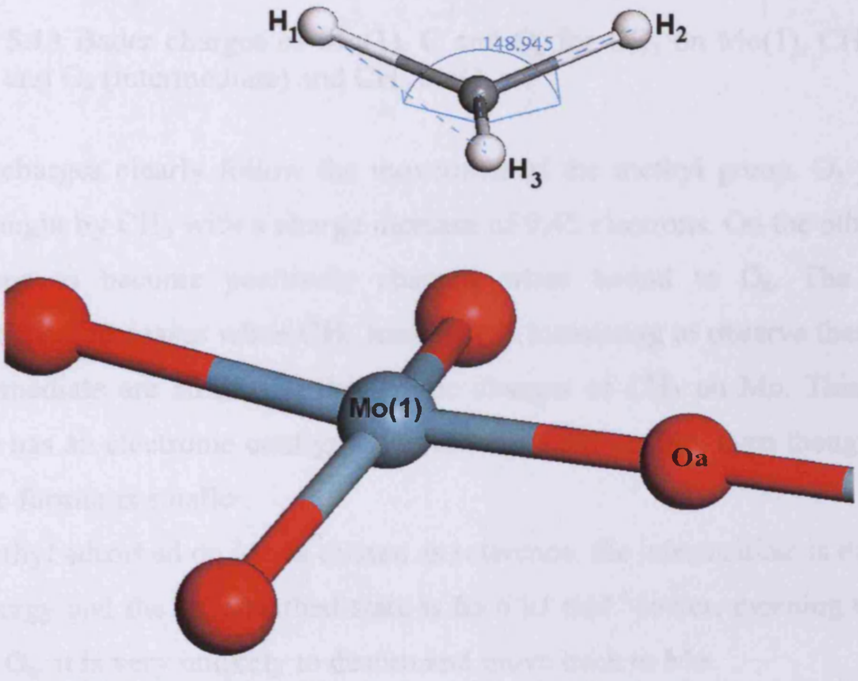

Figure 5.18 Improper dihedral angle of CH_3 in the intermediate geometry. Mo in blue, oxygen in red, carbon in grey and hydrogen in white.

The charge density between CH_3 and the surface is very small as shown by the charge density slice presented in figure 5.19c. A plot of the charge density isosurface in figure 5.19b also shows a deformation of the charge density surface around Mo, with the presence of a small peak in the density pointing toward the carbon of CH_3. The spin in the system is mostly localised on Mo with a spin population of 2.04 (the two unpaired electrons) but there are also small amounts present on both C (0.32) and O_a (0.12), showing that CH_3 is interacting with both Mo and O_a and not only Mo.

The Bader analysis gives atomic charges for Mo, C and O_a of 2.21, -0.23 and -0.99 |e| respectively. We compare in Table 5.13 the charges calculated for different adsorption sites, corresponding to the evolution of CH_3 from Mo to O_a.

Site for CH_3	q(Mo(1)) (|e|)	q(C) (|e|)	q(O_a) (|e|)
Mo(1)	2.33	-0.27	-0.92
Intermediate	2.21	-0.23	-0.99
O_a	1.99	0.80	-1.37

Table 5.13 Bader charges of Mo(1), C and O_a for CH_3 on Mo(1), CH_3 between Mo(1) and O_a (intermediate) and CH_3 on O_a.

The atomic charges clearly follow the movement of the methyl group. O_a profits from the electrons brought by CH_3 with a charge increase of 0.45 electrons. On the other hand, C loses 1.07 electrons to become positively charged when bound to O_a. The charge on the molybdenum also decreases when CH_3 leaves. It is interesting to observe that atomic charges for the intermediate are similar to the atomic charges of CH_3 on Mo. This shows that the intermediate has an electronic configuration close to CH_3 on Mo, even though the adsorption energy of the former is smaller.

If methyl adsorbed on Mo is chosen as reference, the intermediate is then 97.5 kJ mol^{-1} higher in energy and the O_a adsorbed state is 65.6 kJ mol^{-1} lower, meaning that once CH_3 is adsorbed on O_a, it is very unlikely to desorb and move back to Mo.

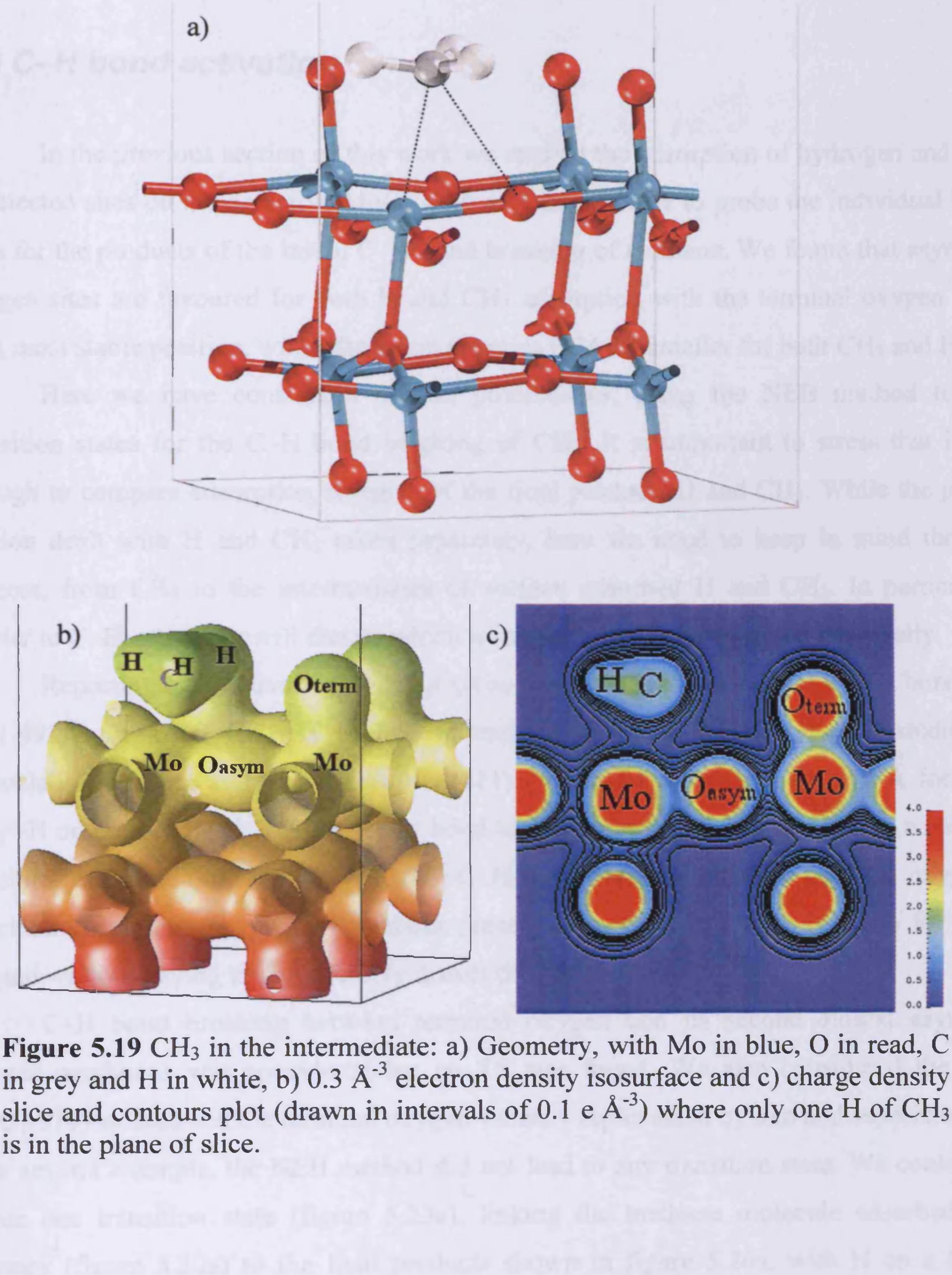
a)
b)
H
H
H
C
Oterm
Mo
Oasym
Mo
c)
H C
Oterm
Mo
Oasym
Mo
4.0
3.5
3.0
2.5
2.0
1.5
1.0
0.5
0.0

Figure 5.19 CH_3 in the intermediate: a) Geometry, with Mo in blue, O in read, C in grey and H in white, b) 0.3 $Å^{-3}$ electron density isosurface and c) charge density slice and contours plot (drawn in intervals of 0.1 e $Å^{-3}$) where only one H of CH_3 is in the plane of slice.

5.6 C–H bond activation

In the previous section of this work we studied the adsorption of hydrogen and methyl at selected sites on the defective $MoO_3(010)$ surface, in order to probe the individual binding sites for the products of the initial C–H bond breaking of methane. We found that asymmetric oxygen sites are favoured for both H and CH_3 adsorption with the terminal oxygen site the next most stable position, with adsorption energies 0.24 eV smaller for both CH_3 and H.

Here we have considered several possibilities, using the NEB method to locate transition states for the C–H bond breaking of CH_4. It is important to stress that it is not enough to compare adsorption energies of the final products H and CH_3. While the previous section dealt with H and CH_3 taken separately, here we need to keep in mind the whole process, from CH_4 to the intermediates of surface adsorbed H and CH_3. In particular the barrier to C–H activation will dictate which intermediates can be accessed kinetically.

Reporting CH_4 activation on Mo_3O_9 clusters, Fu *et al.*[67] calculated a C–H bond length of 1.49 Å for a TS $CH_3\cdots H$ leading to carbide products. Kratzer *et al.*[68] studied CH_4 dissociation on pure and gold-alloyed Ni(111) and found d(C–H) to be 1.59 Å for the TS $CH_3\cdots H$ on pure Ni(111). This expected bond length in the TS already eliminates a number of possible configurations. For example, the C–H bond breaking between terminal oxygen and its closest asymmetric oxygen neighbour presents too small an available space for C–H to expand without having to considerably distort the surface structure.

C–H bond breaking between terminal oxygen and its second closest asymmetric oxygen neighbour was considered but no TS was found. We also considered the perfect $MoO_3(010)$ surface and the terminal oxygen vacancy replenished by oxo and superoxo O_2, but after several attempts, the NEB method did not lead to any transition state. We could finally locate one transition state (figure 5.23a), linking the methane molecule adsorbed in the vacancy (figure 5.20a) to the final products shown in figure 5.26a, with H on a terminal oxygen and CH_3 on the bare molybdenum.

Calculating the activation energy of the C–H bond breaking in CH_4 was not the only important issue in this study. The nature of the bond cleavage is also important, *i.e.* if C–H bond cleavage is homolytic or heterolytic. In a homolytic cleavage the bond breaks evenly, *i.e.* each atom receives one electron. In a heterolytic cleavage the bond is broken unevenly giving both electrons to the most electronegative atom (forming an anion) and no electrons to the other atom (forming a cation). Homolytic cleavage forms free uncharged radicals, while heterolytic cleavage forms ions. As already discussed in subsection 2.1.3, both heterolytic and homolytic processes have been reported in the literature.

In this section we will give details on each stage of the C–H bond breaking: CH_4 adsorption, transition state $CH_3\cdots H$ and final products H and CH_3 on the surface. DFT+U will be used again throughout this section with the same parameters as the ones used for the defective surface in the previous sections. Finally, we will propose a complete mechanism for the C–H bond activation of CH_4 on defective $MoO_3(010)$, deciding on the homolytic/heterolytic issue and results will be discussed in term of activation energy.

5.6.1 CH_4 adsorption

Methane interacts very weakly with the surface (E_{ads}= -0.16 eV). This has already been reported experimentally and would be expected for such a weakly polar molecule.[56]
The "adsorbate" geometry is shown in figure 5.20a. We define H* as the hydrogen atom involved in the C–H bond breaking. The carbon atom is 2.80 Å away from Mo(1), and the hydrogen H* is 2.59 Å from its closest terminal oxygen O_t (Table 5.15). All the C–H bond lengths are almost equal (1.09-1.10 Å), showing again that there is little interaction between CH_4 and the surface. The methane molecule adopts a position minimising the steric hindrance and the angle marked φ in figure 5.20a is slightly increased to 113° compared to the calculated gas phase methane value of 109.5°. The weak interaction of CH_4 with Mo(1) is confirmed by the charge density slice in figure 5.20b. "Gas phase" means one molecule in same simulation box with same parameters.

Bader charge analysis results are presented in Table 5.14 for each stage of the C–H bond breaking.

	$q(O_t)$	$q(H^*)$	$q(C)$	$q(Mo(1))$
CH_4 free	-0.69	-0.03	+0.12	+2.27
CH_4 adsorbed	-0.73	-0.05	+0.02	+2.26
$CH_3 \cdots H$	-0.86	+0.46	-0.45	+2.47
CH_3, H	-1.48	-	-0.28	+2.35

Table 5.14 Bader charges at each stage of the C–H bond breaking of CH_4 on defective $MoO_3(010)$. "CH_4 free" corresponds to the methane molecule in the gas phase, "CH_4 adsorbed" is the methane molecule adsorbed in the vacancy on Mo(1), $CH_3 \cdots H$ is the transition state and "CH_3, H" corresponds to the end of the bond cleavage with H adsorbed on O_t and CH_3 adsorbed on Mo(1).

After CH_4 approaches, the terminal oxygen O_t and the molybdenum Mo(1) have gained a very small amount of electrons, 0.04 and 0.01 elections respectively. This correlates with the very small interaction of CH_4 with the surface.

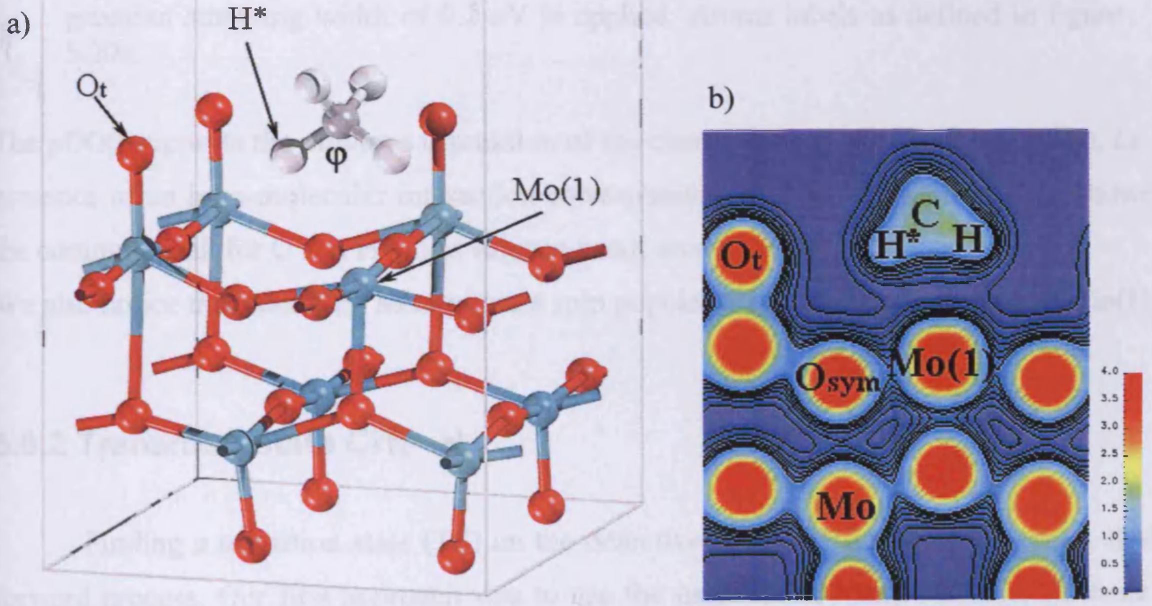

Figure 5.20 a) Geometry of the methane molecule adsorbed in the vacancy on Mo(1) with b) charge density slice and contour plot (drawn in intervals of 0.1 e Å^{-3}) where only two hydrogen atoms of CH_4 are in the plane of the slice. Molybdenum atoms in blue, oxygen in red, carbon in grey and hydrogen in white.

To understand the bonding mechanism involved and the intra- or extra-molecular interactions, we also plot the partial density of states (pDOS, figure 5.21).

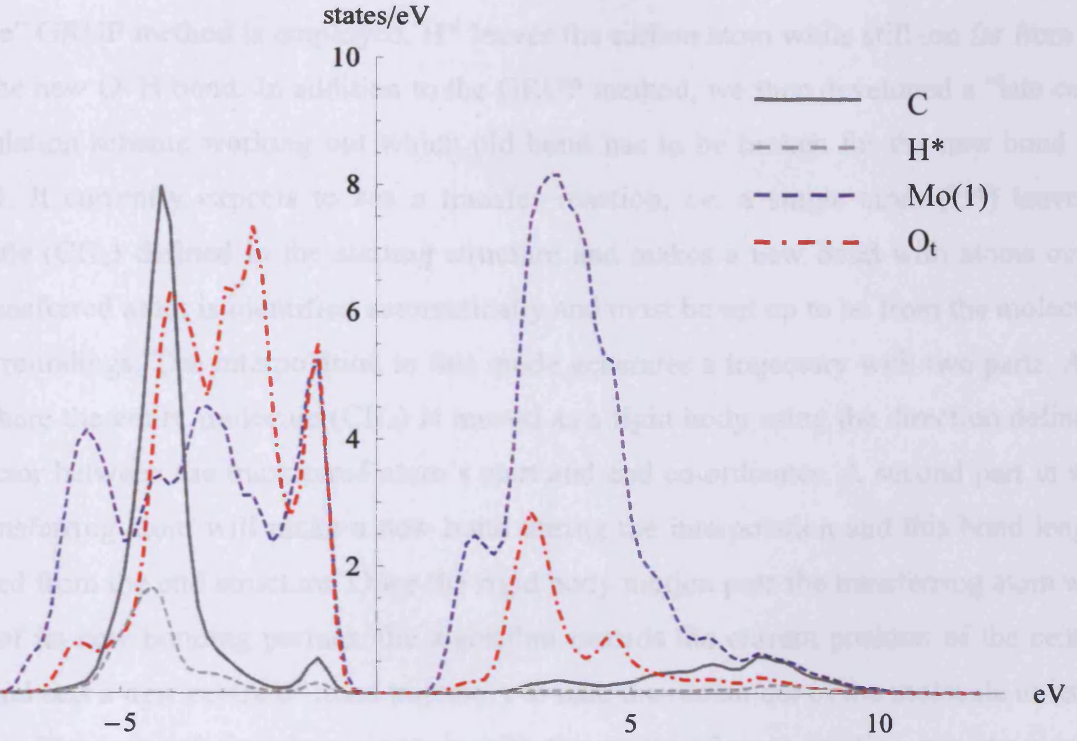

Figure 5.21 Partial density of states for CH_4 adsorbed in the vacancy on Mo(1). A gaussian smearing width of 0.2 eV is applied. Atoms labels as defined in figure 5.20a.

The pDOS supports the previous discussion of the charge density slice in figure 5.20b, *i.e.* the presence of an intra-molecular interaction corresponding to the C–H bond of CH_4, shown by the common peak for C and H in the valence band, around -4 eV.

We also notice that after CH_4 adsorption, a spin population of two is still present on Mo(1).

5.6.2 Transition state $CH_3\cdots H$

Finding a transition state (TS) on the defective $MoO_3(010)$ surface was not a straight forward process. Our first approach was to use the usual linear interpolation to generate the images required by the NEB method but problems arose with the bond lengths of CH_4 being foreshortened as a result of the interpolation process. We had to develop and apply a new interpolation scheme, the GRUP method, as explained in section 4.6. The carbon atom was defined as the centre of the group and only the hydrogen atoms of the methyl were included in the group, not H*.

However, the main difficulty was that when methane approaches the defect, it adsorbs quite far from the terminal oxygen O_t to which the hydrogen H* is added (figure 5.20a). If the "simple" GRUP method is employed, H* leaves the carbon atom while still too far from O_t to form the new O–H bond. In addition to the GRUP method, we then developed a "late centre" interpolation scheme working out which old bond has to be broken for the new bond to be formed. It currently expects to see a transfer reaction, *i.e.* a single atom (H*) leaves the molecule (CH_4) defined in the starting structure and makes a new bond with atoms outside. The transferred atom is identified automatically and must be set up to be from the molecule to the surroundings. The interpolation in this mode generates a trajectory with two parts. A first part where the entire molecule (CH_4) is moved as a rigid body using the direction defined by the vector between the transferred atom's start and end co-ordinates. A second part in which the transferring atom will make a new bond during the interpolation and this bond length is recorded from the end structure. Once the rigid body motion puts the transferring atom within range of its new bonding partner, the algorithm records the current position of the centre of mass and sets a new centre of mass trajectory to take the remainder of the molecule to its final position. The interpolation then proceeds with the centre of mass position moving along the new trajectory direction and the positions of the atoms in the molecule are moved smoothly to their final positions relative to the centre of mass.

Even employing the GRUP and "late centre" methods together, several NEB calculations with different steps size had to be run before any convergence was reached. The first successful NEB calculation included five images and only the last three were relevant, at d(C–H)= 1.16 Å, 1.83 Å and 2.17 Å with energies respectively equal to -223.407 eV, -223.168 eV and -223.632 eV. A second NEB calculation was performed using images number 3 and 5 of the previous run (d(C – H)= 1.16 Å and 2.17 Å) as start and end points for the interpolation of 8 images. This second NEB run also converged, giving the energy profile shown in figure 5.22. This time, the point {1.441 Å; -222.69955 eV} (corresponding to image number 4 of this NEB run) is expected to be close to the true TS. The eigenvector following method was applied to get closer to the TS and a quasi-Newton algorithm (IBRION= 1) was then employed to refine the guess, as detailed in section 4.6.

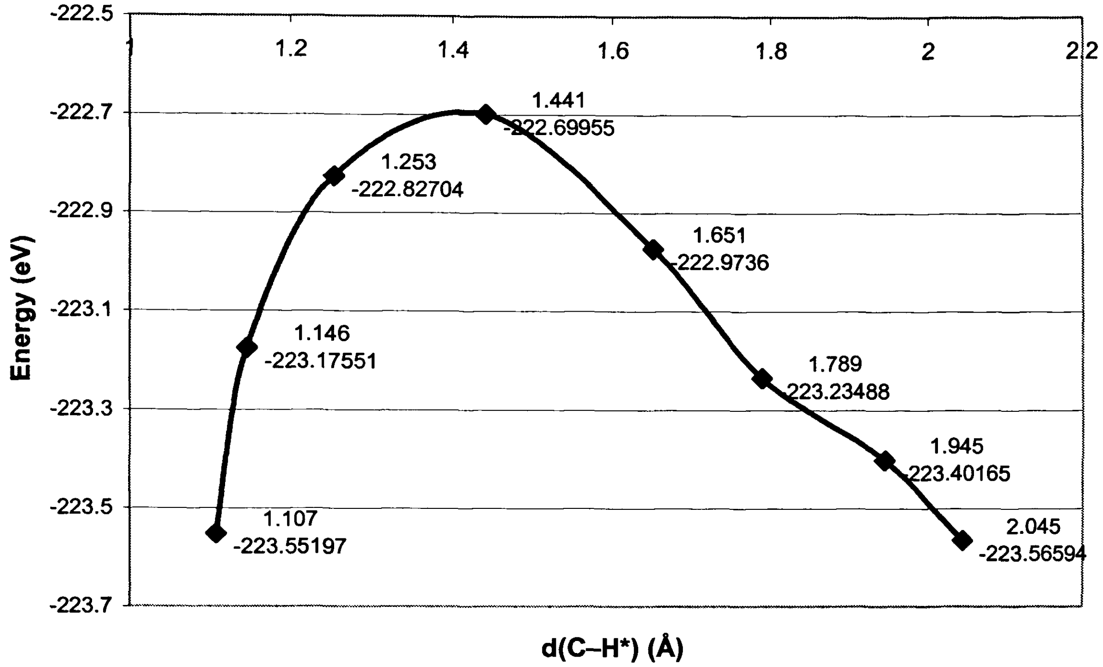

Figure 5.22 NEB (8 images) plot of the search of a TS for the C–H bond breaking of CH_4 on defective $MoO_3(010)$. The total energy of the system is plotted *vs.* the d(C–H*) bond length.

The transition state (figure 5.23a) was first obtained using DFT and then "re-calculated" using DFT+U. The DFT and the DFT+U transition states are very similar with almost identical geometrical properties and imaginary vibrational frequencies of 1187*i* cm^{-1} and 1095*i* cm^{-1} respectively.

To ensure that we have identified a true TS we verified that the forces in the system are converged to almost zero (0.01 eV $Å^{-1}$). The C–H bond length at the transition state geometry is 1.42 Å and is typical of C–H bond breaking in methane[67-69]. The d(O_t–H*) distance has decreased by 1.35 Å (Table 5.15) with O_t tilted toward H*. The carbon, which previously did not interact with the surface, is now closer to Mo(1) (2.36 Å) and there is a build up of charge density between them, as shown by the plot of the isosurface and slice of the charge density (figure 5.23b and c). This also shows the proton transfer from CH_4 to O_t as charge builds up between O_t and CH_3.

The Bader charge analysis provides important information on the nature of the transition state. The C–H bond becomes polarised with q(H*)= +0.46 |e| and q(C)= -0.45 |e| with an equal repartition of charges between C and H*, corresponding to q(H*)= +δ and q(C)= -δ. This suggests C–H bond cleavage is following $H_3C\text{–}H \rightarrow H_3C^- + H^+$, *i.e.* the bond cleavage is heterolytic. In order to assess whether this bond polarisation is solely due to the methane geometry in the TS structure, we perform a Bader charge analysis on CH_4 in the gas phase keeping the exact TS geometry but removing the $MoO_3(010)$ surface. The carbon atom then presents a charge $q(C)= -0.06\ |e|$ and the hydrogen atom a charge $q(H)= 0.07\ |e|$, which is at least six times less than the charges calculated for $CH_3\cdots H$ on the surface. This shows that $MoO_3(010)$ plays a significant role in the activation of methane and that the process is indeed heterolytic, following the scheme proposed in figure 5.28a. The EPR experiment by Kuba *et al.*[70] where it was shown that when *n*-pentane flowed through the tungstated zirconia catalyst, W^{5+} centres and organic radicals formed, has been thought of as lending a direct support to the homolytic mechanism. However, our conclusion of a heterolytic bond cleavage does not rule out their result as it is on a different system and our methyl anion is surface bound so we may form it and still generate radicals as $CH_3\bullet$ leaves the surface ($Mo^{+5}\rightarrow Mo^{+4}$).

We also notice that both O_t and Mo(1) gain some electrons (0.13 and 0.21 respectively).

	d(C–H*)	**d(O_t–H*)**	**d(C–Mo(1))**
CH_4 adsorbed	1.10	2.59	2.80
$CH_3\cdots H$	1.42	1.24	2.36
CH_3, H	2.73	0.98	2.15

Table 5.15 Selected bond lengths in Å for each stage of the C–H bond breaking of CH_4 on defective $MoO_3(010)$. "CH_4 adsorbed" is the methane molecule adsorbed in the vacancy on Mo(1), $CH_3\cdots H$ is the transition state and "CH_3, H" corresponds to the end of the bond cleavage with H adsorbed on O_t and CH_3 adsorbed on Mo(1).

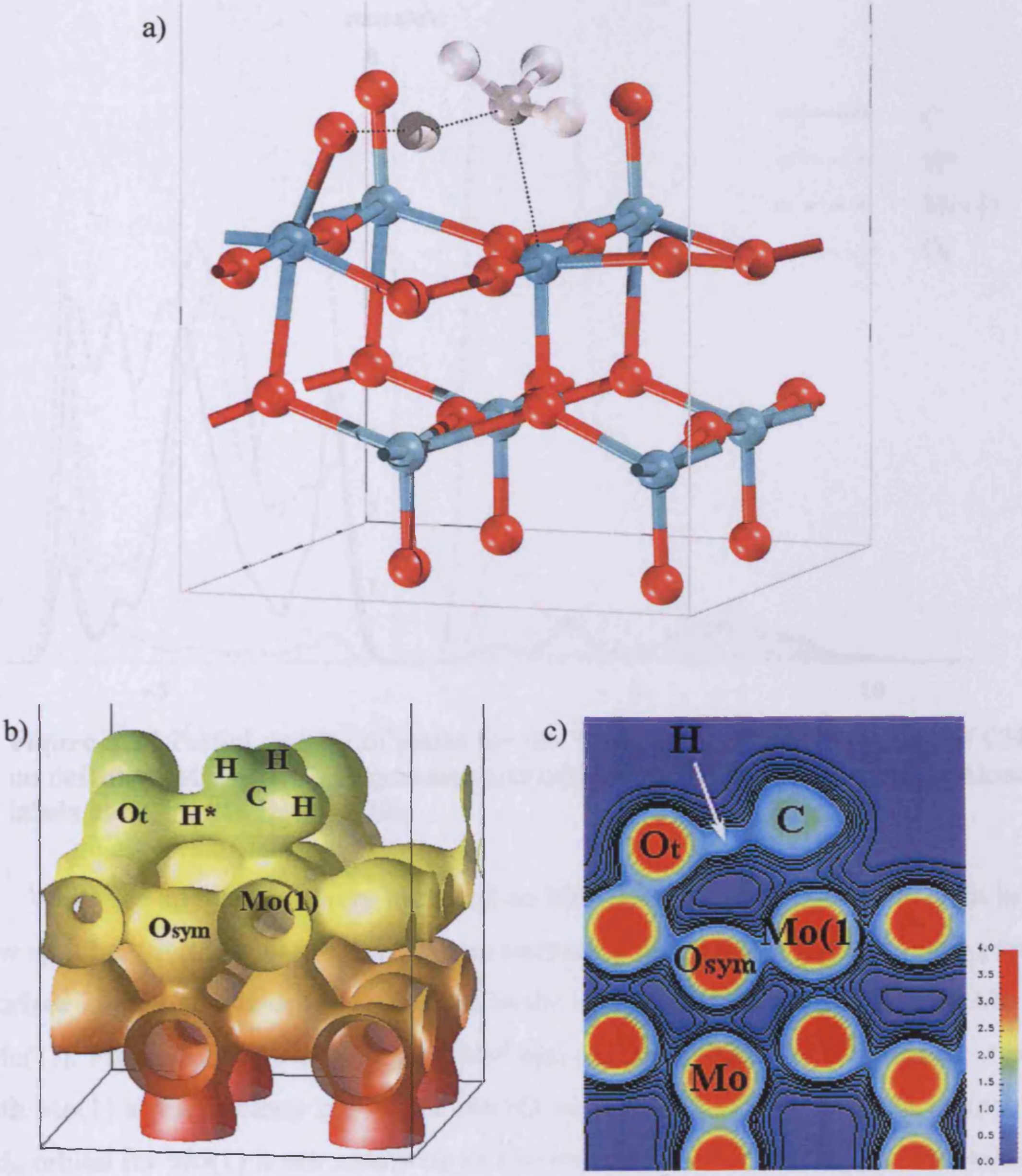

Figure 5.23 a) Geometry of the TS for the C–H bond breaking of CH_4 on defective $MoO_3(010)$, b) 0.3 Å^{-3} electron density iso-surface and c) charge density slice with contours plot (drawn in intervals of 0.1 e Å^{-3}) where no H of CH_3 is clearly in the plane of slice.

The pDOS for $CH_3 \cdots H$ (figure 5.24) is very different from that for CH_4. The most interesting feature is the appearance of a sharp peak at -6.8 eV in the valence band common to O_t, H* and C. This is a consequence of the charge flow between O* and CH_3, including H* in the middle (figure 5.23 b and c). There is also on overlap between C and Mo(1) but less pronounced, as expected from the charge density slice in figure 5.23c.

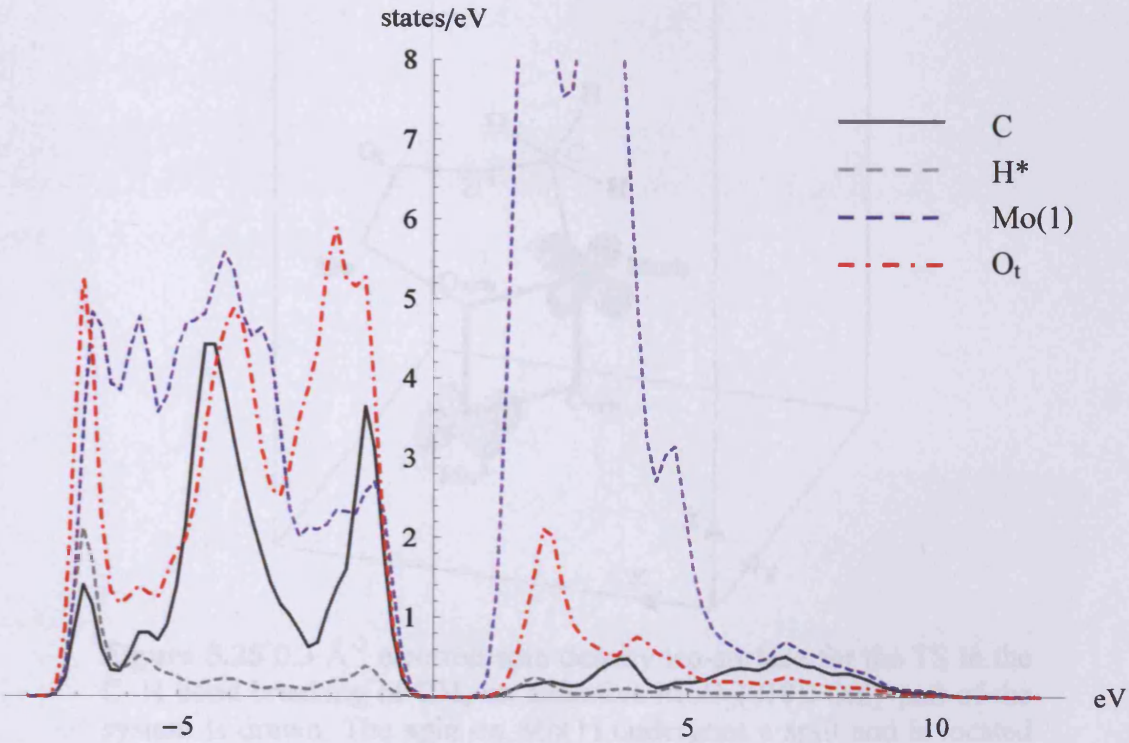

Figure 5.24 Partial density of states for the TS in the C–H bond breaking of CH_4 on defective $MoO_3(010)$. A gaussian smearing width of 0.2 eV is applied. Atoms labels as defined in figure 5.20a.

While the spin was entirely localised on Mo(1) for CH_4 adsorption, the spin in the TS is now split between Mo(1) and Mo^a as represented in figure 5.25, where the spin population iso-surface is plotted. The spin is localized in the molybdenum *d* orbitals (d_{xy} for Mo and d_{xz} for Mo(1)). Figure 5.25 shows well why Mo^a and not some other Mo is involved; it is linked to both Mo(1) at the vacancy and to the Mo=O_t receiving the H* atom by O_s oxygen atoms. The d_{xz} orbital for Mo(1) is not a surprise as it was already one of the orbitals populated by the excess spin for the clean O_t defective surface. The d_{xz} orbital has been populated at the expense of the d_{yz} because of the presence of the methane molecule in a position with two of its H atoms closest to the surface in the (*x*, *z*) plan. The other molybdenum atom has its d_{xy} orbital populated as it still has its terminal oxygen along the *z* axis. It proved impossible to obtain a spin completely localised on Mo(1) for the transition state, even employing higher convergence criterions for the SCF calculations.

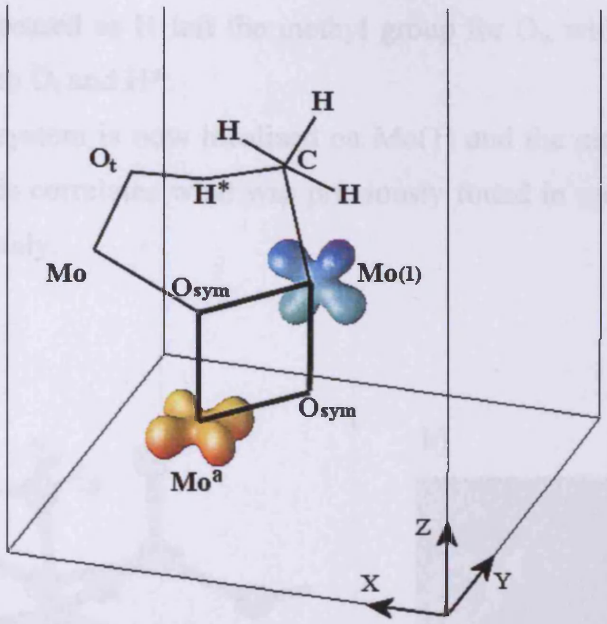

Figure 5.25 0.3 Å^{-3} electron spin density iso-surface for the TS in the C–H bond breaking of CH_4 on defective $MoO_3(010)$. Only part of the system is drawn. The spin on Mo(1) undergoes a split and is located half on Mo(1), half on Mo^a.

In section 5.4 we found that for the clean defective surface a split of the spin in two, between Mo(1) and Mo^a, corresponds to a less stable state than a spin entirely localised on Mo(1) (by 0.20 eV). However, for the transition state, the spin cannot stay on Mo(1) only as the results presented in section 5.5 clearly show a spin of one on Mo(1) for CH_3 adsorption in the vacancy. Also, upon hydrogen adsorption on O_t, a spin of ~ 1.0 was transferred to the molybdenum to which O_t is bound (Mo in figure 5.25).

5.6.3 CH_3 and H adsorbed on the surface

Finally, methyl and hydrogen end up bound to Mo(1) and O_t respectively, figure 5.26a, with d(O_t–H*)= 0.98 Å and d(Mo(1)–C)= 2.16 Å. Compared to CH_4 adsorbed on the surface, the terminal oxygen O_t has gained 0.75 electrons, the carbon has gained 0.30 electrons and the molybdenum has lost 0.08 electrons. The same values are found for H and CH_3 adsorbed separately in the previous section.

H and CH_3 are strongly bound to the surface, as already demonstrated previously and this is reflected by plotting both the slice of the charge density in figure 5.26b and the pDOS in figure 5.27. The pDOS exhibits a sharp peak around -1 eV in the valence band, common to C and Mo(1), while the peak characteristic of the C–H bond previously noticed for the starting point has disappeared as H left the methyl group for O_t, with a new peak appearing around -6 eV, common to O_t and H*.

The spin in the system is now localised on Mo(1) and the molybdenum to which the OH group is bound. This correlates what was previously found in section 5.5 for H and CH_3 adsorption, taken separately.

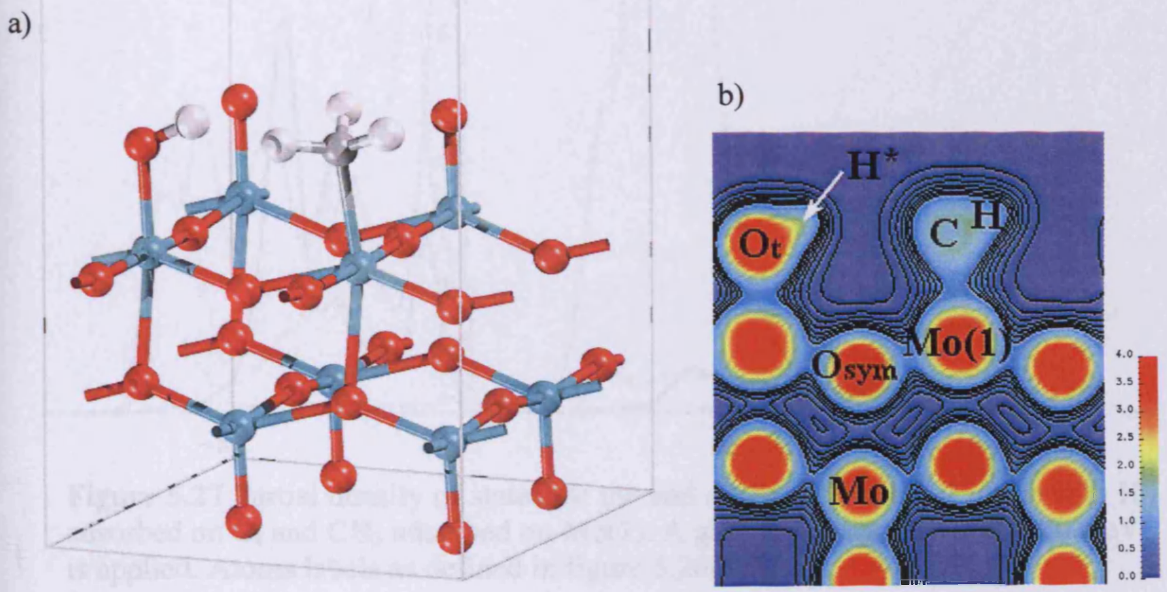

Figure 5.26 (a) Geometry for the end of the C–H bond cleavage with H adsorbed on O_t and CH_3 adsorbed on Mo(1), (b) 0.3 $Å^{-3}$ electron density iso-surface where only one H of CH_3 is in the plane of slice.

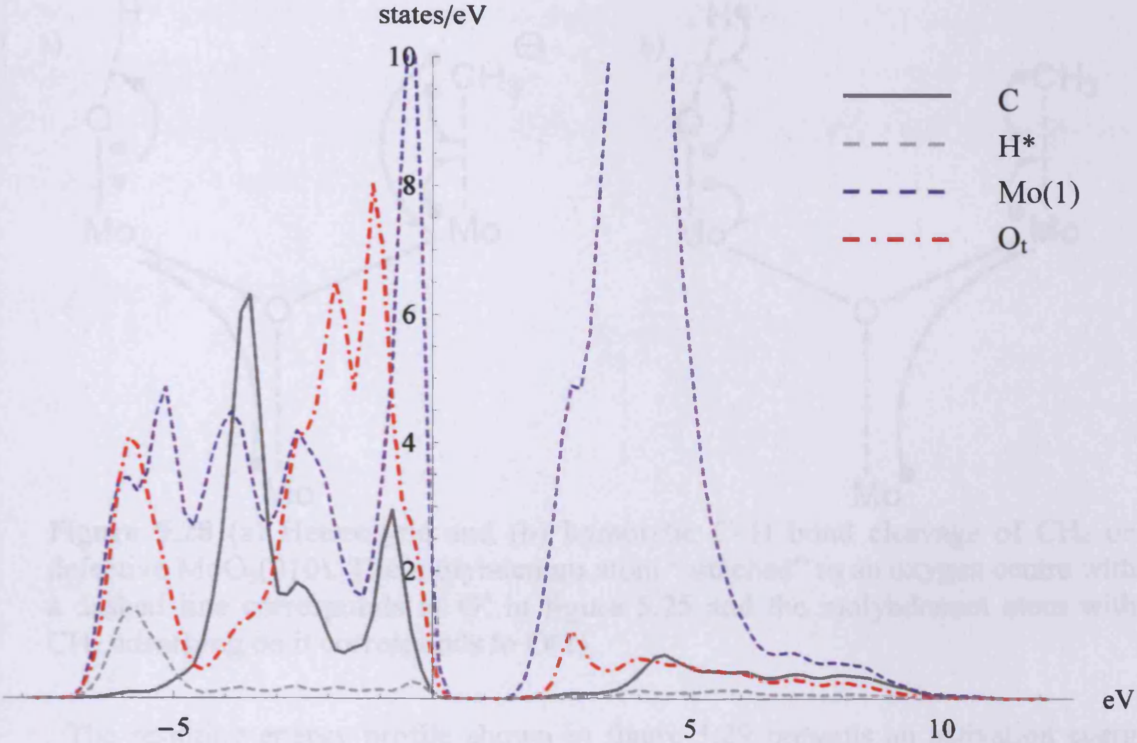

Figure 5.27 Partial density of states for the end of the C–H bond cleavage with H adsorbed on O_t and CH_3 adsorbed on Mo(1). A gaussian smearing width of 0.2 eV is applied. Atoms labels as defined in figure 5.20a.

5.6.4 Reaction mechanism and energy profile

Using the spin populations and Bader charges calculated during the C–H bond cleavage process, we are now able to propose a mechanism as we have shown that the charges exhibited by C and H* in the TS support a heterolytic (figure 5.28a) and not a homolytic cleavage (figure 5.28b). In our heterolytic scheme, a pair of electrons belonging to Mo=O_t is used to create the O_t–H bond since H* has lost its electron in the heterolytic bond cleavage. One electron of the $:CH_3^-$ carbanion is used together with the lone electron of Mo(1) to form the C–Mo(1) bond. The other electron of $:CH_3^-$ is then transferred to Mo(1) which then acquires a spin population of ~ 1.0 as calculated previously. Finally, the lone electron on Mo^a (figure 5.25), created as a result of a split of the spin on Mo(1) during CH_4 activation, is transferred to the molybdenum of Mo–O_t–H which then also acquires a spin of ~ 1.0 as found in the spin population calculated for the end point. In the homolytic cleavage (figure 5.28b), the electrons of the two radicals would be used to form the bonds.

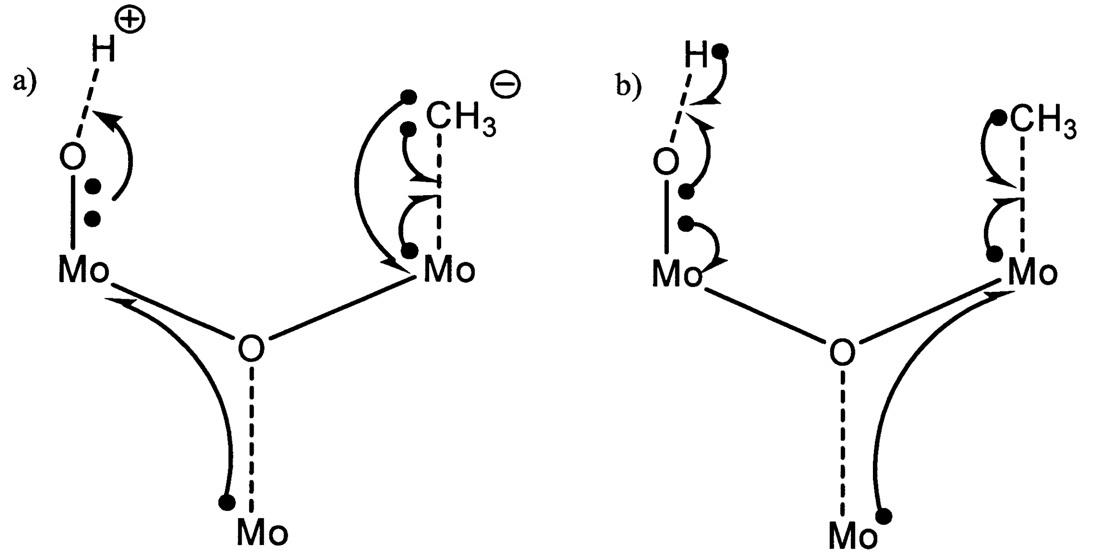

Figure 5.28 (a) Heterolytic and (b) homolytic C–H bond cleavage of CH_4 on defective $MoO_3(010)$. The molybdenum atom "attached" to an oxygen centre with a dashed line corresponds to O^a in figure 5.25 and the molybdenum atom with CH_3 adsorbing on it corresponds to O(1).

The resulting energy profile shown in figure 5.29 presents an activation energy E_a= 129.7 kJ mol^{-1} and a reaction energy ΔH= +28.8 kJ mol^{-1} (endothermic). If we consider the start point with split spin population, E_a is lowered by 19.1 kJ mol^{-1} to 110.6 kJ mol^{-1}. This is consistent with the fact that the split spin state of the perfect surface is 0.2 eV (19.3 kJ mol^{-1}) less stable, *i.e.* higher in energy, than the state with entirely localised spin on Mo(1).

There are no periodic DFT reports for methane activation on MoO_3 giving the activation energy for C–H bond breaking. In order to have an idea of what to expect, we can mention here that Ciobîcă *et al.* calculated an activation energy of 85 kJ mol^{-1} for methane decomposition over Ru(0001).[71] In an experimental study of methane activation by surface oxygen in calcia-stabilized zirconia, Mims observed an activation energy of 115 (± 15) kJ mol^{-1} at 500–750 K.[72] Finally, Ackermann *et al.*[73] reported on the interaction of methane with a Li^0 centre on MgO(100). Employing the Hartree–Fock scheme, they calculated an activation energy of about 116 kJ mol^{-1}, which compares with 109 kJ mol^{-1} calculated by both Børve *et al.*[74] and Orlando *et al.*[75], using respectively cluster models and periodic boundary techniques. Ackermann *et al.*[73] and Børve *et al.*[74] also calculated an endothermic reaction, with reaction energies of 24 kJ mol^{-1} and 37.6 kJ mol^{-1} respectively.

It is also worth emphasising the results recently presented by Fu *et al.*[67] Using a DFT cluster model of MoO_3 containing only 12 atoms, their lowest activation energy for C–H bond breaking of CH_4 was 188.1 kJ mol^{-1} and involved the formation of $\bullet CH_3$ radicals having to rebound quickly in order to form CH_3O. Their closest mechanism to the one we present here leads to a carbide product with an activation energy of 209.4 kJ mol^{-1} for C–H activation. We must also notice that the other proposed mechanisms by Fu *et al.*[67] all exhibit high activation energies ranging from 207.8 to 363.2 kJ mol^{-1}. Methane has a bond strength of 438.1 kJ mol^{-1} and so this second value indicates only a slight lowering of the barrier to C–H bond cleavage in the presence of the catalyst.

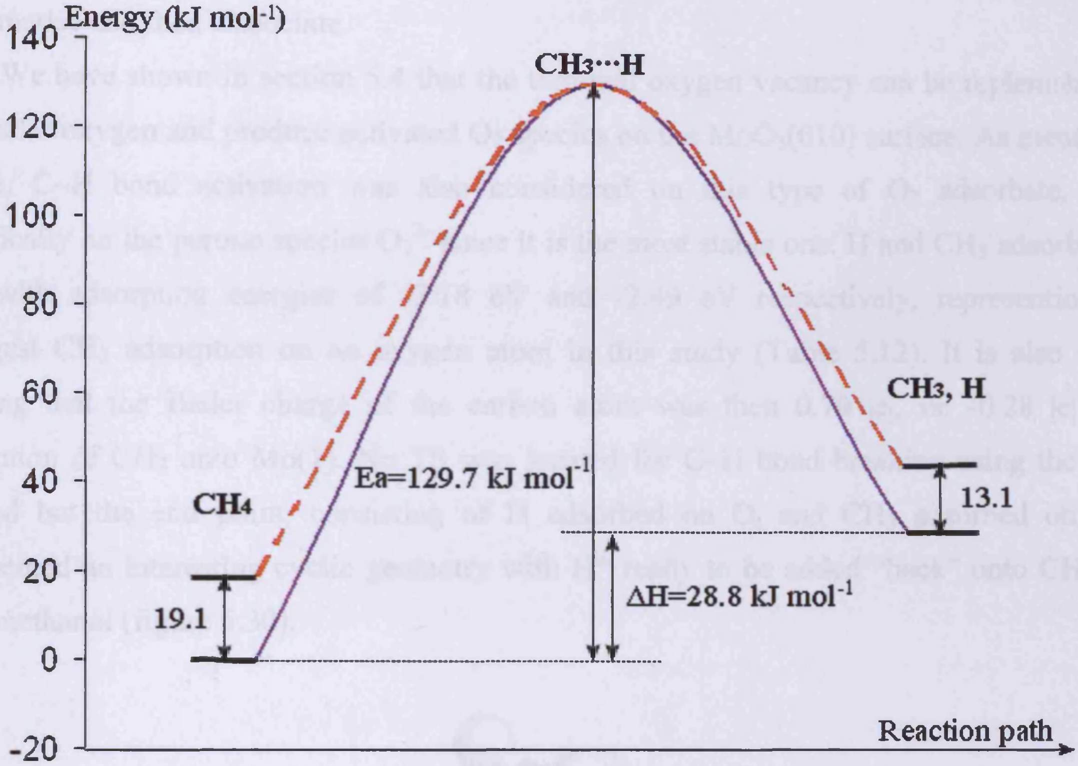

Figure 5.29 Energy profile for the C–H bond activation of CH_4 on defective $MoO_3(010)$. "CH_4" corresponds to the adsorbed state of methane on Mo(1) shown in figure 5.20a, $CH_3 \cdots H$ is the transition state (figure 5.23a) and "CH_3, H" corresponds to the end of the C–H bond cleavage shown in figure 5.26a. E_a is the activation energy and ΔH is the reaction energy. The dashed orange curve corresponds to the reaction occurring with the spin being split over Mo(1) and Mo^a during the whole process.

After C–H bond breaking, CH_3 ends up adsorbed on the molybdenum centre with considerable adsorption energy E_{ads}= -1.7 eV. As already pointed out by Chen *et al.*[55], this might represent a dead end for the catalyst as CH_3 will not go on to react further and form methanol, formaldehyde or C_2 compounds. However, the adsorption energy on molybdenum is the weakest of all and we have to consider that CH_3 might move on under experimental conditions and either supply radicals from the surface for gas phase chemistry or adsorb to asymmetric oxygen. We also previously found that methyl can move from the molybdenum to the asymmetric oxygen, involving a weakly bound intermediate (E_{ads}= -63.7 kJ mol^{-1}). We have to consider that during C–H bond breaking, the methyl group might reach this weakly bound state instead of being adsorbed directly onto the molybdenum. CH_3 could then easily desorb and react in the gas phase or most likely move to the asymmetric oxygen. The latter case is interesting from a chemical point view as the newly formed methoxy group could further loose one hydrogen on Mo and lead to formaldehyde or hydroxymethyl radical •CH_2OH. •CH_2OH is known as an important radical, able to dissociate and give H and CH_2O or isomerise and then dissociate.

We have shown in section 5.4 that the terminal oxygen vacancy can be replenished by molecular oxygen and produce activated O_2 species on the $MoO_3(010)$ surface. As mentioned earlier, C–H bond activation was also considered on this type of O_2 adsorbate, more specifically on the peroxo species O_2^{2-} since it is the most stable one. H and CH_3 adsorbed on O_2^{2-} with adsorption energies of -3.18 eV and -2.49 eV respectively, representing the strongest CH_3 adsorption on an oxygen atom in this study (Table 5.12). It is also worth noticing that the Bader charge of the carbon atom was then 0.70 |e|, *vs.* -0.28 |e| after adsorption of CH_3 onto Mo(1). No TS was located for C–H bond breaking using the NEB method but the end point, consisting of H adsorbed on O_t and CH_3 adsorbed on O_2^{2-}, represented an interesting cyclic geometry with H* ready to be added "back" onto CH_3O to form methanol (figure 5.30).

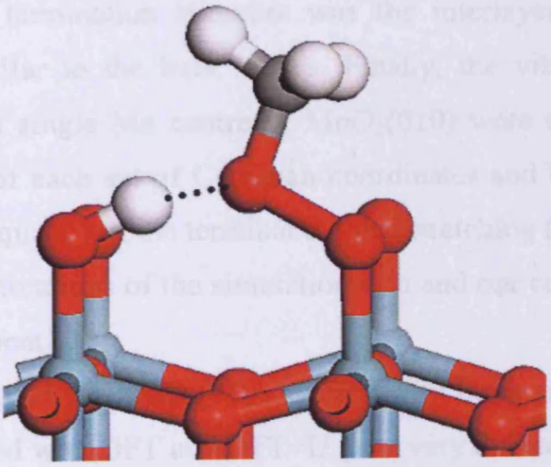

Figure 5.30 H and CH_3 after C–H bond breaking of CH_4 on activated O_2^{2-}.

5.7 Conclusions

Methane activation over the $MoO_3(010)$ surface was studied employing VASP with GGA DFT and GGA DFT+U with the PBE functional. The Nudged Elastic Band method was applied to locate a transition state for the C–H bond breaking.

Several properties were calculated, including the geometry of the structures, adsorption energies, Bader charges, electron and spin density iso-surfaces, densities of states and the vibrational frequencies of the systems.

In bulk MoO_3, the Mo=O_t bond exhibited a covalent nature and the anisotropy in bonding for Mo–O_a was confirmed by plotting the electron density iso-surface. Mo was found to interact with the O_s oxygen atom below it within a bilayer and this oxygen could then be thought of as 3-fold co-ordinated. The valence band region width (5.8 eV) and the band gap (2.1 eV) were calculated, the latter usually being underestimated by DFT. Metal orbitals were found to be present in the valence states, re-enforcing the idea that there is a significant covalent character in the bonding of this solid. The $MoO_3(010)$ surface was then considered, the (010) planes representing an easy cleavage direction for the material due to the weak interaction between bilayers. Upon geometry optimisation, the only significant change compared to the bulk termination structure was the interlayer O_s–Mo bond. The Bader charges were very similar to the bulk values. Finally, the vibrational frequencies of the oxygen atoms around a single Mo centre of $MoO_3(010)$ were computed by displacing the atoms in the direction of each set of Cartesian coordinates and building the Hessian matrix from the forces. The frequency of the terminal oxygen stretching (1023 cm^{-1}) was not strongly coupled to long range vibrations of the simulation slab and our computed results were also in agreement with experiment.

We then considered the $MoO_3(010)$ surface with oxygen vacancies. Defect energies and geometries computed with DFT and DFT+U gave very different results. DFT calculations produced a substantial surface relaxation upon terminal oxygen removal. It was found that DFT failed to localise the two electrons left on the molybdenum after removal of a terminal oxygen. Employing a cluster model with hybrid DFT and the PBE0 functional, we could confirm the localisation of the unpaired electrons on the molybdenum centre, with a calculated spin population of 1.96, indicating that the model represents a metal atom in the triplet state at the defect. This value was then used as reference data to obtain the U-J parameter required by VASP to perform the DFT+U calculations. A value of 6.3 eV gave a spin population of 1.96 on the molybdenum centre and was used throughout the DFT+U calculations. The terminal oxygen was found to be the easiest one to remove, with a defect energy of 4.85 eV, compared to the symmetric (6.86 eV) and asymmetric (5.34 eV) ones. The vibrational frequency for the stretch of the terminal oxygen atoms surrounding the defect was shifted to lower values (by 28 cm^{-1}) for the defective surface *vs.* the perfect surface, in agreement with previous experimental results. Finally, the local defect was re-oxidised with molecular oxygen. The adsorption was found to be exothermic and to occur preferably with the O_2 molecule parallel to the surface, its atoms being on top of the symmetric oxygen centres (E_{ads}= -0.74 eV, peroxo state). The O_2 bond length was then elongated to 1.44 Å and the molecular oxygen activated. The parallel orientation with O_2 on top of the asymmetric oxygen centres was somewhat less stable (E_{ads}= -0.35 eV) and represented a paramagnetic superoxo state with Mo^{5+} and a molecular oxygen dimer bond length of 1.33 Å.

The adsorption of hydrogen and methyl at selected sites on the terminal oxygen defective $MoO_3(010)$ surface was then studied. When employing DFT, H was most strongly adsorbed on the terminal oxygen and CH_3 on the vacancy. However, DFT+U calculations resulted in both H and CH_3 being more strongly adsorbed onto the asymmetric oxygen species. Localising the electrons on Mo, DFT+U increased the population of its $4d_{xz}$ and $4d_{yz}$ orbitals at the expense of the $4d_{z^2}$ orbital, resulting in a poor interaction with H and CH_3. Hydrogen adsorbed on molybdenum with E_{ads}= -1.78 eV, on the terminal oxygen with E_{ads}= -3.04 eV, on the symmetric oxygen with E_{ads}= -2.73 eV and on the asymmetric oxygen with E_{ads}= -3.28 eV. Methyl adsorbed on molybdenum with E_{ads}= -1.67 eV, on the asymmetric oxygen with E_{ads}= -2.35 eV and on the terminal oxygen with E_{ads}= -2.11 eV. Unlike hydrogen, no energy minimum was found for the symmetric oxygen site. O_a lost its asymmetric character upon adsorption of either H or CH_3 and this resulted in higher adsorption energies. A weakly bound state (E_{ads}= -0.66 eV) was found for CH_3 adsorbed between Mo and O_a and was proposed as an intermediate between CH_3 adsorbed on Mo and CH_3 adsorbed on O_a.

Finally, the C–H bond activation in methane was considered. CH_4 was found to adsorb very weakly at the vacancy site (E_{ads}= -0.16 eV). A transition state leading to C–H bond breaking between O_t and Mo was obtained using the NEB method. This TS was characterised by an imaginary frequency of 1095*i* cm^{-1} and forces converged to below 0.01 eV $Å^{-1}$. A C–H bond length of 1.42 Å was calculated and a polarisation of this bond occurred with q(H)= +0.46 |e| and q(C)= -0.45 |e|. A split of the spin was also observed with the bare molybdenum retaining only a spin population of one, the other spin being localised on a molybdenum centre of the bottom layer. Based on the transition state charges and the spin populations calculated throughout the process, a heterolytic process for the C–H bond cleavage was proposed. The carbanion $:CH_3^-$ is bound to the Mo(1) site and a proton transferred to a neighbouring O_t atom to form a hydroxyl group. An activation energy E_a= 129.7 kJ mol^{-1} was calculated and the reaction was found to be endothermic with a reaction energy ΔH= +28.8 kJ mol^{-1}. The activation energy was reduced by 19.1 kJ mol^{-1} when CH_4 adsorption occurred with the bare molybdenum having already lost half of its spin population, *i.e.* if the electronic re-arrangement occurs prior to the bond cleavage.

References

1. J. Haber and E. Lalik, *Catal. Today*, 1997, **33**, 119.
2. A. Bielanski and J. Haber, *Oxygen in Catalysis*. 1991, New York: Marcel Dekker.
3. L.E. Cadus, M.C. Abello, M.F. Gomez, and J.B. Rivarola, *Ind. Eng. Chem. Res.*, 1996, **35**, 14-18.
4. G. Pacchioni, F. Frigoli, and D. Ricci, *Phys. Rev. B*, 2000, **63**, 054102.
5. X.-B. Feng and N.M. Harrison, *Phys. Rev. B*, 2004, **69**, 132502.
6. M. Nolan, S. Grigoleit, D.C. Sayle, S.C. Parker, and G.W. Watson, *Surf. Sci.*, 2005, **576**, 217.
7. L.E. Cadus, M.F. Gomez, and M.C. Abello, *Catal. Lett.*, 1997, **43**, 229.
8. R. Schlögl, A. Knop-Gericke, M. Havecker, U. Wild, D. Frickel, T. Ressler, R.E. Jentoft, J. Wienold, G. Mestle, A. Blume, O. Timpe, and Y. Uchida, *Topics Catal.*, 2001, **15**, 219.
9. A. Magneli, *Nature*, 1950, **115**, 356.
10. E. Serwicka, *Crit. Rev. Surf. Sci.*, 1990, **1**, 27.
11. E. Serwicka, *J. Solid State Chem.*, 1984, **51**, 300.
12. M.R. Smith and U.S. Ozkan, *J. Catal.*, 1993, **142**, 226.
13. M.J.T. Frisch, G. W.; Schlegel, H. B.; Scuseria, G. E.; Robb, M. A.; Cheeseman, J. R.; Montgomery, Jr., J. A.; Vreven, T.; Kudin, K. N.; Burant, J. C.; Millam, J. M.; Iyengar, S. S.; Tomasi, J.; Barone, V.; Mennucci, B.; Cossi, M.; Scalmani, G.; Rega, N.; Petersson, G. A.; Nakatsuji, H.; Hada, M.; Ehara, M.; Toyota, K.; Fukuda, R.; Hasegawa, J.; Ishida, M.; Nakajima, T.; Honda, Y.; Kitao, O.; Nakai, H.; Klene, M.; Li, X.; Knox, J. E.; Hratchian, H. P.; Cross, J. B.; Bakken, V.; Adamo, C.; Jaramillo, J.; Gomperts, R.; Stratmann, R. E.; Yazyev, O.; Austin, A. J.; Cammi, R.; Pomelli, C.; Ochterski, J. W.; Ayala, P. Y.; Morokuma, K.; Voth, G. A.; Salvador, P.; Dannenberg, J. J.; Zakrzewski, V. G.; Dapprich, S.; Daniels, A. D.; Strain, M. C.; Farkas, O.; Malick, D. K.; Rabuck, A. D.; Raghavachari, K.; Foresman, J. B.; Ortiz, J. V.; Cui, Q.; Baboul, A. G.; Clifford, S.; Cioslowski, J.; Stefanov, B. B.; Liu, G.; Liashenko, A.; Piskorz, P.; Komaromi, I.; Martin, R. L.; Fox, D. J.; Keith, T.; Al-Laham, M. A.; Peng, C. Y.; Nanayakkara, A.; Challacombe, M.; Gill, P. M. W.; Johnson, B.; Chen, W.; Wong, M. W.; Gonzalez, C.; Pople, J. A. 2004, Gaussian, Inc.: Wallingford CT. p. Gaussian 03, Revision C.02.
14. H. Jönsson, G. Mills, and K.W. Jacobsen, *Classical and Quantum Dynamics in Condensed Phase Simulations*, ed. B.J. Berne, G. Ciccotti, and D.F. Coker. 1995, Singapore: World Scientific.
15. G. Mills and H. Jönsson, *Phys. Rev. Lett.*, 1995, **72**, 1124.
16. G. Mills, H. Jönsson, and G.K. Schenter, *Surf. Sci.*, 1995, **324**, 305.
17. G. Kresse and J. Hafner, *Phys. Rev. B*, 1993, **47**, 558.
18. G. Kresse and J. Hafner, *Phys. Rev. B*, 1994, **49**, 14251.
19. J.P. Perdew, K. Burke, and M. Ernzerhof, *Phys. Rev. Lett.*, 1996, **77**, 3865-3868.
20. J.P. Perdew, *Phys. Rev. B*, 1986, **33**, 8822.
21. S.H. Vosko, L. Wilk, and M. Nusair, *Can. J. Phys.*, 1980, **58**, 1200.
22. P.E. Blöchl, O. Jepsen, and O.K. Andersen, *Phys. Rev. B*, 1994, **49**, 16223-16233.
23. P.E. Blöchl, *Phys. Rev. B*, 1994, **50**, 17953.
24. G. Kresse and J. Joubert, *Phys. Rev. B*, 1999, **59**, 1758.
25. D. Vanderbilt, *Phys. Rev. B*, 1990, **13**, 5188.
26. H.J. Monkhorst and J.D. Pack, *Phys. Rev. B*, 1976, **13**, 5188.

27. S.L. Dudarev, G.A. Botton, S.Y. Savrasov, C.J. Humphreys, and A.P. Sutton, *Phys. Rev. B*, 1998, **57**, 1505.
28. R. Bader, *Atoms in Molecules: A quantum Theory*. 1990, New York: Oxford University Press.
29. G. Henkelman, A. Arnaldsson, and H. Jónsson, http://theory.cm.utexas.edu/bader/.
30. U.S. Ozkan and R.B. Watson, *Catal. Today*, 2005, **100**, 101-114.
31. M. Ernzerhof and G.E. Scuseria, *J. Chem. Phys.*, 1999, **110**, 5029-5036.
32. P.J. Hay and W.R. Wadt, *J. Chem. Phys.*, 1985, **82**, 270.
33. W.R. Wadt and P.J. Hay, *J. Chem. Phys.*, 1985, **82**, 284.
34. R. Ditchfield, W.J. Hehre, and J.A. Pople, *J. Chem. Phys.*, 1971, **54**, 724.
35. W.J. Hehre, R. Ditchfield, and J.A. Pople, *J. Chem. Phys.*, 1972, **56**, 2257.
36. P.C. Hariharan and J.A. Pople, *Mol. Phys.*, 1974, **27**, 209.
37. M.S. Gordon, *Chem. Phys. Lett.*, 1980, **76**, 163.
38. P.C. Hariharan and J.A. Pople, *Theo. Chim. Acta.*, 1973, **28**, 213.
39. J.-P. Blaudeau, M.P. McGrath, L.A. Curtiss, and L. Radom, *J. Chem. Phys.*, 1997, **107**, 5016.
40. M.M. Francl, W.J. Pietro, W.J. Hehre, J.S. Binkley, D.J. DeFrees, J.A. Pople, and M.S. Gordon, *J. Chem. Phys.*, 1982, **77**, 3654.
41. R.C. Binning and L.A. Curtiss, *J. Comp. Chem.*, 1990, **11**, 1206.
42. V.A. Rassolov, J.A. Pople, M.A. Ratner, and T.L. Windus, *J. Chem. Phys.*, 1998, **109**, 1223.
43. V.A. Rassolov, M.A. Ratner, J.A. Pople, P.C. Redfern, and L.A. Curtiss, *J. Comp. Chem.*, 2001, **22**, 976.
44. F. Corà, A. Patel, N.M. Harrison, R. Dovesi, and C.R.A. Catlow, *J. Mater. Chem.*, 1997, **7**, 959.
45. M. Chen, U.V. Waghmare, C.M. Friend, and E. Kaxiras, *J. Chem. Phys.*, 1998, **109**, 6854-6860.
46. L. Kihlborg, *Ark. Kemi*, 1963, **21**, 357-364.
47. O. Krylov, *Catalysis by Non-Metals*. 1980, New York: Academic Press.
48. R. Erre, M.H. Legay, and J.J. Fropiat, *Surf. Sci.*, 1983, **127**, 69.
49. M. Hybertsen and S.G. Louie, *Comments Condens. Matter Phys.*, 1987, **13**, 5.
50. R. Tokarz-Sobieraj, K. Hermann, M. Witko, A. Blume, G. Mestle, and R. Schlögl, *Surf. Sci.*, 2001, **489**, 107-125.
51. I.R. Beattie and T.R. Gilson, *J. Chem. Soc. A*, 1969, 2322-2327.
52. M. Witko and R. Tokarz-Sobieraj, *Catal. Today*, 2004, **91-92**, 171-176.
53. A. Michalak, K. Hermann, and M. Witko, *Surf. Sci.*, 1996, **366**, 323-336.
54. K. Hermann, M. Witko, and A. Michalak, *Catal. Today*, 1999, **50**, 567-577.
55. M. Chen, C.M. Friend, and E. Kaxiras, *J. Am. Chem. Soc.*, 2001, **123**, 2224-2230.
56. K.T. Queeney and C.M. Friend, *J. Phys. Chem. B*, 2000, **104**, 409-415.
57. K.T. Queeney and C.M. Friend, *J. Phys. Chem. B*, 1998, **102**, 5178-5181.
58. A. Eichler and J. Hafner, *Phys. Rev. Lett.*, 1997, **79**, 4481.
59. M.-L. Bocquet, J. Cerda, and P. Sautet, *Phys. Rev. B*, 1999, **59**, 15437.
60. J.L. Gland, B.A. Sexton, and G.B. Fisher, *Surf. Sci.*, 1980, **95**, 587.
61. S. Lehwald, H. Ihbach, and H. Steininger, *Surf. Sci.*, 1982, **117**, 342.
62. L. Mendelovici and J.H. Lunsford, *J. Catal.*, 1985, **94**, 37-50.
63. A.E. Reed and F. Weinhold, *J. Chem. Phys.*, 1983, **78**, 4066.
64. A.E. Reed and F. Weinhold, *J. Chem. Phys.*, 1985, **83**, 1736-1740.
65. K.T. Queeney, D.A. Chen, and C.M. Friend, *J. Am. Chem. Soc.*, 1997, **119**, 6945-6946.
66. K.T. Queeney and C.M. Friend, *J. Chem. Phys.*, 1998, **109**, 6067-6074.
67. G. Fu, X. Xu, X. Lu, and H. Wan, *J. Am. Chem. Soc.*, 2005, **127**, 3989-3996.

68. P. Kratzer, B. Hammer, and J.K. Nørskov, *J. Chem. Phys.*, 1996, **105**, 5595-5604.
69. J. Westerberg and M.R.A. Blomberg, *J. Phys. Chem. A*, 1998, **102**, 7303-7307.
70. S. Kuba, P.C. Heydorn, R.K. Grasselli, B.C. Gates, M. Che, and H. Knözinger, *Phys. Chem. Chem. Phys.*, 2001, **3**, 146-154.
71. I.M. Ciobîca, F. Frechard, R.A. van Santen, A.W. Kleyn, and J. Hafner, *J. Phys. Chem. B*, 2000, **104**, 3364-3369.
72. C. Mims, *Catal. Lett.*, 2000, **68**, 203-208.
73. L. Ackermann, J.D. Gale, and C.R.A. Catlow, *J. Phys. Chem. B*, 1997, **101**, 10028-10034.
74. K.J. Børve and L.G.M. Petterson, *J. Phys. Chem.*, 1991, **95**, 7401-7405.
75. R. Orlando, F. Corà, R. Millini, G. Perego, and R. Dovesi, *J. Chem. Phys.*, 1996, **105**, 8437.

Chapter 6

Gold adsorption and catalysis on magnesia

This chapter will present the results obtained for gold adsorption and catalysis on magnesia. The first two sections will introduce the subject and give the computational details employed. Adsorption of gold on perfect/defective MgO(001) and kinked MgO(1 3 12) surfaces will then be reported. Finally, the influence of gold oxidation state on CO adsorption will be studied.

6.1 Introduction

Great interest has been shown in recent years in gold catalysts, due to their high catalytic activity at low temperatures in a number of different important reactions which produced a large amount of work devoted to analysing the different factors controlling the activity of gold catalysts (*cf.* section 2.2). The most important appear to be the gold particle size and the nature of the support. However, it is not completely clear if the observed differences are simply related to the concentration of special, uncoordinated surface sites on the Au clusters, or also to electronic and chemical modifications of the adsorption sites by interaction with the different supports.

Gold clusters can be supported on a variety of metal oxides, the TiO_2 system being one of the most studied, including results from both experimental and theoretical sides. Lopez and Nørskov in a periodic DFT study[1] have shown that bonding at the Au/TiO_2(110) interface depends strongly on the Au coverage and that the strong interaction between gold and rutile TiO_2(110) surface does not exist for defect free supports.

More recently, again with a periodic DFT model, Lopez *et al.*[2] reported that gold particles do not bind to a perfect TiO_2 surface but have a binding energy of about 1.6 eV per defect on an oxygen vacancy.

Vijay *et al.*[3] argued that the binding of Au on the reduced TiO_2(110) surface involves a substantial charge transfer to gold and that this will affect the chemistry in which Au will engage, by making the gold clusters negatively charged.

Still on rutile $TiO_2(110)$ and using scanning tunnelling microscopy (STM) with DFT calculations, Wahlström *et al.*[4] found that bridging oxygen vacancies are the active nucleation sites for Au clusters. They showed both experimentally and theoretically that a single oxygen vacancy can bind three Au atoms on average.

Understanding the function of supported metal catalysts at the atomic level is a difficult task given the temperatures and pressures at which such catalysts are operated and the complexity of the catalyst itself. Computational chemistry can then prove very useful in studying the adsorption/nucleation mechanism, including detailed results on the electronic properties of the system or adsorption energies and vibrational frequencies of adsorbed probe molecules such as CO. However, molecular complexity does affect the computational chemist probably more than it does the experimentalist. This is why most work has focused on MgO as a support due to its relative simplicity and stability. Consequently a number of studies have been carried out on the MgO(001) surface.

For small size-selected clusters, Heiz *et al.* have reported that oxygen vacancy point defects on MgO are crucial for the nucleation of active Au clusters[5, 6].

Wallace et al.[7] demonstrated experimentally that surface defects are a key to the nucleation, growth, and stability of metal clusters on metal oxide surfaces.

In a study of the adsorption of Au on O-deficient MgO(001) surface, Yang *et al.*[8] found that the binding of Au on the ideal MgO(001) surface is very weak (E_{ads}= -0.13 eV) while Au adatoms prefer the oxygen vacancy sites with a strongly enhanced adsorption energy of -1.93 eV. Yudanov *et al.* also determined that Cu, Ag and Au exhibit very weak MgO/metal binding.[9]

These studies point out that the interaction of gold with MgO is due to polarization and dispersion with little mixing with the substrate orbitals and is consistent with the fact that MgO is a wide gap insulator.

However, Molina and Hammer[10] reported periodic DFT results on the CO oxidation on Au_{34} nanoparticles supported on perfect MgO (100) with an adsorption energy of -0.88 eV for a single gold atom on oxygen centres of MgO(001). The latter result cannot be considered as purely due to dispersion and polarization.

A detailed understanding of the Au_N/MgO(001) system is still needed. Joint experimental/theoretical studies on Au_8/MgO(001) by Heiz and coworkers[6, 11] have shed light on some of the questions such as "what is the smallest cluster size to catalyse the low-temperature oxidation of CO to CO_2?" or "what is the charging effect of F centres on the gold cluster and CO/O2 adsorption?". However to our knowledge, almost all previous work was carried out on MgO planar surfaces.

Kubo *et al.*[12] performed molecular-dynamics study of the mechanism of Au cluster formation on the MgO(100) plane with a step. They demonstrated that an Au atom trapped in the step plays the role of a nucleation centre for the formation process of the Au cluster on the MgO(100) plane, similar to that on the MgO(100) plane with a point defect.
Recently, Del Vitto *et al.*[13] performed a DFT study of Au atoms and dimers on the MgO(100) surface, including a step. They report that an Au atom's diffusion is stopped only at strong binding sites such as F and F^+ centres (E_{ads}= 3–4 eV), divancies (E_{ads}= 2.3 eV) and to a lesser extent, steps (E_{ads}= 1.3 eV).

In this work we study the adsorption of gold atoms, dimers and Au_{10} clusters on the MgO(001) surface with and without F centres present. A ten atom gold cluster is chosen since Au_8 was found to be the smallest catalytically active size for the catalyzed combustion of CO.[6] We further consider the kinked MgO(1 3 12) surface as kinks are abundant at cleaved and powdered samples of MgO. Furthermore, the kinked surface provides a neutral defect with the possibility of higher Au coordination than simple step. It has also been suggested that electronically excited states and electrons produced at surface terraces can travel to less coordinated sites, such as kinks and corners.[14, 15] As a result, if charge transfer is believed to play a crucial role in the nucleation of gold clusters on MgO(001) and their catalytic activity, kinks at MgO surfaces could be an important feature of the catalyst. Finally, we use CO adsorption on hydroxylated gold atoms as well as Au_{10} clusters, in order to assess the importance of charge transfer and Au oxidation state in supported gold catalysts.

6.2 Computational details

We use a DFT approach based on pseudopotentials and numerical localized atomic orbitals as basis sets. This method, implemented in SIESTA[16], is able to handle a large number of atoms within a periodic supercell approach. Standard norm-conserving pseudopotentials are used as the number of atomic orbitals would exceed any practical limit.

The calculations are performed within the generalized-gradient approximation (GGA), using the exchange-correlation potential developed by Perdew, Burke and Ernzerhof (PBE)[17]. We employ the widely used scalar relativistic Troullier-Martins pseudopotentials[18] with nonlinear core corrections[19] in their fully non-local form[20]. These are generated with the reference configurations $6s^1\ 6p^0\ 5d^{10}$ for Au, $3s^2\ 3p^0\ 3d^0$ for Mg, $2s^2\ 2p^4\ 3d^0$ for O, $2s^2\ 2p^2\ 3d^0$ for C and $1s^1\ 2p^0\ 3d^0$ for H. The cutoff radii for the *s*, *p* and *d* components of the pseudopotentials are 2.40, 2.70 and 1.90 a.u. for Au; 1.90 and 2.30 a.u. for Mg; 1.30 a.u. for O, 1.40 a.u. for C and 0.80 a.u. for H. Relativistic effects are taken into account for Au and a nonlinear core correction[19] is applied for Au and Mg, with r_{pc}= 1.20 a.u. for both, so that the pseudocore charge density equals the charge density outside r_{pc}, and has the smooth form $\rho_{pc}(r) = A \cdot r \cdot \sin(b \cdot r)$ inside that radius with continuous derivatives up the second order at r_{pc}. Furthermore, semi-core $2p^6$ electrons are explicitly treated for Mg when single point energy calculations are performed.

Flexible linear combinations of numerical pseudoatomic orbitals are used as the basis set, allowing for multiple-ξ and polarisation orbitals. In order to limit the range of the basis pseudoatomic orbitals (PAO), they are slightly excited by a common "energy shift" equal here to 0.01 Ry for geometry optimisations, 0.005 Ry for single point energy calculations, and truncated at the resulting radial node. In the present calculations we use single-ξ *s*, *d*-basis and single-*p* polarisation orbital for structure optimisations (SZP) and double-ξ *s*, *d*-basis and single-*p* polarisation orbital for single point energy calculations (DZP). We did check the effects of a change of basis set size from DZP to SZP: The F centre formation energy increases by only 0.03 eV and for CO adsorbed on atomic gold on perfect MgO(001), d(C–O) is unchanged, d(Au–C) is reduced by 0.02 Å, d(Au–O) is increased by 0.01 Å and the angle (Au-C-O) increased by only 0.8°. This leads us to consider that SZP is a suitable basis set for geometry optimisations in this work. However, DZP basis sets are employed for CO and OH groups in all calculations; SZP basis sets do not reproduce the CO stretching frequency in the gas phase, inducing an error of more than 200 cm^{-1}. The basis functions and the electron density are projected onto a uniform real-space grid in order to calculate the Hartree and exchange correlation potentials and matrix elements. The mesh size of the grid is controlled by the "energy cutoff" of the plane waves that can be represented in it without aliasing (here we take 200 Ry) and all the calculations are performed spin-polarised.

The standard diagonalisation solution of the Hamiltonian is used even though SIESTA can employ the so called order-N, linear-scaling method. For the systems we study here (less than 250 atoms), the diagonalisation method is competitive and more convenient than the order-N method. The smearing of the electronic occupations is done using an energy width corresponding to an effective electron temperature of 5 K. A tolerance of 10^{-4} is used for the density matrix to define when the self-consistency has been achieved and conjugate-gradient relaxations are performed until the forces are less than 0.02 eV Å^{-1}.

The MgO(001) surface has been modelled by three-layer slabs. Previous theoretical calculations and electronic structure measurements on ultra thin MgO films have shown that the properties are well converged for three-layer films[21] and increasing the slab thickness to four MgO layers does not affect the binding energies of surface adsorbates[13]. Supercells (6×6) containing 108 atoms each have been used for the (001) surface and the adsorption of gold atoms or gold dimers. Supercells (4×4) would be large enough for the study of a single gold atom or dimer adsorption[13]. As we introduce a ten atom gold cluster, care must be taken that it does not interact with its neighbour repeating units and we employ supercells (8×8) containing 192 Mg/O atoms for Au_{10} adsorption. We further checked the convergence of the results *vs.* the size of the slab and the Au_{10} binding energy is converged to 0.008 eV per cluster. In this chapter, all adsorption and interaction energies are given per cluster for Au_{10}, per dimer for Au_2 and per atom for Au_1. The resulting supercells are orthogonal with $a=b=12.54$ Å and a 36 atom surface for the (6×6) and $a=b=16.72$ Å and a 64 atom surface for the (8×8). The lower layer of the slab is fixed in all calculations involving the MgO(001) surface.

The choice of the surface to model the kink site requires more attention as a dipolar slab can arise which causes major problems since we are using periodic DFT models. Also, while it is easy to fix the bottom layer(s) of a regular MgO(001) surface to simulate the presence of the bulk below the surface, it is not that obvious how to choose which atoms of the bottom of the slab should be fixed with a kinked surface. We want a kinked supercell in which the surface kink is effectively isolated and we tried different Miller indices and finally decided to use the MgO(1 3 10) and MgO(1 3 12) surfaces with five-layer slabs containing 200 and 250 atoms respectively. We checked the convergence versus supercell size and the atomic rearrangement around the kink site, when switching between MgO(1 3 10) and MgO(1 3 12), is less than 0.01 Å. Using five-layer slabs, we optimise all of the layers but find that the middle one plays the role of the bulk and is not affected by the relaxations. The 200 atom slab is used for the single gold atom adsorption (figure 6.18) and the 250 atom slab is used for the Au_{10} gold cluster adsorption (figure 6.22). Adsorbates and defects are situated on one side of the slab with at least 16 Å of vacuum separation to the nearest periodic image cell, which we have checked, is enough even for the adsorption of CO on Au_{10}/MgO as the CO geometry and adsorption energy do not change when the gap is increased beyond 16 Å. The resulting MgO(1 3 10) supercell is orthogonal with a=13.22 Å and b=13.86 Å and presents a 40 atom surface. However, the MgO(1 3 12) supercell is non-orthogonal, with a=13.22 Å, b=17.23 Å, $\alpha=\beta=90°$, $\gamma=107.87°$ and presents a 48 atoms surface.

The large real space supercells reduce the number of k-points required and only the Γ point is included for all calculations. The program developed by Henkelman *et al.*[22] is used to perform Bader charge[23] analysis and XCrySDen[24] is used to display charge density isosurfaces and slices. The vibrational frequencies for CO adsorption are calculated by employing the VIBRA package written by P. Ordejón and available with SIESTA. The latter can compute the force constants matrix and this can be analysed by VIBRA in order to extract the vibrational modes for clusters, linear chains, slabs and crystals. We choose a displacement of 0.01 Å for the computation of the force constants matrix and only CO with its gold atom are displaced. We also modified VIBRA so that it ignores the other atoms and does not impose the translational sum rule, *i.e.* it does not correct the force constants to obtain zero frequencies for the translations.

6.3 Au on the perfect MgO(001) surface

6.3.1 Magnesium oxide and gold

A – Magnesium oxide

The MgO bulk lattice parameter has an optimized value of 4.191 Å, differing by only 0.47 % from the experiment (4.211 Å)[25]. The cell is then fixed in all surface calculations. The 3-layer MgO(001) surface is relaxed with the bottom layer atoms kept fixed and no significant rearrangement is found as expected from the strong ionic character of MgO and the stability of MgO(001). After relaxation, the interlayer spacing is increased by 0.09 Å which represents a 4% change from the bulk. The calculated band gap for the bulk structure is 4.61 eV, significantly smaller than the experimental result[26] at 7.83 eV (a large gap is as expected since MgO is highly ionic). This is due to a well known shortcoming of DFT which fails to describe the relative energies of occupied and unoccupied electron levels.[27] Also, the experimental gap corresponds to the optical gap whereas our theoretical gap should be compared to the photoemission gap, which is smaller as it contains no excitonic effects. DFT band gap results for MgO available in the literature usually range between 4.2 eV and 5.2 eV.[28] The density of states for the bulk material is presented in figure 6.1.

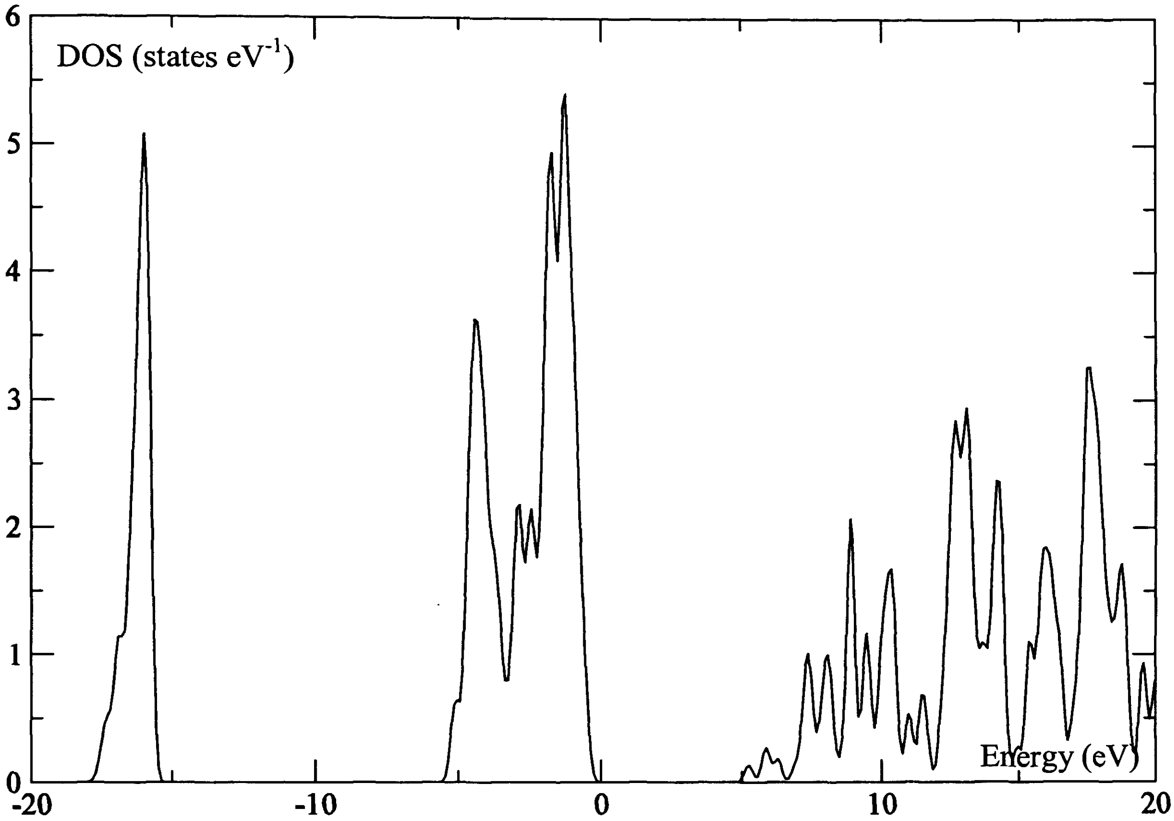

Figure 6.1 Total density of states for bulk MgO. The energy origin is chosen as the highest occupied state and a Gaussian smearing width of 0.2 eV is applied.

The width of the upper valence band is 5.66 eV, which is in good agreement with the experimental values (5 – 6 eV).

The Bader charges for bulk MgO are +1.84 |e| for Mg and -1.84 |e| for O, becoming 1.75 |e| and -1.75 |e| for surface Mg and O respectively after cleavage to create the MgO(001) surface.

B – Gold

Our results are compared to the earlier study of Soler *et al.* in table 6.1. The gold bulk lattice parameter has an optimised value of 4.088 Å, only 0.22 % greater than the experimental value (4.079 Å)[29]. Soler *et al.*, also using SIESTA but with LDA, quote a very similar value (4.069 Å) which is however below experiment as LDA tends to result in over-binding.[30]

	This work	**Soler *et al.*[30]**	**Exp[t]**
Au(s), *a* (Å)	4.088	4.069	4.079 [29]
Au_2, r_e (Å)	2.483	2.460	2.472 [31]

Table 6.1 Lattice parameter a of bulk gold Au(s) and bond length r_e of gold dimer Au_2.

The gold dimer bond length r_e at equilibrium obtained here (2.483 Å) differs from the experimental value (2.472 Å)[31] by only 0.44 %. Dimers are excellent test systems. Using singles and doubles coupled cluster theory with perturbative triples [CCSD(T)][32, 33], Varganov *et al.*[34] calculated a bond length of 2.535 Å for Au_2, which differs by 2.55 % from the experiment even though their method provides a better estimate of dynamic correlation than does DFT. We also tested the gold pseudopotential with Au^+ using AuH. A bond length d(Au–H)=1.564 Å was calculated, *vs.* 1.524 Å obtained experimentally[35].

C – Au_{10} cluster

Using an empirical many-body potential, Wilson and Johnston[36] found the global minima for Au_{10} being a bi-capped square anti-prism structure with D_{4d} symmetry, with a binding energy per atom E_b= 2.10 eV and an average nearest neighbour distance R= 2.78 Å. They performed fifty annealing runs for each of five initial temperatures with different cooling rates governed by the initial temperature and simulation time of the annealing step. Rogan *et al.* found the same optimal geometry for Au_{10}, using both DFT with the PBE functional and classical molecular dynamics in combination with embedded atom potentials.[37] The choice of the geometry shown in figure 6.2 is based on these previous studies in which this was found to be the most stable structure for Au_{10}. In the gas phase the chosen Au_{10} cluster is neutral (further verified by Bader charge analysis) and with the optimised geometry shown in figure 6.2.

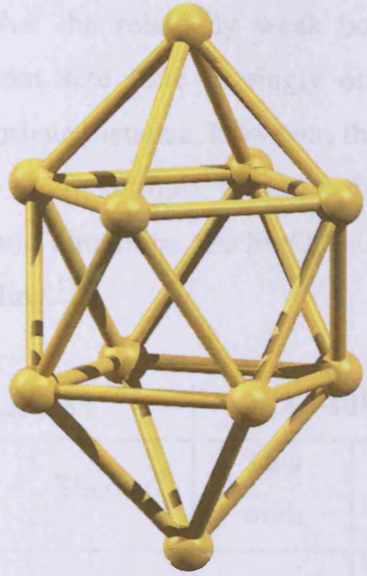

Figure 6.2 Bi-capped square anti-prism optimised geometry for the Au_{10} cluster in the gas phase.

Using SIESTA and the Au PP developed as part of this work, the calculated binding energy per atom is E_b= 2.23 eV and the average nearest neighbours distance is 2.84 Å. These results are in very good agreement with Wilson and Johnston if we consider that PBE has a tendency to underestimate bond lengths and that using localized basis set with SIESTA, there is probably a small amount of energy added to E_b due to “intra molecular” BSSE.

6.3.2 Gold atom and dimer adsorption

The valence electronic structure of Au is characterized by the presence of a filled *d* shell and a singly occupied *s* orbital. In theory, gold could form relatively strong bonds with oxygen atoms of partially reduced oxide surfaces by exchange of their outer electron. Indeed, the highest adsorption energy of Au on the perfect MgO(001) surface is found for the oxygen site (-0.78 eV) with a distance to the substrate of 2.33 Å, in excellent agreement with previous plane-waves studies[10, 38] (Table 6.2). Previous investigations claim that the Au orbitals do not mix efficiently with the O 2*p* band and that the bonding is mainly due to polarization effects and weak ionic bonding.[10, 38] Based on Bader analysis, we find a small charge transfer from the substrate (-0.31 |e|) to Au and so in contrast to previous proposals[9], the bonding cannot be described as mainly due to the polarization of the Au electrons by the surface electric field but has an ionic component.

Yudanov *et al.*[9] pointed out that the relatively weak bonding for Cu, Ag and Au is a consequence of the large adatom size (due to singly occupied valence *s* orbital) which determines the long surface-adsorbate distance. However, they also found a very small mixing of the metal σ orbitals with the O $2p_\sigma$ orbital.[9] Recently, Del Vitto *et al.* presented a plane-wave DFT study of Au atoms and dimers on the MgO(100) surface in which they show the existence of some covalent bonding.[13]

	E_{ads} (eV)		**d(Au-subs) (Å)**		**Bader charge (|e|)**	
Adsorption site	This work	Theory[10]	This work	Theory[38]	Au	Ads. site
O	-0.78 (-1.13)	-0.88	2.33	2.34	-0.31	-1.47
Mg	-0.36 (-0.67)	-0.51	2.71	-	-0.21	1.74
Hollow site	-0.61 (-0.92)	-0.72	2.41	-	-0.27	-
Au_2 (vertical on O)	-1.27 (-1.61)	-1.36	2.19	2.18	-0.07 / -0.25	-1.49
Au_2 (parallel on O)	-0.54 (-1.11)	-	2.52	-	-0.18	-1.60

Table 6.2 Results comparison for gold atom and dimer adsorptions onto the MgO(001) surface. E_{ads} is the adsorption energy, d(Au–subs) is the difference in *z*-components of co-ordinate between Au and the substrate, *i.e.* the adsorption site. Adsorption energies are given with their relative uncorrected value for BSSE in parenthesis. References [10] and [38] both employ plane waves GGA DFT.

To study the charge transfer between Au and the MgO surface we define the charge density difference,

$$\rho_{diff} = \rho(Au/MgO) - \rho(Au) - \rho(MgO) \tag{6.1}$$

which is the difference between the charge density of the Au/MgO system and that for Au and MgO in isolation. ρ_{diff} is positive in the regions where there is a gain of electronic charge upon formation of the complete system, and negative where there is a loss of electronic charge. Figure 6.3a clearly shows the charge flow affects only the gold atom and the oxygen ion onto which it is adsorbed. This indicates that the bond has a very local nature, in agreement with the strong ionic character of MgO which will prevent any charge redistribution within the substrate. The space between Au and the surface does not present an accumulation of charge density and thus suggests that an important contribution to the bonding comes from polarization, in agreement with plane-waves DFT[13].

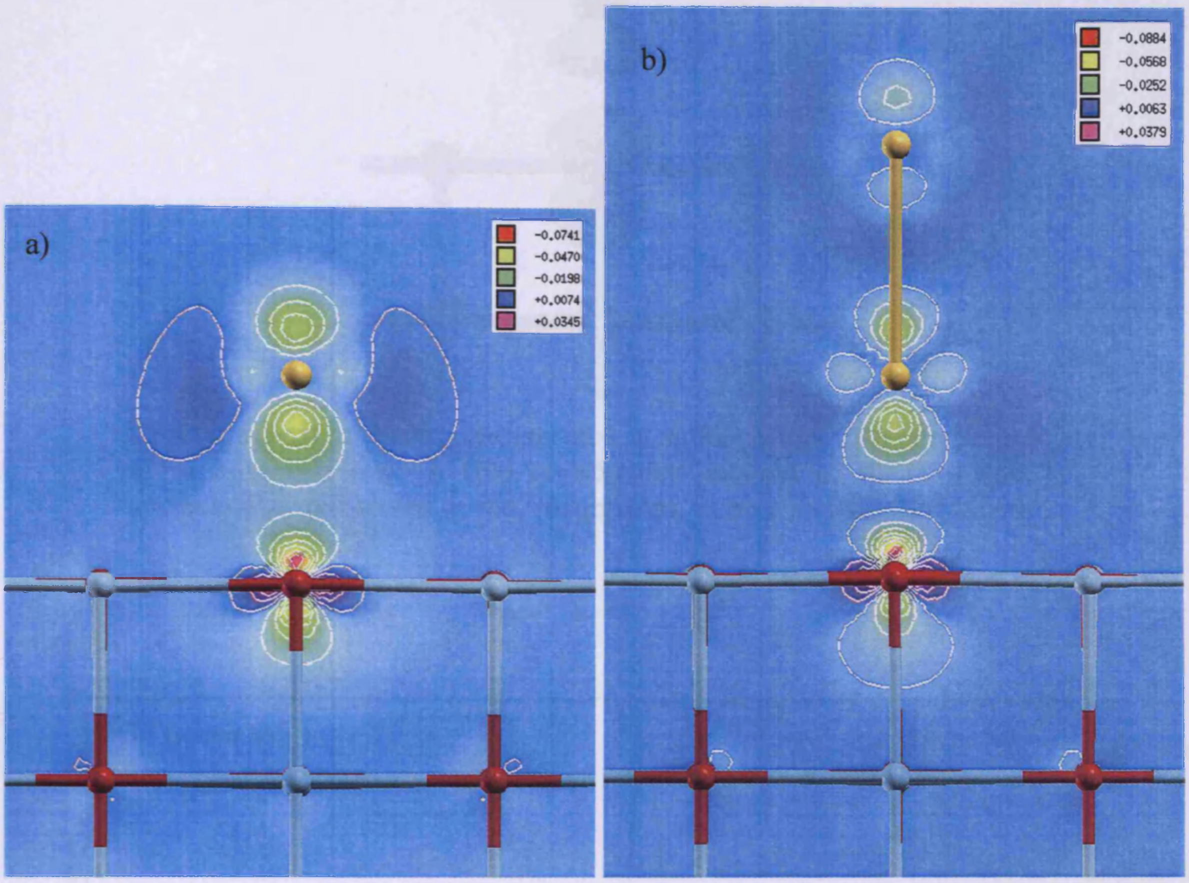

Figure 6.3 Charge density difference for a) Au_1 and b) vertical Au_2 adsorbed onto a five coordinated oxygen atom of the MgO(001) surface. Red/green colours represent charge depletion and blue/purple colours, charge accumulation. Lines are drawn in intervals of 0.01 e a_0^{-3}. Oxygen atoms in red, magnesium in blue.

However, spin delocalisation over the oxygen (figure 6.4) indicates the presence of covalent bonding. This is even more obvious with the analysis of the density of states (DOS) of the Au/MgO(001) system shown in figure 6.5. The DOS shows the presence of an isolated electronic state in the band gap, associated with the Au 6*s* orbital. The latter is mixed with the Au 5*d* level and the 2*p* level of the oxygen atom to which it is bound. As pointed out by Del Vitto *et al.*[13], this confirms that beside the polarization effect, covalent bonding involving the Au and O valence levels plays an important role in the Au–MgO bond strength. The Au 6*s* level is present at about 1 eV above the MgO valence band (figure 6.5). Charge transfer may be a result of the high electron affinity of gold (222.75 kJ mol^{-1}). Oxygen also has a quite high electron affinity (140.98 kJ mol^{-1}) but O^{2-} has already accepted two electrons.

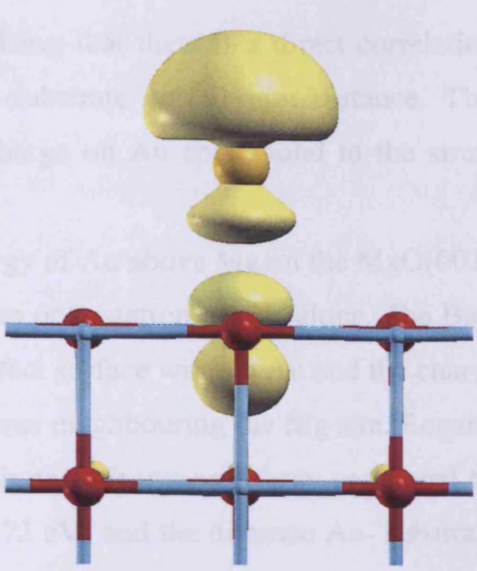

Figure 6.4 Spin density iso-surface at 0.003 e a_0^{-3} for a single gold atom adsorbed onto a five coordinated oxygen of the MgO(001) surface. Oxygen atoms in red, magnesium in blue and gold in yellow.

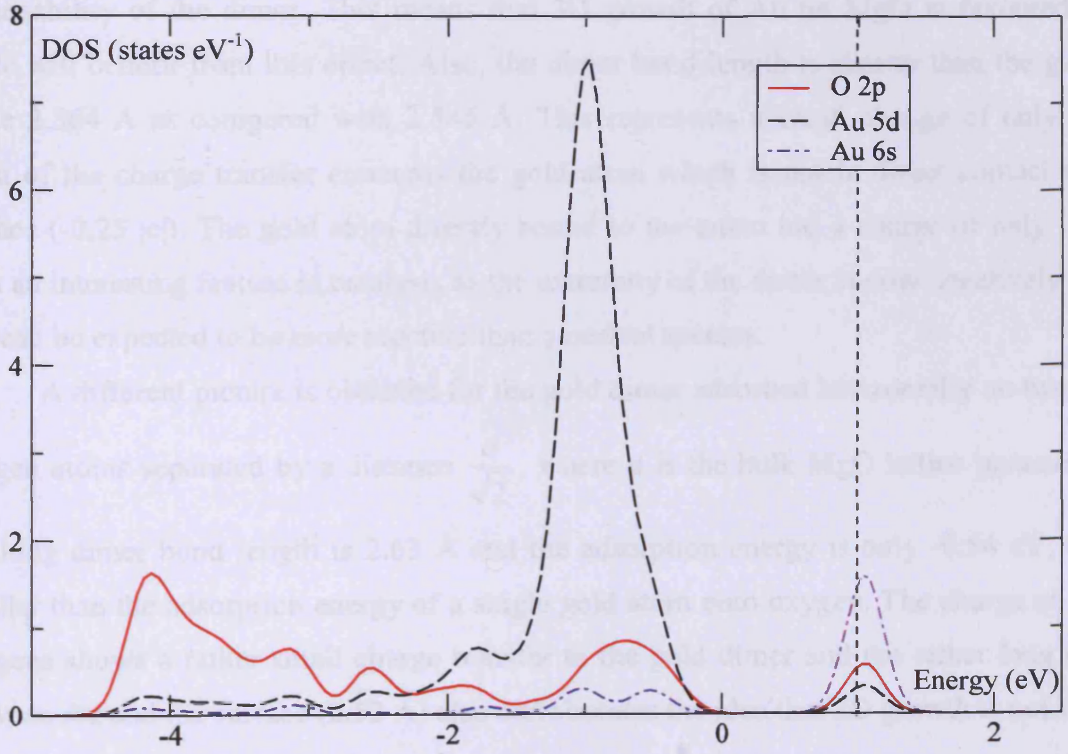

Figure 6.5 Projected density of states onto the Au 6*s*, 5*d* and O 2*p* states for Au adsorbed on a five-coordinated oxygen ion of the MgO(001) surface. A Gaussian smearing width of 0.2 eV is applied. The energy origin is chosen as the top of the 2*p* valence band for the surface oxygen anions not directly interacting with Au. The dotted line represents the Fermi level.

It is also worth noticing that there is a direct correlation between adsorption energy, Bader charge and the Au-substrate equilibrium distance. The shortest Au-substrate bond distance and the highest charge on Au correspond to the strongest Au-substrate interaction (Table 6.2).

The adsorption energy of Au above Mg on the MgO(001) surface is rather weak (-0.51 eV) and appears to be due to polarization effects alone. The Bader charge on Mg is only 0.01 |e| less than that for the perfect surface without Au and the charging of the gold atom (-0.21 |e|) comes from the oxygen atoms neighbouring the Mg site. Regarding the hollow site (or bridge site), there is little change in the adsorption energy compared to the Au atom over the O site (from -0.88 eV on O to -0.72 eV) and the distance Au- substrate is also similar (from 2.33 Å to 2.41 Å).

As pointed out by Molina and Hammer[10], a beneficial effect is observed when Au atoms are on top of other Au atoms in contact with the substrate. The adsorption energy (-1.27 eV) of the gold dimer oriented vertically on the surface oxygen is 61% higher than the adsorption energy of a single gold atom at the same site (-0.78 eV), due to the higher polarisability of the dimer. This means that 3D growth of Au on MgO is favoured as this mode will benefit from this effect. Also, the dimer bond length is shorter than the gas phase value 2.564 Å as compared with 2.545 Å. This represents a small change of only 0.02 Å. Most of the charge transfer concerns the gold atom which is not in direct contact with the surface (-0.25 |e|). The gold atom directly bound to the anion has a charge of only -0.07 |e|. This an interesting feature in catalysis as the extremity of the dimer is now negatively charged and can be expected to be more reactive than a neutral species.

A different picture is obtained for the gold dimer adsorbed horizontally on two surface oxygen atoms separated by a distance $\frac{a}{\sqrt{2}}$, where a is the bulk MgO lattice parameter. The resulting dimer bond length is 2.63 Å and the adsorption energy is only -0.54 eV, 0.24 eV smaller than the adsorption energy of a single gold atom onto oxygen. The charge on the two oxygens shows a rather small charge transfer to the gold dimer and the rather long distance between Au and the surface (2.52 Å) also corroborates the idea that 2D growth is not favoured.

6.3.3 Au_{10} adsorption

Although the geometry presented in figure 6.2 is the most stable one for Au_{10} in the gas phase, this does not hold for Au_{10} on perfect MgO(001). The cluster tends to flatten, optimising its interaction with the surface by increasing contact with oxygen atoms. After observing this for the bi-capped anti-prism structure, we choose a geometry based on a two layer fcc structure for Au_{10} (figure 6.6 and 6.7) with the lower layer containing seven atoms and the top layer three. This structure has been successfully used to model Au_{10} on TiO_2(110) for CO oxidation.[39] Taken alone in the gas phase with the geometry it possesses on MgO(001), Au_{10} is neutral with a binding energy per atom E_b= 2.16 eV, lower than that of the capped anti-prism geometry previously calculated (E_b= 2.23 eV). Different orientations from the one presented here have been tried, but the orientation with a maximum of gold atoms on top of surface oxygens (figure 6.7) is always favoured.

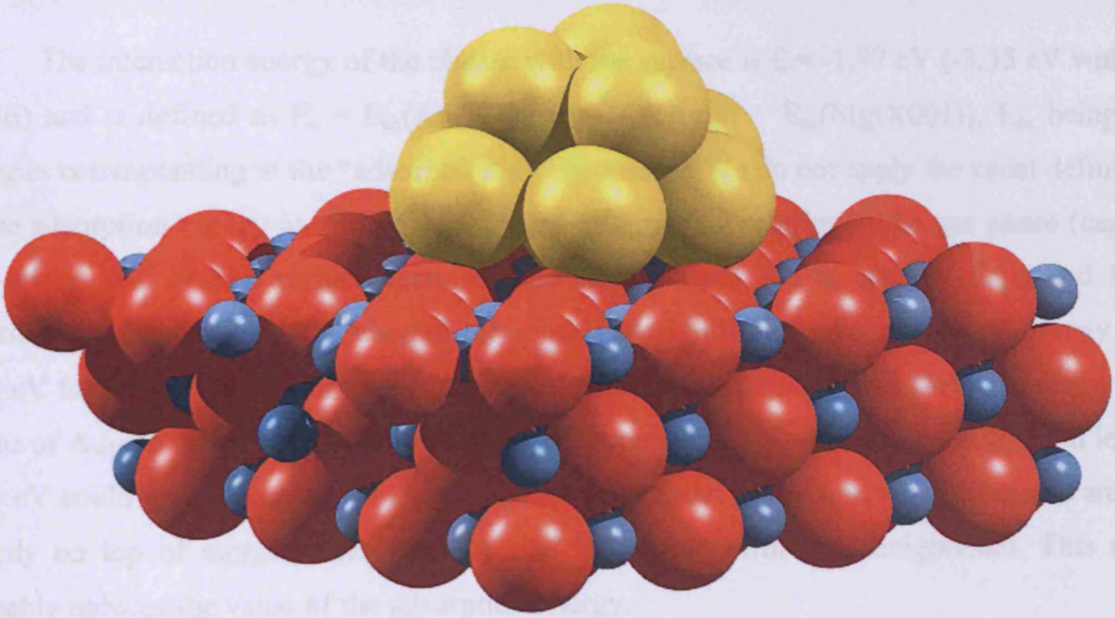

Figure 6.6 Three dimensional representation of the optimised geometry for Au_{10} adsorbed onto the MgO(001) surface. Oxygen atoms in red, magnesium in blue and gold in yellow.

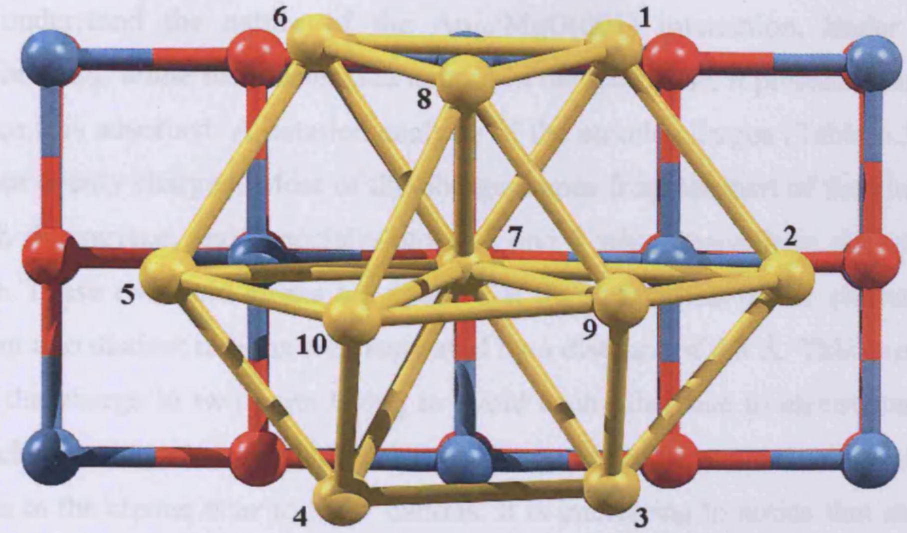

Figure 6.7 Top view of the Au_{10} cluster adsorbed onto the MgO(001) surface with numbering of the gold atoms. Oxygen atoms in red, magnesium in blue and gold in yellow.

The interaction energy of the cluster with the surface is E_i= -1.97 eV (-3.35 eV without BSSE) and is defined as $E_i = E_{as}(Au_{10}/MgO) - [E_{as}(Au_{10}) + E_{as}(MgO(001))]$, E_{as} being the energies corresponding to the "adsorbed state" geometry. We do not apply the usual definition of the adsorption energy as Au_{10} exhibits very different geometries in the gas phase (capped anti-prism) and on the surface (semi-dodecahedra). Since Au is actually deposited from solution, the calculation of a relevant reference state is difficult. An adsorption energy of -0.78 eV for a single gold atom on oxygen was calculated previously and there are seven gold atoms of Au_{10} in direct contact with the surface. As a result, an adsorption energy of at least -5.46 eV could be expected for the cluster. However, most of these seven gold atoms are not exactly on top of oxygen sites and are also interacting with gold neighbours. This most probably reduces the value of the adsorption energy.

The distance between the surface and the bottom layer (basal plane) of the cluster is on average 2.67 Å, with the top layer of Au_{10} being at 4.86 Å (corresponding to an interlayer distance of 2.19 Å). The cluster–surface distance lies within the range previously calculated for single Au atom adsorption, 2.33 – 2.71 Å (Table 6.2) and we can compare directly with the gold atom 7 in figure 6.7 which is 2.49 Å away from its surface oxygen, further than either the single gold atom (2.33 Å) or the dimer (2.19 Å). This reflects directly the strength of the interaction with the surface, *i.e.* the shortest distance, the strongest interaction and the fact that the single Au atom is expected to be closer to the surface since it has no Au neighbours to interact with.

To understand the nature of the Au_{10}/MgO(001) interaction, Bader charges are calculated for Au_{10}. While the cluster was neutral in the gas phase, it presents a total charge of -0.88 |e| once it is adsorbed. A detailed analysis of the atomic charges (Table 6.3) shows that atoms are not evenly charged. Most of the charge comes from the part of the cluster in direct contact with the surface, and especially atoms 2 and 5 which contribute almost 70% of the total charge. These two gold atoms are situated at the extremities of the cluster (figure 6.7) and represent two distinct regions well separated by a distance of 6.3 Å. This corresponds to a splitting of the charge in two parts trying to avoid each other due to electrostatic repulsion. The Bader charges suggest a re-distribution of charge to facilitate an electrostatic interaction of Au atoms in the cluster near to Mg^{2+} cations. It is interesting to notice that atoms 8, 9 and 10 representing the top of the cluster are almost neutral: the charge transfer between the surface and Au_{10} is localized to the bottom of the cluster in direct contact with MgO(001). This is different from what was observed with the dimer adsorption where most of the charge is on the end atom (table 6.2). The charge has probably been donated by the oxygen atoms onto which the gold atoms of the cluster are adsorbed or close enough so that a charge transfer is possible. A Bader charge analysis however shows that the charge on the oxygen centres is only slightly affected ($\delta q \sim 0.02$ |e|).

Gold atom	**Charge (|e|)**	**Gold atom**	**Charge (|e|)**
1	-0.053	6	-0.027
2	**-0.292**	**7**	**0.094**
3	**-0.104**	8	0.007
4	**-0.113**	9	-0.039
5	**-0.316**	10	-0.039

Table 6.3 Breakdown of the Bader charges for the Au_{10} cluster adsorbed on the MgO(001) surface, with a calculated total charge for Au_{10} of -0.882 |e|. Bold and blue characters are used for the most important charges. Atoms numbered according to figure 6.7.

6.4 Au on the defective MgO(001) surface (F centre)

Depending on preparation methods, one of the most common defects on MgO surfaces is the anionic vacancy, namely, the colour centres and the most stable colour centre is the neutral surface O vacancy (F).[40, 41] The removal of neutral oxygen produces an F centre containing two electrons which are trapped by the electrostatic Madelung potential. The F centre formation energy calculated using our methodology is 9.06 eV and compares well with previous results using either embedded cluster method[42] (9.07 eV) or periodic DFT calculations with plane wave basis sets and GGA DFT[43] (9.02 eV).

The presence of a surface O vacancy does not cause much relaxation even for atoms in the surface plane reflecting the electron localization. We find an electron population (Bader) for the O vacancy of 0.98 electrons, the rest being distributed over the nearest substrate ions, *i.e.* the two electrons in the F centre mimic the missing O^{2-} ion. The surface Mg ions around the O vacancy move by 0.021 Å away from the centre of the vacancy along the surface plane while the Mg ion beneath the vacancy also moves away from the vacancy along the surface normal by 0.055 Å. These results are in good agreement with previous studies[40, 44, 45] presented in section 2.2.2.

6.4.1 Au$_1$ adsorption

The adsorption energy for a single gold atom at the vacancy site is E_{ads}= -2.83 eV (-3.25 without BSSE): smaller than periodic DFT[13, 38] (3.12 and 3.17 eV both with GGA) but higher than FLAPW[8] (-1.93 eV also with GGA).

The interfacial distance, *i.e.* the distance between Au and the top layer of the surface, is 1.88 Å. For Ag on a MgO(001) F centre, Zhukovskii and Kotomin[46] report an interfacial distance of 1.81 Å and Matveev *et al.*[47] report an interfacial distance of 1.84 Å.

The Bader charge on the gold atom is -1.12 |e| and the spin density 0.36, with a Bader charge left in the vacancy of -0.38 |e|. Au has gained 0.81 electrons more than in the case of the perfect surface with Au on O and the vacancy site has lost 0.6 electrons compared to the F centre alone. Zhukovskii and Kotomin[46] report that for metal adsorption (Ag and Cu) over the F centre, an electron charge of about 0.5 |e| is transferred from the surface defect to the metal atom, in agreement with our results. The charge density difference in figure 6.8 with an accumulation of charge around the gold atom suggests that the electron density has been removed from the vacancy and transferred to the 6*s* level of Au. This is further supported by the spin population shown in figure 6.9, even though spin density cannot show charge transfer, only spin distribution.

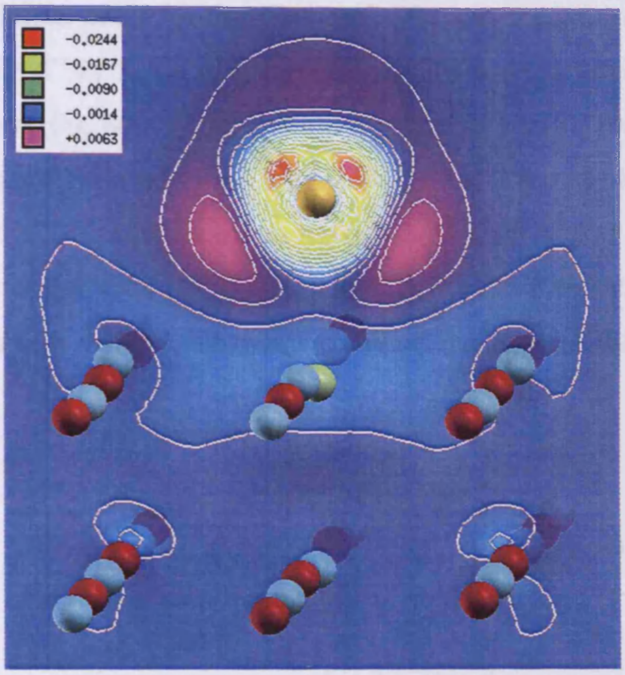

Figure 6.8 Charge density difference for a single gold atom adsorbed on the F centre of the MgO(001) surface. Red/green colours represent charge depletion and blue/purple colours, charge accumulation. Lines are drawn in intervals of 0.002 e a_0^{-3}. Oxygen atoms in red, magnesium in blue.

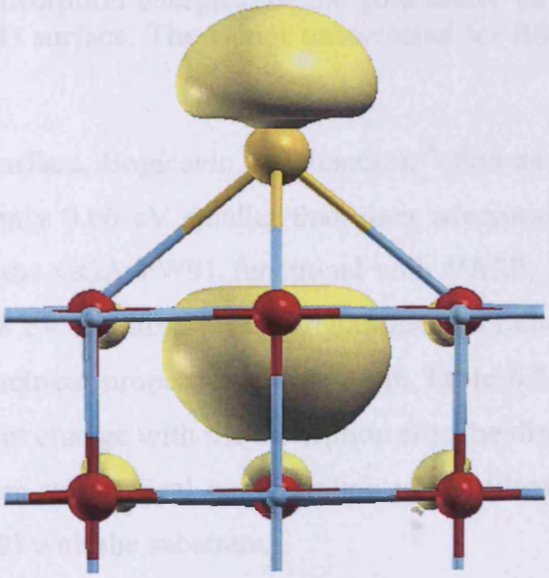

Figure 6.9 Spin density iso-surface at 0.003 e a_0^{-3} for a single gold atom adsorbed on the F centre of the MgO(001) surface. Oxygen atoms in red, magnesium in blue.

6.4.2 Au$_2$ adsorption

Three local minima exist for the dimer adsorbed at the vacancy site. The most stable configuration ("Mg-tilted" in Table 6.4) is with one Au atom directly on top of the vacancy and the other one interacting with a magnesium ion; atoms 1 and 2 respectively in figure 6.10. The two other minima correspond to a tilting toward O and the dimer being perpendicular to the surface respectively. These two minima have only slightly higher energies and the vertical configuration is more stable than the O-tilted one; while the interaction of Au(2) with Mg is stabilising, the interaction with O does not stabilise the dimer with respect to the vertical configuration.

	E_{ads} (eV)	
Adsorption site	This work	VASP[13]
Vertical	-3.38 (-3.86)	-3.89
Mg-tilted	-3.49 (-4.12)	-4.17
O-tilted	-3.33 (-4.00)	-3.91

Table 6.4 Adsorption energies for the gold dimer on the F centre of the MgO(001) surface. The values uncorrected for BSSE are given in parenthesis.

For the perfect surface, Bogicevic and Jennison[38] find an adsorption energy of -2.15 eV for Au$_2$ "vertical", only 0.06 eV smaller than their adsorption energy for Au$_2$ on the F center. However, using the GGA PW91 functional with VASP, Del Vitto *et al.*[13] obtain an energy difference of 2.68 eV for these two configurations, in rather good agreement with our results (2.22 eV). Geometrical properties are given in Table 6.5. While the distance to the surface for Au(1) does not change with the adsorption site, the dimer bond length is increased by more than 0.1 Å from the vertical configuration to the tilted configurations, due to the direct interaction of Au(2) with the substrate.

	Configurations for the adsorption of Au_2 on the F centre (figure 6.10)				
	Au(2) on top of Mg [38]	**Au(2) on top of Mg** [13]	**Au(2) on top of Mg**	**Au(2) on top of O**	**Au_2 vertical**
d(Au(1)–surf)[a] (Å)	1.53	1.69	1.68	1.66	1.71
d(Au(2)–subs) (Å)	3.04[a]	2.81	2.80 (3.11[a])	3.13 (3.88[a])	4.33[a]
d(Au(1)–Au(2)) (Å)	2.72	2.73	2.74	2.72	2.62
Tilt angle θ (degrees)	56.3	57.0	58.5	60.8	0

Table 6.5 Geometrical properties for dimer adsorption on the F centre of the MgO(001) surface. d(Au(1)–surf) represents the interfacial distance for Au(1), *i.e.* the distance to the top layer of the surface. d(Au(2)–subs) represents the distance between Au(2) and the substrate atom it is facing. Note: [a] Adsorption height defined with respect to the average positions of the topmost surface layer atoms.

We have shown that a single gold atom on the clean MgO(001) surface will bind more strongly to oxygen than magnesium. However, the second atom of the dimer, Au(2), interacts more strongly with magnesium associated with the F centre. To understand the bonding mechanism, we plot the charge density difference, figure 6.11, showing clearly that a significant amount of charge has been transferred from the vacancy to both gold atoms of the dimer, (-1.06 |e| and -0.59 |e| for Au(1) and Au(2) respectively) giving a total charge of -1.65 |e|. The gold dimer now being negatively charged, more favourably interacts with magnesium, which probably explains why the most stable configuration is with Au(2) tilted toward Mg. The Bader charge analysis gives a zero charge inside the vacancy since the electron density has been transferred to the dimer. The attraction of Au(2) by Mg is further demonstrated by the movement of Mg toward Au(2) upon dimer adsorption (0.33 Å). On the other hand, for the O-tilted configuration, the oxygen atom moves away from Au(2) by 0.09 Å, *i.e.* away from its initial position in the defective surface before Au_2 adsorbed.

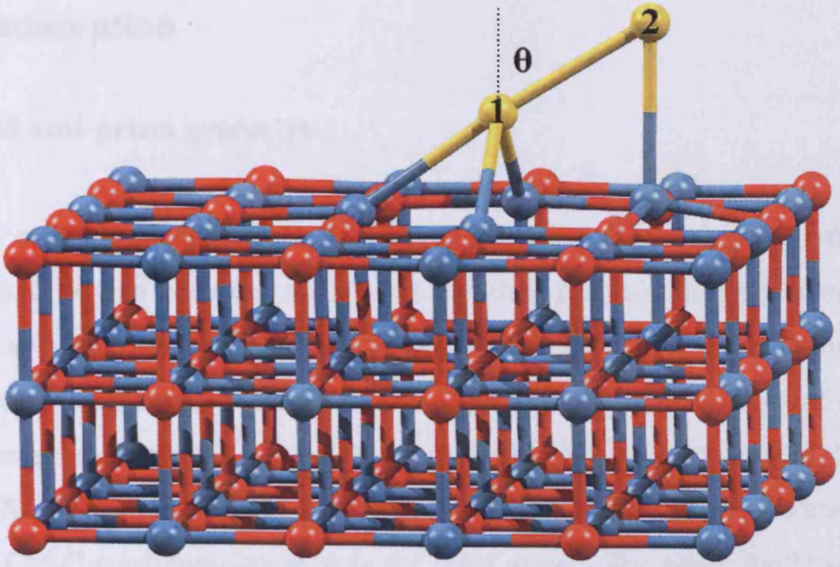

Figure 6.10 Geometry of the gold dimer adsorbed at the F centre of MgO(001) and orientated with its second atom, Au(2), on top of a magnesium ion. θ is the angle formed by Au_2 and the vertical. Oxygen atoms in red, magnesium in blue.

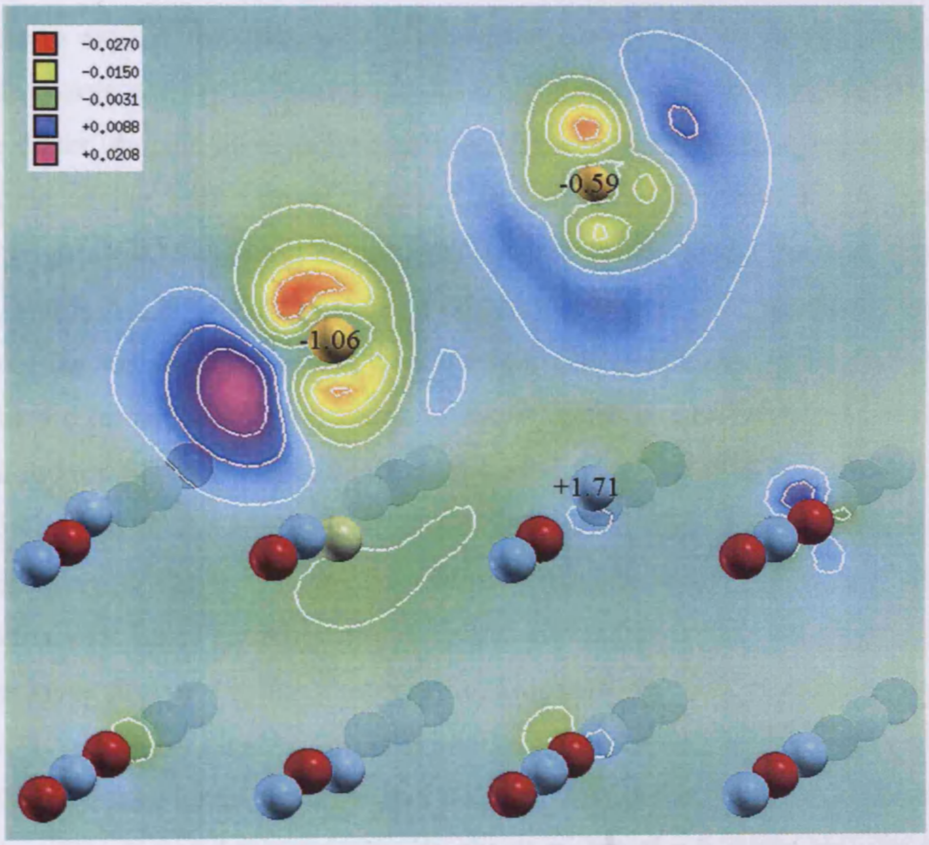

Figure 6.11 Charge density difference for the gold dimer adsorbed on the F centre of the MgO(001) surface; "on top of Mg" orientation. Red/green colours represent charge depletion and blue/purple colours, charge accumulation. Lines are drawn in intervals of 0.005 e a_0^{-3}. Some Bader charges are indicated. Oxygen atoms in red, magnesium in blue.

6.4.3 Au_{10} adsorption

A – Bi-capped anti-prism geometry

The F centre represents an anchorage point for Au_{10} as shown in figure 6.12. Two orientations that we can consider as isomers are then possible. Indeed, once Au_{10} has been adsorbed, it can rotate along its vertical axis Au(1)–Au(6) so that the atoms of the bottom layer (Au(2) to Au(5)) can either lie above oxygen or magnesium atoms of the surface. The adsorption energy is -2.88 eV (-3.76 eV without BSSE) for the "on top of Mg" orientation and -2.71 eV (-3.70 eV without BSSE) for the "on top of O" orientation. We choose to focus on the "on top of Mg" configuration as it is the most stable. The atom Au(1) is attached to the surface via the F centre at a distance of 1.54 Å from the surface top layer, which is smaller than the interfacial distance for a single Au (1.88 Å) or the dimer (1.68 Å). The Au_{10} cluster retains its gas phase geometry. The charge transfer argument used for the dimer can also be applied here to explain the difference in adsorption energy for the two possible orientations. We plot the charge density difference (figure 6.13) and also the spin population (figure 6.14). Unlike the dimer, Au_{10} in its bi-capped anti-prism form presents a spin population, located on all the atoms of the gold cluster (figure 6.14). This is correlated by the charge density difference (figure 6.13) showing an accumulation of charge where the spin is present. More important, atoms Au(2) to Au(5) exhibit a negative charge in their interfacial region with the Mg atoms of the surface. We also perform a Bader charge analysis on the Au_{10} cluster (Table 6.6). As for the dimer, the Bader charge of the F centre is now zero. The gold atom Au(1), directly on the top of the F centre has a charge of -1.06 |e| equal to that of the Au(1) atom in the dimer. The rest of the cluster charge is mainly distributed over the gold atoms Au(2) to Au(5), belonging to the lower layer 2 (Table 6.6). The other gold atoms present similar charges to that calculated for Au_{10} on the perfect MgO(001) surface. The charge on the atoms follows the layer structure of the cluster. It is also worth noticing that the total charge of the cluster (-1.71 |e|) is very close to the total charge of the dimer (-1.65 |e|). This shows that the amount of charge transferred from the surface (F centre) to the gold atoms has reached a limit at ~1.7 |e| and is in good agreement with the fact that the F centre on the oxide surface possesses "only" two electrons. Of course, some of the charge transfer is also expected to come from the MgO(001) O surface atoms, as we have shown previously. The "on top of O" configuration for Au atoms has also been studied and no major difference with the "on top of Mg" was found.

Layer	Gold atom	Charge (|e|)
1	1	**-1.060**
2	**2**	**-0.085**
	3	**-0.112**
	4	**-0.126**
	5	**-0.129**
3	7	-0.029
	8	-0.050
	9	-0.032
	10	-0.042
4	*6*	*-0.040*
	Total	*-1.705*

Table 6.6 Breakdown of the Bader charges for the Au_{10} cluster adsorbed in its bi-capped prism geometry on the F centre of the MgO(001) surface. “Layer” corresponds to the cluster layer to which the gold atoms belong, layer 1 being the closest to the surface. Atoms numbered according to figure 6.12.

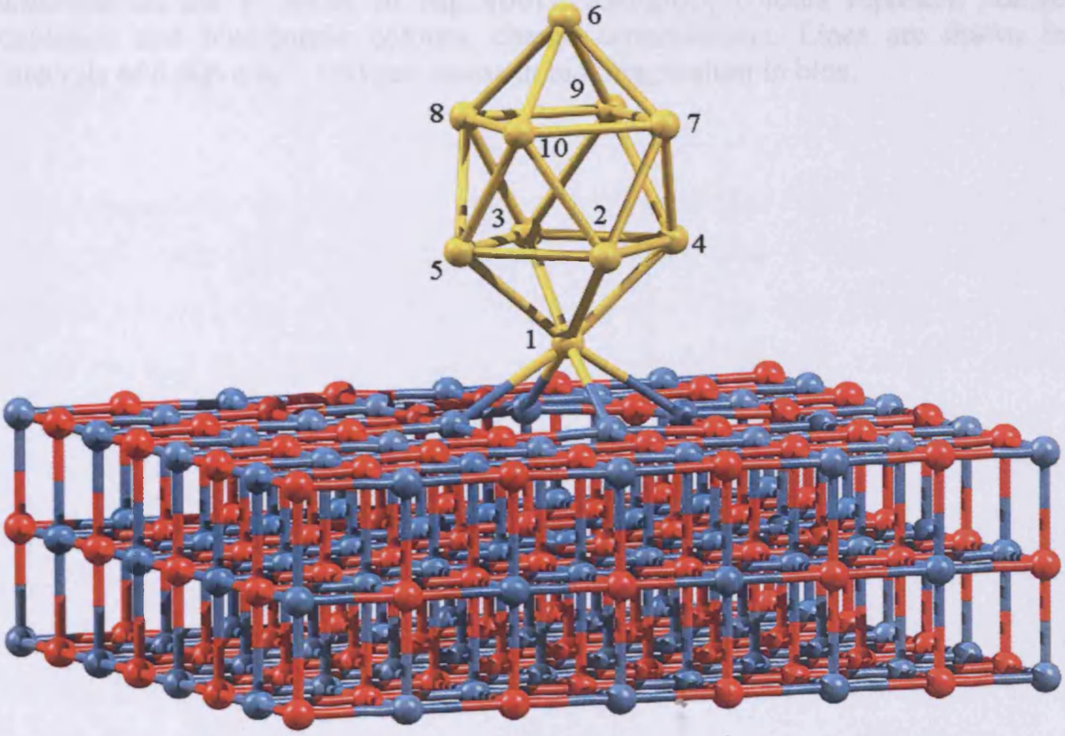

Figure 6.12 Geometry of the bi-capped anti-prism Au_{10} cluster adsorbed on the F centre of MgO(001). Oxygen atoms in red, magnesium in blue.

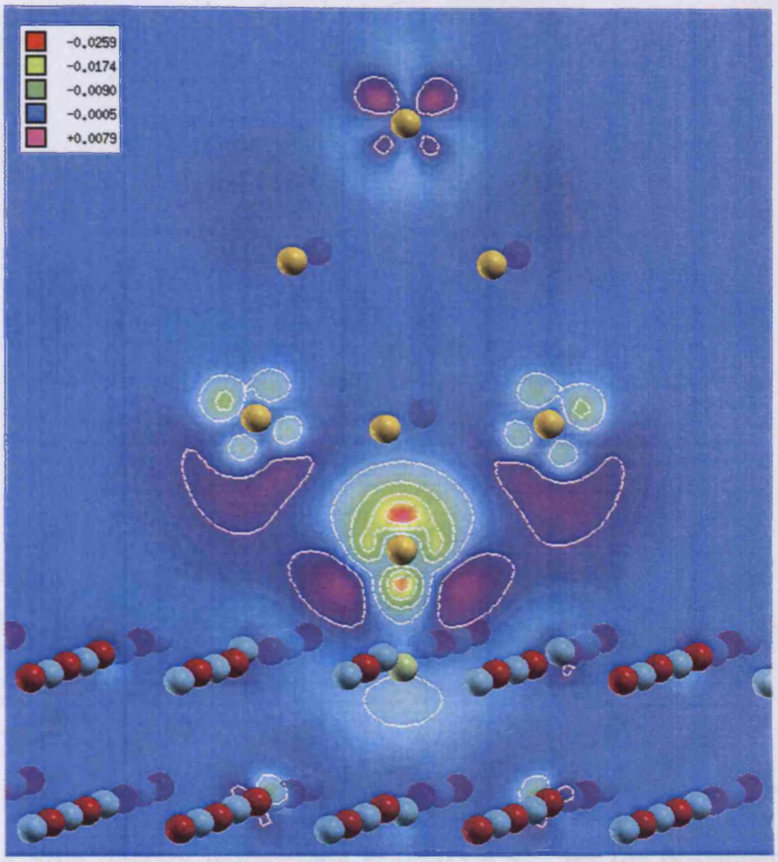

Figure 6.13 Charge density difference for the bi-capped anti-prism Au_{10} cluster adsorbed on the F centre of MgO(001). Red/green colours represent charge depletion and blue/purple colours, charge accumulation. Lines are drawn in intervals of 0.005 e a_0^{-3}. Oxygen atoms in red, magnesium in blue.

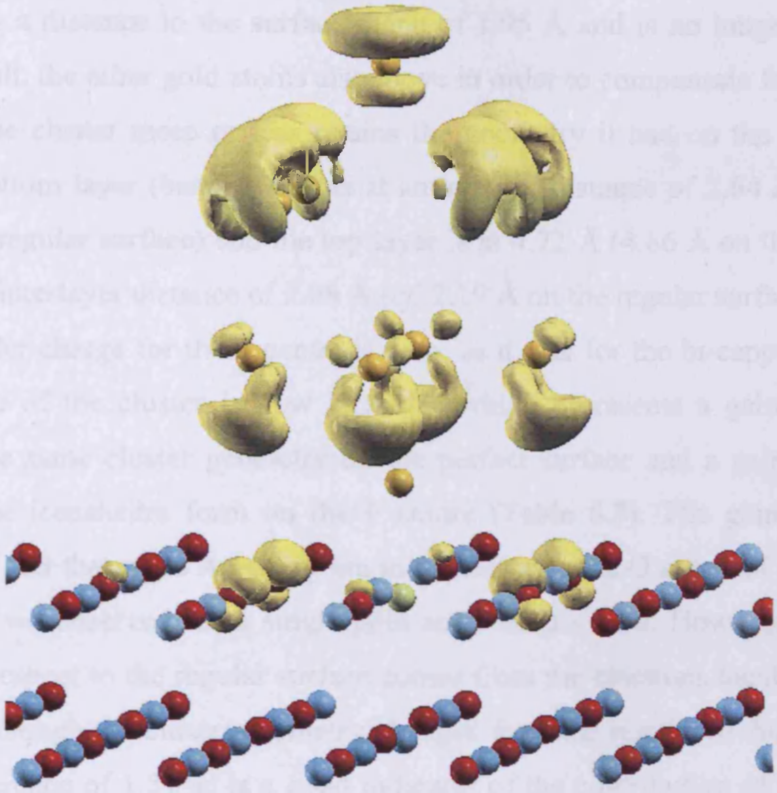

Figure 6.14 Spin density iso-surface at 0.003 e a_0^{-3} for the bi-capped anti-prism Au_{10} cluster adsorbed on the F centre of MgO(001). Oxygen atoms in red, magnesium in blue.

B – Semi-dodecahedra geometry

As calculated previously, the most stable configuration of the Au_{10} cluster in the gas phase is the bi-capped anti-prism form. We have previously shown that it can adsorb at the F centre site and retain its gas phase geometry. However, a semi-dodecahedra geometry based on a (7, 3) close packed structure as introduced for Au_{10} on the perfect MgO(001) surface also has to be considered here. This kind of structure has been used previously for the study of Au_8 and Ni_{12} clusters on F centres[6, 48]. The interaction energy E_i (as defined for Au_{10} on the perfect surface) of the semi-dodecahedra form of Au_{10} with the F centre is -5.43 eV (-6.98 without BSSE corrections). For Au_8 clusters on MgO(100) with F centre, Sanchez *et al.* found a value of -5.56 eV[6], in good agreement with our result. This energy on the F centre is much higher than the one calculated for the same geometry on the perfect surface (-1.97 eV). If we compare the final states for the adsorption of the semi-dodecahedra Au_{10} cluster on the regular surface (figure 6.7) and on the F centre (figure 6.15), we also observe that the main geometrical change comes from Au(7). On the F centre, Au(7) sinks down toward the vacancy, giving a distance to the surface plane of 1.95 Å and is no longer part of the basal plane. As a result, the other gold atoms also move in order to compensate for the displacement of Au(7) but the cluster more or less retains the geometry it had on the perfect MgO(001) surface. The bottom layer (basal plane) is at an average distance of 2.64 Å from the surface (2.67 Å on the regular surface) and the top layer is at 4.72 Å (4.86 Å on the regular surface), which gives an interlayer distance of 2.08 Å (*cf.* 2.19 Å on the regular surface).

The Bader charge for the F centre is zero, as it was for the bi-capped prism form, but the total charge of the cluster is now -2.19 |e|, which represents a gain of 1.31 electrons compared to the same cluster geometry on the perfect surface and a gain of 0.48 electrons compared to the icosahedra form on the F centre (Table 6.7). The gain of 0.48 electrons comes from the fact that more Au atoms are in contact with the O atoms of the surface and the charge transfer we observed for a single gold atom occurs here. However, the gain of 1.31 electrons with respect to the regular surface comes from the electrons localized in the oxygen vacancy. Even though the cluster geometry changes from the regular to the defective surface, the charge difference of 1.31 |e| is a good indicator of the contribution of the F centre to the charge transfer. Aside from Au(7) holding almost half the total charge of the cluster, the basal plane atoms are more negatively charged than the atoms of the top layer (Au(8), Au(9) and Au(10)). As a result, most of the charge (96%) is concentrated in the bottom layer of the Au_{10} cluster. This is further confirmed by the plot of the charge difference density in figure 6.16 clearly showing the charge accumulation around Au(7) (dark blue).

This charge flow directed from the F centre into the gold cluster has been reported by Yoon *et al.*[11]

We did not study a cluster “flat” on the surface as the planar structures found for small free Au_n clusters ($n \leq 10$)[49-51] are likely to rearrange perpendicular, and not parallel, to the MgO substrate when adsorbed over it.[10]

Gold atom	**Charge** (|e|)	**Gold atom**	**Charge** (|e|)
1	**-0.206**	**6**	**-0.182**
2	**-0.244**	7	-0.947
3	**-0.155**	8	-0.061
4	**-0.118**	9	-0.007
5	**-0.251**	10	-0.023

Table 6.7 Breakdown of the Bader charges for the Au_{10} cluster adsorbed in its semi-dodecahedra geometry on the F centre of the MgO(001) surface. Results for the bottom layer presented in bold characters. Atoms numbered according to figure 6.15. The calculated total charge for Au_{10} is -2.194 |e|.

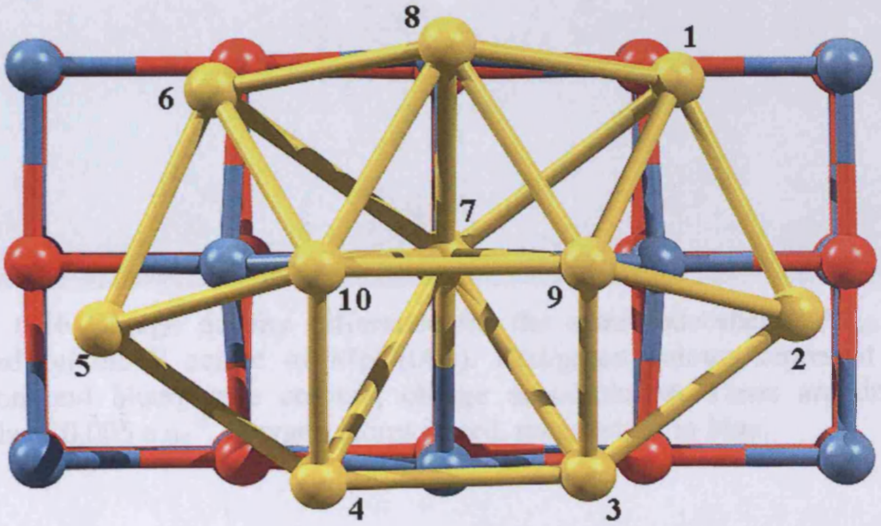

Figure 6.15 Top view of the Au_{10} cluster adsorbed in its semi-dodecahedra geometry on the F centre of the MgO(001) surface with numbering of the gold atoms. Oxygen atoms in red, magnesium in blue.

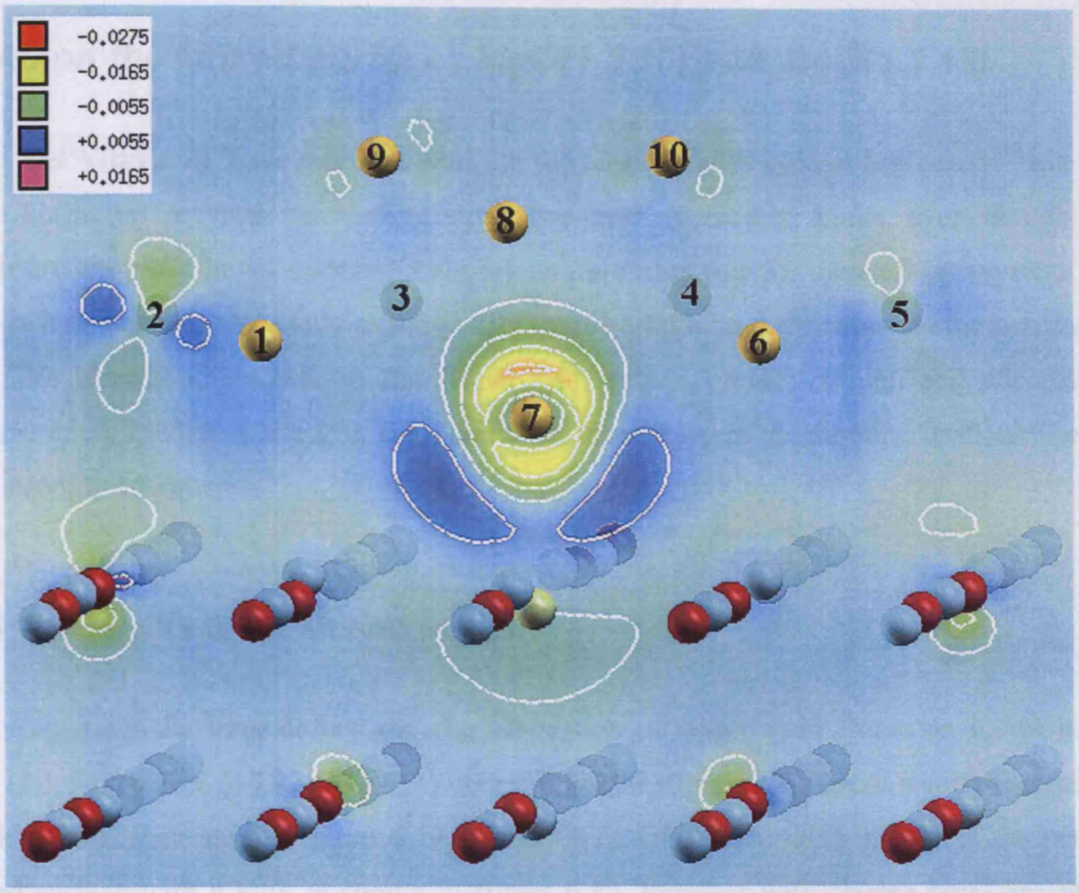

Figure 6.16 Charge density difference for the semi-dodecahedra Au_{10} cluster adsorbed on the F centre of MgO(001). Red/green colours represent charge depletion and blue/purple colours, charge accumulation. Lines are drawn in intervals of 0.005 e a_0^{-3}. Oxygen atoms in red, magnesium in blue.

6.5 Au on the kinked surfaces MgO(1 3 10) and MgO(1 3 12)

Del Vitto *et al.* have reported work on the adsorption of gold at MgO steps[13] but as far as we know, no previous theoretical study has ever considered kinks, even though these defects are abundant in the material and play an important role for the Au/MgO system. Kink sites are interesting in this study as they will provide a high co-ordination site for a surface Au atom. We already know Au on flat MgO(001) surface prefers oxygen and adsorbs with negative energy, so if it sits in a kink site with three oxygen neighbours, it should be even more strongly adsorbed.

6.5.1 The MgO(1 3 10) kinked surface

To study the kink defect and the adsorption of single gold atoms on it, we use the MgO (1 3 10) surface (13.22×13.86 Å) containing 200 atoms. We choose a surface exhibiting a kink with oxygen atoms (figure 6.17, atoms O(1), O(10) and O(11)). Part of the resulting relaxed surface with a kink is shown in figure 6.17, together with chosen bond lengths and atoms numbering.

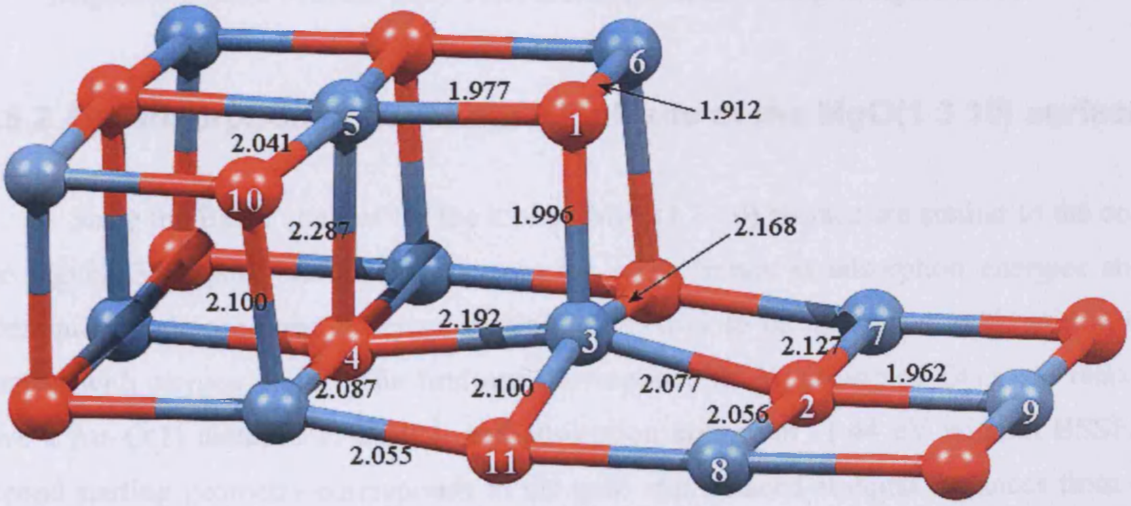

Figure 6.17 Detail of the oxygen kink site on MgO(1 3 10). O(1) has moved inward, towards Mg(5) and Mg(6). Bond lengths given in Å. Oxygen atoms in red, magnesium in blue. 23 atoms are represented.

The calculated Mg–O bond length for bulk MgO was 2.096 Å. By comparison to the results presented in figure 6.17 we can conclude that the kinked surface has undergone a degree of relaxation much greater than for the regular MgO(001) surface. The main changes concern the kink region, with, for example, an upward displacement of Mg(3) and a change in the angle defined by O(1), Mg(5) and O(10) (from 90° to 107.4°). The Mg kink presents similar geometrical changes.

We also perform a Bader charge analysis (Table 6.8) which shows that apart from O(1) (which lost some electrons), there is no major charge change around the kink site compared to the MgO(001) surface. This could be different if there was an F centre present on the terrace as the kink site is believed to be capable of trapping electrons and holes.[42]

Atom	**Charge** (|e|)	**Atom**	**Charge** (|e|)
O(1)	-1.65	Mg(6)	1.70
O(2)	-1.72	Mg(7)	1.74
Mg(3)	1.76	Mg(8)	1.74
O(4)	-1.75	Mg(9)	1.73
Mg(5)	1.73	Mg_B	1.74

Table 6.8 Bader charges for selected atoms of the oxygen kink site on the MgO(1 3 10) surface. Corresponding atom numbers are shown in figure 6.17. Mg_B is the magnesium atom beneath O(2). Atoms numbered according to figure 6.17.

6.5.2 Au_1 adsorption at the oxygen kink site of the MgO(1 3 10) surface

Since the Bader charges for the kinked MgO(1 3 10) surface are similar to the ones on the regular MgO(001) surface, we expect the same trends in adsorption energies and we consequently choose three different starting geometries to be optimised, with gold in direct contact with oxygen atoms. The first one corresponds to Au on top of O(1) and relaxed to give a Au–O(1) distance of 2.21 Å and adsorption energy of -1.44 eV without BSSE. The second starting geometry corresponds to the gold atom placed at equal distances from O(1), O(10) and O(11). This configuration is expected to give the highest adsorption energy as gold is in contact with three oxygens. However, during the optimisation the gold atom moves out of the kink to become bound to O(1) and O(2) (figure 6.18 and 6.19), this geometry corresponding to the third configuration we have tried. Adsorption on the terrace has also been tested but results are very similar to the adsorption of Au on the oxygen of the regular

MgO(001) surface. As a result, we focus on the configuration shown in figure 6.19, corresponding to the most stable adsorption state of Au at the kink site of MgO(1 3 10). Studying gold adsorption at steps of MgO, Del Vitto *et al.*[13] found a similar configuration for the most stable adsorption site, with the gold atom interacting with both the four-coordinated oxygen of the step and the five-coordinated oxygen of the lower plane. As we are dealing with a kink, the four-coordinated oxygen of the step becomes three-coordinated (O(1) in figure 6.19). We obtain an adsorption energy E_{ads}= -1.08 eV (-1.54 eV without BSSE corrections) which is 28% higher than on the terrace. Del Vitto *et al.*[13] reported a binding energy of -1.26 eV at the MgO step, 40% higher than on their terrace site. Our structure is shown in figure 6.18 with all the atoms included in the calculation representing a total of 201 atoms. Details of the geometry are given in figure 6.19.

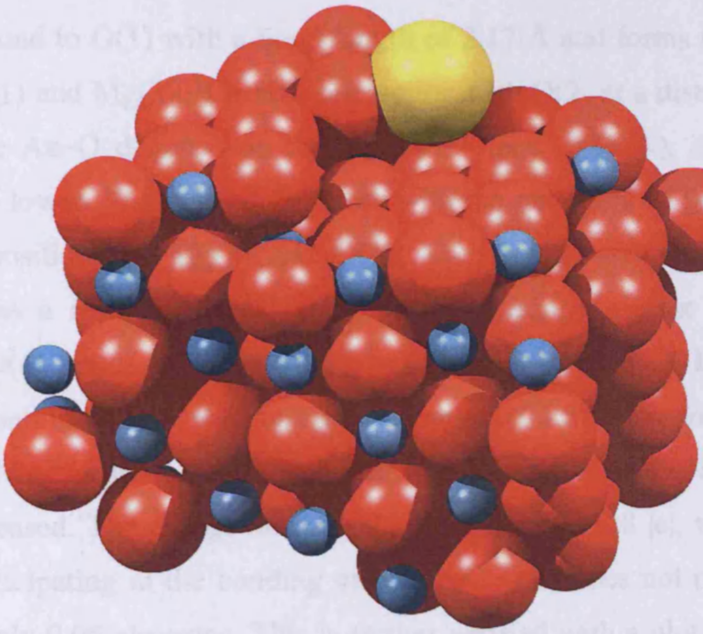

Figure 6.18 Three-dimensional representation of the gold atom adsorbed at the oxygen kink site of the MgO(1 3 10) surface. All the atoms of the system are represented, totally 201 atoms, *i.e.* 100 Mg, 100 O and one Au. Oxygen atoms in red, magnesium in blue.

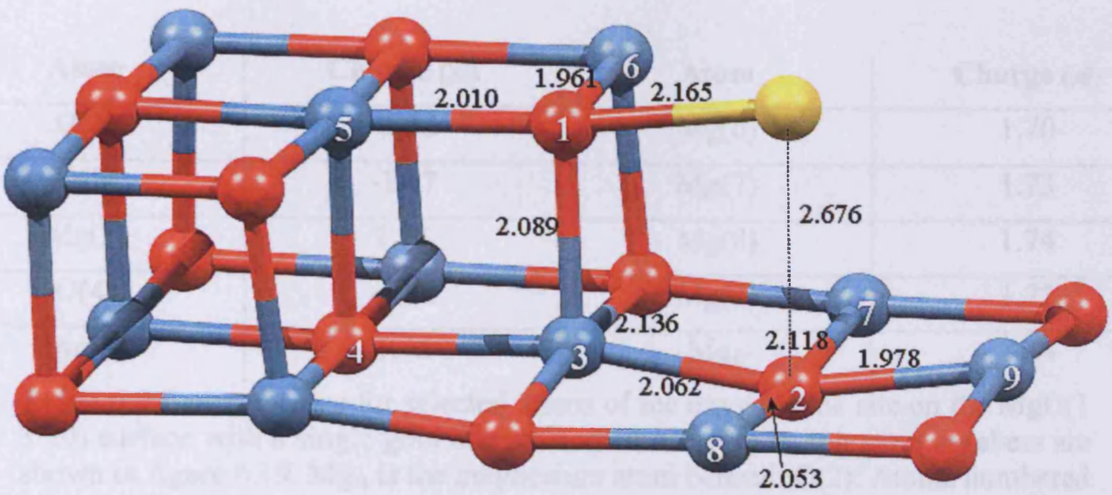

Figure 6.19 Detail of the gold atom adsorbed at the oxygen kink site of the MgO(1 3 10) surface. Selected distances are displayed in Å. Oxygen atoms in red, magnesium in blue. d(O–Mg)= 2.043 Å for the perfect surface.

Gold is bound to O(1) with a bond length of 2.17 Å and forms a bond angle θ of 96° with the atoms O(1) and Mg(3). It is also interacting with O(2) at a distance of 2.68 Å which is longer than the Au–O distance on the regular surface (2.33 Å), showing the Au–O(2) interaction here is lower. The main differences with the geometry of the clean MgO(1 3 10) surface are the positions of Mg(3) and O(1). The upward movement of Mg(3) is less pronounced and as a result, d(Mg(3)–O(1)) is increased by almost 0.1 Å when gold is adsorbed. Also, O(1) bonds to Mg(5) and Mg(6) are lengthened. A Bader charge analysis provides an explanation for this. O(1) has now a charge of -1.38 |e|, representing a loss of 0.27 electrons after gold adsorption. As a result, the bonds involving O(1) are weakened and the bond lengths increased. The charge on the gold atom being -0.28 |e|, we conclude that only O(1) is really participating in the bonding mechanism. O(2) does not play an important role since it has lost only 0.05 electrons. This is further verified with a plot of the spin density in figure 6.21 and the charge difference density in figure 6.20.

Atom	Charge (|e|)	Atom	Charge (|e|)
O(1)	**-1.38**	Mg(6)	1.70
O(2)	-1.67	Mg(7)	1.73
Mg(3)	1.75	Mg(8)	1.74
O(4)	-1.74	Mg(9)	1.72
Mg(5)	1.75	Mg$_B$	1.74

Table 6.9 Bader charges for selected atoms of the oxygen kink site on the MgO(1 3 10) surface with a single gold atom adsorbed. Corresponding atom numbers are shown in figure 6.19. Mg$_B$ is the magnesium atom beneath O(2). Atoms numbered according to figure 6.19.

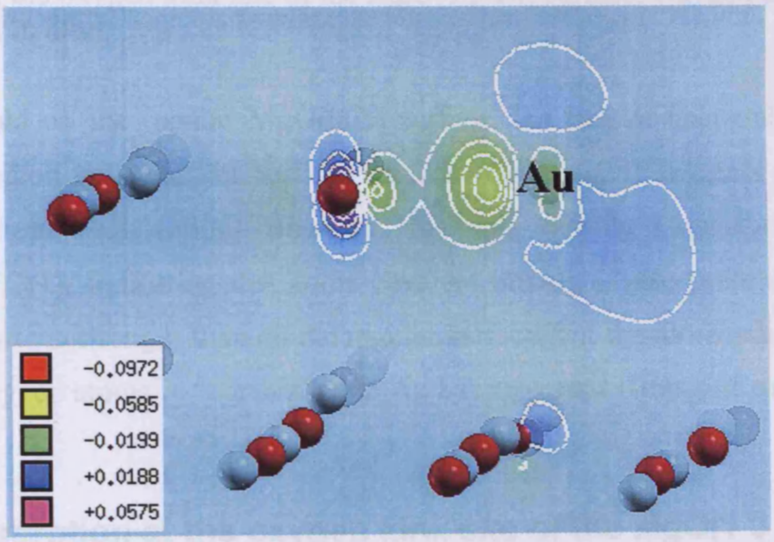

Figure 6.20 Charge density difference for a single gold atom adsorbed at the oxygen kink site of the MgO(1 3 10) surface. Red/green colours represent charge depletion and blue/purple colours, charge accumulation. Lines are drawn in intervals of 0.01 e a_0^{-3}. Oxygen atoms in red, magnesium in blue.

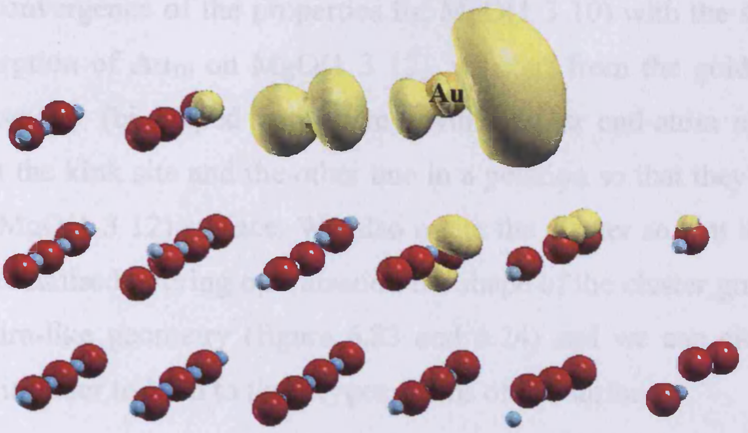

Figure 6.21 Spin density iso-surface at 0.003 e a_0^{-3} for a single gold atom adsorbed at the oxygen kink site of the MgO(1 3 10) surface. Oxygen atoms in red, magnesium in blue.

As for gold on the regular MgO(001) surface, the lack of accumulation of electron density in the region between Au and the surface (figure 6.20) suggests that the bonding comes mainly from polarization. However, the spin density (figure 6.21) is partially delocalised over O(1), indicating that some covalent mixing is also present. The binding of gold at the kink site is stronger than on the regular surface, but the mechanism is similar, only the number of oxygen atoms in "contact" with Au has increased (from one to two).

6.5.3 Au_{10} adsorption at the oxygen kink site of the MgO(1 3 12) surface

We have shown that a ten atom gold cluster can adsorb on MgO(001) and present different configurations, depending on the presence of an F centre. The kinked surface exhibits oxygen atoms at the kink site which are readily available to gold atoms. As a result, we expect a strong interaction with Au_{10}. We change to MgO(1 3 12) from MgO(1 3 10) as the cluster occupies more space than a single atom and interaction with its neighbour repeating units has to be avoided. We also checked that the single gold atom adsorption on the bigger slab gives the same results as on the smaller one. The MgO(1 3 12) slab we choose (figure 6.22) is made of 250 atoms and reaches the limits of DFT with diagonalisation methods on current supercomputers, most calculations presented here were run on HPCx. The MgO(1 3 16) surface with 320 atoms was also tested, but unfortunately, this system size takes us beyond any reasonable computational time, even using 64 processors on an IBM High Performance Computing machine.

Overall, the geometrical properties of MgO(1 3 12) are the same as MgO(1 3 10) which shows the convergence of the properties for MgO(1 3 10) with the size of the system. To study the adsorption of Au_{10} on MgO(1 3 12), we start from the gold cluster in its gas phase optimal geometry (bi-capped anti-prism), with an Au end-atom of one of the two pyramids placed at the kink site and the other one in a position so that they form a parallel to the normal of the MgO(1 3 12) surface. We also rotate the cluster so that its interaction with oxygen atoms is maximised. During optimisation the shape of the cluster gradually changes to adopt a dodecahedra-like geometry (figure 6.23 and 6.24) and we can clearly see the gold atoms rearranging in order to bind to the oxygen atoms of the surface.

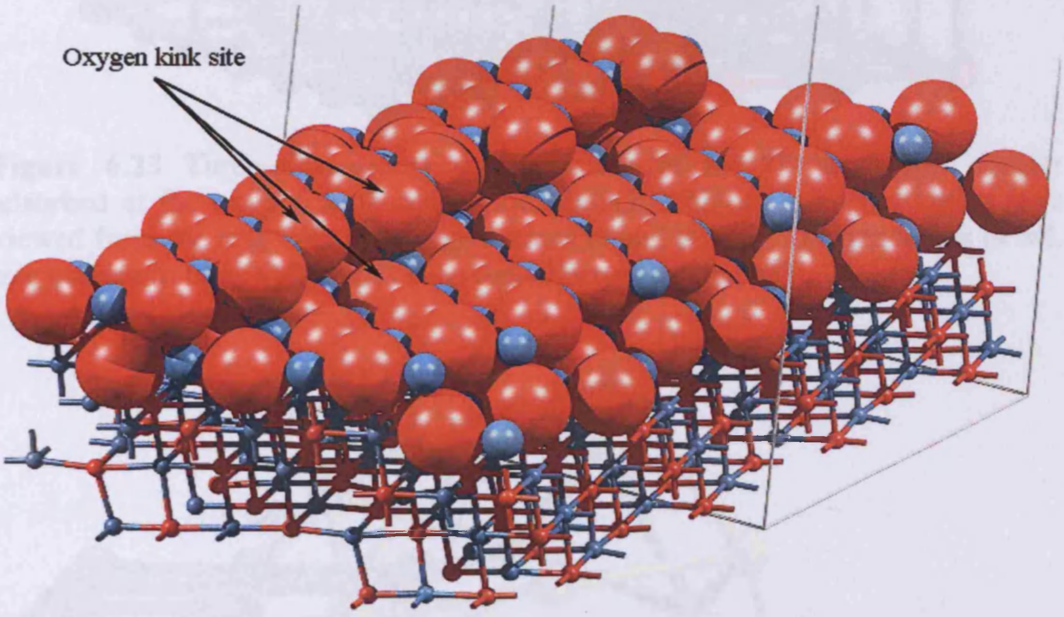

Fig 6.22 The MgO(1 3 12) kinked surface repeated twice along the direction containing the kink sites. The bottom of the slab is represented with balls and sticks. The periodic cell of the studied system is shown in grey lines.

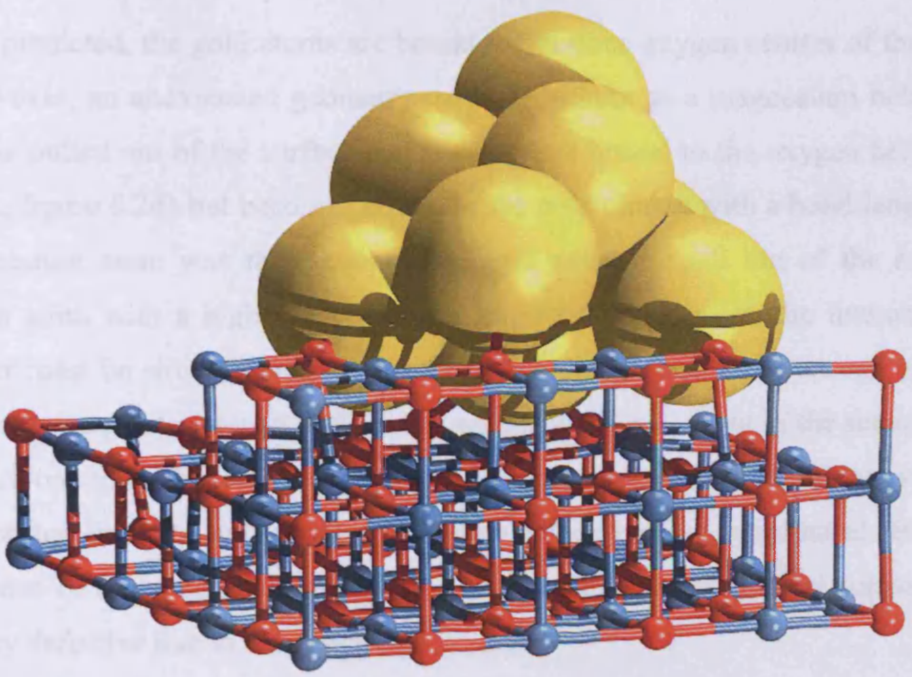

Figure 6.23 Three-dimensional representation of the 10 atom gold cluster adsorbed at the oxygen kink site of the MgO(1 3 12) surface. The kink site is viewed from the rear with the oxygen atoms bound to Au_{10}. Oxygen atoms in red, magnesium in blue. Only part of the model is represented here.

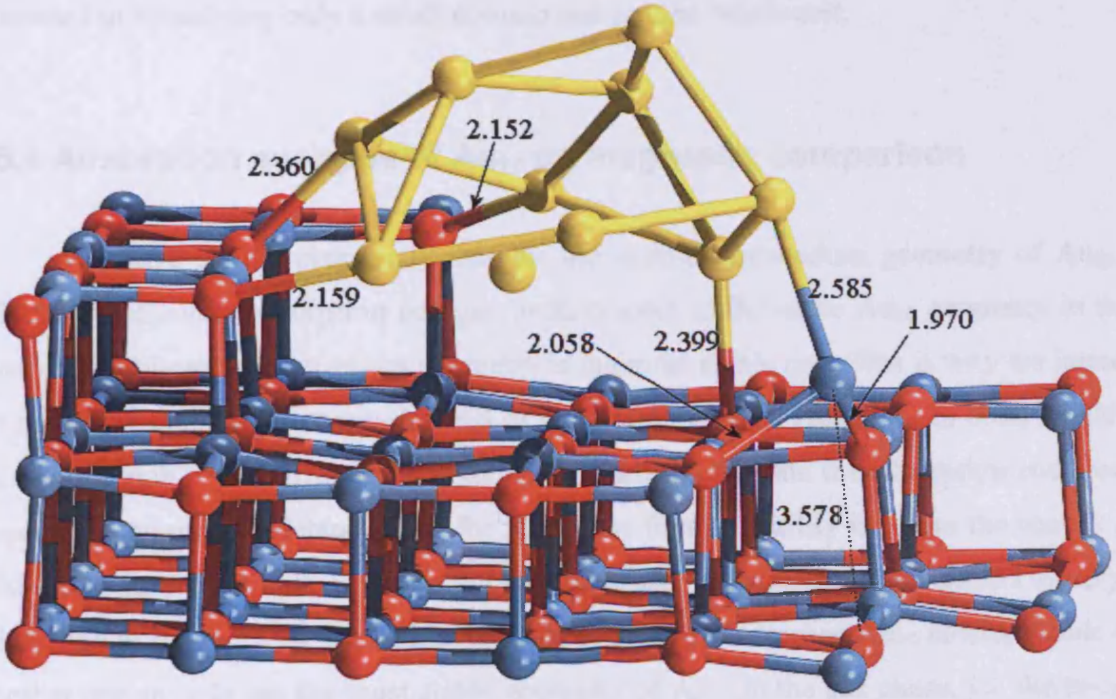

Figure 6.24 Detail of the 10 atom gold cluster adsorbed at the oxygen kink site of the MgO(1 3 12) surface. Selected distances are displayed in Å. Oxygen atoms in red, magnesium in blue.

As predicted, the gold atoms are bound to the three oxygen centres of the kink (figure 6.23). However, an unexpected geometry variation occurs as a magnesium belonging to the next kink is pulled out of the surface and is no longer bound to the oxygen below it (d(Mg–O)=3.58 Å, figure 6.24) but becomes bound to the gold cluster with a bond length of 2.59 Å. This magnesium atom was three-coordinated and easier to pull out of the surface than a magnesium atom with a higher coordination number. Nonetheless, the interaction with the gold cluster must be strong enough to create such a displacement and we can expect Au_{10} to be negatively charged to interact sufficiently with Mg and pull it out of the surface. Of course, if the terrace on which the Au_{10} cluster is put down was bigger, the interaction with Mg would probably be too weak to pull it out as Mg would then be five-coordinated. However, such high densities of kinks can be expected in the materials used as catalyst supports which are intrinsically defective due to their high surface area.

The slab we use to model the MgO(1 3 12) surface being non-orthogonal, we cannot convert the SIESTA *.RHO output file to a *.cube file and perform a Bader charge analysis or plot the charge difference density. A modification of the code used for the conversion is on its way but this involves some sophisticated interpolation. The main idea being that one might be interested in visualising only a small domain and not the whole cell.

6.5.4 Adsorption energies of Au_{10} on magnesia: comparison

We have shown previously that for the semi-dodecahedron geometry of Au_{10}, it is difficult to calculate adsorption energies with respect to the same Au_{10} geometry in the gas phase as the bi-capped anti-prism geometry is the most stable one. This is why we introduced the notion of interaction energy instead of adsorption energy. However, in order to compare the relative stability of different structures, we need to calculate the adsorption energies with respect to a common reference state for Au_{10}. The first possibility is to use the energy of ten gold atoms in the Au bulk structure but the adsorption energies are then shifted to very high values due to the fact that the bulk is less stable than any adsorbed Au_{10} cluster (Table 6.10). Another option is to use the most stable geometry of Au_{10} in the gas phase, *i.e.* the bi-capped anti-prism, so that the adsorption energies have more physical sense.

	E_{ads} (eV) for the reference state:	
	Bulk (10 atoms)	**$Au_{10(g)}$** [a]
Bi-capped anti-prism on F centre (facing Mg)	-26.70	**-2.88**
Semi-dodecahedron on perfect MgO(001)	-24.70	**-0.88**
Semi-dodecahedron on F centre	-27.53	**-3.71**
Au_{10} at the oxygen kink site of MgO(1 3 12)	-34.62	**-10.80**

Table 6.10 Adsorption energies on magnesia for Au_{10} in different structures (BSSE corrections included). Note: [a] Reference state corresponding to the bi-capped anti-prism Au_{10} cluster in the gas phase.

We can see that the highest adsorption energy, and by far, is found for Au_{10} at the oxygen kink site of MgO(1 3 12). This shows a strong interaction of gold with magnesia. The adsorption energy on the F centre of MgO(001) is higher for the semi-dodecahedron geometry than it is for the bi-capped anti-prism (0.83 eV difference). Finally, the perfect surface does not represent a strong adsorption support for Au_{10}, with an adsorption energy 2.83 eV smaller for semi-dodecahedron Au_{10} than it is on the F centre.

6.6 Au oxidation state: effects on CO adsorption

Although it is now well known that supported gold catalysts are very active for several chemical reactions, there is an ongoing debate regarding the active oxidation state of Au and the mechanisms behind its activity. CO oxidation is an important reaction on supported Au but the oxidation state of the active species is unclear. Calculations by Molina and Hammer show that CO oxidation on TiO_2 supported Au is possible for Au in the Au^0 state as small particles.[52] However, Guzmann *et al.* found that the rate is poor for pure Au^0 and requires mixture of Au^0 and Au^I.[53] Haruta[54] reported an activation energy for CO oxidation which is practically zero whereas Hammer *et al.*[52] calculated a low but significant barrier. Cox *et al.*[55] studied the reactivity and saturation of small gold clusters (cations, neutrals and anions) towards several molecules and found that the reactivity not only depends strongly on cluster size but also on the cluster charge state.

Molecular adsorption of CO on other metallic surfaces is also well known for its use as a probe, since adsorbed CO usually gives rise to strong absorptions in infrared spectra at the (C–O) stretching frequency. The CO stretching frequency can provide information on the surface coordination of the molecule.[56]

To look at different oxidation states we employ a systematic set of calculations. Since supported gold is prepared by deposition from aqueous media, we will use OH^- as a common ligand and study the series Au, AuOH, $Au(OH)_2$, $Au(OH)_3$ adsorbed on flat and kinked MgO surfaces to represent Au^0, Au^I, Au^{II} and Au^{III} respectively. We will first use a single gold atom and then a ten atom cluster. The use of a single gold atom model is important to clearly understand the trends found for Au oxidation state and will provide us with a reference with which to compare larger systems.

6.6.1 Single gold atom

The free CO molecule in the gas phase was optimised at the same level of theory as used in surface calculation (DZP basis set with a cutoff of 0.01 Ry) giving a bond length of 1.15 Å and a vibrational stretching frequency $\upsilon(CO)= 2107\ cm^{-1}$. The experimental vibrational frequency[57] for gas phase CO is 2143 cm^{-1} so we apply a correction factor of 2143/2107 (1.017) to all our calculated $\upsilon(CO)$ from here. The Bader charges are also computed, with $q(C)= +1.74\ |e|$ and $q(O)= -1.74\ |e|$. The CO molecule is actually a peculiar case as there is a seeming contradiction between the different electronegativities of C and O and the small dipole moment for this system (calculated to be 0.25 D here, 0.27 D with MP2[58] and measured to be 0.12 D experimentally). This small dipole moment can lead to believe that the atoms should be roughly electroneutral, based on the simple idea that the dipole moment is the result of separation of charge. There is a large charge transfer from C to O but there is also a large opposing polarisation of the remaining charge on the carbon atom (unlike what one would expect for spherical ions). It is this large opposing polarisation which produces a large dampening of the dipole moment, cancelling the contribution from charge transfer, and making the overall dipole nearly zero.

In order to test the validity of our method, we first study the test case Au_2CO in the gas phase and compare our results to a previous study[59] employing the Born–Oppenheimer local-spin-density molecular dynamics method[60] (Table 6.11).

	d(Au–Au) (Å)	**d(Au–C) (Å)**	**d(C–O) (Å)**	**υ(CO) (cm^{-1})**
This work	2.51	1.95	1.159	2140
BO–LSD–MD[59]	2.52	1.93	1.149	2147

Table 6.11 Bond lengths and CO stretching vibrational frequency for a single CO molecule adsorbed on Au_2 in the gas phase with a linear “end-bonded” structure Au_2–CO (figure 6.25)

Au_2CO is a gas phase species in which Au is in the zero oxidation state. Our results agree well with the ones from Häkkinen and Landman[59] and the calculated υ(CO) only differs by 0.3 %. The geometry is linear, *i.e.* the Au-C-O angle is 180°. Recently, Jiang and Xu[61] observed from the reaction of laser-ablated gold atoms with CO in excess argon at 7 K, an infrared absorption of 2131.9 cm^{-1}, assigned to Au_2CO. The difference between our calculated vibrational frequency (2140 cm^{-1}) and this observation is only 8.1 cm^{-1}. In figure 6.25 we plot the geometry of Au_2CO and the charge density difference supporting the bonding mechanism proposed by Häkkinen and Landman. This mechanism is synergic, since the drift of metal electrons, referred to as back-bonding, into CO orbitals, will tend to make the CO as a whole negative, hence to increase its basicity via the *s* orbital of carbon; at the same time the drift of electrons to the metal in the O–bond tends to make the CO positive, thus enhancing the acceptor strength of the *p* orbitals. As a result and up to some point, the effects of *s* bond formation strengthen the *p* bonding, and *vice versa.*[62]

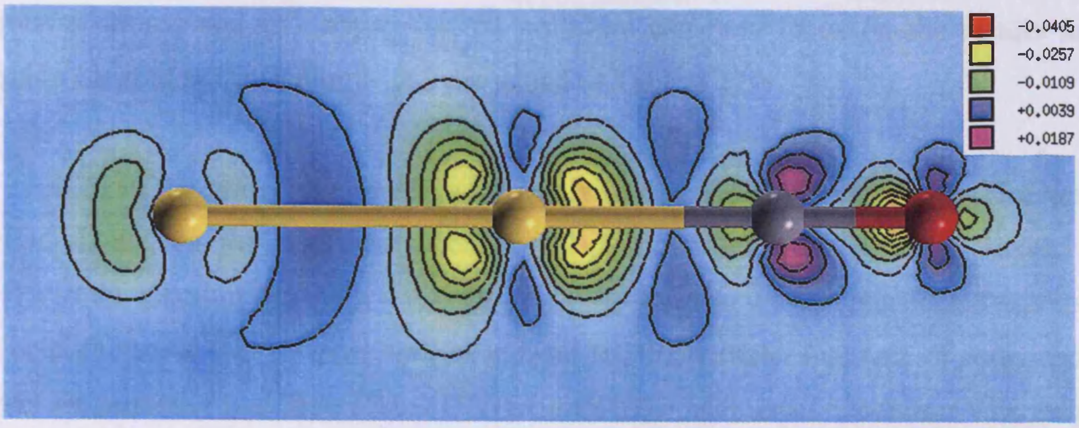

Figure 6.25 Charge density difference for the Au_2CO complex. Red/green colours represent charge depletion and blue/purple colours, charge accumulation. Lines are drawn in intervals of 0.005 e a_0^{-3}. Oxygen atoms in red, carbon in grey.

	Au^0 (F centre)	**Au^0 (on O_{5c})**	**$Au^I(OH)$ (on kink)**	**$Au^{II}(OH)_2$**	**$Au^{III}O(OH)$**	**$Au^{III}(OH)_3$**
q(Au) (|e|) without CO	-1.12	-0.31	+0.22	+0.56	+0.68	+0.81
q(Au) (|e|)	-1.21	-0.03	+0.40	+0.69	+0.59	+0.92
E_{ads} (eV)	-0.66	-1.41	-2.17	-0.44	-0.51	2.44
without BSSE	-0.93	-1.67	-2.42	-0.67	-0.73	2.18
d(C–O) (Å)	1.186	1.189	1.173	1.168	1.169	1.158
d(C–Au) (Å)	2.122	2.270	2.190	2.090	2.097	1.998
Au-C-O (deg)	147.5	134.3	120.1	133.5	130.3	170.6
δq(C) (|e|)	-0.23	-0.17	-0.06	+0.07	+0.03	-1.35
δq(O) (|e|)	-0.06	-0.07	-0.10	-0.11	-0.09	+1.27
δq(CO) (|e|)	-0.29	-0.24	-0.16	-0.04	-0.06	-0.08
υ(CO) (cm^{-1})	1825	1824	1945	1997	1986	2114

Table 6.12 Calculated properties for CO adsorbed onto monoatomic gold on MgO with different oxidation states and atomic charges for Au. q(X) represents the Bader charge of species X, δq(X) is the change of charge of species X between free CO molecule in the gas phase and adsorbed CO, υ(CO) is the stretching vibrational frequency of CO once adsorbed on Au. The other properties are self-explanatory. q(C)= +1.74 |e| and q(O)= -1.74 |e| for CO in the gas phase.

Having verified that our model is capable of treating both gold adsorption on MgO (previous sections) and CO adsorption on gold, we can now focus on the results for CO adsorption on gold supported on MgO, presented in Table 6.12.

$AuCl_3$ is the main species for gold catalysts but under pH conditions of deposition $Au(OH)_3$ should be the dominant species.[63] It is possible that H_2O is eliminated from $Au(OH)_3$ in the reaction $Au(OH)_3 \rightarrow AuO(OH) + H_2O$ and so we also considered this species. It has been proposed that cationic species present at the perimeter interface of supported gold catalysts are probably $Au(OH)_3$ / $AuO(OH)$ or $Au(OH)$, under usual conditions wherever H_2O is present at concentrations above 1 ppm.[64]

When we first started the study of CO on $Au^I(OH)$ on the flat MgO(001) surface, the optimised geometry (figure 6.26) revealed that Au detaches from its five-coordinated oxygen, at a new distance of 2.60 Å, *vs.* 2.10 Å without CO. As a result, the distance of Au to the oxygen atom of the hydroxyl group decreased by more than 7 %, from 2.22 Å to 2.05 Å. It then becomes difficult to compare the properties to the ones calculated for the rest of the complexes. For example, the opposite was obtained for $Au^{II}(OH)_2$, where $d(Au–O_{5c})$ decreased by 2.2 % and d(Au–OH) increased by 2.2 % upon CO adsorption. We then decided to switch to our previously optimised gold atom on the kinked surface MgO(1 3 10). As for the flat surface, one hydroxyl group was added to model Au^I.

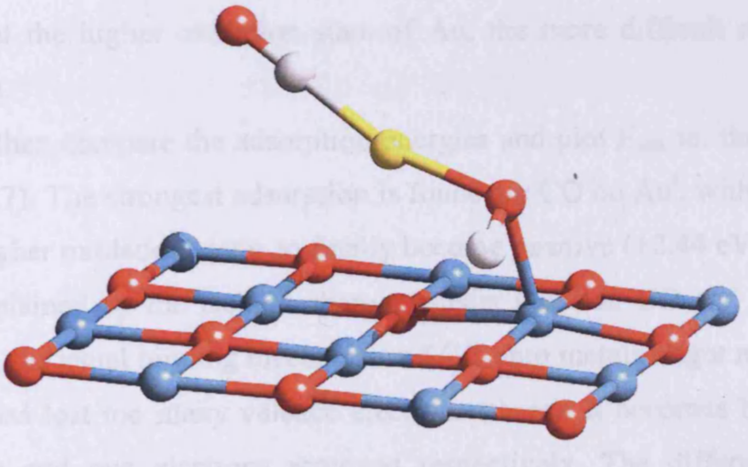

Figure 6.26 Geometry of the Au(OH) complex on the MgO(001) surface with one CO molecule adsorbed onto Au. Au-C-O= 179.5°; $\upsilon(CO)$= 2122 cm^{-1}. Oxygen atoms in red, magnesium in blue, carbon in grey and hydrogen in white.

In the rest of this subsection, we will not detail the results oxidation state by oxidation state, but instead, compare the calculated properties so that it is possible to extract trends, which is one of the main goals of this study. As a point of comparison, on the close-packed surface Au(111), CO adsorbs on the top site with E_{ads}= +0.12 eV using RPBE[65] and -0.24 eV using PW91[66], with d(C–O)= 1.15 Å and υ(CO)= 2072 cm^{-1} (including a correction factor 2143/2136 since the experimental value is 2143 cm^{-1}).[67]

The first important calculated property is the charge of the gold atom without any CO molecule. As shown in Table 6.12, the charge increases from -1.12 |e| when Au is on the F centre, to +0.81 |e| for Au(III) represented by $Au(OH)_3$. We showed previously that the important charge for the F centre system comes from a charge transfer from the vacancy to the gold atom, which could then be considered as Au^-. The Au(0) atom adsorbed on an five-coordinated oxygen centre O_{5c} has a charge of -0.31 |e|, much less than that on the F centre as the charge transfer decreases. As soon as we switch to cationic gold $Au^I(OH)$, the charge on Au becomes positive (+0.22 |e|) but not exactly +1 |e| as gold has a semi-covalent bond with the hydroxyl group. This positive charge increases with the oxidation state; for Au(II) it is +0.56 |e| and +0.81 |e| for Au(III). This continuous increase of charge with formal oxidation state is consistent with our model to represent the different oxidation states of gold.

When CO is adsorbed onto Au, the gold atom looses electrons and this reflects in its calculated Bader charge (Table 6.12), with a loss of 0.28 electrons for Au, 0.18 electrons for $Au^I(OH)$, 0.13 electrons for $Au^{II}(OH)_2$ and 0.11 electrons for $Au^{III}(OH)_3$. There is however an exception with the F centre system where Au has actually gained 0.09 electrons after CO adsorption, due to the F centre acting as a reservoir of electrons. The trend in the electron loss also reflects that the higher oxidation state of Au, the more difficult it becomes to obtain electrons from it.

We can then compare the adsorption energies and plot E_{ads} *vs.* the charge on the gold atom (figure 6.27). The strongest adsorption is found for CO on Au^I, with E_{ads}= -2.17 eV, and decreases for higher oxidation states to finally become positive (+2.44 eV) in the case of Au^{III}. This can be explained by the lack of charge transfer between CO and Au shown in figure 6.33c. For Au^{III}, the usual binding mechanism of CO onto metals might not apply anymore as the gold atom has lost too many valence electrons (three). It becomes better for Au(II) and Au(I) with two and one electrons removed respectively. The difference of 1.73 eV in adsorption energy between Au(I) and Au(II) can be explained by analysing the charge transfer to the CO molecule δq(CO). δq(CO) decreases constantly with q(Au) decreasing, except for Au^{III} which represents a special case. The CO molecule can take up as much as 0.29 electrons for Au^0 F centre and this dramatically decreases to 0.04 electrons in the case of Au(II). This trend is also directly reflected in the calculated vibrational frequencies of CO stretching. The absorption frequency of CO adsorbed on metal surfaces depends strongly on the population of the 2π* orbital, as occupation of this anti-bonding orbital weakens the C–O bond. To assess this, d(C–O) is quoted in Table 6.12. Furthermore, the C–O stretch vibration shifts to lower frequency in a manner that is correlated with increased charging of the complex, as well as with the estimated increase in the population of the anti-bonding state. The latter is given by the calculated excess electronic charge on the adsorbed molecule CO as it results from back-donation into the CO(2π*) anti-bonding state.[11] The difference in the degree of back-donation is manifested in a variation of the stretch frequencies of the adsorbed CO molecules. Finally, CO adsorbs more strongly on Au^0 O_{5c} than it does on Au^0 F centre. A detailed explanation for the bonding mechanism of CO on metals is given in the appendix.

Interestingly, the Au-C-O angle follows the same trend as E_{ads} (figure 6.28) and flattens when the electron transfer between Au and CO becomes smaller. It is believed the electron promotion to only one of the initially degenerated CO(π*) orbitals breaks the symmetry.[59] Although CO is traditionally considered to adsorb perpendicularly to a metal surface, a recent STM study reported tilted adsorption geometries for CO ligands of FeCO and $Fe(CO)_2$ complexes on Ag(110) being caused by the local electronic structure of the Fe atom[68]. A theoretical study of these systems by Yuan *et al.*[69] based on Frontier Orbitals Theory[70] (FOT) found these tilted configurations occur for metals presenting partially occupied *d* orbitals, which is not the case of Au in its ground state. As already reported by Häkkinen and Landman[59] for the Au_2^- anion, the adsorption angle can be an indicator of the charge state of the host, in our case the gold atom supported on MgO(001).

Figures 6.29 to 6.33 show the geometries for both adsorbed CO and the support alone. Plots of the charge density difference are also given.

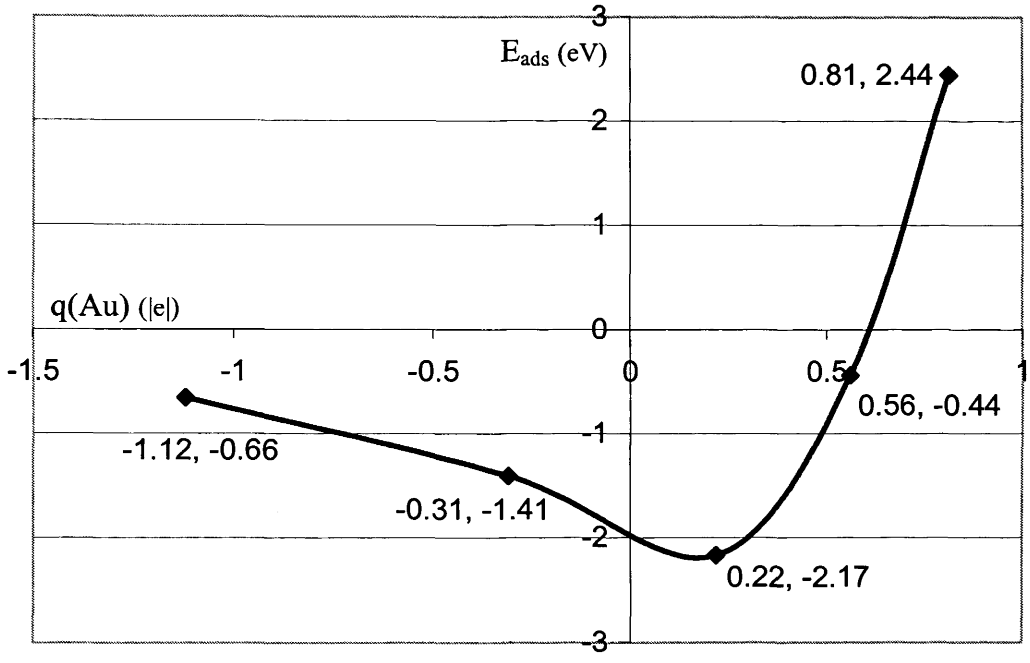

Figure 6.27 Adsorption energy (E_{ads}) of CO on a single gold atom supported on MgO, as a function of the charge of this gold atom without CO, q(Au).

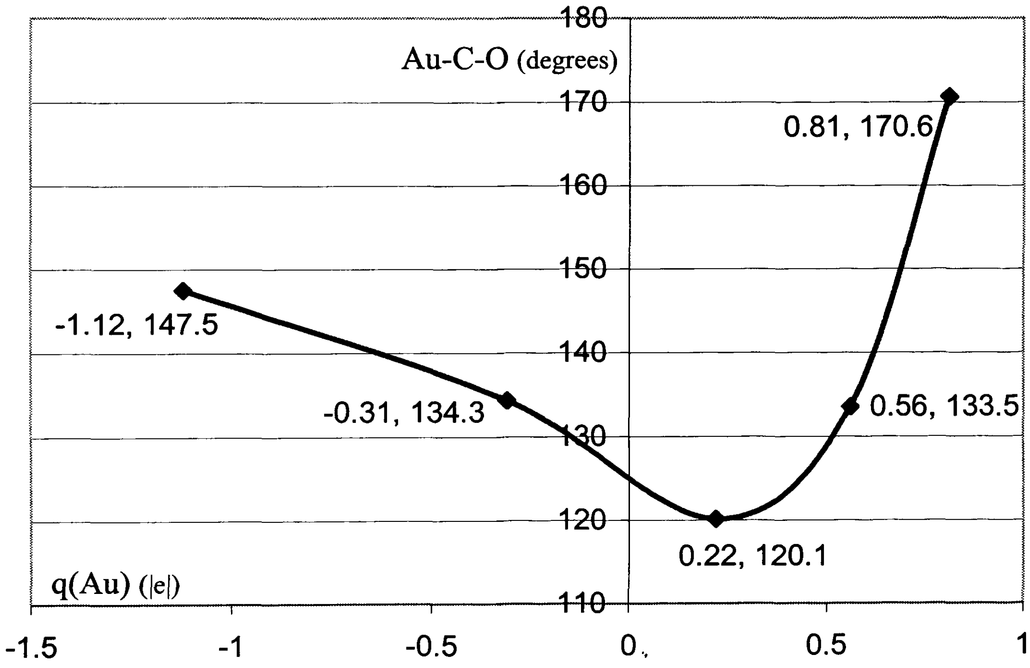

Figure 6.28 Bond angle Au-C-O for CO on a single gold atom supported on MgO, as a function of the charge of this gold atom without CO, q(Au).

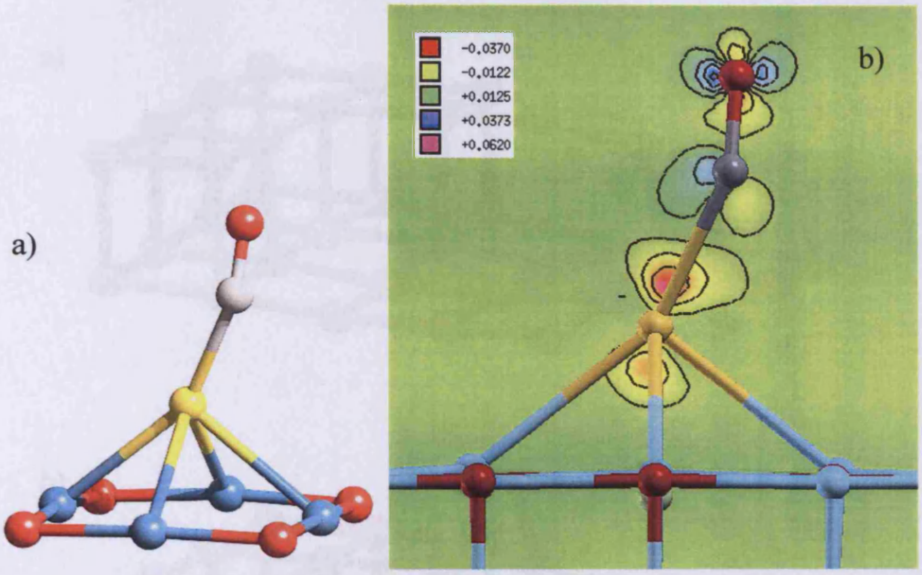

Figure 6.29 Geometry (a) and charge density difference (b) for CO adsorbed on Au_1 at the F centre of the MgO(001) surface. Red/green colours represent charge depletion and blue/purple colours, charge accumulation. Lines are drawn in intervals of 0.01 e a_0^{-3}. Oxygen atoms in red magnesium in blue, carbon in grey.

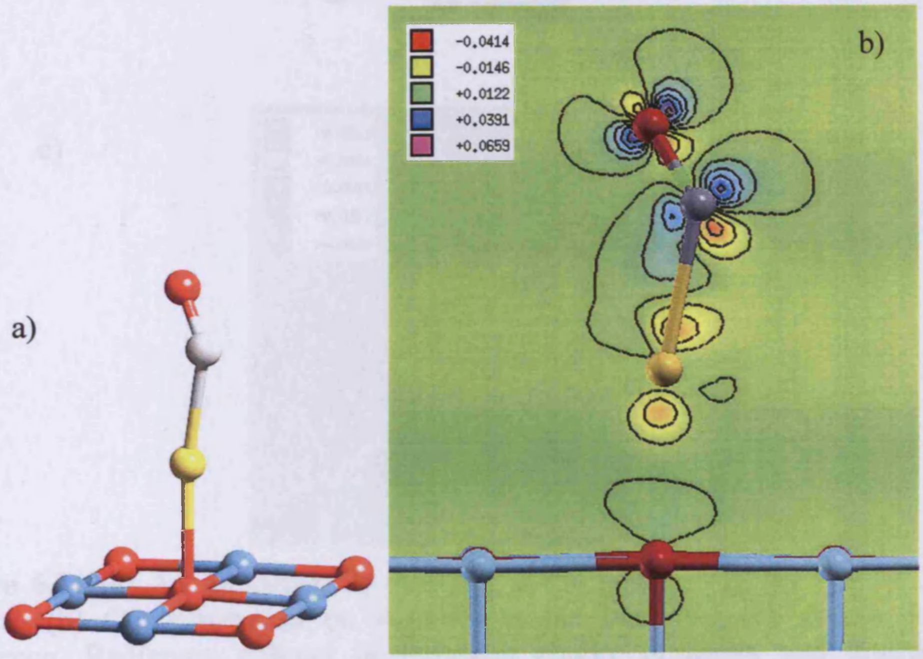

Figure 6.30 Geometry (a) and charge density difference (b) for CO adsorbed on Au_1 at a five-coordinated oxygen centre O_{5c} of the MgO(001) surface. Red/green colours represent charge depletion and blue/purple colours, charge accumulation. Lines are drawn in intervals of 0.01 e a_0^{-3}. Oxygen atoms in red magnesium in blue, carbon in grey.

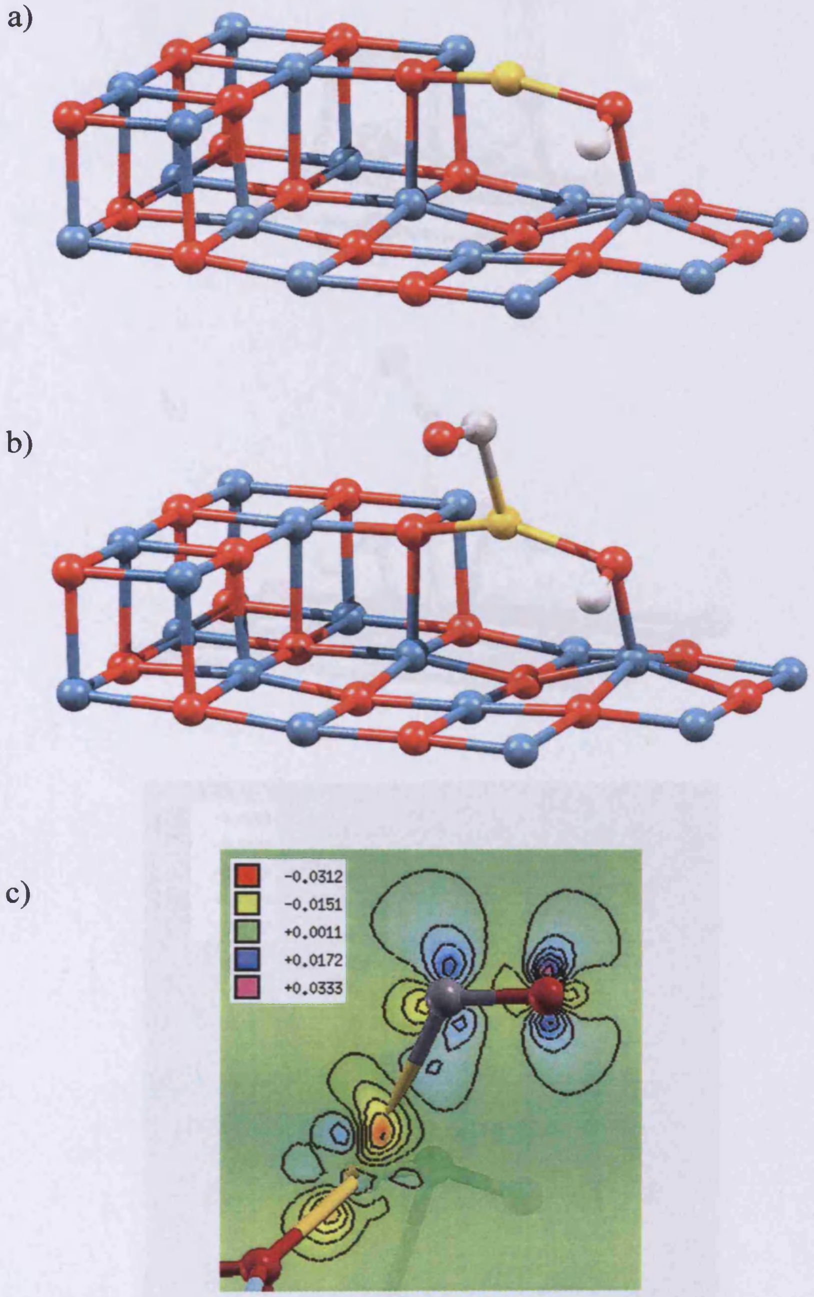

Figure 6.31 (a) Au^I modelled by Au(OH) at the kink site of the MgO(1 3 10) surface. (b) CO adsorption on Au(OH) at the kink and (c) charge density difference. Red/green colours in represent charge depletion and blue/purple colours, charge accumulation. Lines are drawn in intervals of 0.05 $e\ a_0^{-3}$. Oxygen atoms in red magnesium in blue, carbon in grey.

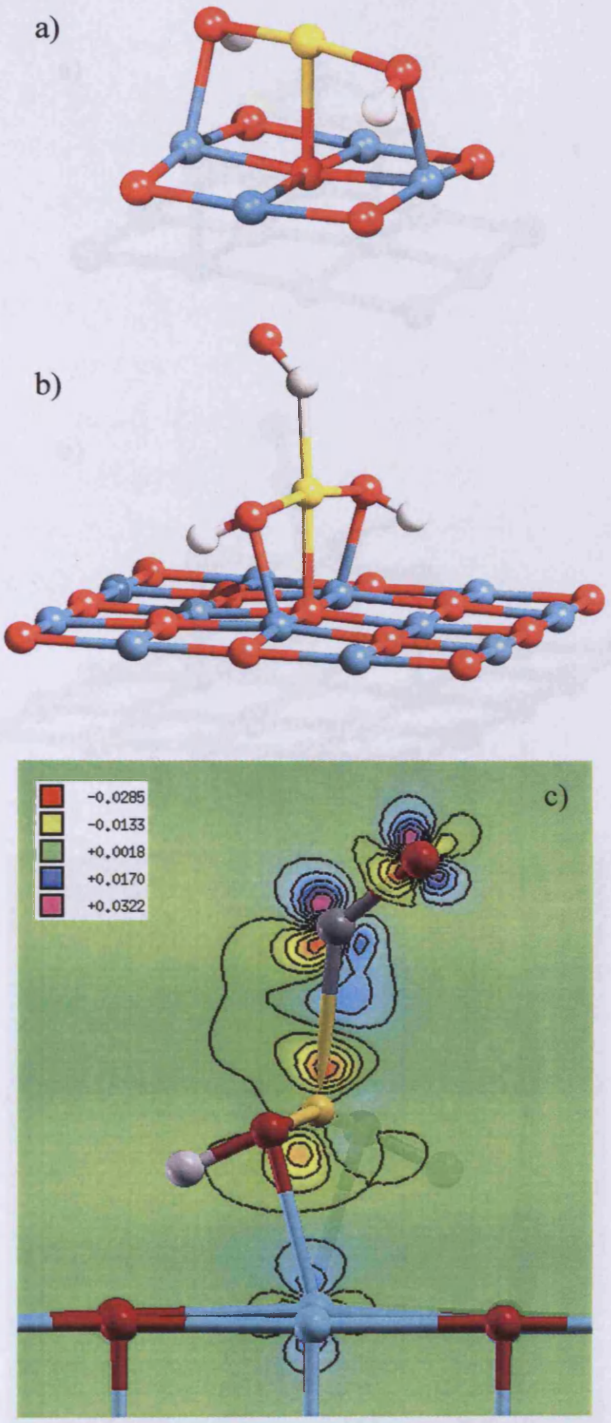

Figure 6.32 (a) Au^{II} modelled by $Au(OH)_2$ on the non-defective MgO(001) surface. (b) CO adsorption on $Au(OH)_2$ and (c) charge density difference. Red/green colours in represent charge depletion and blue/purple colours, charge accumulation. Lines are drawn in intervals of 0.005 e a_0^{-3}. Oxygen atoms in red magnesium in blue, carbon in grey.

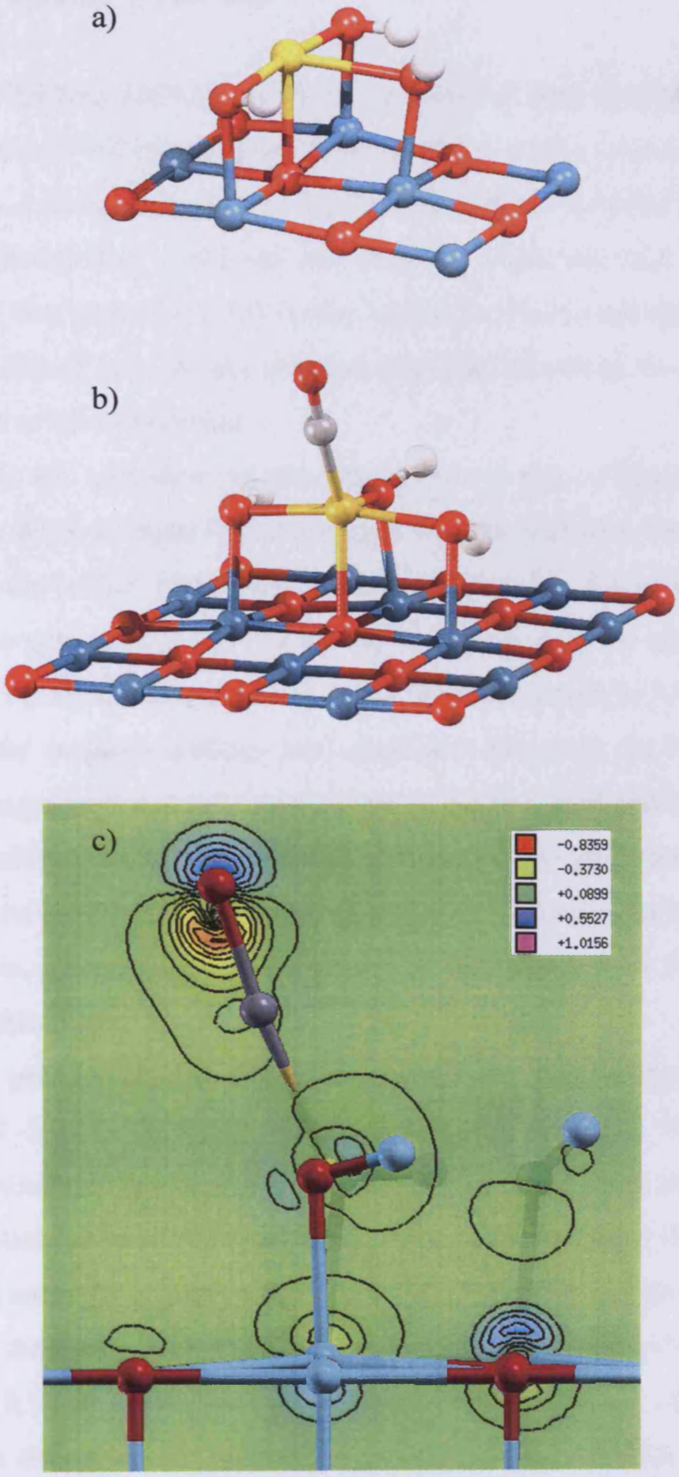

Figure 6.33 (a) Au^{III} modelled by $Au(OH)_3$ on the non-defective MgO(001) surface. (b) CO adsorption on $Au(OH)_3$ and (c) charge density difference. Red/green colours in represent charge depletion and blue/purple colours, charge accumulation. Lines are drawn in intervals of 0.1 e a_0^{-3}. Oxygen atoms in red magnesium in blue, carbon in grey.

6.6.2 Au_{10} with one or three CO

Now that a binding mechanism for CO adsorption onto Au_1/MgO has been proposed and that the relevance of Au charging has been assessed, we can move to a more complicated system, *i.e.* the Au_{10} cluster supported on MgO(001), with and without F centre.

We have shown that F centres can play an important role by acting as electron reservoirs. We will first adsorb one CO on the supported cluster and then add two more CO in order to test the ability of Au_{10} to take on more than one adsorbate, *i.e.* we will put the system in a situation closer to the experiment.

The CO molecules are adsorbed on the top atoms of Au_{10} (figure 6.34 and 6.35). The geometry resulting from a single CO adsorption is quite different for the perfect and the F centre surface. For the perfect MgO(001) surface (figure 6.34), the gold atoms underneath the Au–CO group have split with a distance d(Au(2)–Au(3))= 4.27 Å. On the contrary, in the F centre case (figure 6.35), this distance is 2.73 Å, to be compared to 2.87 Å (2.78 Å) for Au_{10} on F centre (perfect surface) without any adsorbate. However, in both cases, a structural change occurs during adsorption (or in the course of the reaction) and is a manifestation of the "structural fluxtionality" of clusters.[71] Similar splitting of two gold atoms is seen for three CO molecules adsorption in the perfect surface system, with d(Au(2)–Au(3))= 4.45 Å, while the F centre system, again, presents an almost unchanged distance at 2.74 Å. Calculated properties are presented in Table 6.13.

As studied previously, the charge on the gold cluster, q(Au_{10}), is -0.88 |e| on the perfect surface and -2.19 |e| on the F centre, without any adsorbate. When CO molecules are adsorbed, the magnitude of this charge decreases for both the perfect and the F centre surfaces. After three CO molecules have been adsorbed, q(Au_{10})= -0.56 |e| for the perfect surface and -1.87 |e| for the F centre. It is important to note that regardless of the system, the degree of electron transfer is the same for both systems. Addition of one (three) CO molecule(s) reduces the gold cluster by 0.12 (0.32) electrons on the perfect surface and 0.14 (0.32) electrons on the F centre. Also, the charge on the gold atom to which CO molecules are bound is almost a constant, +0.15 |e| to +0.18 |e|. This shows that the charge inside Au_{10} is not uniform, which was also the case for the clusters without adsorbate.

Interestingly, the charging of the CO molecule, δq(CO), does not follow exactly the trends extracted from the results of CO adsorption on a single gold atom. The charge transfer for the perfect surface case (0.13 electrons) is less than on the vacancy (0.08 electrons).

However, when three CO molecules are adsorbed, δq(CO) decreases on average from -0.13 |e| to -0.10 |e| on the perfect surface.

The adsorption energy of one CO molecule on the gold cluster supported on the perfect MgO(001) surface (-3.13 eV) is higher than that on the F centre (-2.97 eV), as was found for the single gold atom. The d(C–O) bond length for the three CO molecules adsorbed instead of one or when the system is changed from the perfect surface to the F centre is 1.19 Å, close to what was found for the single atom Au^0. The distance of the carbon to the gold atom d(C–Au) is also almost a constant at 1.99 Å and is shorter than all the d(C–Au) distances calculated for the single gold atom, especially Au^0. This is usually believed to be due to an even more extensive development of M–C π-back-bonding.[62]

Finally, the CO stretching vibrational frequency is calculated and ranges from 1768 cm^{-1} for one CO molecule on Au_{10} supported on the perfect surface, to 1834 cm^{-1} for three CO molecules adsorbed on Au_{10} supported on the F centre surface. These frequencies are quite low and similar to what was calculated for the single Au^0 atom. The charge on the gold cluster plays a direct and important role again. On the perfect surface, the frequency increases by 31 cm^{-1} when three CO molecules are adsorbed instead of one. On the F centre, the frequency only increases by 5 cm^{-1}. This correlates with what was found for the single gold atom. The F centre acts a charge reservoir and it does not matter how many CO molecules are adsorbed (i.e. one or three), it can provide them with enough electrons and the vibrational frequency changes only marginally (only by 5 cm^{-1}). On the contrary, this does not hold for the gold cluster supported on the perfect surface, and there is a significant change of more than 30 cm^{-1} in the calculated CO stretch frequency.

Also, the bond angle Au-C-O has a value roughly equal to 160°, reflecting the rather small charge transfer to the CO molecule, illustrated by δq(CO) in Table 6.13.

We can already conclude here that the ten atom gold cluster supported on the MgO(001) surface with or without F centre, is not saturated by one or even three adsorbed CO molecules. We can expect the cluster to adsorb more than three CO molecules and in the next subsection we will put Au_{10} in a "saturation" condition.

It must be noticed that several configurations and adsorption sites for CO seem possible, other than with one molecule on each of the topmost three atoms of Au_{10}. As none of these has been attempted; the work is therefore non conclusive as several alternative and competitive configurations are possible.

	Perfect, 1 CO	Perfect, 3 CO	F centre, 1 CO	F centre, 3 CO
υ(CO) (cm^{-1})	1768	1799	1829	1834
E_{ads} (ev)	-3.13	-3.81^a	-2.97	-3.47^a
without BSSE	-3.40	-4.62^a	-3.27	-4.30^a
d(C–O) (Å)	1.193	*1.19*	1.188	*1.19*
d(C–Au) (Å)	1.985	*1.98*	1.969	*1.99*
Au-C-O (degree)	152.9	*159.6*	169.2	*161.2*
q(Au_{10}) (|e|) without CO	-0.88		-2.19	
q(Au_{10}) (|e|)	-0.76	-0.56	-2.05	-1.87
q(Au) (|e|)	+0.17	*+0.16*	+0.18	*+0.15*
δq(C) (|e|)	-0.10	*-0.05*	+0.01	*-0.05*
δq(O) (|e|)	-0.03	*-0.05*	-0.09	*-0.06*
δq(CO) (|e|)	-0.13	*-0.10*	-0.08	*-0.11*

Table 6.13 Calculated properties for CO adsorbed onto Au_{10} supported on MgO(001), with and without F centre. q(X) represents the Bader charge of species X, δq(X) is the change of charge of species X between free CO molecule in the gas phase and adsorbed CO, υ(CO) is the stretching vibrational frequency of CO once adsorbed on Au. The other properties are self-explanatory. ^{a} E_{ads} for three CO molecules.

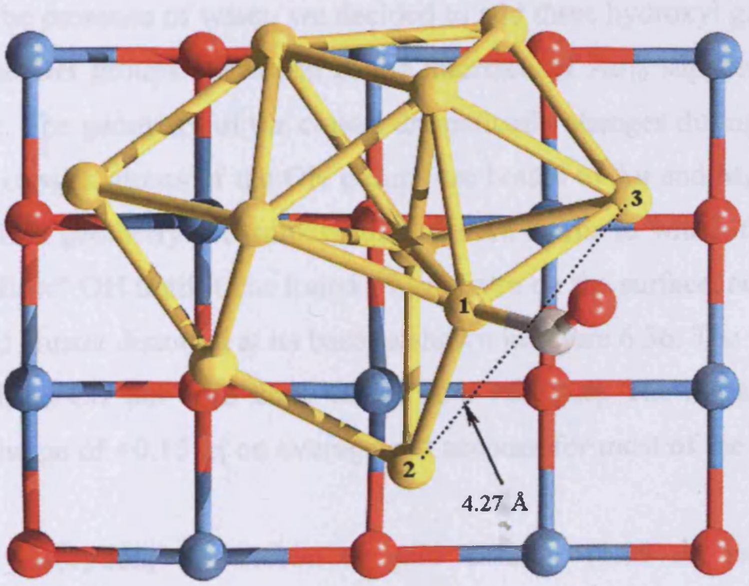

Figure 6.34 Geometry of the CO molecule adsorbed onto Au_{10} supported on the non-defective MgO(001) surface. Oxygen atoms in red, magnesium in blue and carbon in grey.

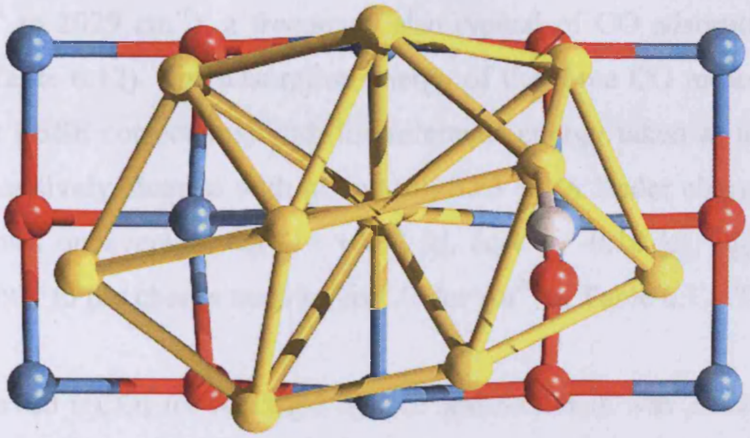

Figure 6.35 Geometry of the CO molecule adsorbed onto Au_{10} supported on the F centre of MgO(001). Oxygen atoms in red, magnesium in blue and carbon in grey.

6.6.3 Au_{10} with three CO and three OH

Most work in surface science is done in ultrahigh vacuum, while measurement of the activity of real catalysts are conducted in fixed bed flow reactors using reactant gas containing moisture of at least 1 ppm, usually 10 ppm. It was speculated that H_2O enhances the dissociation of O_2 at the perimeter interface around Au particles, stabilising the cationic species; the presence of OH^- groups is also expected.[64] In order to increase the oxidation state of Au and model the presence of water, we decided to add three hydroxyl groups as presented in figure 6.36. The OH groups are added at the interface of Au_{10} supported on the perfect MgO(001) surface. The geometry of the cluster dramatically changes during the course of the optimisation. The oxygen atoms of the OH groups are bound to Au and Mg at the same time in the final optimised geometry. To achieve this, the Au atoms to which the OH groups are bound have to “follow” OH until it has found a Mg centre on the surface, acting as an anchor. The result is a gold cluster distorted at its base as shown in figure 6.36. The total Bader charge of the cluster without CO but with three OH is now +0.52 |e|. The Au atoms with an OH group, present a charge of +0.15 |e| on average and account for most of the positive charge of Au_{10}.

After CO adsorption, the carbon to gold distance (1.99 Å) remains unchanged compared to what it was without the presence of any OH groups (1.98 Å) but the CO bond length has decreased from ~1.19 Å to 1.163 Å, which, we have shown, is typical of CO adsorbed on cationic gold. As a result, the calculated vibrational frequency shifts by 205 cm^{-1} (from 1824 cm^{-1} to 2029 cm^{-1}), a frequency also typical of CO adsorption on monoatomic oxidised gold (Table 6.12). The adsorption energy of the three CO molecules is -3.87 eV (-4.63 eV without BSSE corrections) with the reference energy taken as that of $3\times CO_{(g)}$. The gold cluster is positively charged with $q(Au_{10})= +0.83$ |e|. A Bader charge analysis on the C and O atoms gives on average, $\delta q(C)= +0.02$ |e|, $\delta q(O)= -0.10$ |e|, $\delta q(CO)= -0.08$ |e| and corresponds exactly to the charge transfer on CO for Au^{III} in Table 6.12. The average Au-C-O angle is 162.6°.

The observed $\upsilon(CO)$ for Au/MgO by Lee and Schwank was 2040 cm^{-1} and attributed to multi-bonded CO.[72] This value is very close to our calculated $\upsilon(CO)$ of 2029 cm^{-1} for CO on "saturated" Au_{10} and does not correspond to a negatively charged cluster in our model. We believe that a comparison to the $\upsilon(CO)$ values calculated can give an estimate of the amount of charging and thereby provide information on the underlying substrate sites. We have shown that supported anionic Au can provide for stronger π-back-donation than the cationic species. It must be noticed that in contrast to most other transition metals the *d*-shell in Au is closed and lowered in energy and consequently appears to be less important for the bonding in gold carbonyls. This is reflected in the blue shift of ~100 cm^{-1} for ν(CO) in cations of Au clusters compared to rhodium.[73] Also, a polarisation effect is believed to influence the CO bond strength: on positively charged metal centres the electric field opposes the polarisation of the bonding orbitals of CO, leading to a strengthening of the C–O bond and to a rising of the stretching force constant.[74]

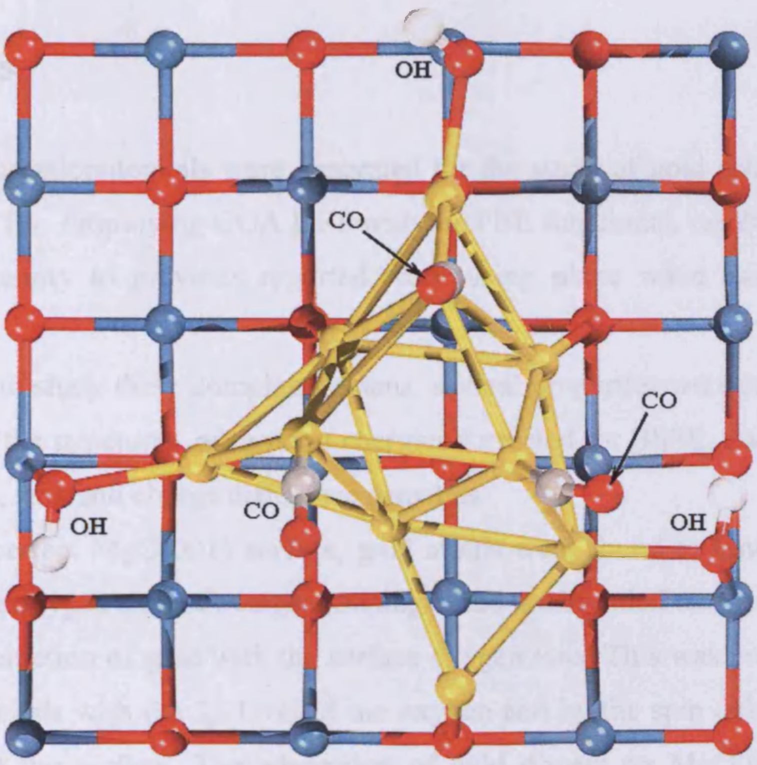

Figure 6.36 Au_{10} cluster supported on non-defective MgO(001) with three CO molecules adsorbed on the top and three OH groups adsorbed at the interface. Oxygen atoms in red, magnesium in blue, carbon in grey and hydrogen in white.

Conclusions

Several pseudopotentials were generated for the study of gold catalysts supported on MgO with SIESTA. Employing GGA DFT with the PBE functional, results were shown to be of equivalent quality to previous reported work using plane wave basis sets for similar systems.

In order to study these complex systems, several properties were calculated, including the geometry of the structures, adsorption energies corrected for BSSE, Bader atomic charges, density of states, spin and charge difference densities.

On the perfect MgO(001) surface, gold atoms were found to bind more strongly on five-coordinated oxygen sites. Covalent bonding could not be ruled out and was found to play a role in the interaction of gold with the surface oxygen ions. This was proven by the mixing of the Au 6*s* orbitals with the 2*p* level of the oxygen and by the spin delocalisation over the oxygen atom of the surface. The adsorption of gold dimers on MgO(001), vertically and parallel to the surface, clearly showed that three-dimensional growth is favoured over two-dimensional growth. Even though the gold dimer in its vertical orientation presents only one atom in contact with a surface oxygen, its adsorption energy was found to be 0.49 eV higher than that of a single gold atom on the same site. As for the dimer parallel to the surface, in its most stable orientation, the adsorption energy was found to be 0.24 eV less than that of the single gold atom on a five-coordinated oxygen, even though the dimer in this case had two gold atoms in direct contact with the surface oxygens. The Au_{10} cluster in its semi-dodecahedra geometry was adsorbed onto the MgO(001) surface and was found to interact quite strongly with the oxygen atoms, presenting an interaction energy of -1.97 eV with the surface. The cluster was globally negatively charged (-0.88 |e|) and this charge was located on the bottom layer of the semi-dodecahedra structure.

A defect on MgO(001) was then introduced as a surface oxygen was removed, creating a F centre with two localised electrons. A single gold atom was first added on this oxygen vacancy and found to be strongly adsorbed, with an adsorption energy (-2.83 eV) almost four times higher than that for the gold atom on the five-coordinated oxygen. A consequent charge transfer from the F centre to the gold atom occurred and the latter was then negatively charged (-1.12 |e|), having gained 0.81 electrons *vs.* the perfect surface. On the F centre, the gold dimer was found to be more strongly adsorbed with a gold atom directly on top of the vacancy and the other one on top of a surface magnesium. The favoured binding to magnesium was explained by the fact that upon adsorption onto the F centre, the gold dimer becomes negatively charged (-1.65 |e|) and is further stabilised by interacting with a surface cation. Finally, the ten atom gold cluster was adsorbed onto the F centre, in both bi-capped anti-prism and semi-dodecahedron geometries. The bi-capped anti-prism geometry retained its gas phase structure, the F centres acting as an anchorage point. The semi-dodecahedra cluster was found to bind more strongly to the F centre than the bi-capped anti-prism one, with an interaction energy of -5.43 eV, almost twice that of the bi-capped anti-prism. However in both cases, the charge distribution in the cluster followed a layer-like ordering, with the bottom layers always more negatively charged than the top ones. The semi-dodecahedra structure was found to be more negatively charged (-2.19 |e|) than the bi-capped prism (-1.71 |e|) since more gold atoms were in direct contact with surface oxygens.

Kink sites are believed to play an important role in the activity of many catalysts. The MgO(1 3 10) and MgO(1 3 12) kinked surfaces were employed to study the interaction of gold with this kind of defect. The strongest adsorption for a single gold atom at the kink site of the MgO(1 3 10) surface was calculated to be -1.08 eV, 0.3 eV higher than that on a five-coordinated oxygen of the MgO(001) surface. The gold atom then exhibits a charge of -0.28 |e|, which we calculated, was donated from only one particular oxygen atom of the kink site. As for the perfect MgO(001) surface, covalent bonding played a non-negligible role. The Au_{10} cluster was adsorbed at the kink site of the MgO(1 3 12) surface. Although starting from a bi-capped geometry, the structure of the cluster dramatically changed during geometry optimisation to adopt a semi-dodecahedra-like structure. A high binding energy of more than 10 eV was calculated and the gold atoms interacted preferably with the oxygen atoms of the kink. As the cluster became negatively charged, it also interacted strongly with a magnesium atom belonging to the next kink site of the surface.

Lastly, hydroxyl groups were employed to tailor the gold charge and CO was used as a probe molecule in order to assess the importance of the oxidation state in Au/MgO catalysts. It was found that increasing the number of OH groups also increases the oxidation state of gold. A single gold atom on the perfect MgO(001) surface was first employed in order to obtain initial trends. The CO stretching vibrational frequency ν(CO) increased with an increase of the oxidation state of the gold atom. This was explained by a decrease of the charge transfer to the CO molecule as gold lost electrons while seeing its oxidation state augmented. It was also noticed that the AuCO bond angle can be used as an indicator of the charge state of the host and follows the same trends as the adsorption energy. The strongest interaction of CO with gold was obtained for Au(I) (E_{ads}=-2.17 eV). Gold in its Au(III) oxidation state was however not able to chemisorb CO (E_{ads}= +2.44 eV). We then turned our attention to the Au_{10} gold cluster in its semi-dodecahedra geometry, adsorbed on MgO(001) where both the perfect surface and F centre cases were considered. A steady decrease of the Au_{10} negative charge was observed as the number of adsorbed CO increased. Each adsorbed CO molecule brought the gold clusters closer to a cationic state, the F centre acting as a reservoir of electrons. However, even with three CO molecules adsorbed on Au_{10} supported on the perfect MgO(001) surface, the gold cluster retained a negative charge, reflected in the calculated ν(CO), all lower than experimentally observed. Adding three hydroxyl groups at the interface with the perfect MgO(001) surface was finally found to be enough to make the cluster positively charged (+0.83 |e|) when it has three CO molecules adsorbed. The calculated ν(CO) is then 2029 cm^{-1}, representing an increase of 230 cm^{-1} *vs.* the same system without any OH groups.

References

1. N. Lopez and J.K. Nørskov, *Surf. Sci.*, 2002, **515**, 175-186.
2. N. Lopez, J.K. Nørskov, T.V.W. Janssens, A. Carlsson, A. Puig-Molina, B.S. Clausen, and J.-D. Grunwaldt, *J. Catal.*, 2004, **225**, 86-94.
3. A. Vijay, G. Mills, and H. Metiu, *J. Chem. Phys.*, 2003, **118**, 6536-6551.
4. E. Wahlström, N. Lopez, R. Schaub, P. Thostrup, A. Rønnau, C. Africh, E. Lægsgaard, J.K. Nørskov, and F. Besenbacher, *Phys. Rev. Lett.*, 2003, **90**, 026101-1.
5. H. Hakkinen, S. Abbet, A. Sanchez, U. Heiz, and U. Landman, *Angew. Chem. Int.*, 2003, **42**, 1297-1300.
6. A. Sanchez, S. Abbet, U. Heiz, W.-D. Schneider, H. Hakkinen, R.N. Barnett, and U. Landman, *J. Phys. Chem. A*, 1999, **103**, 9573-9578.
7. W.T. Wallace, B.K. Min, and D.W. Goodman, *J. Mol. Catal. A: Chem.*, 2005, **228**, 3-10.
8. Z. Yang, R. Wu, Q. Zhang, and D.W. Goodman, *Phys. Rev. B*, 2002, **65**, 155407.
9. I. Yudanov, G. Pacchioni, K. Neyman, and N. Rösch, *J. Phys. Chem. B*, 1997, **101**, 2786-2792.
10. L.M. Molina and B. Hammer, *Phys. Rev. B*, 2004, **69**, 155424.
11. B. Yoon, H. Häkkinen, U. Landman, A.S. Wörz, J.-M. Antonietti, S. Abbet, K. Judai, and U. Heiz, *Science*, 2005, **307**, 403-407.
12. M. Kubo, R. Miura, R. Yamauchi, R. Vetrivel, and A. Miyamoto, *Appl. Surf. Sci.*, 1995, **89**, 131-139.
13. A. Del Vitto, G. Pacchioni, F. Delbecq, and P. Sautet, *J. Phys. Chem. B*, 2005, **109**, 8040-8048.
14. M. Anpo, Y. Yamada, Y. Kubokawa, S. Coluccia, and A. Zecchina, *J. Chem. Soc., Faraday Trans. 1*, 1988, **84**, 751-764.
15. E. Garrone, A. Zecchina, and F.S. Stone, *Philos. Mag. B*, 1980, **42**, 683.
16. J.M. Soler, E. Artacho, J.D. Gale, A. García, J. Junquera, P. Ordejón, and D. Sánchez-Portal, *J. Phys.: Condens. Matter*, 2002, **14**, 2745-2779.
17. J.P. Perdew, K. Burke, and M. Ernzerhof, *Phys. Rev. Lett.*, 1996, **77**, 3865-3868.
18. N. Troullier and J.L. Martins, *Phys. Rev. B*, 1991, **43**, 1993.
19. S.G. Louie, S. Froyen, and M.L. Cohen, *Phys. Rev. B*, 1982, **26**, 1738.
20. L. Kleinman and D.M. Bylander, *Phys. Rev. Lett.*, 1982, **48**, 1425.
21. S. Schinkte, S. Messerli, M. Pivetta, F. Patthey, L. Libioulle, M. Stengel, A. De Vita, and W.-D. Schneider, *Phys. Rev. Lett.*, 2001, **87**, 276801.
22. G. Henkelman, A. Arnaldsson, and H. Jónsson, *Comput. Mat. Sci.*, 2005, (in press).
23. R. Bader, *Atoms in Molecules: A quantum Theory*. 1990, New York: Oxford University Press.
24. A. Kokalj, *J. Mol. Graphics Modelling*, 1999, **17**, 176-179.
25. D. Taylor, *Brit. Ceram. Trans. J.*, 1984, **83**, 5-9.
26. R.C. Whited, C.J. Flaten, and W.C. Walker, *Solid State Commun,*, 1973, **13**, 1903-1905.
27. M. Hybertsen and S.G. Louie, *Comments Condens. Matter Phys.*, 1987, **13**, 5.
28. U. Schönberger and F. Aryasetiawan, *Phys. Rev. B*, 1995, **52**, 8788-8793.
29. M.E. Straumanis, *J. Mater. Sci.*, 1988, **23**, 757-760.
30. J.M. Soler, M.R. Beltrán, K. Michaelian, I.L. Garzón, P. Ordejón, D. Sánchez-Portal, and E. Artacho, *Phys. Rev. B*, 2000, **61**, 5771-5780.
31. K.P. Huber and G. Herzberg, *Molecular Spectra and Molecular Structure Constants of Diatomic Molecules*. 1979, New York: Van Nostrand.
32. R.J. Bartlett, *J. Phys. Chem.*, 1989, **93**, 1697.

33. C. Hampel, K. Peterson, and H.-J. Werner, *Chem. Phys. Lett.*, 1992, **190**, 1.
34. S.A. Varganov, R.M. Olson, and M.S. Gordon, *J. Chem. Phys.*, 2003, **119**, 2531-2537.
35. U. Kaldor and B.A. Hess, *Chem. Phys. Lett.*, 1994, **230**, 1-7.
36. N.T. Wilson and R.L. Johnston, *Eur. Phys. J. D*, 2000, **12**, 161-169.
37. J. Rogan, R. Ramírez, A.H. Romero, and M. Kiwi, *Eur. Phys. J. D*, 2003, **28**, 219-228.
38. A. Bogicevic and D.R. Jennison, *Surf. Sci.*, 2002, **515**, L481-L486.
39. N. Lopez and J.K. Nørskov, *J. Am. Chem. Soc.*, 2002, **124**, 11262-11263.
40. E. Scorza, U. Birkenheuer, and C. Pisani, *J. Phys. Chem.*, 1997, **107**, 9645.
41. G. Pacchioni and P. Pescarmona, *Surf. Sci.*, 1998, **657**, 412.
42. P.V. Sushko, A.L. Shluger, and C.R.A. Catlow, *Surf. Sci.*, 2000, **450**, 153.
43. A.L. Shluger, L.N. Kantorovitch, A.I. Livshits, and M.J. Gillan, *Phys. Rev. B*, 1997, **56**, 15332.
44. A.M. Ferrari and G. Pacchioni, *J. Phys. Chem.*, 1995, **107**, 9645.
45. L.N. Kantorovitch, J.M. Holender, and M.J. Gillan, *Surf. Sci.*, 1995, **343**, 221.
46. Y.F. Zhukovskii and E.A. Kotomin, *Phys. Stat. Sol. (c)*, 2005, **2**, 347-350.
47. A.V. Matveev, K.M. Neuman, I.V. Yudanov, and N. Rösch, *Surf. Sci.*, 1999, **246**, 123.
48. C. Di Valentin, L. Giordano, G. Pacchioni, and N. Rösch, *Surf. Sci.*, 2003, **522**, 175-184.
49. H. Häkkinen and U. Landman, *Phys. Rev. B*, 2000, **62**, R2287.
50. H. Häkkinen, M. Moseler, and U. Landman, *Phys. Rev. Lett.*, 2002, **89**, 033401.
51. F. Furche, R. Ahlrichs, P. Weis, C. Jacob, S. Gilb, T. Bierweiller, and M.M. Kappes, *J. Chem. Phys.*, 2002, **117**, 6982.
52. L.M. Molina, M.D. Rasmussen, and B. Hammer, *J. Chem. Phys.*, 2004, **120**, 7673-7680.
53. J. Guzmann and B.C. Gates, *J. Am. Chem. Soc.*, 2004, **126**, 2672-2673.
54. M. Haruta, *CATTECH*, 2002, **6**, 102-115.
55. D.M. Cox, R. Brickman, K. Creegan, and A. Kaldor, *Z. Phys. D.*, 1991, **19**, 353-355.
56. T. Tabakova, F. Boccuzzi, M. Manzoli, and D. Andreeva, *Appl. Cat. A: General*, 2003, **252**, 385-397.
57. M.D. Brookes and A.R.W. McKellar, *J. Chem. Phys.*, 1999, **111**, 7321-7328.
58. K.L. Bak, J. Gauss, T. Helgaker, P. Jørgensen, and J. Olsen, *Chem. Phys. Lett.*, 2000, **319**, 563.
59. H. Häkkinen and U. Landman, *J. Am. Chem. Soc.*, 2001, **123**, 9704-9705.
60. R.N. Barnett and U. Landman, *Phys. Rev. B*, 1993, **48**, 2081-2097.
61. L. Jiang and Q. Xu, *J. Phys. Chem. A*, 2005, **109**, 1026-1032.
62. F.A. Cotton, G. Wilkinson, C.A. Murillo, and M. Bochmann, *Advanced Inorganic Chemistry, Sixth Edition*. 1999, New York: John Wiley & Sons, Inc.
63. F. Moreau, G.C. Bond, and A.O. Taylor, *Chem. Commun.*, 2004, 1642-1643.
64. M. Haruta, *J. New. Mat. Electrochem. Systems*, 2004, **7**, 163-172.
65. Y.K. Zhang and W.T. Yang, *Phys. Rev. Lett.*, 1998, **80**, 890.
66. J.P. Perdew, *Phys. Rev. B*, 1986, **33**, 8822.
67. M. Gajdoš, A. Eichler, and J. Hafner, *J. Phys.: Condens. Matter*, 2004, **16**, 1141-1164.
68. H.J. Lee and W. Ho, *Science*, 1999, **286**, 1719.
69. L.-F. Yuan, J. Yang, Q. Li, and Q.-S. Zhu, *Phys. Rev. B*, 2001, **65**, 035415.
70. R. Hoffmann, *Solids and Surfaces: A Chemist's View of Bonding in Extended Structures*. 1988: VCH, Verlag GmbH.
71. H. Häkkinen, S. Abbet, A. Sanchez, U. Heiz, and U. Landman, *Angew. Chem. Int.*, 2003, **42**, 1297-1300.
72. J. Lee, Y, and J. Schwank, *J. Catal.*, 1986, **102**, 207.
73. A. Fielicke, G. von Helden, G. Meijer, D.B. Pedersen, B. Simard, and D.M. Rayner, *J. Phys. Chem. B*, 2004, **108**, 14591.
74. A.S. Goldman and K. Krough-Jerspersen, *J. Am. Chem. Soc.*, 1996, **118**.

Chapter 7

General conclusions

The direct partial oxidation of methane and the catalysis by gold of various chemical reactions are topics of such complexity that suitable theoretical methods have only recently been developed. Modern computational techniques employing periodic DFT, whether using established plane wave basis set codes such as VASP, or recent local basis set methodologies as implemented in SIESTA, have played a crucial role in this work to elucidate fundamental processes.

Although largely accepted as an accurate method, DFT was shown to suffer from the electron self-interaction problem. The terminal oxygen defective $MoO_3(010)$ surface with two unpaired electrons on a molybdenum centre represented a difficult test case that DFT failed. On the other hand, both hybrid DFT, and DFT+U, were able to localise the two electrons. Hybrid DFT with the PBE0 functional was used to fit the Dudarev's parameter U–J in DFT+U and good correlations were found between the two methods. Infrared spectroscopy results[1] were in excellent agreement with the calculated vibrational frequency of the terminal oxygen stretch and the presence of two peaks in the experiment was reported to be due to the presence of terminal oxygen vacancy sites on the $MoO_3(010)$ surface. Molecular oxygen adsorbed readily on these defects to produce activated peroxo and superoxo species, the latter forcing its molybdenum substrate into a +V oxidation state, which has previously been detected by EPR.[2]

Methyl and hydrogen adsorption at the defect site was then studied in order to probe the chemical reactivity of methane. Employing DFT+U, the asymmetric oxygen centre was found to be preferred for both H and CH_3 adsorption and the site lost its asymmetric character upon adsorption. Unlike predicted in previous DFT calculations[3], the bare molybdenum exhibited the weakest interaction with the adsorbate and hybrid DFT calculations suggested this to be due to an increase in the population of the $4d_{xz}$ and $4d_{yz}$ orbitals after terminal oxygen removal when DFT+U is employed. Not only was CH_3 calculated to be weakly bound to Mo but it was also found to be weakly adsorbed in an intermediate stage between Mo and its closest asymmetric oxygen, suggesting possible mobility for CH_3 on the surface.

A transition state for CH_4 activation on the terminal oxygen defective $MoO_3(010)$ surface was located with H and CH_3 respectively interacting with terminal oxygen and molybdenum atoms. A Bader charge analysis of this transition state revealed the C–H bond to be polarised and this, coupled with spin population analysis where the spin on the molybdenum splits in two, indicated the cleavage to be heterolytic. An activation energy of 129.7 kJ mol^{-1} was computed and further lowered by 19.1 kJ mol^{-1} when CH_4 adsorption occurred on the bare molybdenum having already lost half of its spin population.

Gold adsorption and catalytic activity were studied on different morphologies of magnesia, including flat and kinked surfaces. On flat MgO(001), atomic gold was found to adsorb preferentially at five-coordinated oxygen sites and a non-negligible amount of covalent bonding was calculated. This contradicted the general idea that interaction is mainly due to polarization effects and weak ionic bonding.[4-6] Comparing the adsorption energies of Au_2 in different configurations, we also showed that three-dimensional growth is favoured over two-dimensional growth. Finally, the adsorbed Au_{10} cluster in a semi-dodecahedra geometry acquired a negative charge of -0.88 |e| which was located on the bottom layer of the cluster, as recently reported for Au_8[7].

On MgO(001), atomic gold adsorbed four times more strongly on a F centre than on a five-coordinated oxygen atom. This adsorption was accompanied by a significant charge transfer to the gold atom (0.81 more electrons than on the five-coordinated oxygen site). As for Au_{10} on the perfect MgO(001) surface, the charge distribution in the adsorbed gold clusters on an F centre followed a layer-like ordering, with the bottom layers always more negatively charged than the top ones. The semi-dodecahedra geometry was found to adsorb more strongly and to present a more important charging than the bi-capped anti-prism structure.

Atomic gold was then adsorbed at the oxygen kink site of the MgO(1 3 10) surface and presented an adsorption energy 0.30 eV higher than that on a five-coordinated oxygen of MgO(001). Depending on the catalyst preparation method, kink defects concentration can be more important than F centres concentration and our results suggest that gold atoms will preferentially adsorb at oxygen kink sites. The Au_{10} cluster was also adsorbed at the oxygen kink site of the MgO(1 3 12) surface and a strong interaction with oxygen was reported.

Finally, the influence of the gold oxidation state on the catalytic activity was assessed by tailoring the gold charge with hydroxyl groups and using CO as a probe molecule. Both atomic gold and Au_{10} clusters were employed and led to the same trend, *i.e.* the CO stretching vibrational frequency increased with an increase of the oxidation state of Au. While the strongest interaction of CO with atomic gold was obtained for Au(I), Au(III) did not have a favourable adsorption energy for chemisorbed CO, correlating recent experimental results showing that Au(I) is needed for the catalyst to be active[8]. Increasing the number of adsorbates (CO or OH) on the Au_{10} cluster also reduced its negative charge, bringing the cluster to a cationic state. However, in this case the F centre helped Au_{10} to retain a negative charge and thus increased the ability of the catalyst to adsorb more molecules. Unlike the positively charged cluster, the calculated stretching vibrational frequencies of CO adsorbed on a negatively charged gold particle were all lower than the reported experimental values[9], showing that the working catalyst should exhibit $Au^{\delta+}$ particles.

DFT, hybrid DFT and DFT+U have proved to be powerful techniques for the study of chemical reactions on the surfaces of metal oxides such as MoO_3 and MgO. The quality of the PP used is certainly as important as the quality and efficiency of the code itself. While VASP is widely known for its PP database, SIESTA is a rather recent code and requires the development of PP case by case. In this work, the gold PP we generated gave results of similar quality to the more established plane wave basis set codes. Density functional theory gives directly the density of electrons in the system being studied, this can be used to display inter-atomic interactions and calculate Bader charges. Geometrical properties and vibrational frequencies can also be calculated and we have shown that the obtained results are often in very good agreement with the experiment. Finally, localised basis set codes such as SIESTA, present an interesting alternative to plane wave basis set codes such as VASP, permitting the study of systems containing several hundreds of atoms.

The study of methane activation on defective $MoO_3(010)$ provided useful and new results both from a theoretical (DFT+U) and practical (C–H bond cleavage) point of view. The next step will consist in considering the oxidation of the methyl group, as already started with the study of activated oxygen species at the vacancy sites.

Gold supported on MgO was for the first time theoretically studied at kink sites with systems exhibiting more than 250 atoms. One of the most controversial subjects in gold catalysis, namely the oxidation state of Au, was successfully modelled and the ability to adsorb CO was studied. Having solely focused on adsorption processes, CO oxidation should now be studied and for that, an equivalent to the NEB method has to be implemented in SIESTA.

References

1. K.T. Queeney and C.M. Friend, *J. Phys. Chem. B*, 1998, **102**, 5178-5181.
2. L.E. Cadus, M.C. Abello, M.F. Gomez, and J.B. Rivarola, *Ind. Eng. Chem. Res.*, 1996, **35**, 14-18.
3. M. Chen, C.M. Friend, and E. Kaxiras, *J. Am. Chem. Soc.*, 2001, **123**, 2224-2230.
4. I. Yudanov, G. Pacchioni, K. Neyman, and N. Rösch, *J. Phys. Chem. B*, 1997, **101**, 2786-2792.
5. A. Bogicevic and D.R. Jennison, *Surf. Sci.*, 2002, **515**, L481-L486.
6. L.M. Molina and B. Hammer, *Phys. Rev. B*, 2004, **69**, 155424.
7. B. Yoon, H. Häkkinen, U. Landman, A.S. Wörz, J.-M. Antonietti, S. Abbet, K. Judai, and U. Heiz, *Science*, 2005, **307**, 403-407.
8. J. Guzmann and B.C. Gates, *J. Am. Chem. Soc.*, 2004, **126**, 2672-2673.
9. J. Lee, Y, and J. Schwank, *J. Catal.*, 1986, **102**, 207.

Appendix: The Metal–CO bonding mechanism

The CO molecules usually adsorb in an upright position with the intermolecular axis perpendicular to the metal surface, with the carbon atom at the bottom bonded to the metal surface, while the oxygen atom is not in direct contact with the surface. Fig. A.1 illustrates the outermost molecular orbitals of the CO molecule and indicates how the CO molecule binds to the metal surface (platinum for example).

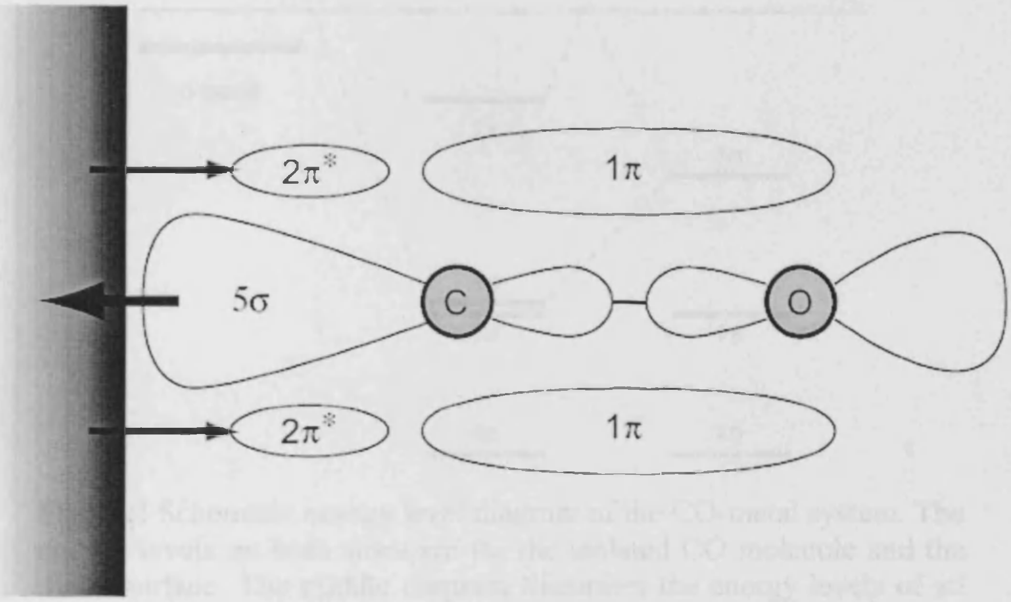

Fig. A.1 Schematic diagram showing the bonding character of a CO molecule adsorbed on a metal surface. The CO–metal bond is provided by the most extended orbital of the molecule which is the 5σ orbital. Charge back donation from the metal into the formerly empty 2π* orbitals is indicated by thin arrows.[1]

The energetically highest occupied orbital and thus also the spatially most extended one is the 5σ orbital which is located mainly on the carbon atom. Therefore, it is intuitively reasonable that the CO molecule tries to attach its "softest" part to the metal surface in the surface chemical bond. The initial step in binding is therefore a 5σ-to-metal charge transfer. This charge transfer is compensated partly by back donation of charge from the metal surface onto the CO molecule. This back donated charge is into an orbital that is a mixture of the 2π* of the free CO molecule with the metal *d* band.[2] It is interesting to note that in the free CO molecule, the 2π* orbital is about 1.5 eV above the vacuum level E_v, and the hybridisation with the metal *d* band causes it to locate below E_v.[3]

Fig. A.2 illustrates the energy levels of the orbitals for free CO molecules and chemisorbed CO molecules on metal surfaces.

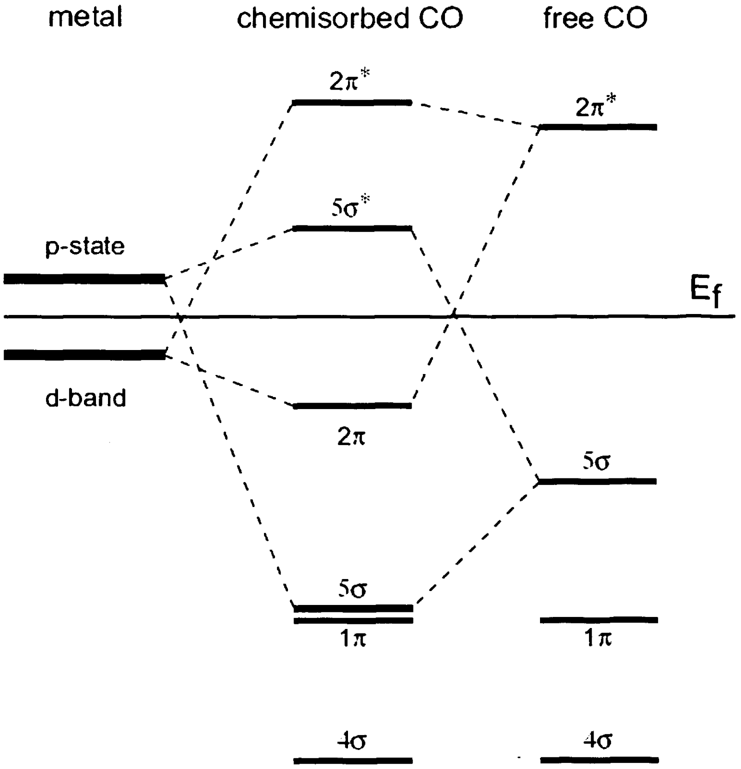

Fig. A.2 Schematic energy level diagram of the CO-metal system. The energy levels on both sides are for the isolated CO molecule and the metal surface. The middle diagram illustrates the energy levels of an adsorbed CO molecule. Band splitting for the adsorbed CO happens for the 5σ and 2π* levels due to hybridisation with the metal *d* band and the *p* orbitals.[1]

When CO molecules are brought into contact with a metal surface, the 5σ orbital of the CO molecule interacts with the *p* orbital of the metal atoms; the 5σ orbital mixes into bonding/anti-bonding combinations with the *d* band of the metal. The resulting bonding state is energetically only slightly higher than the 1π orbital, in contrast to its much higher energy position originally. The 2π* orbital also interacts with the *d* band causing a splitting into a bonding and an anti-bonding state. The bonding state is located well below the Fermi-edge E_f in energy, and hence provides a back donation channel for charge transferring from the metal to the CO molecule.

In a valence bond model the adsorption process can also be viewed as the partial breaking of the internal bonds in the CO gas molecule which is then compensated by the formation of the surface chemical bond to the metal substrate.[4]

References

1. S. Hüfner, *Photoelectron Spectroscopy*. 1995, New York: Springer-Verlag.
2. G. Blyholder, *J. Vac. Sci. Technol.*, 1974, **11**, 865-868.
3. J.E. Demuth, D. Schmeisser, and P. Avouris, *Phys. Rev. Lett.*, 1981, **47**, 1166-1169.
4. A. Föhlisch, M. Nyberg, M. Bennich, L. Triguero, J. Hasselström, O. Karis, L.G.M. Pettersson, and A. Nilsson, *J. Chem. Phys.*, 2000, **112**, 1946-1958.